



The University of
Nottingham

UNITED KINGDOM • CHINA • MALAYSIA

Department of Chemical and Environmental Engineering

Characterisation of Churn Flow Coalescers (CFC) in Vertical Pipes

By

Aimé Uzochukwu Kanu, BEng (Hons)

Thesis submitted to the University of Nottingham
For the degree of Doctor of Philosophy

June 2013

ABSTRACT

The Gas-Liquid Cylindrical Cyclone (GLCC) separator is commonly used for the separation of oil and gas mixtures flowing from the well head. Similar to the design used by other separators, it has an inlet and two outlets for gas and liquid respectively. However, the inlet to the separator can either be single or dual type. The pipeline connection from the upstream preconditioning equipment (CFC) is inclined downwards and has a tangential inlet slot. The essence of having a downward inclination is to promote pre-separation of the fluid phases. On the other hand, a tangential inlet promotes circular fluid motion thereby inducing separation of the fluid phases by centrifugal forces.

Due to the complex behaviour of the flow within the GLCC, liquid carry over (LCO) as drops into the gas phase pipeline and gas carry under (GCU) as bubbles into the liquid phase pipeline are inevitable. Both phenomena greatly reduce the purity of the fluid phases at the outlets. To overcome this challenge, it has been proposed from field experiments carried out by Chevron Energy Technology Company, to precondition the influent flow in an upstream vertical pipe before entrance to the GLCC. In order words, a suggested solution to overcoming liquid carry over (LCO) and gas carry under (GCU) is to precondition the oil/gas mixture by forcing small bubbles/drops of 3 – 5mm in diameter to coalesce in an upstream vertical pipe. The upstream vertical preconditioner is known as a Churn Flow Coalescer (CFC). This is because the churn flow regime is the most suitable for the coalescence of both liquid and gas phases. Therefore, it is in the scope of this research work to carry out detailed preconditioning experiments within an upstream vertical pipe that serves the purpose of a Churn Flow Coalescer (CFC). All experiments in this research work have been carried out in the Chemical and Environmental Engineering L3 laboratory at the University of Nottingham. Although, the churn flow regime is specifically the most suitable for the GLCC, the operational envelope for the initial set of experiments spans the bubble to churn regimes. This

is because the experiments were performed with the aim of delineating the conditions for the inception of typical churn flow in a large diameter pipe. These set of experiments were conducted in a 121mm internal diameter, 5.3m in length vertical pipe using air and water as the operating fluids. In these experiments, slug flow characterised by a Taylor bubble and a liquid slug was not observed. The churn flow regime is made up of two sub-regimes namely: liquid bridging of the gas core and formation of huge waves. The former is a phenomenon that occurs when the liquid phase forms a bridge as a result of radial coalescence of the wave crests flowing about the pipe centreline and momentarily blocks the entire pipe cross-section. The huge waves occur when the liquid phase flows as waves on the inner walls of the pipe and about the pipe centreline having large amplitudes. Between bubble to churn flow regimes in these experiments, four regimes were observed namely, discrete bubbly flow and spherical cap bubbly flow which make up the bubbly flow regime, churn turbulent regime (transition region) and typical churn flow regime. These experiments paved way for detailed experiments to be carried within the churn flow regime.

Detailed churn flow experiments were then carried out in a large scale closed loop facility having an internal diameter of 127mm and a longer vertical pipe of 11m. The rationale for performing the experiments in this facility is because the facility offered a wider range of conditions within the churn flow compared to the first experimental rig facility. Data was acquired at $L/D = 2.4, 7.1, 30.7, 35.4$ and 82.7 which represent different axial distances from the gas-liquid injection at the base of the test section. Air and water were also used as the operating fluids. The void fraction data acquired at different axial distance from the injection varies logarithmically with increase in axial distance. The flow can be considered to be developed at $L/D = 82.7$ based on the void fraction. In addition, the frequency of liquid bridging of the gas core decays with increasing distance from the injection (downstream)

while the frequency of the huge waves and liquid structures entrained in the gas core increases downstream from the injection due to coalescence.

Finally, the effect of viscosity in the churn flow regime was investigated using air-glycerol/water as the fluid pairs in the same large scale loop facility. Two glycerol/water mixtures were used having viscosities of 12.2cP and 16.2cP respectively. The data was acquired at a suitable axial distance from the injection at $L/D = 65.5$. In this experimental campaign, the size and frequency of the liquid structures entrained in the gas core are larger compared to the liquid structures present when experiments were carried out using air-water as the operating fluids. As a result, this gives a bi-modal probability distribution for air-glycerol/water compared to air-water. Similar to the air-water experiments, the liquid bridging operating condition gives a high degree of coalescence of both phases. The mechanism of entrained liquid structure formation has been proposed based on the comparative study to the air-water experiments. A model has also been developed that predicts the effective length of pipe for the Churn Flow Coalescer (CFC). Overall, the liquid bridging sub-regime of churn flow should be the prevailing condition in the CFC to enhance proper separation of gas and liquid phases in the downstream GLCC separator.

LIST OF PUBLICATIONS

1. Kanu U.O.A., Hewakandamby N. B., Azzopardi B.J. and Kouba G.E. (2010). In favour of churn flow: further insights using advanced instrumentation. 8th International Conference on Multiphase Flow (ICMF) 2013, Jeju, Korea, May 26 – 31.
2. Kanu U.O.A., Hewakandamby N. B., Azzopardi B.J. and Kouba G.E. (2010). CFD simulation of churn flow using volume of fluid (VOF) model. 8th International Conference on Multiphase Flow (ICMF) 2013, Jeju, Korea, May 26 – 31.

DEDICATION

I dedicate this thesis to my Heavenly Father.

The King of kings and LORD of Lords.

Daddy Thank You, Thank You and Thank You Forever and Ever.

O God of Abraham, Isaac and Jacob I am truly GRATEFUL!!

...But the people who know their God, shall be Strong and do Great Exploits,

Daniel 11:32(Bible).

ACKNOWLEDGEMENTS

I will like to use this opportunity to thank my Mum and Dad for their help, love, provision, patience, guidance and support during this research project. I will like to thank my Aunty Bebe and other aunties, Uncle Clem and other uncles for their constant call to check whether I am still in my right frame of mind, their prayers and support. Also, my Grandma, Mrs Helen Okwuego, Ezinne my cousin and other cousins for their prayers and support.

To my supervisors Dr Buddhi Hewakandamby and Professor Barry Azzopardi for catering for me throughout the course of my PhD and their insightful discussions. They made me love churn flow. Thank you my *adopted* parents. Also to Gene Kouba of Chevron Energy Technology for his help and support

I will also like to thank all my colleagues, Mukhtar Abdulkadir, Nazrul Yusoff, Safa Sharaf, Peter Van der Meulen, Valente Hernandez-Perez, Lokman Abdulkareem, Mohammed Zangana, Abolore Abdulahi, Ezekiel Agunlejika, Olumayowa Kajero, Komonibo Ebiundu, Katerina Loizou, Voon Wong, Shara Mohammed, Zoe Rose, Stacy-Ann Lange, Rajab Omar and Josep Escrig for their help, discussions, prayers and support. Thanks guys!

To Paul Brahman who also goes by the name ‘Dadio’. Thank you so much for your tireless and unrelenting help during this project. Also, to the head technician Phil Bennett and other technicians, Fred, Reg, Mick, Mel and Marion for their co-operation, help and support. To a great number of people in the industry I worked with. Thanks you all for your help and support.

To all my friends at St Barnabas Cathedral Nottingham, God bless you immensely. To the Lord Jesus Christ, the only Son of God who said to me: “My grace is sufficient, for my strength is made perfect in your weakness”... Amen. Thank you Lord, for it truly is. You are the MASTER. I am useless without you.

TABLE OF CONTENT

ABSTRACT	ii
LIST OF PUBLICATIONS	v
DEDICATION.....	vi
ACKNOWLEDGEMENTS	vii
TABLE OF CONTENT.....	viii
LIST OF FIGURES	xii
LIST OF TABLES	xxiv
CHAPTER 1.....	1
THESIS INTRODUCTION.....	1
1.1. Introduction.....	1
1.2. Background to Research	5
1.3. Problem Statement	6
1.4. Methodology	7
1.4.1. Experimental methods	7
1.5. Structure of Thesis	9
CHAPTER 2.....	12
LITERATURE REVIEW	12
2.1. Introduction.....	12
2.1.1. <i>Two phase flow (Separated Flow concept)</i>	12
2.1.1.1. <i>Void fraction</i>	12
2.1.1.2. <i>Pressure drop</i>	15
2.2. <i>Introduction to gas-liquid flow regimes</i>	16
2.2.1. <i>Gas-liquid flow regimes in vertical pipe</i>	16
2.2.1.1. <i>Bubbly flow</i>	16
2.2.1.2. <i>Slug flow</i>	16
2.2.1.3. <i>Churn flow</i>	17
2.2.1.4. <i>Annular flow</i>	18
2.2.1.5. <i>Wispy-annular flow</i>	19
2.3. <i>Flow Pattern maps</i>	20
2.3.1. <i>Experimental flow pattern map</i>	21
2.3.2. <i>Theoretical pattern map</i>	22
2.3.3. <i>Flow pattern transition mechanisms: Theoretical approach</i>	23
2.3.3.1. <i>Transition from Bubble flow</i>	23

<i>Type 1. Lenticular deformation</i>	25
<i>Type 2. Cigar-shaped deformation</i>	25
<i>Type 3. Bulgy deformation</i>	25
2.3.3.2. <i>Slug/Churn Transitions</i>	29
(a) <i>Wake effect mechanism</i>	31
(b) <i>Flooding mechanism</i>	32
(c) <i>Entrance effect mechanism</i>	33
(d) <i>Bubble coalescence mechanism</i>	34
2.3.3.3. <i>Churn/Annular Transitions</i>	34
2.4. <i>Further insights into churn flow</i>	43
2.4.1. <i>Pressure effects</i>	45
2.4.2. <i>Entrained fraction</i>	47
2.4.3. <i>Huge (Large) waves</i>	54
2.5. <i>Conclusion on Literature review</i>	57
CHAPTER 3	58
EXPERIMENTAL ARRANGEMENTS	58
3.1. 121mm internal diameter facility.....	58
3.1.1. <i>Overview of experimental facility</i>	58
3.1.2. <i>Start-up considerations</i>	60
3.1.3. <i>Injection device</i>	61
3.1.4. <i>Electromagnetic flowmeter (EMF)</i>	62
3.1.5. <i>Wire mesh sensor (WMS) data acquisition electronics</i>	64
3.1.5.1. <i>Permittivity measurement</i>	66
3.1.5.2. <i>Calibration routine</i>	67
3.1.5.3. <i>Wire mesh sensor performance evaluation</i>	69
3.1.6. <i>High speed visualization</i>	74
3.2. 127mm internal diameter facility.....	75
3.2.1. <i>Operating procedures for air-water experiments on 127mm ID facility</i>	75
3.2.2. <i>Operating procedures for air-glycerol/water experiments on 127mm ID facility</i>	79
3.2.2.1. <i>WMS data extraction applicable to air-glycerol/water experiments</i>	83
3.2.3. <i>Control processes for the 127mm internal diameter facility</i>	85
3.2.4. <i>Flowrate data acquisition</i>	85

CHAPTER 4	86
ESTABLISHING FLOW PATTERN TRANSITIONS FOR A CO-CURRENT AIR-WATER FLOW IN A LARGE DIAMETER VERTICAL PIPE	86
4.1. Introduction.....	86
4.2. Results.....	88
4.2.1. <i>Time series analysis</i>	88
4.2.2. <i>Extracted high-speed images</i>	91
4.2.3. <i>Cross sectional phase distribution</i>	94
4.2.4. <i>Statistical analysis of time series of void fraction</i>	95
4.2.5. <i>Interfacial structures</i>	101
4.2.6. <i>Spectral analysis</i>	106
4.2.7. <i>Radial phase distribution</i>	115
4.2.8. <i>Bubble size distribution</i>	121
4.3. <i>Further analysis to establish the bubble to churn transition</i>	124
4.3.1. <i>Drift flux model</i>	124
4.3.2. <i>Flow regime identification</i>	126
4.4. Summary	131
CHAPTER 5	133
BEHAVIOUR OF CHURN FLOW AND INSIGHTS INTO FLOW REGIME PHENOMENON	133
5.1. Introduction.....	133
5.2. Results.....	134
5.2.1. <i>Time Series of void fraction</i>	135
5.2.2. <i>Interfacial structures present</i>	139
5.2.2.1. <i>Interfacial structures at L/D = 7.1</i>	140
5.2.2.2. <i>Interfacial structures at L/D = 35.4</i>	143
5.2.2.3. <i>Interfacial structures at L/D = 82.7</i>	147
5.2.3. <i>Qualitative assessment on the cross section phase distribution</i>	152
5.2.4. <i>Extraction of chordal data</i>	154
5.2.5. <i>Statistical analysis of time series data</i>	161
5.2.6. <i>Spectral analysis of time series data</i>	164
5.2.7. <i>Stability analysis by method of Barnea (1986)</i>	172
5.3. Summary	178
CHAPTER 6	178
EFFECT OF LIQUID VISCOSITY ON CHURN FLOW PATTERN IN VERTICAL UPWARD GAS-LIQUID FLOW	180
6.1. Introduction.....	180

6.2. Results.....	182
6.2.1. <i>Comparison of time series data for air-water and air-glycerol/water</i>	182
6.2.2. <i>Comparison glycerol-water data with void fraction correlations.....</i>	187
6.2.3. <i>Probability density function (PDF) of time series data</i>	191
6.2.4. <i>Comparison of interfacial structures for air-glycerol/water and air-water.....</i>	194
6.2.5. <i>Extraction of base film and huge wave characteristics from liquid holdup</i>	196
6.2.6. <i>Analysis of time series in frequency domain</i>	203
6.2.6.1. <i>Qualitative assessment of entrained liquid structures</i>	210
6.2.6.2. <i>Establishing relevant threshold from time series data</i>	216
6.3. Further analysis of experimental data	226
6.3.1. <i>Flow pattern map.....</i>	228
6.3.2. <i>Flow structure characterisation using Weber number.....</i>	230
6.4. Churn flow coalescer model development	234
6.5. Summary	239
CHAPTER 7	241
CONCLUSIONS	241
CHAPTER 4 Conclusions - Bubbly to Churn flow transition <i>air-water experiments.....</i>	241
CHAPTER 5 Conclusions - Further insights into Churn flow <i>air-water experiments</i>	243
CHAPTER 6 Conclusions - Effect of liquid viscosity in Churn flow <i>air-glycerol/water experiments.....</i>	245
FUTURE WORK AND RECOMMENDATIONS	247
REFERENCES	249
NOMENCLATURE	260
APPENDIX A	262
APPENDIX B	263
APPENDIX C	265
APPENDIX D	266
APPENDIX E	269
APPENDIX F.....	272
UNCERTAINTY ANALYSIS	272

LIST OF FIGURES

Figure 1.1.Schematic of Chevron's GLCC showing multiphase metering loop Kouba and Shoham ,1995).(A) Multiphase flow from well-head (B) Gas (C) Liquid (D) Multiphase flow to pipeline.....	2
Figure 1.2. 'S' Curve for development ranking for Separation technology, Kouba and Shoham, 1995) (reproduced).	3
Figure 1.3. World's largest GLCC installed by Caltex Pacific Indonesia (CPI), (Tulsa University Separation Technology Projects website (TUSTP).	4
Figure 1.4. Laboratory Model of GLCC with Control Systems at the University of Tulsa, (Chirinos, 2008).	6
Figure 1.5. Research Layout for Churn Flow preconditioning experiments performed in this work.	11
Figure 2.1. Concept of gas-liquid flow in a pipe,(Azzopardi, 2006).	14
Figure 2.2. (a) Bubbly (b) Slug (c) Churn (d) Annular flow regimes in upward two-phase flow in vertical pipes (McQuillan and Whalley,1985).	17
Figure 2.3. (a) Wisp recorded by X-ray photography by Hewitt and Roberts (1969) 32mm pipe diameter(left) (b) Type of wisps from Hernandez <i>et al.</i> (2010) 67mm pipe diameter revealed by wire mesh sensor studies(right).....	20
Figure 2.4. Experimental flow pattern map of (Hewitt and Robert,1969).....	22
Figure 2.5. Theoretical flow pattern map of (Taitel <i>et al.</i> , 1980).	23
Figure 2.6. (a)-(c) Various types of deformation from Lenticular to Bulgy respectively, (Hinze, 1955).	25
Figure 2.7. Bubbly Flow pattern transitions from the work of (Ohnuki and Akimoto, 2000).	26
Figure 2.8. Bubble packing and coalescing pattern (Mishima and Ishii,1984).	28
Figure 2.9. Transitions from slug to churn flow.	30
Figure 2.10. Flow reversal and Flooding illustration in (a) and (b) respectively where the blue and red arrows are the liquid and gas inlets, (Hewitt and Hall-Taylor, 1970).....	35
Figure 2.11. Flooding data from McQuillan (1985) retrieved from (Govan <i>et al.</i> , 1991).....	36
Figure 2.12. Types of geometries used in flooding studies, (Govan <i>et al.</i> , 1991)	37
Figure 2.13. Flooding mechanism in test section with Porous outlet, (Govan <i>et al.</i> , 1991)....	39
Figure 2.14. Flooding mechanism in test section with Porous outlet, (Govan <i>et al.</i> , 1991)...	40
Figure 2.15. Flooding mechanism in test section with square-edged outlet, (Govan <i>et al.</i> , 1991).	41

Figure 2.16. Effect of liquid outlet geometry on Flooding, (Govan <i>et al.</i> ,1991).....	42
Figure 2.17. Optical arrangement for photochromic dye tracing (Hewitt <i>et al.</i> , 1985)	44
Figure 2.18. Postulated mechanism of churn flow (Hewitt <i>et al.</i> ,1985).....	45
Figure 2.19. Pressure gradient distribution against dimensionless gas velocity for gas-liquid flows in vertical pipes Owen (1986) retrieved from (Barbosa <i>et al.</i> ,2001b).	46
Figure 2.20. Mechanism of drop breakup (Azzopardi, 1997).....	48
Figure 2.21. Effect of gas velocity on entrained fraction on different pipe diameter.....	49
Figure 2.22. Droplet concentration in churn flow and annular flow, (Barbosa <i>et al.</i> , 2002)....	50
Figure 2.23. Comparison of experimental entrained fraction with correlation proposed by (Barbosa <i>et al.</i> ,2002).....	51
Figure 2.24. Schematic of T-junction retrieved from (Azzopardi, 2005).....	52
Figure 2.25. Showing accuracy of proposed entrance fraction correlation, (Azzopardi and Wren, 2004).	53
Figure 2.26. Identification of huge wave according to Barbosa <i>et al.</i> (2001b) and Wang <i>et al.</i> , (2012) in the left and right respectively.	54
Figure 2.27. Representative three dimensional structures developed on a semi-circular cross-section of the tube (Sekoguchi and Takeishi, 1989). (a) $U_{gs} = 5\text{m/s}$ and $U_{ls} = 0.3\text{m/s}$, (b) $U_{gs} = 7\text{m/s}$ and $U_{ls} = 0.3\text{m/s}$, and (c) $U_{gs} = 5\text{m/s}$ and $U_{ls} = 0.1\text{m/s}$ respectively.	55
Figure 2.28.Cross-sectional views of liquid lump, (Sekoguchi and Takeishi, 1989). The gas and liquid are shown as white and black respectively. Sekoguchi and Takeishi (1989 pointed out that huge waves have a higher transit velocity than liquid slugs.....	56
Figure 3.1. Schematic of the main parts of the 121mm internal diameter experimental facility, showing data acquisition location.....	59
Figure 3.2. (a) Vortex breaker (b) Flow straighteners installed (second straightener rotated 90°).	60
Figure 3.3. Designed venturi injection device used on the 121mm internal diameter, 5.3m in length experimental facility. The injection used is a modified venturi injection device having an air chamber to allow air flow.	62
Figure 3.4. Conventional electromagnetic flowmeter (EMF) from work done by (Cha <i>et al.</i> , 2002).	63
Figure 3.5. Block diagram for detecting and processing of signals, Cha <i>et al.</i> (2002).....	64
Figure 3.6. (a) Block diagram of capacitance sensor(b) Temporal excitation scheme of the transmitter electrodes with sinusoidal voltage excitation and the point of digitization with a an ADC controlled by the sample-and-hold signal, (Thiele <i>et al.</i> ,2009).....	65

Figure 3.7. Equivalent one-channel circuit for measuring the permittivity using the Capacitance wire mesh sensor (WMS), (Thiele <i>et al.</i> , 2009)	67
Figure 3.8. 32 x 32 Wire mesh sensor manufactured by Helmholtz-Zentrum Dresden-Rossendorf (HZDR) formerly known as Forschungszentrum Dresden-Rossendorf (FZDR).	69
Figure 3.9. Measured voltages from the measurement of different substance in a relative permittivity range of 1 – 80 according to (Thiele <i>et al.</i> , 2009).....	70
Figure 3.10. Histogram of the standard deviation in the measures voltages on each transmitter-receiver pair from 1000 frames for the evaluation of instrumental noise according to (Thiele <i>et al.</i> , 2009).....	71
Figure 3.11. Electronics time response for a permittivity step according to (Thiele <i>et al.</i> , 2009)	72
Figure 3.12. (a) Measured phase fraction distribution. (b) Calculated lines of equal phase fraction according to (Thiele <i>et al.</i> , 2009).	72
Figure 3.13. Experimental setup for the depth sensitivity estimation (b) Wetting level as a function of liquid film thickness measured in the experimental evaluation of depth sensitivity according to (Thiele <i>et al.</i> , 2009).....	73
Figure 3.14. High-speed setup for the 121mm internal diameter, 5.3m in length facility.....	74
Figure 3.15. Large scale two phase flow experimental facility. Schematic originally done by Omebere (2006) who previously worked on the facility. The internal diameter of the test section is 127mm and is 11m in length.....	77
Figure 3.16. (a) Pipe-in-pipe annulus type injection (b) Other component of the 127mm internal diameter facility.....	78
Figure 3.17. Liquid ring compressor motors as components of the 127mm internal diameter experimental facility.	79
Figure 3.18. Procedure for charging separator tank with glycerol and water respectively.	80
Figure 3.19. Beaker containing clear glycerol-water solution after 20-30 minutes start-up and shutdown of test facility. System power contributes significantly to mixing of pure glycerol and water to give a clear glycerol-water solution.	81
Figure 3.20. Brookfield Viscometer used in measuring viscosity.....	82
Figure 3.21. Obtaining surface tension of glycerol-water.	82
Figure 3.22. Data acquisition part of the test section showing test section with off white clear glycerol/water solution.....	83
Figure 3.23. Data acquisition workstation for air-glycerol/water experiments.	84

Figure 4.1. (a)-(d) Void fraction variation with time for constant liquid superficial velocities of 0.018m/s, 0.041m/s, 0.075m/s and 0.13m/s respectively. The gas superficial velocity is indicated in plot (d).....	89
Figure 4.2. High speed images captured using a Phantom v12.1 camera for (a) $U_{gs} = 0.21\text{m/s}$ and (b) $U_{gs} = 3.58\text{m/s}$ while keeping the liquid superficial velocity constant at $U_{ls} = 0.018\text{m/s}$	91
Figure 4.3. High speed images captured using a Phantom v12.1 camera for (a) $U_{gs} = 0.21\text{m/s}$ and (b) $U_{gs} = 3.58\text{m/s}$ while keeping the liquid superficial velocity constant at $U_{ls} = 0.13\text{m/s}$	933
Figure 4.4. Frame sequence for $U_{gs} = 0.21\text{m/s}$, 1.03m/s and 3.58m/s from top to bottom respectively at constant liquid superficial velocity of 0.13m/s extracted from the wire mesh sensor data.....	94
Figure 4.5. Variation of PDF with void fraction for increasing gas superficial velocities at constant liquid superficial velocity.	95
Figure 4.6. Variation of standard deviation, skewness and kurtosis of the time series data with gas superficial velocity.	97
Figure 4.7. Variation of mean void fraction with dimensionless gas velocity. Further comparisons have been made to the data of Szalinski et al. (2010) where bubble, slug and churn flows were observed in a 67mm diameter pipe having a length of 6m.	100
Figure 4.8. Interfacial structures at gas superficial velocities of 0.21m/s , 1.03m/s and 3.58m/s , for a constant liquid superficial velocity of 0.018m/s	101
Figure 4.9. Interfacial structures at gas superficial velocities of 0.21m/s , 1.03m/s and 3.58m/s , for a constant liquid superficial velocity of 0.075m/s	103
Figure 4.10. Interfacial structures at gas superficial velocities of 0.21m/s , 1.03m/s and 3.58m/s , for a constant liquid superficial velocity of 0.13m/s . Outline of huge waves (assumed to be <i>sinusoidal</i>) is shown in red. Liquid bridging of the gas core can either by complete or incomplete. Complete liquid bridging means radial coalescence of huge waves while in incomplete liquid bridging this is absent	104
Figure 4.11. Variation of PSD with Frequency for constant liquid superficial velocity and increasing gas superficial velocity as indicated.	107
Figure 4.12. Effect of liquid superficial velocity on the variation of PSD with Frequency for constant gas superficial velocity. Two distinct peaks can be observed. The peak at higher end of the spectrum can be attributed to the formation of wisps/huge waves.	108

Figure 4.13. Variation of dominant frequency with gas superficial velocity. Further comparison to the work done in a 67mm internal diameter pipe of (Hernandez -Perez <i>et al.</i> , 2010).....	110
Figure 4.14. Variation of gas based Strouhal number against Lockhart –Martinelli parameter by method of Azzopardi (2004).....	112
Figure 4.15. Comparison of experimental and predicted gas based Strouhal number according to Kaji <i>et al.</i> , (2009).....	113
Figure 4.16. Comparison of experimental and predicted Strouhal number based on mixture velocity according to Kaji <i>et al.</i> , (2009).....	113
Figure 4.17. Variation of gas based Strouhal number with mean void fraction comparison with (Kaji <i>et al.</i> , 2009).....	114
Figure 4.18. Variation of the gas based Strouhal number against dimensionless gas superficial velocity in equation (4.5) showing comparison with (Hernandez- Perez <i>et al.</i> , 2010). The periodicity of the structures for bubbly, slug and churn flows obtained by spectral analysis for data in the 67mm internal diameter pipe of Hernandez- Perez <i>et al.</i> (2010) can be said to be similar to the periodicity of the structures in the present work for a direct transition from bubbly to churn flows when air-water are the operating fluids.	115
Figure 4.19. Time-average variation of radial void fraction with dimensionless radial distance at constant liquid superficial velocities.....	116
Figure 4.20. (a) and (b) Experimental and predicted radial void fraction variation with dimensionless radial distance for constant liquid superficial velocities of 0.018m/s and 0.13m/s respectively.	118
Figure 4.21. Power law exponent variations with gas superficial velocity and comparison with the work of (Szalinski <i>et al.</i> ,2010).....	119
Figure 4.22. Holdup parameter against gas superficial velocity.....	120
Figure 4.23. Bubble size distributions for selected gas superficial velocity and increasing liquid superficial velocity of 0.018m/s, 0.075m/s and 0.13m/s from left to right respectively.	122
Figure 4.24. Bubble size distribution variation with dimensionless bubble diameter and comparison with (Szalinski <i>et al.</i> , 2010).	123
Figure 4.25. Variation of mean gas velocity with mixture velocity. Comparisons with the work of Omebere-Iyari <i>et al.</i> (2008) and Ohnuki and Akimoto(1996) from the conditions they observed bubbly flow to the churn-turbulent regime.....	125

Figure 4.26. Flow regime identification with blue, red and green transition lines of Taitel <i>et al.</i> (1980) and Schlegel <i>et al.</i> (2009) in 102mm diameter pipe.	127
Figure 4.27. Effect of larger diameter pipe from the work of Schlegel <i>et al.</i> (2009)	127
Figure 4.28. Comparison with transition lines of (Omebere-Iyari <i>et al.</i> , 2008).	128
Figure 4.29. Establishing the transition to typical churn flow with the inclusion of transition lines from the work done by previous authors. Hewitt and Robert (1969) (dash black line), Taitel <i>et al</i> (1980)(purple line), Sekoguchi and Takeishi (1989)(light-red line), Jayanti and Hewitt (1992)(light-blue line) and Sekoguchi and Mori (1997)(orange line).	129
Figure 4.30. Variation of mean gas velocity with mixture velocity and identification of regimes present.	130
Figure 5.1(a). Time series of void fraction at L/D = 35.4 and 82.7 axial distance from the injection for a liquid superficial velocity of 0.03m/s.	135
Figure 5.1(b). Time series of void fraction at L/D = 35.4 and 82.7 axial distance from the injection for a liquid superficial velocity of 0.24m/s. The dash line represents the occurrence of liquid bridging or the time between successive troughs.	137
Figure 5.2. Time series of void fraction at each axial distance shown in the graph(left) from the injection point for constant superficial gas velocity $U_{gs} = 3.26\text{m/s}$ for (a) $U_{ls} = 0.03\text{m/s}$ (b) $U_{ls} = 0.24\text{m/s}$	138
Figure 5.3. Interfacial structure of operating conditions at L/D = 7.1 for constant liquid superficial velocity of 0.03m/s, (a) $U_{gs} = 3.70\text{m/s}$ (b) 6.59m/s (c) 8.81m/s (Dark blue – suspended liquid, light blue – gas and purple – containing pipe) and the continuous phases were removed for clarity.	140
Figure 5.4. Interfacial structure of operating conditions at L/D = 7.1 for constant liquid superficial velocity of 0.13m/s (a) 5.28m/s (b) 7.08m/s (c) 10.58m/s . (Dark blue – suspended liquid, light blue – gas and purple – containing cylinder) and the continuous phases were removed for clarity.....	141
Figure 5.5. Interfacial structure of operating conditions at L/D = 7.1 for constant liquid superficial velocity of 0.24m/s (a) $U_{gs} = 4.54\text{m/s}$ (b) 7.20m/s (c) 11.42m/s (Dark blue – suspended liquid, light blue – gas and purple – containing cylinder) and the continuous phases were removed for clarity.	142
Figure 5.6. Interfacial structure of operating conditions at L/D = 35.4 for constant liquid superficial velocity of 0.03m/s (a) 3.70m/s (b) 6.59m/s (c) 8.81m/s (Dark blue – suspended liquid, light blue – gas and purple – containing cylinder) and the continuous phases were removed for clarity.....	144

Figure 5.7. Interfacial structure of operating conditions at L/D = 35.4 for constant liquid superficial velocity of 0.13m/s (a) 5.28m/s (b) 7.08m/s(c) 10.58m/s (Dark blue – suspended liquid, light blue – gas and purple – containing cylinder) and the continuous phases were removed for clarity. Outline of huge waves indicated in red.....	145
Figure 5.8. Interfacial structure of operating conditions at L/D = 35.4 for constant liquid superficial velocity of 0.24m/s (a) 4.54m/s (b) 7.20m/s(c) 11.42m/s. (Dark blue – suspended liquid, light blue – gas and purple – containing cylinder) and the continuous phases were removed for clarity.....	146
Figure 5.9. Interfacial structure of operating conditions at L/D = 82.7 for constant liquid superficial velocity of 0.03m/s (a) 3.70m/s (b) 6.59m/s(c) 8.81m/s (Dark blue – suspended liquid, light blue – gas and purple – containing cylinder) and the continuous phases were removed for clarity.....	149
Figure 5.10. Interfacial structure of operating conditions at L/D = 82.7 for constant liquid superficial velocity of 0.13m/s (a) 5.28m/s (b) 7.08m/s(c) 10.58m/s (Dark blue – suspended liquid, light blue – gas and purple – containing cylinder) and the continuous phases were removed for clarity.....	150
Figure 5.11. Interfacial structure of operating conditions at L/D = 82.7 for constant liquid superficial velocity of 0.24m/s (a) 4.54m/s (b) 7.20m/s (c) 11.42m/s. (Dark blue – suspended liquid, light blue – gas and purple – containing cylinder) and the continuous phases were removed for clarity.....	151
Figure 5.12. Stability of Huge waves and Liquid slugs within pipe cross-section in (a) and (b) respectively. Selected frame were extracted from the data at L/D = 35.4.....	153
Figure 5.13. Illustration of chordal void fraction extraction from wire mesh sensor data.	154
Figure 5.14. Time series of chordal void fraction at L/D = 7.1 (a) X = 16, Y = 16, (b) and(c) represent interfacial structures for a constant liquid superficial velocity of 0.24m/s and for gas superficial velocities of 4.54m/s, 5.76m/s, 7.20m/s, 8.11m/s and 11.42m/s from top to bottom respectively.....	156
Figure 5.15. Time series of chordal void fraction at L/D = 35.4 (a) X = 16, Y = 16, (b) and(c) represent interfacial structures for a constant liquid superficial velocity of 0.24m/s and for gas superficial velocities of 4.54m/s, 5.76m/s, 7.20m/s, 8.11m/s and 11.42m/s from top to bottom respectively.....	157
Figure 5.16. (1a-d) High speed images at gas superficial velocity of 3.26m/s and 11.42m/s for constant liquid superficial velocity of 0.24 at L/D = 82.7	159

Figure 5.17. Variation of mean void fraction with axial distance from injection for liquid superficial velocities of 0.03m/s, 0.13m/s, 0.18m/s and 0.24m/s as indicated in the respective plots.....	162
Figure 5.18. Variation of standard deviation and skewness of void fraction with dimensionless axial distance at liquid superficial velocities of 0.13m/s, 0.18m/s and 0.24m/s respectively.....	163
Figure 5.19. Power spectral density variation with frequency at a constant liquid superficial velocity of 0.18m/s.....	164
Figure 5.20. Variation of dominant frequency with dimensionless axial distance at liquid superficial velocities of 0.03m/s, 0.13m/s, 0.18m/s and 0.24m/s in (a)-(d) respectively.	165
Figure 5.21. Variation of dominant frequency with gas superficial velocity with comparisons made with the data of Omebere-Iyari (2006) who experimented on the same test facility and acquired data at $L/D = 65.5$. From his analysis, the flow is developed at this axial distance from the injection .The liquid superficial velocities for his cases are 0.05m/s in (a) and 0.1m/s in (b) and (c) respectively.	166
Figure 5.22. Comparison of experimental and predicted gas-based Strouhal number according to Kaji <i>et al.</i> (2009) against liquid holdup.....	169
Figure 5.23. Comparison of experimental and predicted gas based Strouhal number according to (Kaji <i>et al.</i> , 2009).....	170
Figure 5.24. Variation of Strouhal number based on mixture velocity with dimensionless axial distance (compared to the skewness variation with axial distance in Figure 5.18)	171
Figure 5.25. Variation of dimensionless parameter with Lockhart-Martinelli parameter by method of (Barnea, 1986) for data acquired at $L/D = 7.1$	173
Figure 5.26. Variation of dimensionless parameter with Lockhart-Martinelli parameter by method of (Barnea, 1986) for data acquired at $L/D = 35.4$	174
Figure 5.27. Variation of dimensionless parameter with Lockhart-Martinelli parameter by method of (Barnea, 1986) for data acquired at $L/D = 82.7$	174
Figure 5.28. Variation of dimensionless parameter suggested by Barnea (1986) against dimensionless axial distance for constant liquid superficial velocities.	176
Figure 5.29. Variation of dimensionless parameter according to Barnea (1986) against predicted Strouhal number based on mixture velocity according to (Kaji <i>et al.</i> , 2009). The data seems to be well correlated at $L/D = 82.7$ for the liquid superficial velocities.....	178

Figure 6.1. Variation of void fraction with time showing comparison of the air-water data (black line) with air-glycerol/water data at 12.2cP (green line) and 16.2cP (red line) at an average liquid superficial velocity of 0.11m/s.....	183
Figure 6.2. Variation of void fraction with time showing comparison of the air-water data (black line) with air-glycerol/water data at 12.2cP (green line) and 16.2cP (red line) at an average liquid superficial velocity of 0.17m/s.....	184
Figure 6.3. Variation of void fraction with time showing comparison of the air-water data (black line) with air-glycerol/water data at 12.2cP (green line) and 16.2cP (red line) at an average liquid superficial velocity of 0.26m/s.....	185
Figure 6.4. Variation of mean void fraction with gas superficial velocity for 12.2cP glycerol solution (\square) and 16.2cP glycerol solution (Δ) with comparisons made with air-water data at $L/D = 35.4$ (\blacklozenge) and 82.7 (\bullet) respectively. (a)-(d) represent constant average liquid superficial velocities of 0.03m/s, 0.11m/s, 0.17m/s and 0.26m/s respectively.....	187
Figure 6.5. Comparison of experimental void fraction for air-glycerol/water at 12.2cP and air-water with predicted void fraction values obtained from correlations proposed by Wallis (1969), Premoli <i>et al.</i> (1970), Chisholm (1972) and Cioncolini and Thome (2012) respectively. The correlation proposed by these workers can be found in Appendix B. Average liquid superficial velocities have been indicated in plots (a) – (d) respectively.	188
Figure 6.6. Probability density function variation with void fraction showing comparison with air-water data (green line) while blue and red lines represent 12.2cP and 16.2cP glycerol solutions respectively. (1a)-(1c) represent average constant liquid superficial velocity of 0.03m/s, 0.11m/s and 0.18m/s respectively.....	192
Figure 6.7. Probability density function variation with void fraction showing comparison with air-water data (green line) while blue and red lines represent 12.2cP and 16.2cP glycerol solutions respectively for and average constant liquid superficial velocity of 0.26m/s. More comparisons can be made at this liquid superficial velocity.....	193
Figure 6.8. Comparison of interfacial structures for 12.2cP, 16.2cP glycerol solutions and air-water data at $L/D = 82.7$ and 35.4 respectively for an average constant liquid superficial of 0.24m/s. Gas superficial velocity are indicated atop structures. The small waves that have been identified have smaller amplitudes than huge waves.....	195
Figure 6.9. Extracting probability density distributions of huge waves and base film from liquid holdup for gas superficial velocities indicated in plots at an average constant liquid superficial velocity of 0.17m/s.....	197

Figure 6.10. Extracting Probability density distributions of huge waves and base film from liquid holdup for gas superficial velocities indicated in plots at an average constant liquid superficial velocity of 0.27m/s.....	198
Figure 6.11. Area plot of huge wave and base film showing comparison with glycerol-water solutions and air-water data with gas superficial velocities indicated in plots for an average constant liquid superficial velocity of 0.11m/s.....	200
Figure 6.12. Area plot of huge wave and base film showing comparison with glycerol-water solutions and air-water data with gas superficial velocities indicated in plots for an average constant liquid superficial velocity of 0.27m/s.....	201
Figure 6.13. Autocorrelation variations with delay time at liquid superficial velocity of 0.27m/s for glycerol-water solution of 12.2cP. Auto-correlation of the time series data is carried out since we are dealing with a chaotic time series data.	204
Figure 6.14. Autocorrelation variations with delay time at liquid superficial velocity of 0.26m/s for glycerol-water solution of 16.2cP. Auto-correlation of the time series data is carried out since we are dealing with a chaotic time series data.	205
Figure 6.15. Autocorrelation variation with time and power spectral density against frequency placed side by side for glycerol-water solutions and air-water data at axial distances of L/D = 35.4 and 82.7 for average constant liquid superficial velocity in (a)-(c) of 0.11m/s.....	206
Figure 6.16. Autocorrelation variation with time and power spectral density against frequency placed side by side for glycerol-water solutions and air-water data at axial distances of L/D = 35.4 and 82.7 for constant liquid superficial velocity of 0.27m/s.	207
Figure 6.17. Dominant frequency against gas superficial velocity for glycerol-water solutions indicated in plots.....	209
Figure 6.18. Assessment of the wisp structures from selected frames of 12.2cP glycerol-water data. Gas and liquid superficial velocity are given as of 4.19m/s and 0.27m/s respectively.	212
Figure 6.19. Assessing the wisp structures from selected frames of 16.2cP glycerol-water data. Gas and liquid superficial velocity are given as of 3.98m/s and 0.26m/s respectively.	213
Figure 6.20. Contour filled plots of cross sectional area according to figure 6.18 for frames 3547 and 10843 respectively. This method is proposed for calculating wisp size cross-sectionally.	214
Figure 6.21. Mechanism of entrained liquid structure formation in the gas core. The gas and liquid superficial velocity are given as of 4.19m/s and 0.27m/s respectively for the 12.2cP glycerol/water data.....	215

Figure 6.22. Schematic of the quasi-steady condition of churn flow on the left hand side has been used to sift relevant churn flow thresholds based on *theoretical approach*. This may only hold for when the flow can be considered to be developed at $L/D = 65.5$ as suggested by Omebere-Iyari (2006) and as in the present work. Reference can be made to the work of (Wang *et al.*, 2012). Meanwhile, the gas-liquid phase distribution from the *experimental perspective* is shown on the right hand side depicting the occurrence of huge waves. The vertical projection (for a 1s time interval) and cross-sectional projection are shown respectively.....216

Figure 6.23. Applying thresholds to time series data based on figure 7.38 and tallying it to the occurrence of interfacial structures. Orange boxes represent where wisps were observed, red circles are for huge waves and green circles are probably smaller amplitude waves compared to huge wave for 12.2cP glycerol solution and gas and liquid superficial velocities of 4.85m/s and 0.11m/s.....218

Figure 6.24. Similar identification as in figure 6.23 where the gas and liquid superficial velocities are given as 4.19m/s and 0.27m/s and pipe bridging or the formation of liquid slugs show as orange circle.....219

Figure 6.25. Dominant frequency variations with gas superficial velocity showing comparison of 12.2cP and 16.2cP data at an average constant liquid superficial velocity of 0.17m/s. Sub-frequency variations which can be regarded as appearance frequencies are also shown where N_S are small amplitude waves compared to huge waves N_H while N_B is the appearance frequency of liquid bridging of the gas core.....221

Figure 6.26. Dominant frequency variations with gas superficial velocity showing comparison of 12.2cP and 16.2cP data at an average constant liquid superficial velocity of 0.24m/s.....222

Figure 6.27. Dominant frequency from power spectral density analysis against gas superficial velocity showing effect of liquid viscosity and axial distance. These are for an average constant liquid superficial velocity in (a)-(c) of 0.11m/s, 0.17m/s and 0.26m/s respectively. Square indicates air-water data at $L/D = 35.4$. Blue, red and green circles represents 12.2cP, 16.2cP glycerol-water data and air-water data at $L/D = 82.7$223

Figure 6.28. Dominant frequency variation with viscosity for an average constant liquid superficial velocity from (a) – (d)respectively of 0.03m/s, 0.11m/s 0.17m/s and 0.27m/s for selected gas superficial velocities. Red, blue and green are air-water data at $L/D = 82.7$ and air-glycerol/water at 12.2cP and 16.2cP respectively.....224

Figure 6.29. Variations of dimensionless parameter against Lockhart-Martinelli parameter according to Barnea (1986), Isoholdup lines have been indicated. Red and orange circles indicate air-water data at L/D = 35.4 and 82.7. 'A' is the typical churn flow behaviour region and 'B' wispy-annular flow region above <i>x-axis</i> . Below the <i>x-axis</i> is typical annular flow region, 'C'.....	227
Figure 6.30. Flow pattern map (a) shows comparison of bridging transition lines of Furukawa and Fukano (2001), B and C to present data A for 12.2cP glycerol-water data. (b) Shows the conditions were huge waves are observed. Transition line to annular regime cannot be plotted as that data was not collected.....	229
Figure 6.31. Flow pattern map showing specification conditions where pipe bridging and huge waves was observed for 16.2cP glycerol-water data. No bridging transition line has been obtained for this data as the phenomenon was not observed (please refer to Figure 6.25).	230
Figure 6.32. Variation of weber number against relative velocity for 12.2cP and 16.2cP glycerol-water data.....	232
Figure 6.33. Variation of Weber number against Relative velocity. The 12.2cP and 16.2cP data are shown as square and triangle respectively. Air-water data at L/D = 35.4 and 82.7 are shown as orange circle and blue diamond while data of Azzopardi (2012) is shown as green circle.....	233
Figure 6.34. Proposed modification of Weber number and variation with gas superficial velocity for 12.2cP (left) and 16.2cP (right) glycerol-water data respectively.....	233
Figure 6.35. Similar variation with gas superficial velocity showing effect of increasing liquid superficial velocity for constant average liquid superficial velocities of 0.03m/s, 0.11m/s, 0.17m/s and 0.26m/s. The 12.2cP glycerol/water data (\square) and 16.2cP glycerol/water data (Δ) are compared with the air-water data at L/D = 35.4(\blacklozenge) and 82.7 (\bullet) respectively.....	234
Figure 6.36. Flooding velocity against inverse liquid Reynolds number for air/water, air-glycerol/water (12.2cP) and air-glycerol/water (16.2cP) respectively. Predicted values of flooding are shown as blue filled circles while experimental conditions where liquid bridging was observed are shown as red filled circles.	237

LIST OF TABLES

Table 2.1. Review on flow pattern maps	21
Table 3.1. Properties of fluids used on 121mm diameter facility.....	61
Table 3.2. Properties of fluids used on 127mm diameter facility(air-water experiments)	79
Table 3.3. Properties of fluids used on 127mm diameter facility with water as the reference case for glycerol-water solutions at 25°C	82

CHAPTER 1

THESIS INTRODUCTION

1.1. Introduction

Over the last few decades, the efficient separation of gas-liquid mixtures applicable to offshore and onshore petroleum industries have become increasingly important. The production of oil after exploration and effective transportation is inevitably accompanied by the presence of natural gas and water. To this end, it is necessary to employ the use of efficient separators to separate small bubbles/drops from the continuous phase which are formed due to shear.

Conventional separators have been used as the main separation methods or pre-conditioning equipment placed before gravity settlers. Some of these archaic vessel-type separators utilised in oil industry are large, heavy and expensive to purchase and operate where the limitations are most severely felt in offshore operations in cases of escalating platform costs.

Due to the high cost associated with these separators the oil industry have shown a great interest in the development of novel alternatives that are compact, low in weight and low in capital/operating costs. One of such firmly established alternatives is the Gas Liquid Cylindrical Cyclone (GLCC) separator, (Kouba and Shoham, 1995).

The simple and compact arrangement as shown in Figure 1.1 consists of a vertical pipe (also known as an upstream pre-conditioner-CFC) with a tangential inlet and horizontal outlets for gas and liquid. The tangential inlet to the body of the GLCC induces a swirl to the flow thereby producing centrifugal force which is an order of magnitude higher than the force of gravity.

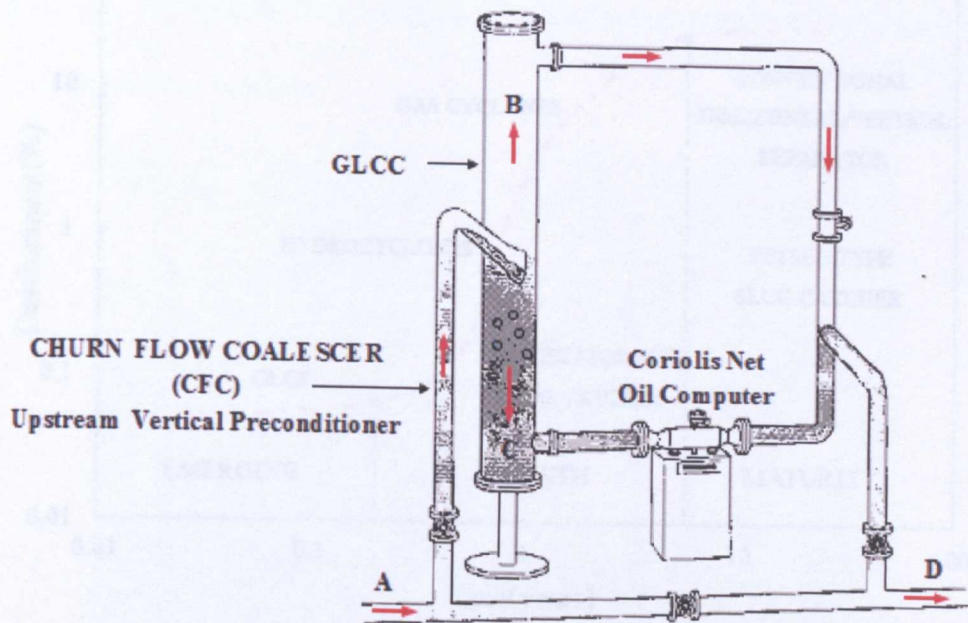


Figure 1.1. Schematic of Chevron's GLCC showing multiphase metering loop Kouba and Shoham ,1995).(A) Multiphase flow from well-head (B) Gas (C) Liquid (D) Multiphase flow to pipeline.

The effect of both centrifugal and gravitational forces pushes the liquid outward and downward towards the liquid exit while the gas phase is driven upwards towards the gas exit due to buoyancy effect.

Unlike other conventional separators that have been in existence for several years, the development of the GLCC is still at the emerging stages as shown in Figure 1.2. This is mostly due to the difficulty in predicting accurately the hydrodynamics where complex flow regimes exist. For example, above the inlet to the GLCC, bubbly, slug, churn flow regimes may be present while below the inlet the flow consists of a liquid vortex and a gas core, (Kouba and Shoham, 1995).

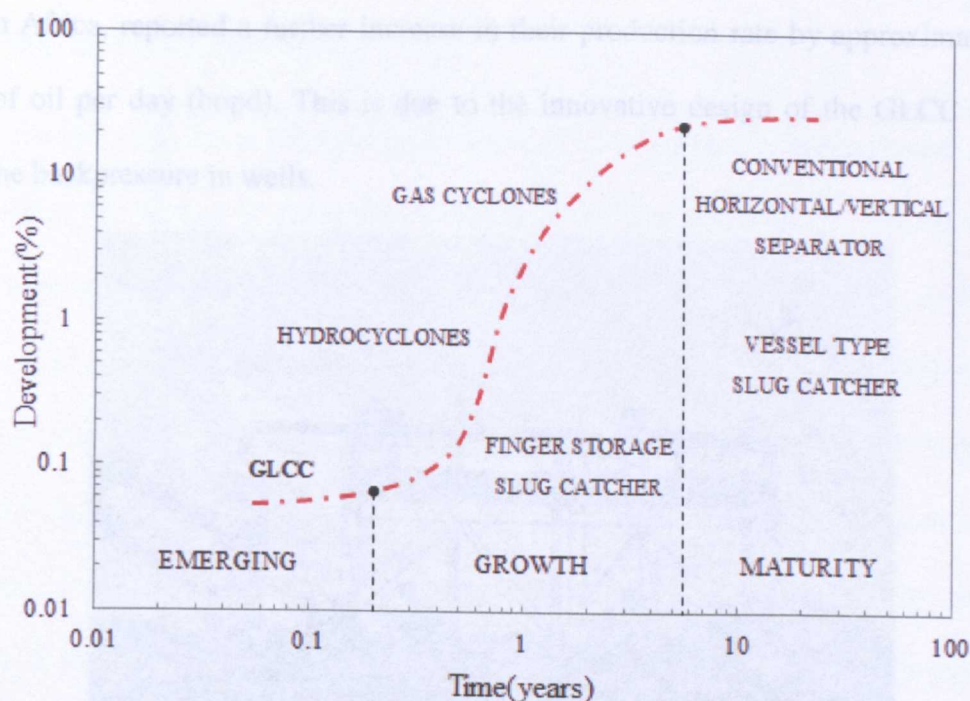


Figure 1.2. ‘S’ Curve for development ranking for Separation technology, Kouba and Shoham, 1995) (reproduced).

Furthermore, the GLCC is limited by liquid carry over (LCO) in the gas stream in form of drops and gas carry under (GCU) in form of bubbles in the liquid stream, (Kouba and Shoham, 1995). The entrainment of drops and bubbles in the liquid and gas streams respectively, reduces the outlet purity of the phases.

Overall, there is a lack of understanding of the hydrodynamics present in the GLCC. Therefore, the inability to predict its performance hinders the wide application of the equipment. Nevertheless, the potential applications of GLCC include: control of gas-liquid ratio(GLR) for multiphase flow meters and pumps, portable well test metering, steam quality metering, flare gas scrubbing, primary surface or subsea separation and pre-separation upstream of slug catchers or primary separators, (Kouba and Shoham 1995). Figures 1.3(a) and (b) shows the installed GLCC equipment at Caltex pacific, Indonesia.

In addition, the GLCC separator has been found to boost offshore production. Recently in June 2011, the Takula Field in offshore Angola, which is Chevron’s best producer in

Southern Africa, reported a further increase in their production rate by approximately 2,100 barrels of oil per day (bopd). This is due to the innovative design of the GLCC that helps reduce the backpressure in wells.



(a)



(b)

Figure 1.3. World's largest GLCC installed by Caltex Pacific Indonesia (CPI), (Tulsa University Separation Technology Projects website (TUSTP)).

1.2. Background to Research

Tulsa University Separation Technology Projects (TUSTP) which was established in 1994 is a Joint Industry Project of 15 companies developing the idea of the GLCC concept to achieve efficient separation of gas-liquid mixtures. Experiments have been carried out by Kouba and Shoham (1995) and they concluded that Computational Fluid Dynamics (CFD) simulations are too computationally intensive, time consuming and complicated to apply to large systems such as the GLCC. Also, subsequent modelling of the hydrodynamics of flow in a GLCC is impractical, therefore, making it an insufficient design tool. They stated that mechanistic modelling is a reasonable compromise between empirical formulations and the complexities of CFD. The combination of both presents itself as a realistic approach to obtaining a useful tool for the design and performance predictions for the GLCC.

Chirinos (1998) has carried out experiments on a small scale model of the GLCC at University of Tulsa shown in Figure 1.4. From the experiments, a mechanistic model was obtained for liquid carry over (LCO) under upstream churn flow conditions.

Apart from this, no detailed work has been reported to be carried out on the upstream preconditioning equipment (CFC) placed before the GLCC. Consequently, this creates a lacuna in understanding of the overall system hydrodynamics. This is because the behaviour within the GLCC may be greatly influenced by the conditions prevailing in the upstream preconditioner.

However, a great amount of work has been carried out in small and large diameter vertical pipes and for the major flow regimes namely: bubbly, slug, churn and annular flows. These regimes will be discussed in chapter 2.



Figure 1.4. Laboratory Model of GLCC with Control Systems at the University of Tulsa, (Chirinos, 2008).

1.3. Problem Statement

The separation efficiency of a GLCC is affected by the existence of small bubbles/drops in the range of 3-5 mm in the inflow mixture in both liquid and gas outlets as they do not separate under the centrifugal forces. It is important that these entrained bubbles/drops should be made to coalesce in an upstream vertical pipe to enhance proper separation in a downstream GLCC separator. However, the limitations in pump capacities and the viscosities of the crude oil prevent increasing the helical flow intensity within the GLCC. As a result, the separation of smaller bubbles/drops proves difficult. A suggested solution to overcoming this difficulty is to precondition the oil/gas mixture by forcing small bubbles/drops to coalesce in an upstream preconditioning equipment shown in Figure 1.1 also known as Churn Flow Coalescer(CFC). This research focuses on developing an inline pre-processing CFC unit by first seeking the knowledge of the relevant flow regimes.

Oil and gas flow in most cases have bubbly and churn flow conditions present within vertical pipes or flexible risers. In a previous work by Szalinski *et al.* (2010), it has been reported that the bubble size increases within the churn flow regime when the viscosity increases. However, the parameter space is not only limited to the flow variables but extends to the geometric variables of the vertical pipe. It is in the remit of this work to develop a Churn Flow Coalescer (CFC) model that could be employed in designing the preconditioner to the GLCC. The model will be eventually obtained after a series of detailed and in-depth experiments. The measured flow parameters such as cross-sectional averaged void fraction will help form a database that will be used eventually in the CFC design. On the other hand, the predictive model will estimate with reasonable uncertainty the optimum height for the CFC to induce coalescence of small bubbles/drops. Therefore, this will avert to a large extent problems of LCO and GCU in the downstream GLCC separators. Having said this, the objectives include:

- ✓ Establishing the bubble to churn flow regime boundary in a large diameter pipe.
- ✓ Performing air-water churn flow development experiments.
- ✓ Investigating the effect of viscosity in churn flow. Comparisons were made to the air-water data.
- ✓ Establishing a predictive model for the upstream vertical pipe after data reconciliation.

1.4. Methodology

1.4.1. Experimental methods

The experimental campaigns to achieve the stated objective above were performed on two different rig facilities. The first experimental rig was built, commissioned and experiments were performed accordingly. The aim of the experiments was to delineate the bubble to churn flow transition in a large diameter pipe. The test section has an internal diameter of 121mm

and is 5.3m in length. Air and water were used as the operating fluids. An injection device was used to introduce the two phase flow mixture into the test section. The phase fraction data was obtained using a 32 x 32 capacitance wire mesh sensor (WMS) at a frequency of 1000Hz and an acquisition time of 30s at $L/D = 35$. These experiments were carried out at atmospheric conditions.

From the field experiments performed by Kouba and Shoham (1995), the churn flow pattern has been identified as the desirable flow regime that induces a high degree of coalescence in both gas and liquid phases. As a result of the coalescence in the liquid phase, larger liquid structures are formed that are easily separated within the GLCC. To this end, experiments have been conducted within the churn flow pattern on a second experimental facility. The rationale for performing the experiments in this facility is because the facility offered a wider range of operating conditions compared to the first experimental rig facility. It was purposely built for churn and annular flow experiments.

The experimental rig is a large-scale closed loop Transient Multiphase Flow (TMF) facility. It has an internal diameter of 127mm and is 11m in length. The aim of the experiments was to have better insights into the churn flow pattern and suggest the optimum conditions needed for the churn flow coalescer (CFC). Air and water were used as the operating fluids. A phase mixer at the base of the test section was used to introduce the two phase flow mixture into the test section. The phase fraction data was obtained using a 32 x 32 capacitance wire mesh sensor (WMS) at a frequency of 1000Hz and an acquisition time of 30s at five axial distances from the injection, $L/D = 2.4, 7.1, 30.7, 35.4$ and 82.7 .

Further tests investigating the effect of liquid viscosity using air-glycerol/water at 12.2cP and 16.2cP respectively were performed. The WMS that was used in the first rig experiments to acquire data was used in this facility for the same purpose. Also, high speed imaging was

used and the frames were acquired at 1000frames per second. All experiments were carried out in the L3 Chemical Engineering Laboratory at the University of Nottingham.

1.5. Structure of Thesis

The overall layout of the thesis is given below:

- Chapter 1: Introduction**

This chapter gives an introduction to the research project. It discusses on the rationale for the use of a GLCC and the need for detailed experiments to be performed on the necessary upstream equipment to enhance its operation which is the churn flow coalescer (CFC). The aforementioned equipment preconditions the flow before it eventually enters the GLCC. Therefore, this leads to a more efficient separation of the gas-liquid mixtures in the GLCC.

- Chapter 2: Literature review**

In this chapter, a review of relevant literature is presented. It discusses the fundamentals of multiphase flow and in particular two phase flow. The discussions focus on the bubble and churn flow regimes since they were both investigated in this work.

- Chapter 3: Experimental arrangements**

In this chapter, the experimental facilities used to perform vertical two phase upward flow experiments are discussed. Two different facilities were used and the experimental arrangement and operating procedures are discussed in detail.

- Chapter 4: Establishing flow pattern transition in co-current vertical pipe**

This chapter investigates the bubbly to churn transition and establishes the operating range for the transition from the former to the latter in a large diameter pipe.

- **Chapter 5: Behaviour of churn flow and further insight into flow regime phenomenon**

From the work in chapter 4, the operating conditions for the inception of typical churn flow is used as initial conditions amongst a full range of conditions. Experiments are conducted at different axial distances from the injection. By doing this, the churn flow behaviour is studied at different axial distances upstream from the injection and important features within the regime are identified.

- **Chapter 6: Effect of liquid viscosity on churn flow pattern**

By changing the viscosity of the fluid from the reference case of air-water used in chapter 5, the effect of viscosity on churn flow behaviour has been investigated. Data has been acquired at a suitable axial distance from the injection based on the work done in chapter 5. In this work, the CFC model has been proposed after taking into consideration the liquid viscosity. The model is developed based on the most suitable operating conditions which induces a high degree of coalescence to take place.

- **Chapter 7: Conclusions and future work**

This chapter discusses on the conclusions of the work carried out in this project and future work has also been suggested.

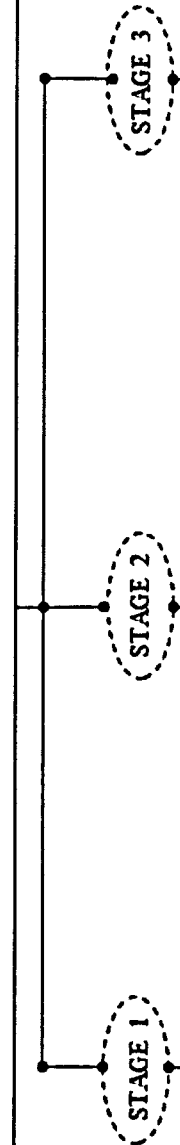
Figure 1.5 gives a summary of the research layout for the experiments performed in this work.

CHURN FLOW COALESCER(CFC) PRECONDITIONING EXPERIMENTS FOR GAS- LIQUID CYLINDRICAL CYCLONE (GLCC)

APPLICATIONS

RESEARCH WORK LAYOUT

AIM: Suitable operating condition that enhances coalescence of fluid phases



1.1. RE SEARCH: BUBBLE TO CHURN TRANSITION IN A LARGE DIAMETER PIPE

1.2. AIM: Establishing operating conditions for the transition to churn flow in a large diameter pipe.

1.3. RESULT: Operating conditions for inception of typical Churn flow delineated.

2.1. RE SEARCH: INSIGHTS INTO CHURN FLOW BEHAVIOUR

2.2. AIM: Churn flow experiments at different axial distances from gas- liquid injection point.

2.3. RESULT: Two Sub-regimes present within churn flow. More large liquid structures entrained in gas core downstream compared to upstream.

3.1. RE SEARCH: EFFECT OF VISCOSITY IN CHURN FLOW.

3.2. AIM: Effect of viscosity on flow behaviour

3.3. RESULTS: Larger structures entrained in gas core. Encourages an increased degree of coalescence.

1.4. RE SEARCH CONTRIBUTION/PROGRESS:
Operating condition used as initial conditions in STAGE 2.

2.4. RE SEARCH CONTRIBUTION/PROGRESS:
Sub-regime behaviour ascertained and effect of further preconditioning examined in stage 2b.
Viscosity tests examined in stage 3.

3.4. RE SEARCH CONTRIBUTION/PROGRESS:
Appropriate condition for CFC obtained taking the effect of viscosity into consideration.

Figure 1.5. Research Layout for Churn Flow preconditioning experiments performed in this work.

CHAPTER 2

LITERATURE REVIEW

2.1. Introduction

When more than one phase flows in a conduit, namely: gas, liquid and solid, this occurrence is considered as multiphase flow. In consideration of the flows in industrial equipment such as in the production of hydrocarbons, power generation and those in chemical industries, multiphase flow occurs in all facets of these industrial applications. The flow can be of various forms, that is, by the combination of the phases above: **Gas-Liquid-Solid**, **Gas-Liquid-liquid** and **Solid-Liquid-liquid**. However, for the remit of this work, this thesis concentrates on an aspect of multiphase flow, two phase gas-liquid flows.

When these two phases, gas and liquid, flow in the same pipe for instance, a deformable interface is formed between them. Furthermore, the gas or liquid occupies a certain fraction of the pipe cross-sectional area. From general consensus, the fraction of the pipe cross-section occupied by the gas phase is known as the void fraction, (Azzopardi, 2006). The term liquid holdup or liquid fraction is given to the fraction of the pipe cross-section occupied by the liquid phase. The section below sheds more light on related terms as regards two-phase gas-liquid flow.

2.1.1. *Two phase flow (Separated Flow concept)*

2.1.1.1. *Void fraction*

From the discussion above, the void fraction is mathematically given below as, (Azzopardi, 2006):

$$\alpha_g = \frac{A_g}{A_c} \quad (2.1)$$

where A_g and A_c are the area occupied by the gas phase and the cross-sectional area respectively. The liquid holdup on the other hand is given as:

$$\alpha_L = 1 - \alpha_g \quad (2.2)$$

When these two phases flow in the pipe as shown in Figure 2.1, they travel at a particular mass flowrate referred to as the total mass flowrate which is the sum of the flowrate of the phases.

$$\dot{M}_T = \dot{M}_g + \dot{M}_l \quad (2.3)$$

where \dot{M}_T , \dot{M}_g and \dot{M}_l are the total mass flowrate and mass flowrate of the gas and liquid phases respectively.

The fraction of the flow travelling as gas/vapour is called the quality and is given as:

$$x_g = \frac{\dot{M}_g}{\dot{M}_g + \dot{M}_l} \quad (2.4)$$

The volume fluxes of the phases give the gas and liquid superficial velocities. This represents the velocity at which each phase will travel as if occupying the entire pipe cross section.

$$\text{Gas superficial velocity, } U_{gs} = \frac{\dot{m}x_g}{\rho_g} \quad (2.5)$$

$$\text{Liquid superficial velocity, } U_{ls} = \frac{\dot{m}(1-x_g)}{\rho_l} \quad (2.6)$$

From equations (2.1) and (2.5), the mean gas velocity is given in equation (2.7). On the other hand, the mean liquid velocity is given in equation (2.8) from equations (2.2) and (2.6).

$$\text{Mean gas velocity, } U_g = \frac{U_{gs}}{\alpha_g} \quad (2.7)$$

$$\text{Mean liquid velocity, } U_l = \frac{U_{ls}}{\alpha_L} \quad (2.8)$$

In consideration of the mass balances for each phase, the void fraction can also be defined as:

$$\alpha_g = \frac{1}{\left(1 + \frac{U_g}{U_l} \frac{(1-x_g)\rho_g}{x_g\rho_l} \right)} \quad (2.9)$$

where (U_g/U_l) is the ratio of the mean velocities for the gas and liquid phases and is known as the slip ratio, U_R . When $U_g = U_l$, so that $U_R = 1$, this is known as homogenous flow. In this case the equation (2.9) becomes:

$$\alpha_{gH} = \frac{1}{\left(1 + \frac{(1-x_g)\rho_g}{x_g\rho_l} \right)} \quad (2.10)$$

Predicted correlations also exist for void fraction. The ones used in the present work as in chapter 6 are given in Appendix C.

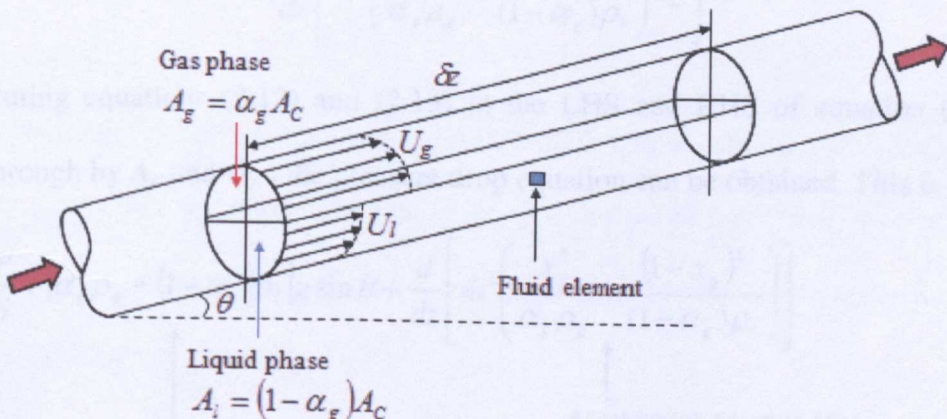


Figure 2.1. Concept of gas-liquid flow in a pipe (Azzopardi, 2006).

2.1.1.2. Pressure drop

In consideration of a finite fluid element within the pipe as shown in Figure 2.1, a force balance can be written.

$$\text{The net applied force in the direction of the flow} = \text{Rate of increase of momentum of the fluid element in the flow direction} \quad (2.11)$$

The net force is contribution of the effects of hydrostatic pressure due to the length of the pipe, wall shear stress and the gravitational forces. Therefore, the net applied force which is the left hand side (LHS) of equation (2.11) is given as:

$$\text{net force} = -\frac{dp}{dz} \delta A_C - [\alpha_g \rho_g + (1-\alpha_g) \rho_l] g \sin \theta \delta A_C - \bar{\tau} \delta z P \quad (2.12)$$

where dp/dz is the pressure drop.

On the other hand, RHS of equation (2.11) is given as:

$$\text{Rate of momentum transport} = \frac{d}{dz} \left[\dot{m}^2 \left(\frac{x_g^2}{\alpha_g \rho_g} + \frac{(1-x_g)^2}{(1-\alpha_g) \rho_l} \right) A_C \right] \delta z \quad (2.13)$$

By substituting equations (2.12) and (2.13) in the LHS and RHS of equation (2.11) and dividing through by A_C and δz , the pressure drop equation can be obtained. This is given as:

$$-\frac{dp}{dz} = \bar{\tau} \frac{P}{S} + [\alpha_g \rho_g + (1-\alpha_g) \rho_l] g \sin \theta + \frac{d}{dz} \left[\dot{m}^2 \left(\frac{x_g^2}{\alpha_g \rho_g} + \frac{(1-x_g)^2}{(1-\alpha_g) \rho_l} \right) \right] \quad (2.14)$$

↑ ↑ ↑
 Frictional pressure drop Gravitational pressure drop Acceleration pressure drop
 ↑
 Total pressure drop

The equations (2.1) – (2.14) represent the fundamental two phase flow equations.

2.2. Introduction to gas-liquid flow regimes

In a well shaken fizzy drink, there is the presence of gas represented as bubbles and the surrounding liquid conceiving the existence of two fluid phases. When closely observed, the lighter of the two phases, which are the gas bubbles, rise quickly and are arranged almost uniformly within the liquid. A close interaction between the gas bubbles and the liquid can also be observed. Similarly, when gas-liquid mixtures or liquid-liquid mixtures flow through a pipe, the two phases arrange themselves in a variety of patterns known as flow regimes, (Azzopardi, 2006). These flow regimes are found in most industrial processes and are of four major types: bubbly, slug, churn and annular flow patterns where the fizzy drink example may probably be classified as bubbly flow regime.

2.2.1. Gas-liquid flow regimes in vertical pipe

The flow regimes present in vertical two-phase upward flow are discussed below.

2.2.1.1. Bubbly flow

In bubbly flow, the gas phase flows as discrete bubbles in a continuous/continuum phase. This occurs at very low gas superficial velocities. The gas bubbles rise with a velocity greater than that of the liquid. Figure 2.2(a) shows a schematic of the bubbly flow regime from the work of (McQuillan and Whalley, 1985).

2.2.1.2. Slug flow

As the gas superficial velocity increases, the bubble number density increases accordingly. The largest bubbles are of the same order of size with the diameter of pipe otherwise known as “Taylor bubbles”. By definition, a Taylor bubble is a constant pressure surface, whose shape is that of a cylinder bounded on top by a bullet shaped nose and at the bottom by a distorted flat tail, (Cheng, 1997). Leading and trailing Taylor bubbles are separated by structures similar to bubbly flow beneath them commonly known as liquid slugs. Also,

contributing to its formation is the presence of a downward moving thin liquid film between the Taylor bubbles and the pipe wall. Figure 2.2(b) from the work of McQuillan and Whalley (1985) shows the slug flow regime as one of the two phase gas-liquid flow regimes.

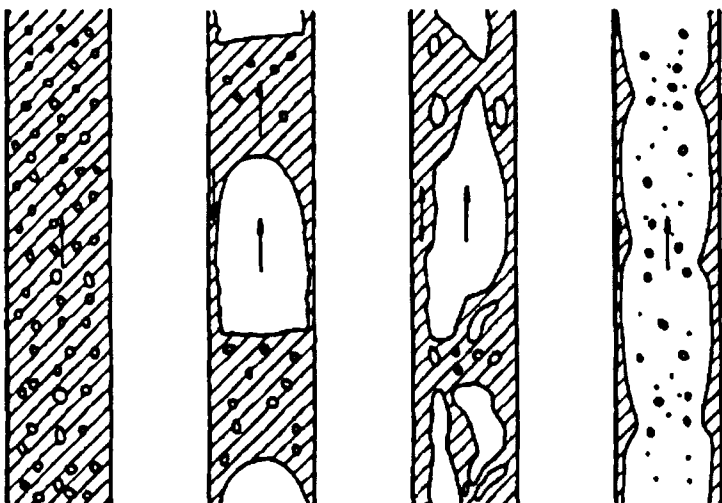


Figure 2.2. (a) Bubbly (b) Slug (c) Churn (d) Annular flow regimes in upward two-phase flow in vertical pipes (McQuillan and Whalley, 1985).

2.2.1.3. *Churn flow*

Figure 2.2(c) shows the schematic of the churn flow regime. Therefore, from the slug flow regime, as the gas flowrate increases bubbles become narrower and more or less irregular in shape. The bullet shape nose of the Taylor bubbles is suppressed to form large irregular shaped bubbles and the continuity of liquid slugs between successive Taylor bubbles is repeatedly destroyed by the high gas inertia pertaining to the flow. This occurrence causes the liquid slug to fall, thereby accumulating a volume of liquid with entrained bubbles that bridge the pipe. This is occasionally lifted by the fast moving gas phase giving an oscillatory behaviour. In addition, the falling liquid film previously surrounding the Taylor bubbles is no longer observed.

Hewitt and Hall-Taylor (1970) initially identified that the behaviour above is a well-marked region between slug and annular flow as shown in Figure 2.2(c). Therefore, they were the first to ascribe the name “churn flow” to this flow behaviour. In large diameter pipes, they added that this instability eventually results in the complete destruction of the slug flow thereby translating into a direct transition from bubbly to churn flow accompanied with ‘churning’ or oscillatory motion. However, this may depend on the viscosity of the continuous phase. Some other workers have referred to this flow regime as ‘semi-annular flow’, (Nicklin and Davidson, 1962). However, Hewitt and Hall-Taylor (1970) stated that the appellation, churn flow, should be given to it as it encompasses the whole flow region. McQuillan and Whalley (1985) stated that the churn flow regime is a highly disordered regime where the vertical motion of the liquid is oscillatory. Azzopardi and Wren (2004) attributed the flow regime as the least understood of all of the flow patterns as regards vertical two phase upward flow.

2.2.1.4. Annular flow

As the direct opposite to the bubbly flow regime, here, the gas flows continuously along the core of the pipe. The more or less dispersed liquid phase flows partially as liquid films along the pipe walls moving upwards in a wavy manner and as droplets in the gas core. The schematic of the flow regime is shown in Figure 2.2(d). The liquid film may or may not contain gas bubbles and the continuous gas core which occupies most of the pipe cross-section may not contain entrained droplets, (Hewitt and Hall-Taylor, 1970). In general, the liquid film is typically uniform about the pipe cross-section.

2.2.1.5. *Wispy-annular flow*

Another interesting behaviour that has been observed in vertical upward two phase flow is the wispy-annular flow regime. The appellation ‘wispy-annular flow’ was initially given its name by (Bennet *et al.*, 1965). They stated that:

“.....wispy annular regime was characterised by the nature of the entrained phase. The phase appeared to flow in large agglomerates somewhat resembling ectoplasm.”

In agreement with Bennet *et al.* (1965), Hewitt and Hall-Taylor(1970) stated that the entrained phases is agglomerated into large lumps or ‘wisps’ and the size of these ‘wisps’ are dependent on the gas velocity. This is because when the latter increases, the size decreases. Hewitt and Hall-Taylor (1970) added that this regime may occur as a result of the breakdown of slug flow at high mass velocities. In this velocity range the behaviour below the large gas bubbles tend to become unstable and a frothy “finger” is formed around the bubble axis. As the velocity increases, annular flow is entered but the “fingers” still exist and require a finite distance to breakup. From another perspective, as a result of the instabilities of the shear and gravity forces which develop at the gas-liquid interface, this forms liquid structures in the core. Hewitt and Hall-Taylor (1970) added that the wispy-annular flow regime can be entered as a result of droplet coalescence when the gas velocity is reduced for any reason.

Hernandez-Perez *et al.* (2010) agreed with Hewitt and Hall-Taylor on the fact this regime occurs at high flow rates in what should be the typical annular flow. They added that the annular flow regime is made more complex by the presence of wisps in the gas core. They identified them from visual observation of which they appear as dark patches when viewed through a transparent pipe wall. Hawkes *et al.* (2001) pointed out that the views of these wisps through the transparent pipe wall are blurred by the wavy liquid film interface.

McQuillan and Whalley (1985) suggested that the annular flow pattern can be subdivided into two regimes: wispy-annular flow and non-wispy annular flow. In corroboration to the

above workers, they stated that the wispy annular flow occurs as a result of the agglomeration of droplets in the gas core to form streaks of liquid or wisps. Figure 2.3 shows the wisps observed by (Hewitt and Roberts, 1969 and Hernandez *et al.*, 2010).

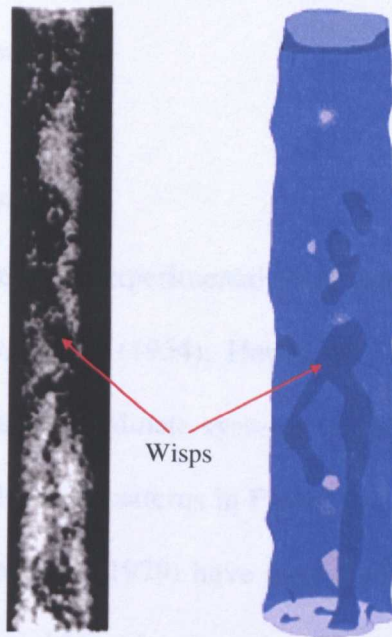


Figure 2.3. (a) Wisp recorded by X-ray photography by Hewitt and Roberts (1969) 32mm pipe diameter(left) (b) Type of wisps from Hernandez *et al.* (2010) 67mm pipe diameter revealed by wire mesh sensor studies(right).

Froth and mist flow are other regimes that exist in vertical two phase gas-liquid flows. The froth flow is covered partly by churn flow and annular flow. The mist flow regime is defined as one of complete dispersion of the liquid in the gas phase.

2.3. Flow Pattern maps

The only way to represent results of observation of flow patterns described above is to plot them on a graph where the x - y coordinates are represented by the gas and liquid superficial

velocities respectively of the two phases. When the observations are recorded, transition lines are drawn on this graph to represent the extent of the boundaries between the flow regimes. From general consensus, this is known as “flow pattern map”.

These flow pattern maps can be of two forms, (McQuillan and Whalley, 1985). They are given as: (a) Experimental flow pattern map (b) Theoretical flow pattern map. This will be discussed in the sections below.

2.3.1. *Experimental flow pattern map*

These flow pattern maps arise from experimental work done by researchers for a particular fluid pair and pipe geometry. Baker (1954), Hewitt and Roberts (1969) and Taitel *et al.* (1980), proposed their respective coordinate systems as shown in Table 2.1 below. Taitel *et al.* (1980) concluded that all the flow patterns in Figure 2.2 cannot be represented by a single coordinate pair. However, Weisman (1979) have identified different scaling parameters that may be used to overcome this problem. An example of an experimental flow pattern is shown in Figure 2.4 from the work of (Hewitt and Roberts, 1969).

Table 2.1. Review on flow pattern maps

Author	Year of Publication	Map Coordinates	
		<i>x-abscissa</i>	<i>y-ordinate</i>
Baker	1954	U_{gs}	U_{ls}
Hewitt and Roberts	1969	$\rho_g U_{gs}^2$	$\rho_g U_{ls}^2$
Taitel <i>et al.</i>	1980	U_{gs}	U_{ls}

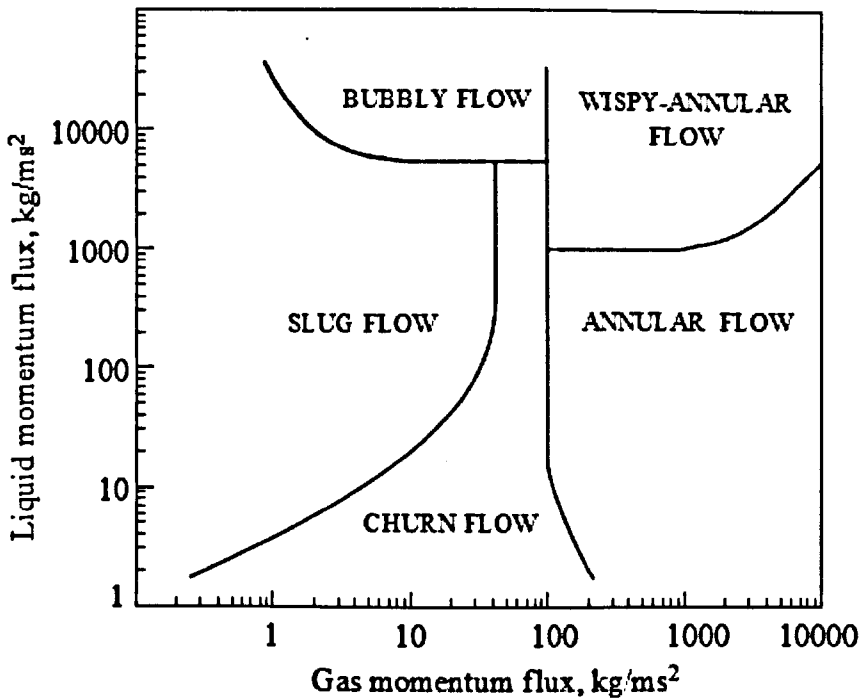


Figure 2.4. Experimental flow pattern map of (Hewitt and Roberts, 1969).

2.3.2. Theoretical pattern map

As an alternative to the experimental flow pattern maps, previous workers such as Taitel *et al.* (1980) and Mishima and Ishii (1984) obtained theoretical flow pattern maps by initially considering the conditions necessary for the existence of each of the flow pattern. This basis allowed them to postulate mechanisms by which the transitions between the various flow patterns might occur. Afterwards, these transitions were modelled to produce a series of equations. Therefore, when the phase physical properties and pipe diameter are known, this enabled the flow pattern boundaries to be calculated. Figure 2.5 shows an example of a theoretical flow pattern map by (Taitel *et al.*, 1980).

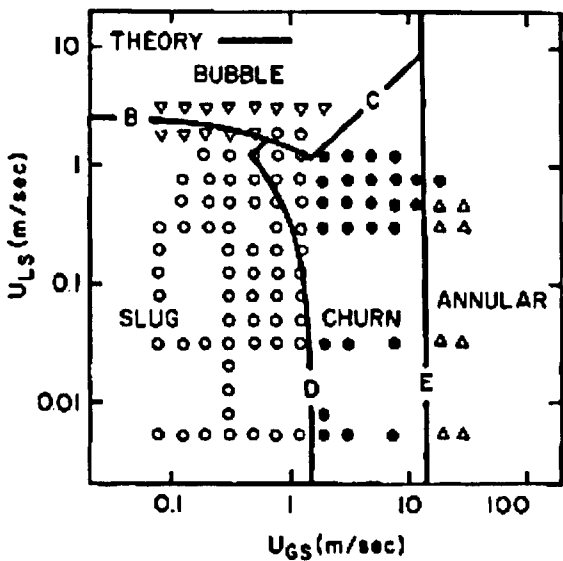


Figure 2.5. Theoretical flow pattern map of (Taitel *et al.*, 1980).

2.3.3. Flow pattern transition mechanisms: Theoretical approach

2.3.3.1. Transition from Bubble flow

The presence of gas bubbles in a continuous liquid gives rise to bubble to bubble collisions that may or may not lead to the coalescence of bubbles. Coalescence occurs when two fluid particles such as bubbles in this case join together to form a larger one. Coalescence of bubbles is a phenomenon which occurs rapidly in pure liquids and at a slower rate in mixtures, (Marrucci, 1968). According to Marrucci (1968), the coalescence process occurs in three stages. Initially, there is collision between two bubbles that force them against each other by the turbulent dynamic pressure. This forms a thin film between their interfaces. Afterwards, the fluid within this film is drained until it reaches a critical thickness at which molecular attractive forces dominate, quickly promoting film rupture and leading to coalescence.

Chesters (1991) considered the coalescence mechanism described above to be a complex phenomenon. This is because it not only involves the interaction of bubbles with surrounding

liquid but between bubbles themselves when they are brought together by the external flow or body forces.

Howarth (1964) suggested that whether coalescence will occur or not depends on the impact of colliding bubbles. He suggested that when the approach velocity of two colliding bubbles exceeds a critical value, during “energetic collisions”, immediate coalescence without liquid film capturing and thinning will be the dominant mechanism.

Other researchers such as Doubliez (1991) and Duinveld (1994) based on experimental observation used the critical approach velocity model. Based on this model, Lehr and Mewes (1999) and Lehr *et al.* (2002) suggested that small approach velocities lead to a high probability of coalescence or high coalescence efficiencies. Therefore, the premise of coalescence that has been corroborated among workers can be identified as both contact and collision.

Liao and Lucas (2010) also identified collision between bubbles to be caused by their relative velocity and added that the relative motion may occur due to the variety of mechanisms classified into five sources in a turbulent flow:

- (a.) *Motion induced by turbulent fluctuations in the surrounding continuous phase*
- (b.) *Motion induced by mean velocity gradient in the flow*
- (c.) *Different bubble rise velocities induced by buoyancy and body forces*
- (d.) *Bubble capture in an eddy*
- (e.) *Wake interactions or helical/zigzag trajectories*

Furthermore, since the collision between bubbles does not necessarily mean coalescence will take place, the coalescence efficiency is introduced. The frequency of coalescence occurring is determined by both collision frequency and coalescence efficiency. The former is determined by the mechanism of bubble collisions and the latter is determined by the critical velocity model, film drainage model and energy model. It is important to note that the

deformation of the bubble is a prerequisite for coalescence to occur. Therefore, as suggested by Hinze (1955), they can be of the following kinds.

Type 1. Lenticular deformation

The fluid particle is flattened, forming in the initial stages an oblate ellipsoid which further deforms into a torus. Afterwards, due to stretching, breaks into many small fluid particles.

Type 2. Cigar-shaped deformation

The fluid particle becomes more elongated forming in the initial stages a prolate ellipsoid until ultimately a long cylindrical thread is formed which breaks up into small fluid particles.

Type 3. Bulgy deformation

As the surface of the fluid particle is deformed locally, it bulges and protuberance occurs, thus parts of the fluid particle become bodily separated. Figure 2.6 shows the schematic of the types of deformation.

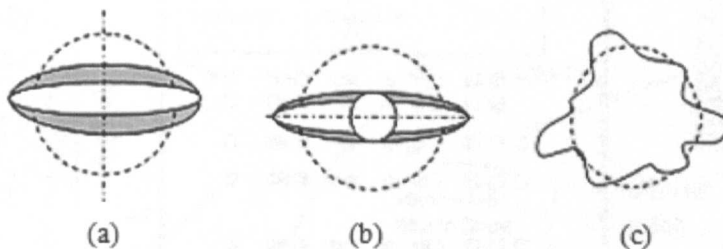


Figure 2.6. (a)-(c) Various types of deformation from Lenticular to Bulgy respectively,
(Hinze, 1955).

The deformation can also occur due to a decrease in hydrostatic pressure with increase in axial distance from the base a riser. This decrease will lead to an increase in the bubble size. When this occurs, there is a tendency of the bubbles to either remain close to the wall or travel within the core of the pipe. Serizawa and Kataoka (1988) classified regions of the bubbly flow where bubbles exhibit a core and wall peak behaviour. Core peak behaviour occurs when larger bubbles occupy most of the cross-section of the pipe and are basically

travelling within the core/centre of the pipe. Wall peak behaviour on the other hand, occurs when smaller bubbles occupy the wall region of the pipe. In between the core and wall peak distribution, there is a transition region where bubbles exhibit an unstable behaviour. This has been expressed by Zuber and Findlay (1965) as the churn-turbulent region.

This region is not similar to the typical churn flow regime and therefore should not be confused with it. The churn turbulent behaviour of bubbles has also been observed by Ohnuki and Akimoto (2000). The observations of Ohnuki and Akimoto (2000) can be shown in Figure 2.7. Therefore, it can be agreed upon that the transition from the bubbly flow to the succeeding regime is as a result of deformation and an increased degree of coalescence of bubbles. By considering a situation where bubbles form a cubic lattice, Radovich and Moassis (1962) have shown that the frequency of collision is proportional to the mean fluctuating bubble velocity.

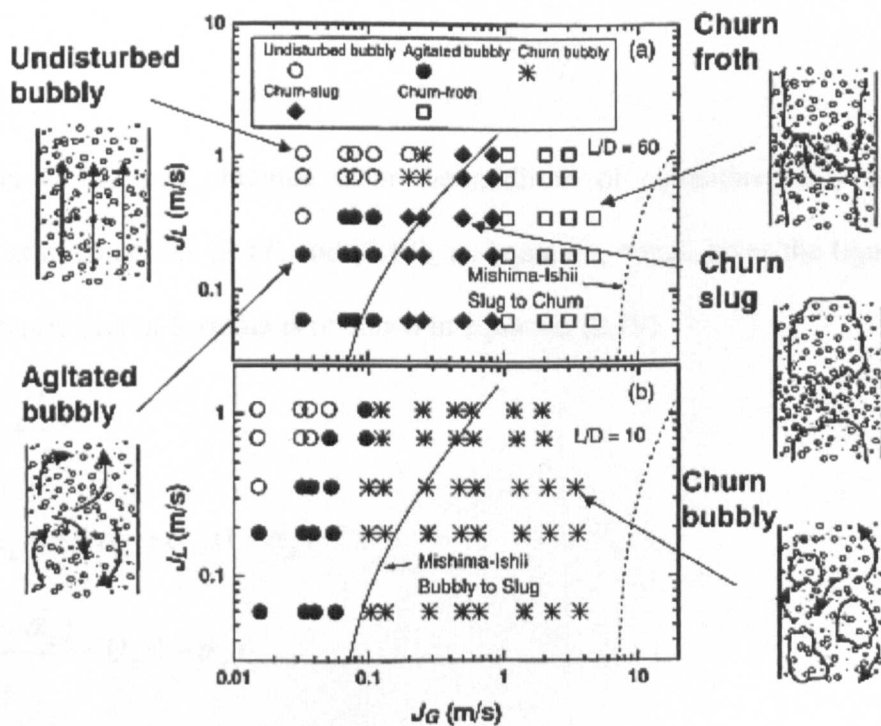


Figure 2.7. Bubbly Flow pattern transitions from the work of (Ohnuki and Akimoto, 2000).

To determine the frequency of collisions, they suggested equation (2.15) below:

$$f = \frac{\bar{c}}{D_b \left[\left(\frac{0.74}{\alpha_g} \right)^{\frac{1}{3}} - 1 \right]^5} \quad (2.15)$$

where \bar{c} is the mean fluctuating velocity, D_b is the bubble diameter and α_g is the void fraction. The frequency of collisions was found to be dependent on void fraction increasing more than 0.25-0.30. For a void fraction value below 0.08 there are few collisions hence the transition to slug flow would be extremely slow, (Hewitt and Hall Taylor, 1970).

Taitel *et al.* (1980) stated in their work that at very low liquid rate, with negligible degree of turbulence present, the criteria for transition from bubbly to slug flow is that the void fraction reaches 0.25. Taitel *et al.* (1980) suggested that the rise velocity of the bubbles can be given as:

$$U_o = U_l + U_g \quad (2.16)$$

The equation (2.16) was obtained from the addition of equations (2.7) and (2.8). By substitution as in equations (2.17) and (2.18), an equation, which gives the liquid superficial velocity as the subject of formula is obtained in equation (2.19).

$$U_o = \frac{U_{ls}}{1 - \alpha_g} + \frac{U_{gs}}{\alpha_g} \quad (2.17)$$

$$U_o (1 - \alpha_g) \alpha_g = U_{ls} \alpha_g + U_{gs} (1 - \alpha_g) \quad (2.18)$$

$$U_{ls} = \frac{U_{gs} (1 - \alpha_g)}{\alpha_g} - U_o (1 - \alpha_g) \quad (2.19)$$

From the equation proposed by Harmathy (1960) the relative velocity U_o of large bubbles is given as:

$$U_o = 1.53 \left(g \frac{(\rho_l - \rho_g) \sigma_l}{\rho_l^2} \right)^{0.25} \quad (2.20)$$

where ρ_l , ρ_g and σ are the density of the liquid, density of gas and the surface tension respectively.

Substituting this equation in (2.19) gives:

$$U_{ls} = \frac{U_{gs}(1-\alpha_g)}{\alpha_g} - 1.53 \left(g \frac{(\rho_l - \rho_g) \sigma_l}{\rho_l^2} \right)^{0.25} (1-\alpha_g) \quad (2.21)$$

However if the above criterion of Taitel *et al.* (1980) for a critical void fraction of 0.25 is used, the criterion for the bubble to slug transition is given in equation (2.22):

$$U_{ls} = 3U_{gs} - 1.148 \left[\frac{g \sigma (\rho_l - \rho_g)}{\rho_l^2} \right]^{0.25} \quad (2.22)$$

Mishima and Ishii (1984) suggested that a critical void fraction of 0.30 marks the bubble to slug transition. By assuming that bubbles distribute themselves in a tetrahedral pattern in which each bubble fluctuates, there is an existence of a sphere influence on each bubble. Although this sphere can overlap, the summation of the sphere volumes equals the total volume.

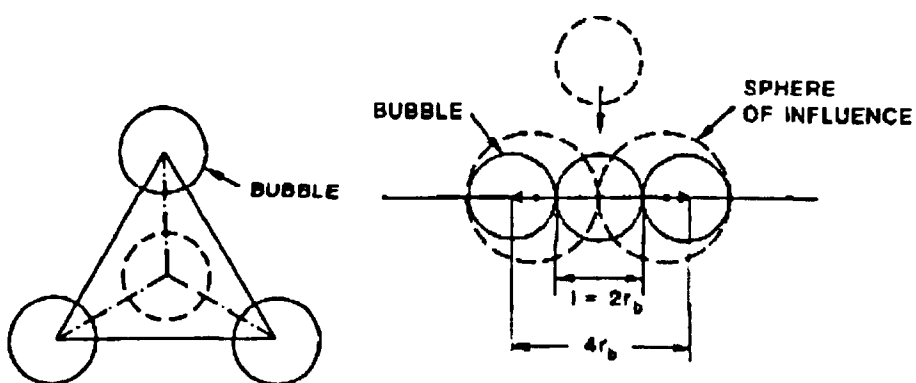


Figure 2.8. Bubble packing and coalescing pattern (Mishima and Ishii, 1984).

If the maximum possible gap between two bubbles is less than a bubble diameter ($2r_b$) the number of collisions and the degree of coalescence is very large. This has been shown in Figure 2.8.

Considering the geometric distribution in Figure 2.8, they derived the following equation (2.23):

$$U_{ls} = \left(\frac{3.33}{C_o} - 1 \right) U_{gs} - \frac{0.76}{C_o} \left(\frac{\sigma_g(\rho_l - \rho_g)}{\rho_l^2} \right)^{0.25} \quad (2.23)$$

where C_o is the distribution parameter and is given as:

$$C_o = 1.2 - 0.2 \sqrt{\frac{\rho_g}{\rho_l}} \quad (\text{Round tubes}) \quad (2.24)$$

$$C_o = 1.35 - 0.35 \sqrt{\frac{\rho_g}{\rho_l}} \quad (\text{Rectangular tubes}) \quad (2.25)$$

According to Hewitt and Hall-Taylor (1970), a factor which may be important in delaying the transition from bubbly to slug flow is interfacial contamination. Radovcich and Moissis (1962) initially stated that this contamination may increase when the water is circulated in a loop. Consequently, coalescence changes and this may lead to progressive change in flow pattern. Also the method of injection or production of the gas in pipe also affects coalescence.

2.3.3.2. Slug/Churn Transitions

As indicated in sub-section 2.2.1.2, when the gas superficial velocity increases from the bubbly flow regime, it results into the formation of Taylor bubbles that almost occupy the cross-section of the pipe. According to Van Hout *et al.* (1992) behind the Taylor bubble is the wake region, in which discrete bubbles torn from the Taylor bubble follow the liquid wake vortices and void fraction is large due to high degree of turbulence. Another region below the wake region is the developed region in which the void distribution is similar to that in the

bubbly flow pattern, (Chen and Brill, 1997). Between the two regions, i.e. the wake region and the developed region there is an intermediate region where discrete gas bubbles are injected into this intermediate region from the bottom of the wake region close to the centre of the pipe. Therefore, with an increase in the gas superficial velocity there is an increase in the degree of turbulence. Consequently, this leads to shrinking of the developed region and hence the slug length decreases. Figure 2.9 shows the schematic of the transition from slug to churn flow.

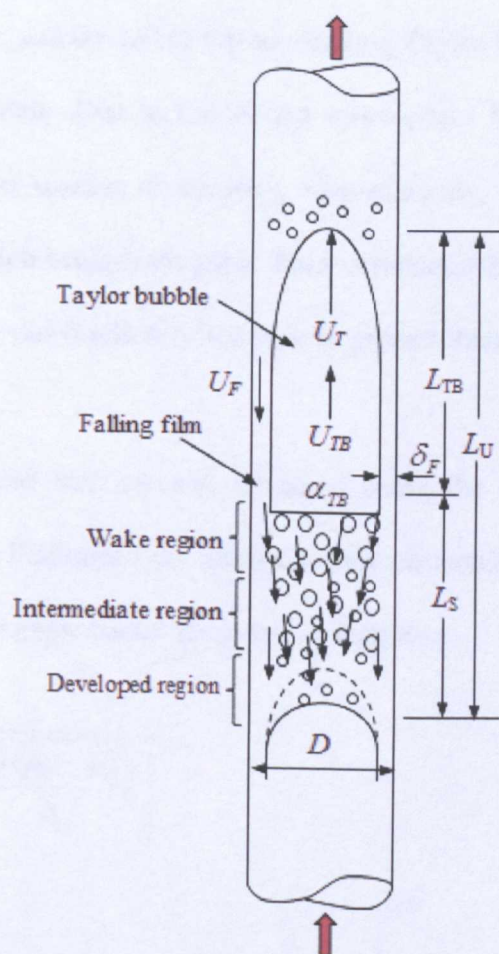


Figure 2.9. Transitions from slug to churn flow (Chen and Brill, 1997) (reproduced).

Earlier workers such as Mishima and Ishii (1984), McQuillan and Whalley (1985), Dukler and Taitel (1986), Brauner and Barnea (1986) and Jayanti and Hewitt (1992) have classified the slug to churn flow regime transition into four general schools of thought which will be discussed briefly below.

(a) *Wake effect mechanism*

Similar to the observations of Chen and Brill(1967) above, Mishima and Ishii (1984) observed that before the slug to churn transition takes place the slug bubbles are lined up right next to each other and the tail of the succeeding Taylor bubble starts to touch the nose of the trailing Taylor bubble. Due to the strong wake effect formed, the liquid slugs become unstable and unable to sustain its identity. Consequently, the destruction and creation of liquid slugs occurs which bridges the pipe. They concluded that the transition of slug to churn flow occurs when the void fraction in the pipe is greater than the mean void fraction over the Taylor bubble region.

The cross-sectional void fraction was obtained using the drift flux model of Zuber and Findlay, (1965). From Potential flow analysis, they obtained an expression for void fraction in Taylor bubble. Their expressions are given as follows:

$$\alpha_s = \frac{U_{gs}}{C_0 U_m + 0.35 \sqrt{\frac{gD(\rho_l - \rho_g)}{\rho_l}}} \quad (2.26)$$

$$\alpha_{TB} \geq 1 - 0.813 \times \left\{ \frac{U_m (C_0 - 1) + 0.35 \sqrt{(\Delta \rho g D / \rho_l)}}{U_m + 0.75 \sqrt{\left(\frac{\Delta \rho g D}{\rho_l} \right) \left(\frac{\Delta \rho g D^3}{\rho_l v_l^2} \right)^{1/8}}} \right\}^{0.75} \quad (2.27)$$

where α_{TB} is the void fraction in the Taylor bubble, U_m is the mixture velocity ($U_{ls} + U_{gs}$), $\Delta \rho$ is the difference ($\rho_l - \rho_g$) and v_l is the kinematic viscosity (μ_l / ρ_l).

(b) Flooding mechanism

Another mechanism for the slug to churn transition was proposed by (Nicklin and Davidson, 1962). This occurs when there is flooding in the liquid film flowing around the Taylor bubble. This is manifested by the onset of upward liquid film flow in the countercurrent flow of a falling liquid film and upward-flowing gas stream. This situation occurs inside the Taylor bubble in slug flow and slug/churn transition is reached when the fluid velocities are such that flooding occurs.

According to Hewitt and Hall-Taylor (1970), this phenomenon can also be arrived at when gas and liquid are smoothly separated at the ends of the tube. They stated that if the gas velocity is gradually increased in what they observed to be a falling film region, a point is reached which large waves are formed on the liquid film and are carried upwards by the gas phase. This results in the transport of liquid above the injection point. Therefore, a region arises where both climbing and falling film flows are occurring simultaneously. This transition is what they referred to as flooding.

Wallis (1962) proposed a semi-empirical equation given as:

$$(U_g^*)^{\frac{1}{2}} + (U_l^*)^{\frac{1}{2}} = C \quad (2.28)$$

where C is a constant whose value Wallis suggested should be around unity. U_g^* and U_l^* are defined as:

$$U_g^* = U_{gs} \left[\frac{\rho_g}{gD(\rho_l - \rho_g)} \right]^{\frac{1}{2}} \quad (2.29)$$

$$U_l^* = U_{ls} \left[\frac{\rho_l}{gD(\rho_l - \rho_g)} \right]^{\frac{1}{2}} \quad (2.30)$$

Since flooding has been observed to occur in Taylor bubbles, McQuillan and Whalley (1985) proposed that the velocity of the phases can also be represented as the velocity of the Taylor bubble (U_{bs}) and the liquid film velocity (U_{fs}) respectively given as:

$$U_{bs}^* = U_{bs} \left[\frac{\rho_g}{gD(\rho_g - \rho_l)} \right]^{\frac{1}{2}} \quad (2.31)$$

$$U_{fs}^* = U_{fs} \left[\frac{\rho_g}{gD(\rho_g - \rho_l)} \right]^{\frac{1}{2}} \quad (2.32)$$

Nicklin and Davidson (1962) also proposed an equation for the velocity of Taylor bubbles which is given as:

$$U_{bs} = 1.2(U_{gs} + U_{ls}) + 0.35(gD)^{\frac{1}{2}} \quad (2.33)$$

The film thickness can also be calculated using the expression for a laminar falling film Nusselt (1916) in equation (2.34) and the film velocity in equation (2.32) can be obtained in equation (2.35) as:

$$\delta = \left[\frac{3U_{fs}D\mu_l}{4g(\rho_l - \rho_g)} \right]^{\frac{1}{3}} \quad (2.34)$$

where μ_l the dynamic viscosity and the film velocity can be given as:

$$U_{fs} = U_{TB} - (U_{gs} + U_{ls}) \quad (2.35)$$

(c) Entrance effect mechanism

From the perspective of Taitel *et al.* (1980), they considered the slug to churn transition as an entrance phenomenon. At the inlet where the two phase flow is introduced into the test section, there is the formation of short liquid slugs and Taylor bubbles. Due to a high degree of turbulence at the entrance to the test section, this results into instabilities in the liquid slug.

These slugs then collapse as they evolve along the vertical pipe and they can be referred to as unstable slugs.

However, if the pipe is of a sufficient length, the unstable slugs collapse and merge with incoming slugs to form stable slugs. Therefore, based on pipe diameter and velocity of the fluid phases, a certain axial distance can be calculated for stable slugs to be formed. This has been given by Taitel *et al.* (1980) as:

$$\frac{l_e}{D} = 40.6 \left(\frac{(U_{gs} + U_{ls})}{\sqrt{gD}} + 0.22 \right) \quad (2.36)$$

(d) Bubble coalescence mechanism

For a constant liquid superficial velocity, an increase in gas superficial velocity from the slug flow can also lead to the formation of highly aerated liquid slugs. Ordinarily, the bubbles in the liquid slug region are dispersed and similar to the bubbly flow regime. The aerated slugs are an indication of the fact that the void fraction in this region increases due to the close contact between bubbles. In other words, more and more bubbles are closely packed in a cubic lattice. Therefore, the close contact between them will give rise to the formation of thin films discussed earlier in section 2.3.3.1, as prerequisites for coalescence to occur. The critical void fraction is given by Brauner and Barnea (1986) as 0.52. They developed a model for void fraction in liquid slug as follows:

$$\alpha_s = 0.058 \left[d_c \left(\frac{2f_w(U_{ls} + U_{gs})^3}{D} \right) \left(\frac{\rho_l}{\sigma_l} \right)^{0.6} - 0.725 \right]^2 \quad (2.37)$$

where f_w is the friction factor based on the mixture velocity.

2.3.3.3. Churn/Annular Transitions

The churn to annular flow transition is closely related to flooding and flow reversal. According to Hewitt and Hall-Taylor (1970), if the upward flow of gas is gradually increased,

a point is reached at which large waves are formed on the liquid film and are carried upward by the gas phase.

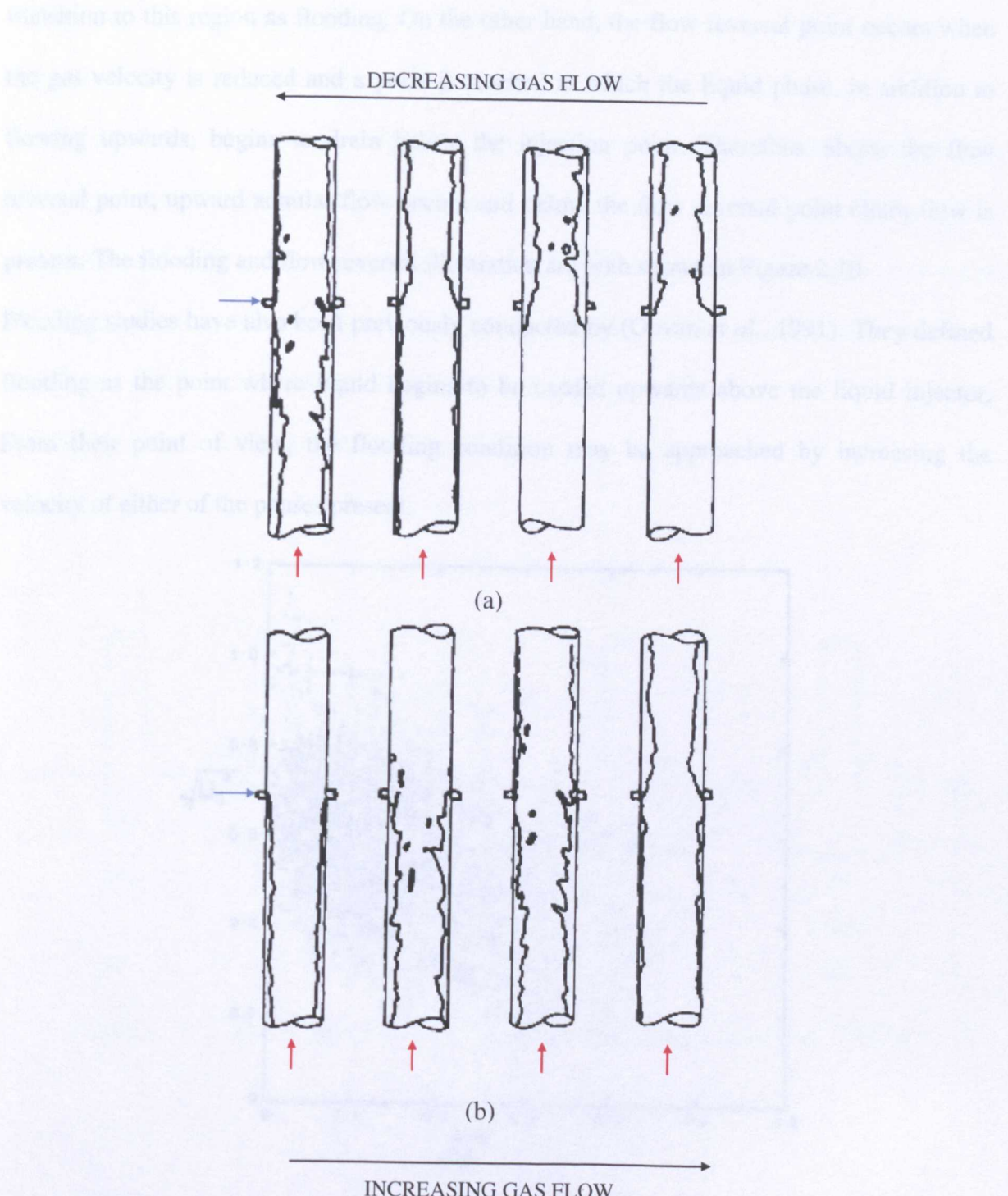


Figure 2.10. Flow reversal and Flooding illustration in (a) and (b) respectively where the blue and red arrows are the liquid and gas inlets, (Hewitt and Hall-Taylor, 1970).

Consequently, the liquid is transported above the injection point as in Figure 2.10 and a region is entered where climbing and falling film occur simultaneously. They termed the transition to this region as flooding. On the other hand, the flow reversal point occurs when the gas velocity is reduced and a point is reached at which the liquid phase, in addition to flowing upwards, begins to drain below the injection point. Therefore, above the flow reversal point, upward annular flow occurs and below the flow reversal point churn flow is present. The flooding and flow reversal illustration are both shown in Figure 2.10.

Flooding studies have also been previously conducted by (Govan *et al.*, 1991). They defined flooding as the point where liquid begins to be carried upwards above the liquid injector. From their point of view, the flooding condition may be approached by increasing the velocity of either of the phases present.

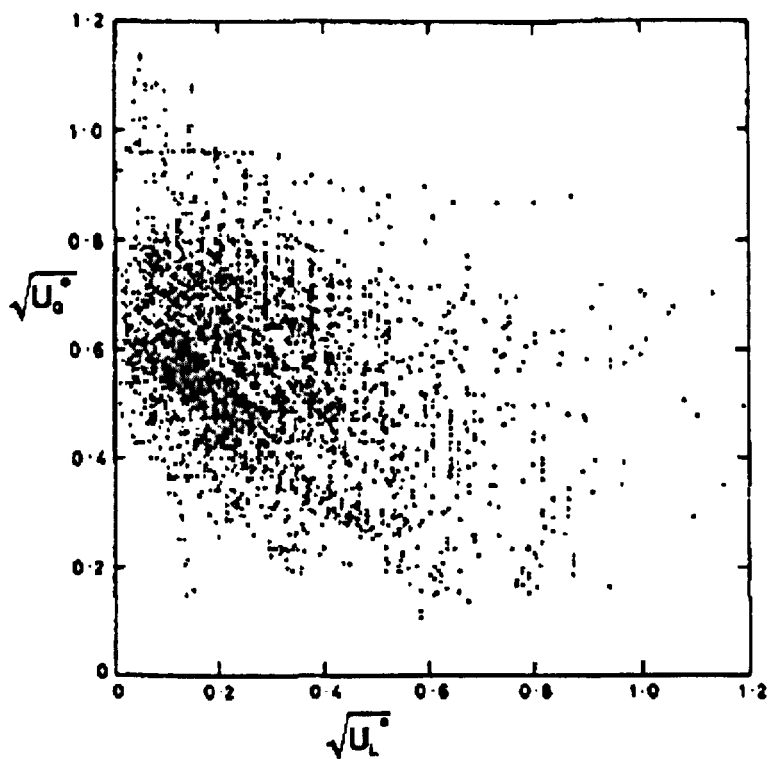


Figure 2.11. Flooding data from McQuillan (1985) retrieved from (Govan *et al.*, 1991).

On the other hand, they defined a term “deflooding” as the point where the pure counter current flow region is reinstated on reduction of flow after flooding occurs. They identified the fact that the geometry of the test section has a major influence on the onset of flooding, that is, the inlet and outlet configurations for gas and liquid phases.

As a result, there is a lot of disparity in the flooding data previously reviewed by McQuillan (1985) as shown in Figure 2.11. The types of geometries used by researchers to investigate flooding according to the review of Bankoff and Lee (1986) are the (a) Porous wall outlet ,(b) and (c) tapered (or bell mouth) outlets, (d) and (e) square edged outlet as shown in Figure 2.12. These will be discussed below from the work of (Govan *et al.*, 1991) as they suggested that flooding and churn flow are closely related.

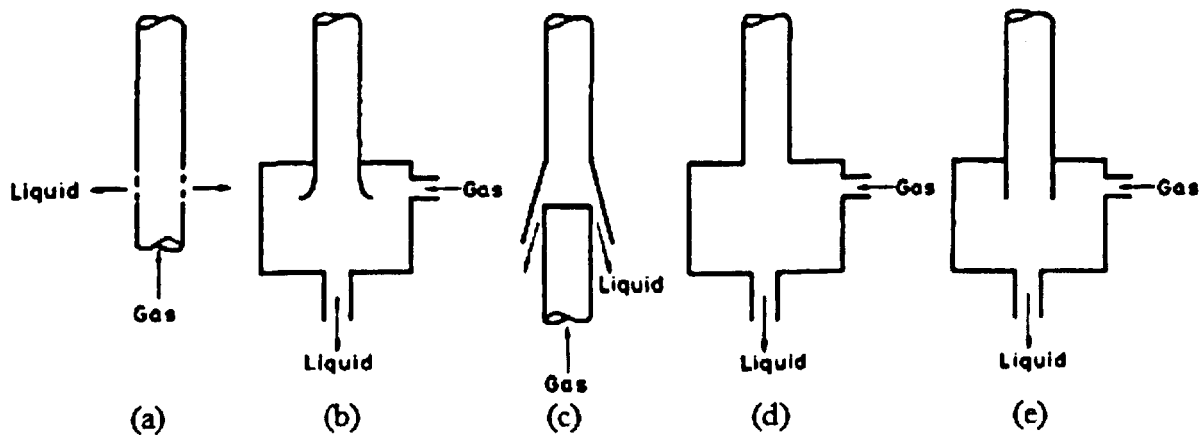


Figure 2.12. Types of geometries used in flooding studies, (Govan *et al.*, 1991).

(a) *Porous wall outlet*

As regards the porous outlet in Figure 2.12(a), for a given liquid flowrate, the gas flowrate was set at a low value so that a falling film is created. At a constant test-section pressure and high liquid flowrates, the gas flowrate was then gradually increased until flooding occurred. This was due to the formation of a single wave near the outlet sinter travelling upwards above the liquid injection point.

Conversely, for a low liquid flowrate and increasing gas flowrate there was the formation of small intermittent waves travelling upwards on the falling film. However, the intermittent waves formed did not travel beyond the liquid injection point. Both of the above observations have been shown in Figure 2.13.

When the gas flowrate was further increased, splashing occurred as a signature to the flooding phenomenon above the liquid injection. The gas flowrate was further increased above this point and the downflow of liquid or deflooding was measured.

From the relationship between the downflow curve and the flooding curve the following observation were made:

- (a) The downflow curve lies below the flooding curve at high flowrates. This is because flooding corresponds to the formation of a huge (large) wave near the bottom of the test section. These huge waves are transported upwards beyond the liquid injection point.
- (b) At low liquid flow rates, the downflow curve is above the flooding curve. They explained this occurrence in terms of the “hanging-film” phenomenon where the film exists but with no net flow. The corresponding downflow near the wall balances the upflow near the interface.

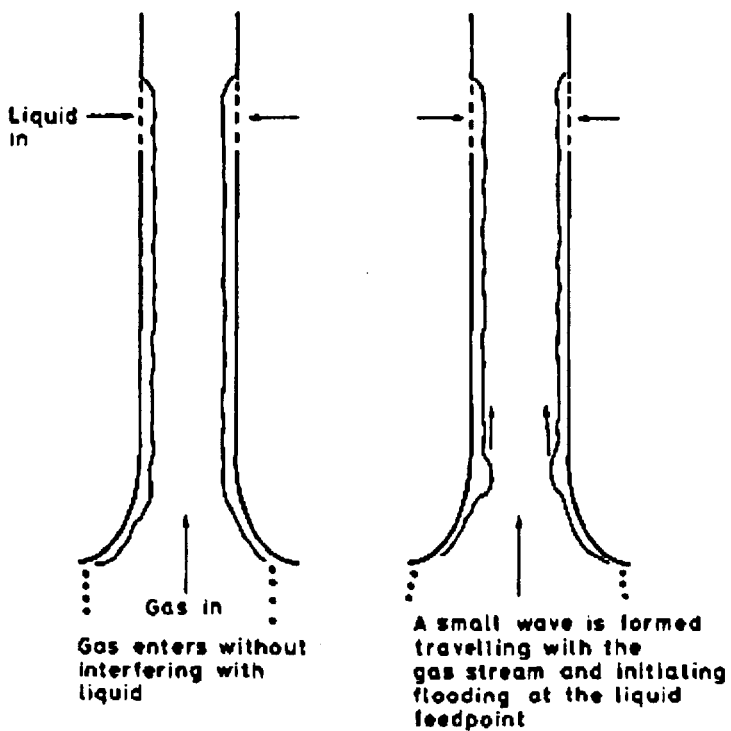


Figure 2.13. Flooding mechanism in test section with Porous outlet, (Govan *et al.*, 1991).

(b) Tapered outlet

When the outlet was tapered the flooding and deflooding occurrences were similar. Compared to the sequence of events observed using the porous section, here, as the gas flowrate increases above flooding, an interaction occurs between the gas and the falling film to form a standing wave at the narrowest part of the taper. When this happens the pipe is filled with a churn-type flow as a result of the reduction in liquid penetration.

On the other hand, when the gas flowrate is reduced a smooth falling film is formed as shown in Figure 2.14.

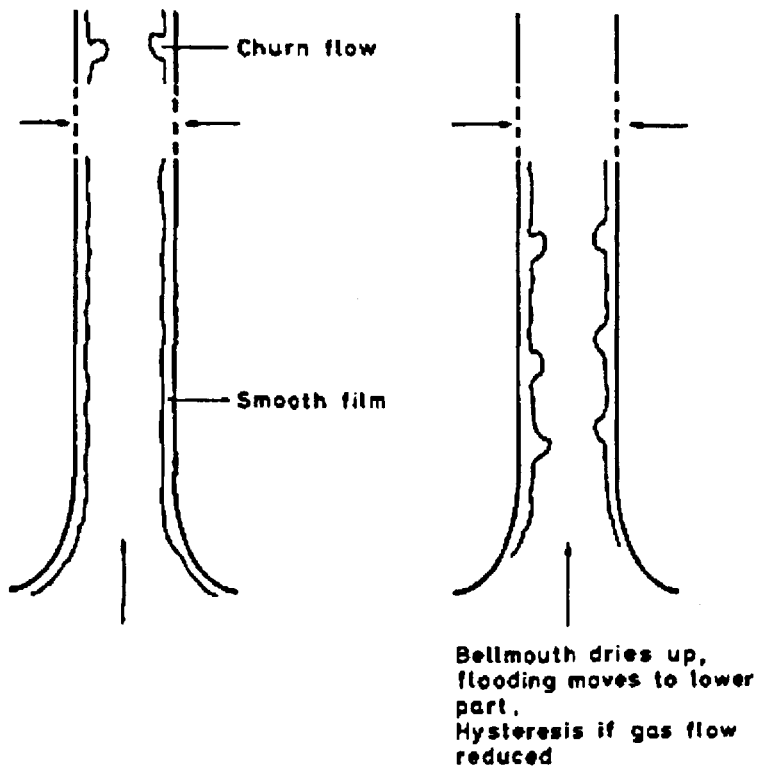


Figure 2.14. Flooding mechanism in test section with Porous outlet, (Govan *et al.*, 1991).

(c) *Square-edged outlet*

In this type of liquid outlet, there is the existence of thick standing waves formed at very low gas flowrates. As will be discussed in a subsequent section, “entrainment” phenomenon occurs when the gas flowrate is increased. This phenomenon is as a result of high gas inertia, which tears the drops from the crest of the wave formed into the gas core. However, most of these drops have been observed to be redeposited on the falling film. The waves formed increase in height and they reduce the flow area and prevent the continuous flow of gas. Therefore flooding takes place at lower gas flowrates than for the other geometries used above and always occurs at the bottom of the test section. The reason behind the flooding effect at the bottom of the test section is because as the gas flowrate increases the rate at which water can escape from the bottom of the test section becomes less than the liquid input. This means that the bottom part of the test section becomes filled with a churn-type flow rising beyond the liquid injector. The effect of a square-edge outlet is shown in Figure 2.15.

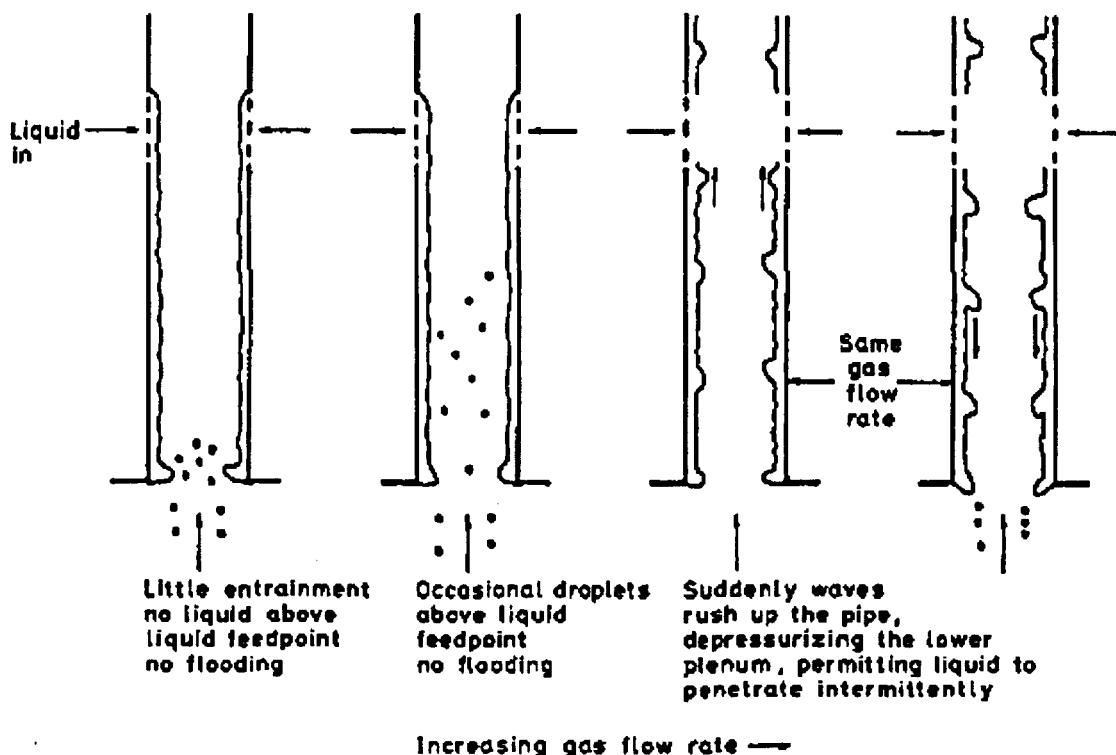


Figure 2.15. Flooding mechanism in test section with square-edged outlet, (Govan *et al.*, 1991).

The effect of geometry has also been summarized in Figure 2.16. In conclusion, it shows that flooding phenomenon is influenced by the smoothness and sharpness of the gas-liquid entrance conditions. From the work of McQuillan and Whalley (1985), before flooding occurs, they observed the downward movement of interfacial waves on the surface of the liquid film. As the flooding terrain is entered, the interfacial waves grow and move upwards rapidly. Therefore, flooding occurs when only one wave is transported and the large upward flowing waves can be repeatedly formed at the liquid injector since the liquid flowrate is sufficient enough due to drainage from the preceding waves. Also, when flooding conditions is present in the test section, there is the rapid growth of waves, which are transported upwards and carried beyond the liquid injection point. Flooding and flow reversal both constitute the major limiting factors in processes such as mass transfer in packed columns,

reflux condensation and nuclear reactor cooling systems, (Jayanti *et al.*, 1996, Vijayan *et al.*, 2001).

Both groups of authors mentioned above investigated the effect of tube diameter on flooding. For example Vijayan *et al.* (2001) conducted experiments on three different inner diameters namely 25, 67 and 99mm with smooth inlet and outlet conditions for air and water.

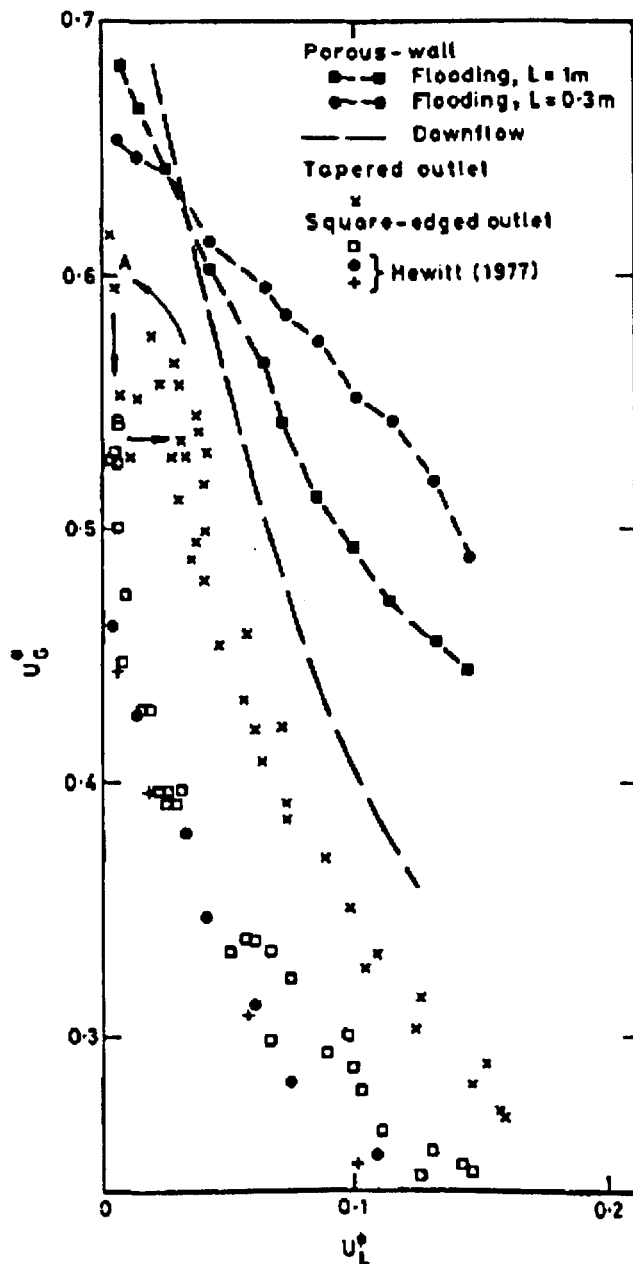


Figure 2.16. Effect of liquid outlet geometry on Flooding, (Govan *et al.*, 1991).

They agreed with the work of Jayanti *et al.* (1996) who contributed theoretically to the notions on flooding that the tube diameter has a determining effect in the way flooding occurs. Similar to the work of Govan *et al.* (1991), they likened the flooding effect to the upward transport of waves created near the liquid outlet and carryover of droplets in the test section. From the above discussions on the flooding experiments conducted by previous workers, it shows close ties exist with the churn flow phenomenon. Since churn flow studies will also be conducted in this work, the following section discusses the mechanism of churn flow in detail.

2.4. *Further insights into churn flow*

Churn flow regime is the most chaotic of all the regimes as shown in Figure 2.2. Hitherto, there has not been any generalised model associated with this regime. However, observations by Hewitt *et al.* (1985) using a photochromic dye tracing liquid, ascertained significant occurrences within this regime. Their experimental arrangement is shown below in Figure 2.17. Similar to the flooding phenomenon described above by Govan *et al.* (1991), large standing waves are formed near the liquid entrance point and eventually they grow to the point that they are levitated by the high gas inertia and consequently transported upwards as shown in Figure 2.18. Between successive standing waves, there is flow reversal. This instantaneous countercurrent flow is in form of a falling film or base film as regarded by other workers such as (Azzopardi and Wren, 2004). The liquid which is transported upwards in form of large waves, pick up liquid from falling film ahead of them and also shed liquid in the form of droplets. This falling film interrupts the trailing wave flowing upwards.

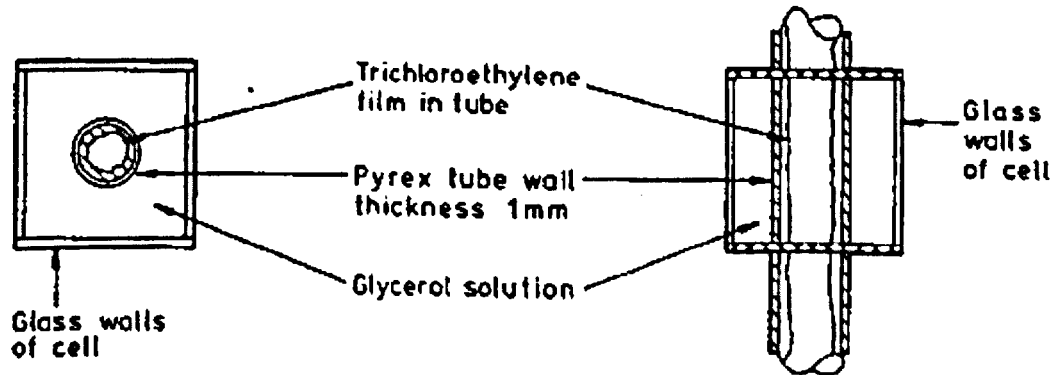
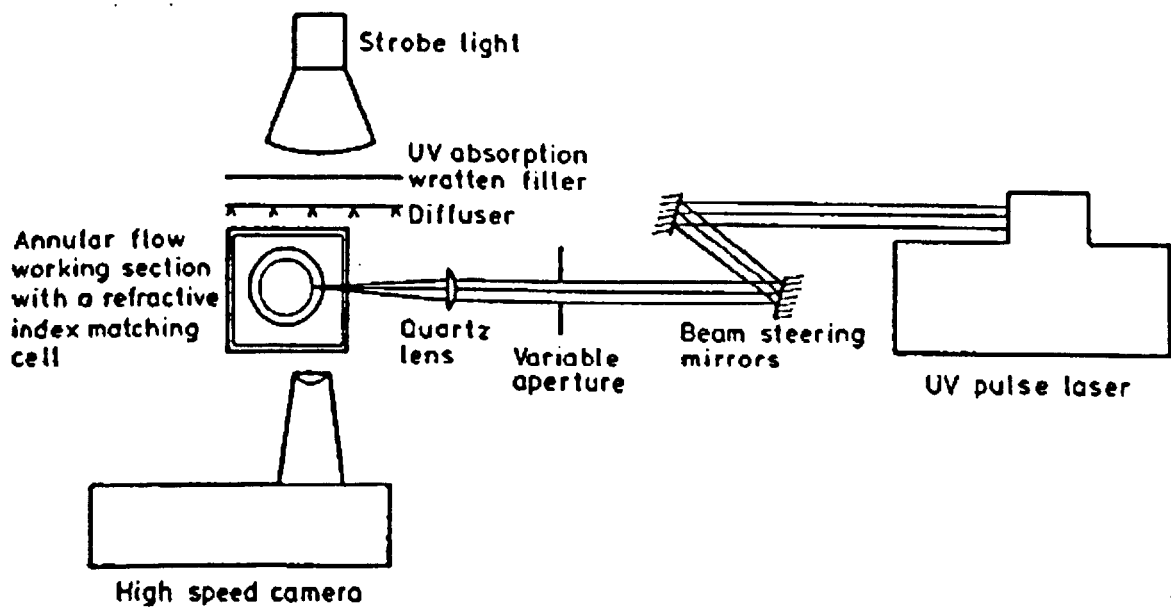


Figure 2.17. Optical arrangement for photochromic dye tracing (Hewitt *et al.*, 1985)

Retrieved from Barbosa *et al.* (2001a). Hewitt *et al.* (1985) contributed immensely to the understanding of the churn flow phenomenon.

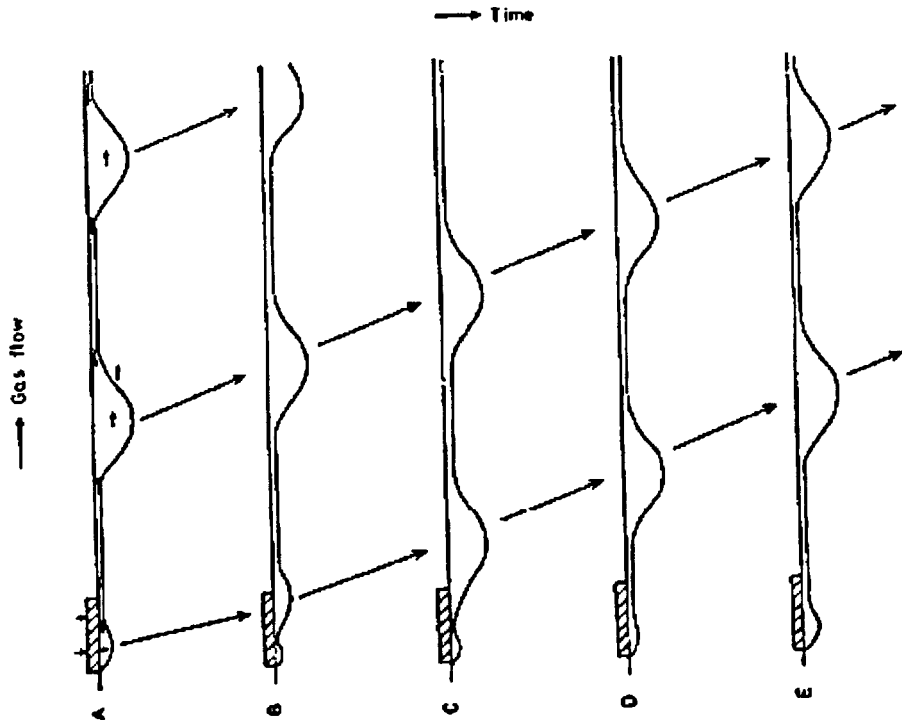


Figure 2.18. Postulated mechanism of churn flow (Hewitt *et al.*, 1985).

According to Barbosa *et al.* (2001b), there is a close relationship between flooding and churn flow. However, they suggested the latter should not be confused with the former. Therefore, to clarify to a reasonable extent the characteristics of the churn flow regime, the flow characteristics and terminologies in corroboration with the general opinions of the flow will be discussed.

2.4.1. Pressure effects

When the destruction of Taylor bubble occurs due to the inception of flooding type waves this has an adverse effect on the system pressure. This has been illustrated from the data of Owen (1986) shown in Figure 2.19.

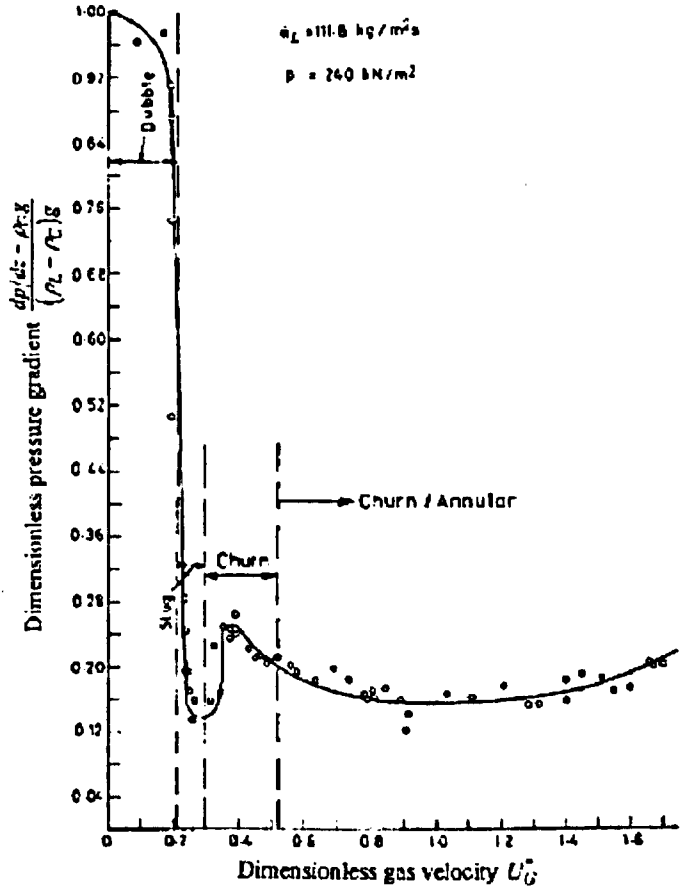


Figure 2.19. Pressure gradient distribution against dimensionless gas velocity for gas-liquid flows in vertical pipes Owen (1986) retrieved from (Barbosa *et al.*, 2001b).

They plotted a graph of dimensionless pressure gradient against the dimensionless gas velocity in equation (2.29). They observed that as the gas flowrate increases the pressure gradient decreases with increasing gas flowrate.

Beyond, a dimensionless gas velocity of 0.4 for a constant liquid flowrate the pressure gradient begins to increase. As shown in Figure 2.19, they stated that the decrease and increase in profile is due to the presence of churn flow regime (gravity dominated) and annular flow regime (friction dominated) respectively.

2.4.2. Entrained fraction

Another facet of churn flow that has received great attention is the concentration of drops in the gas core or entrained fraction. This has been previously addressed by (Barbosa *et al.*, 2002, Azzopardi and Wren, 2004 and Ahmad *et al.*, 2010). As discussed earlier, these drops are formed when high gas inertia tears off ligaments from the crest of the wave, (Azzopardi, 1983). Therefore, it can be said that the concentration of drops entrained in the gas core can primarily be a function of the thickness of the liquid film or wave height.

The entrained fraction itself can be defined as follows, (Barbosa *et al.*, 2002):

$$E_{TF} = \frac{\dot{M}_{LE}}{\dot{M}_L} \quad (2.38)$$

where \dot{M}_{LE} is the mass flowrate of entrained droplet and the \dot{M}_L is the mass flowrate of liquid phase. In churn flow, the method of drop entrainment is known as bag-breakup occurring at high flowrates as in Figure 2.20. This form of droplet entrainment occurs where the gas ‘undercuts’ a large wave forming and open-ended bubble with a thick filament rim.

Gas pressure builds up within the bubble or bag causing it to expand and eventually burst. Azzopardi (1983) proposed that for drop breakup the boundary between bag and ligament breakup can described using a dimensionless Weber number. Azzopardi (1983) used a wave height to mean film thickness ratio of approximately 3.5.

He found a good agreement with a transition boundary for:

$$We = \frac{\rho_g U_{gs}^2 \delta_f}{\sigma} = 25 \quad (2.39)$$

Barbosa *et al.* (2001a) stated that in churn flow, liquid entrainment in the gas core can be quite large. However, the entrainment fraction reduces with increasing gas velocity shown in Figure 2.21, as the wave action is suppressed.

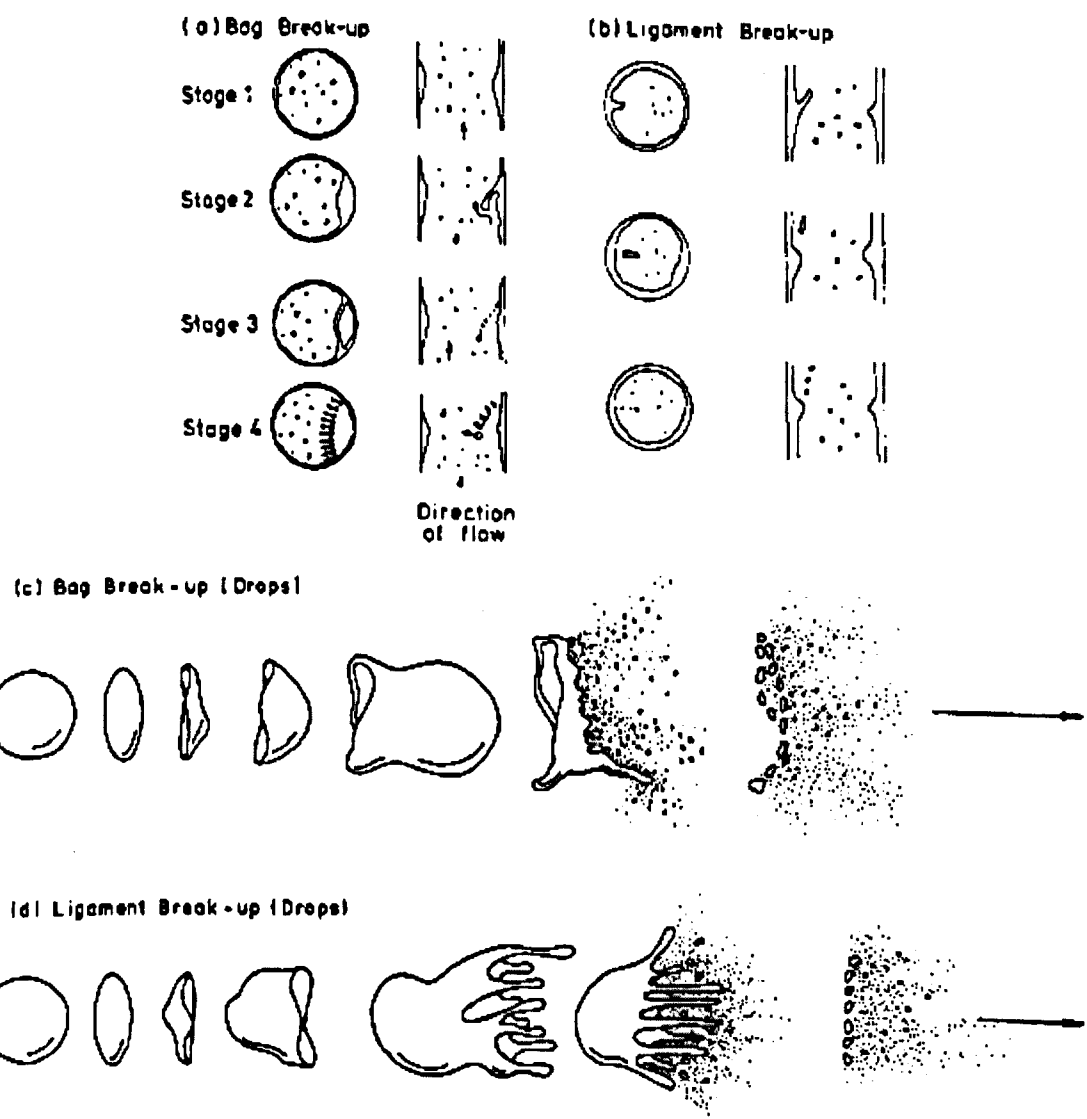


Figure 2.20. Mechanism of drop breakup (Azzopardi, 1997).

Barbosa et al. (2002) developed a correlation for entrained fraction which is given as

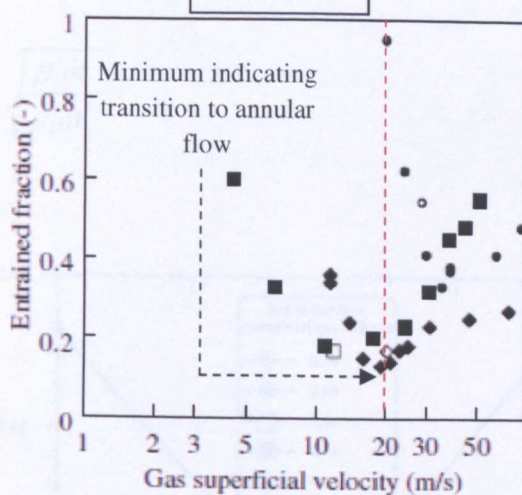


Figure 2.21. Effect of gas velocity on entrained fraction on different pipe diameter
(Barbosa *et al.*, 2002).

This is contrary to an increasing entrained fraction when the gas velocity increases in annular flow. They investigated this further using an isokinetic probe technique to determine the entrained fraction as shown in Figure 2.22. The probe can be used to measure the gas and liquid volume flowrate as a function of position across the tube. The other method of obtaining the entrained fraction is by sucking off all of the film and is known as the film extraction method. This was used by Azzopardi and Zaidi (2000) to suck off the film with the minimum amount of gas using either a porous wall or slot device.

This conventional method of obtaining the entrained fraction proposes a special challenge because of the bi-directional nature of the flow in the wall region, (Barbosa *et al.*, 2001a). This also posed a special challenge to Azzopardi and Zaidi (2000) to the point that they recorded an anomalous behaviour. From their work, they stated that in an attempt to execute the film extraction method, there is a tendency for liquid take off to increase with gas take off; two values of film flowrate might then be deduced.

Barbosa *et al.* (2001) developed a correlation for entrained fraction of drops in the gas core which is given as:

$$E_{TF} \% = 0.95 + 345.55 D^2 \sqrt{\frac{\rho_l \dot{m}_l}{\rho_l \dot{m}_g}} \quad (2.40)$$

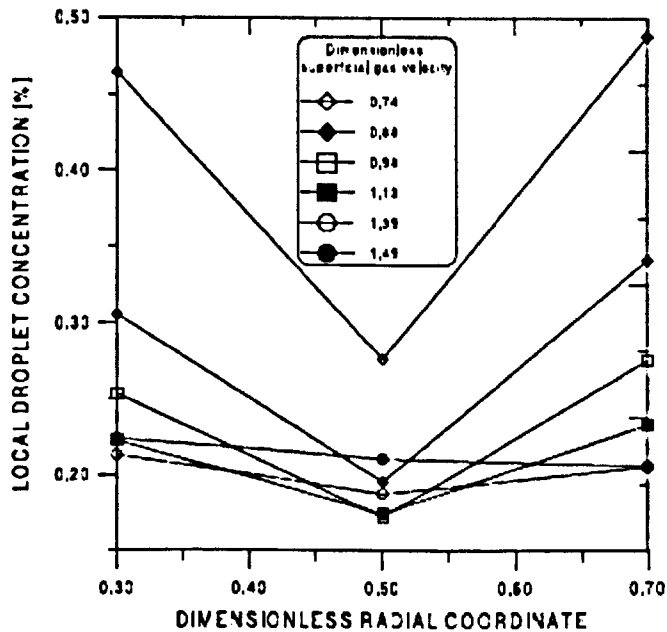


Figure 2.22. Droplet concentration in churn flow and annular flow, (Barbosa *et al.*, 2002).

From the measurement using the isokinetic probe, they added that the in churn flow, as regards drops concentration, there is a peak close to the wall as shown in Figure 2.22. However, for annular flow the drop concentration is constant across the tube diameter. This is due to the mechanisms of drop disintegration as in Figure 2.20. They plotted their predicted values against experimental values in equation (2.40) as shown in Figure 2.23.

It is also interesting to note that the trend for increasing gas superficial velocity is the same for the pressure gradient and entrained fraction in Figure 2.19 and 2.21. This is also due to the different drop breakup mechanisms occurring when different forces dominate.

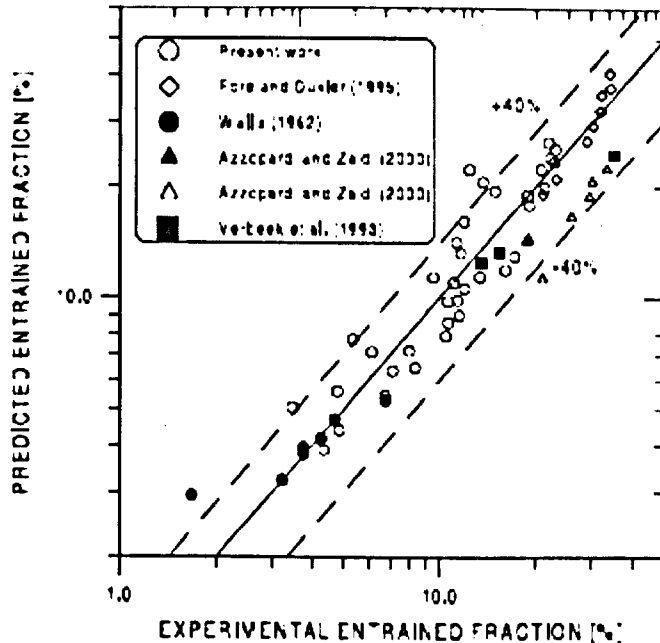


Figure 2.23. Comparison of experimental entrained fraction with correlation proposed by (Barbosa *et al.*, 2002).

The transition to the annular flow regime occurs when the dimensionless gas velocity is equal to 1. Van't Westende *et al.* (2007) used a dimensionless densimetric Froude number as a transition criterion and is given as:

$$Fr \approx \frac{U_{sg}^2}{gD} \frac{\rho_g}{\rho_l - \rho_g} \approx 1 \quad (2.41)$$

They said this corresponds to when the gas superficial velocity equals 20m/s. This has been indicated with a red dashed line in Figure 2.21 of entrained fraction against gas superficial velocity given by (Barbosa *et al.*, 2002).

When the gas superficial velocity is less than 20m/s, that is, for a Froude number of less than 1, the liquid film thickness and the wave height become much larger. This is as a result of a decrease in interfacial shear stress. To transit to annular flow regime, the interfacial shear stress has to increase to balance the increasing weight of the liquid film hence the pressure gradient decreases.

Compared to equation (2.40), Azzopardi and Wren (2004) used their T-junction data to obtain dimensional equations for the entrained fraction. First, they argued that fluids with lower momentum fluxes will be most easily diverted into the side arm of a T-junction. Schematic of T-junction has been shown in Figure 2.24 retrieved from (Azzopardi, 2005).

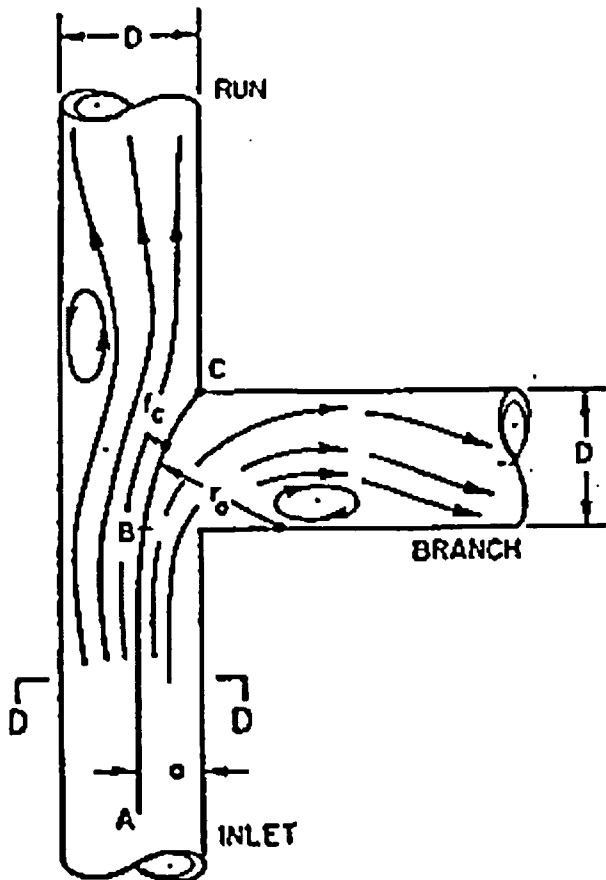


Figure 2.24. Schematic of T-junction retrieved from (Azzopardi, 2005).

When conditions of the system pressure are low there is a likelihood that similar momentum fluxes will exist for gas and liquid phases. However, this momentum fluxes are lower than those for drops. Therefore gas and liquid will be diverted into the side arm. They said that the entrained fraction can be backed out if phase splits were known, that is, using an equation which describes phase maldistribution in annular flow below. This was based on the perspective that in churn flow there is entrainment and the presence of a base film.

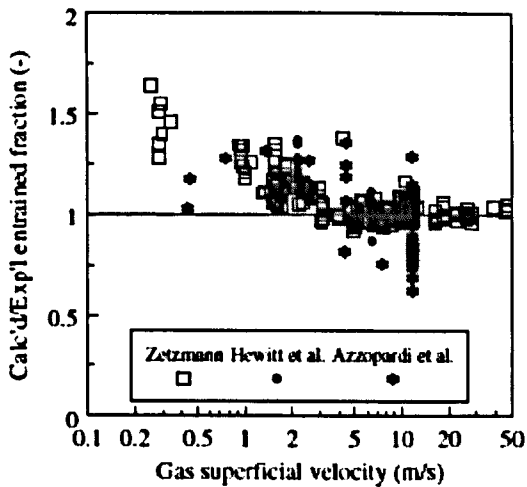


Figure 2.25. Showing accuracy of proposed entrance fraction correlation, (Azzopardi and Wren, 2004).

They identified various data from literature and backed out entrained fraction.

$$\frac{\dot{M}_{g3}}{\dot{M}_{g1}} = \frac{1}{2\pi} \left[\left(\frac{2\pi}{\{1 - E_{TF}\}K} \frac{\dot{M}_{l3}}{\dot{M}_{l1}} \right) - \sin \left(\frac{2\pi}{\{1 - E_{TF}\}K} \frac{\dot{M}_{l3}}{\dot{M}_{l1}} \right) \right] \quad (2.42)$$

where \dot{M}_g are \dot{M} , the mass flowrates if the gas and liquid and the subscripts 1 and 3 refer to the main pipe and side arm respectively, E_{TF} is the entrained fraction and K is a factor that take into consideration the effect of side arm to main pipe diameters. The resulting dimensional equations have an error of 3% and standard deviation of 11% is given below:

$$E_{TF} = 0.47U_{gs}^{0.16}U_{ls}^{0.35} \quad \text{for } U_{gs} < 5 \text{ m/s} \quad (2.43)$$

$$E_{TF} = 0.6U_{ls}^{0.35} \quad \text{for } U_{gs} > 5 \text{ m/s} \quad (2.44)$$

According to Azzopardi and Wren (2004), they concluded that the entrained fraction is carried upwards by the gas phase as drops. In addition, they are also carried as huge (large) waves. This will be discussed in the next section.

2.4.3. Huge (Large) waves

When the liquid phase flowing as waves on the inner walls of the pipe has large amplitudes, these are known as huge waves. Figure 2.26, shows the identification of huge waves based on the work of (Barbosa *et al.*, 2001b and Wang *et al.*, 2012). To investigate the large waves formed in the churn flow regime, Sekoguchi and Takeishi (1989) used a specially designed phase-sensing device, Supermultiple-ring-electrode (Super-REP) probes, which consists of 94 pairs of ring-shaped electrodes probes.

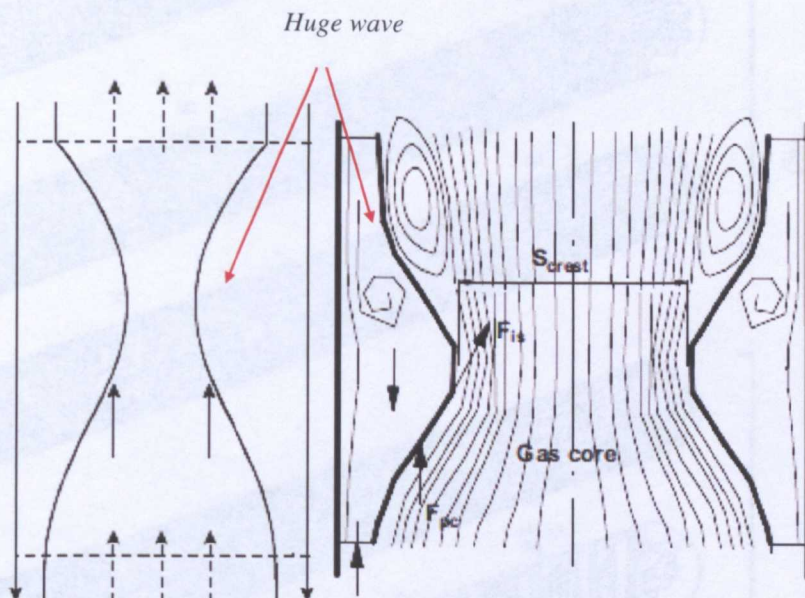


Figure 2.26. Identification of huge wave according to Barbosa *et al.* (2001b) and Wang *et al.*, (2012) in the left and right respectively.

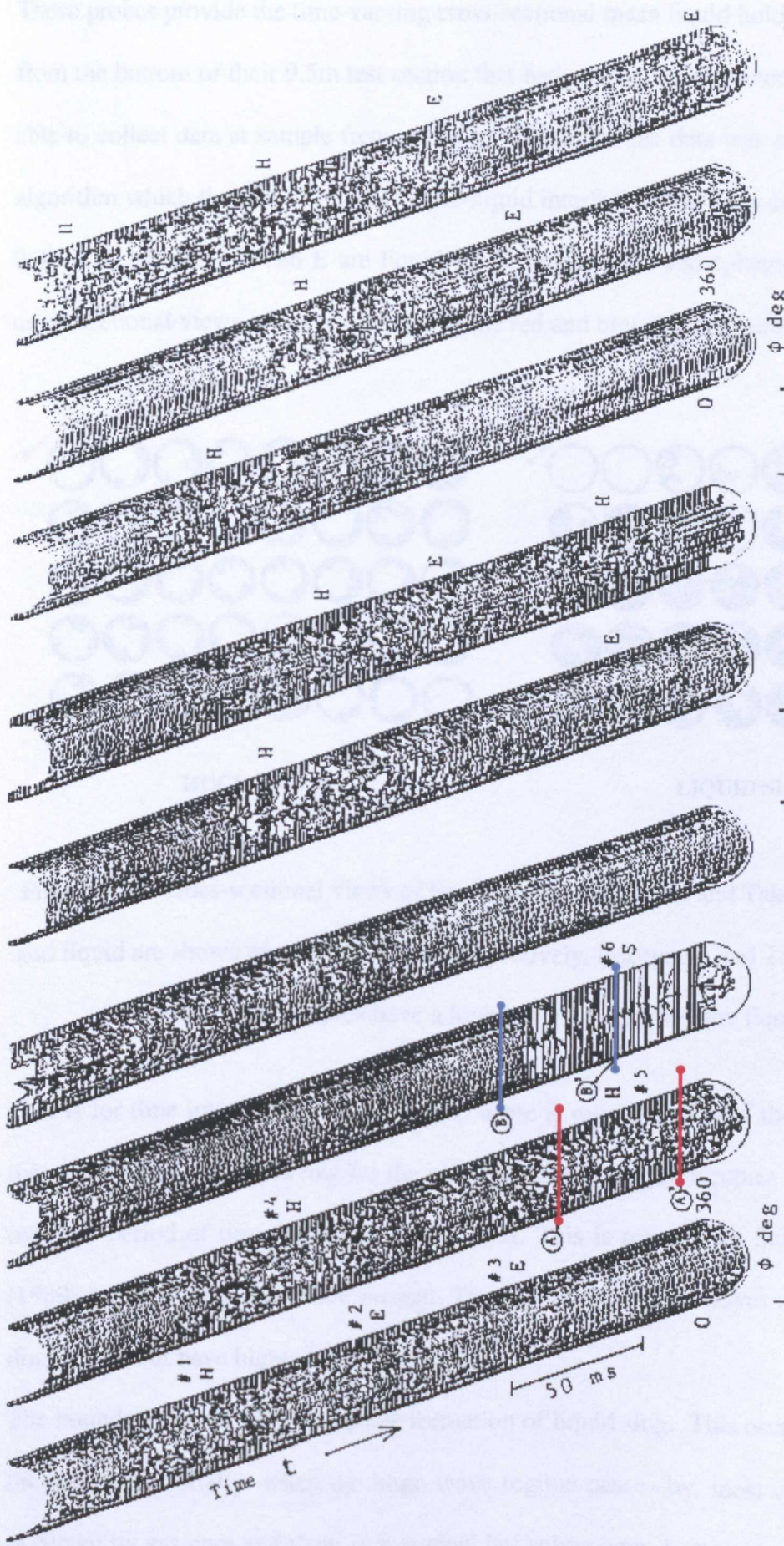


Figure 2.27. Representative three dimensional structures developed on a semi-circular cross-section of the tube (Sekoguchi and Takeishi, 1989).
 (a) $U_{gs} = 5\text{m/s}$ and $U_{ls} = 0.3\text{m/s}$, (b) $U_{gs} = 7\text{m/s}$ and $U_{ls} = 0.3\text{m/s}$, and (c) $U_{gs} = 5\text{m/s}$ and $U_{ls} = 0.1\text{m/s}$ respectively.

These probes provide the time-varying cross-sectional mean liquid holdup value located 4.1m from the bottom of their 9.5m test section that had an internal diameter of 25.8mm. They are able to collect data at sample frequencies of 400Hz and the data was analysed using a novel algorithm which they developed. The gas-liquid interfacial structures can be shown in Figure 2.27. The letters S, H and E are liquid slugs, huge waves and ephemeral large waves. The cross-sectional views of the boundaries of the red and blue lines are shown in Figure 2.28.

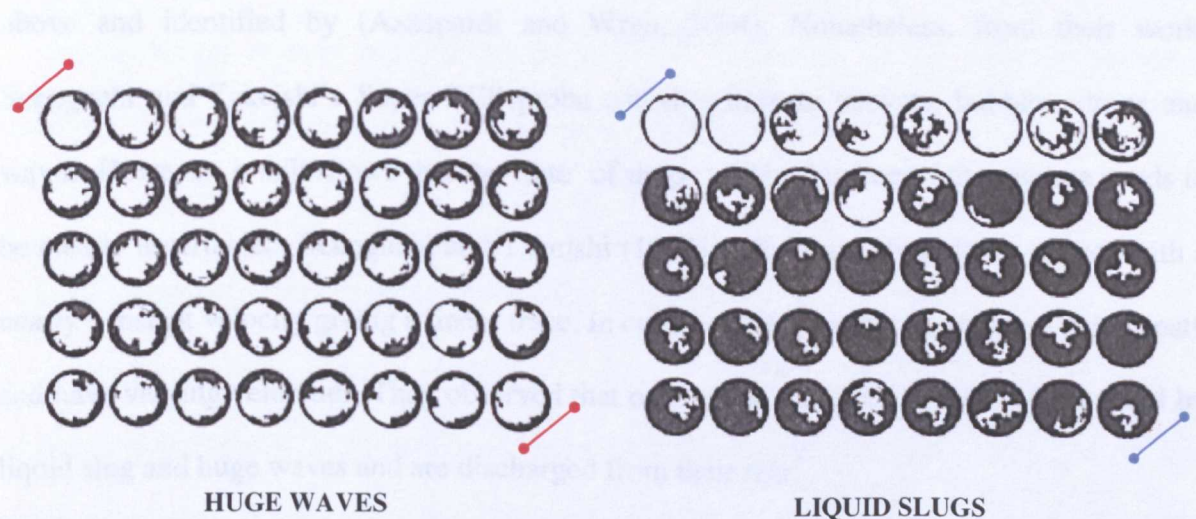


Figure 2.28. Cross-sectional views of liquid lump, (Sekoguchi and Takeishi, 1989). The gas and liquid are shown as white and black respectively. Sekoguchi and Takeishi (1989) pointed out that huge waves have a higher transit velocity than liquid slugs.

This is for time interval of 1ms where the white is representative of the gas and the black is that of the liquid. It shows that for the red line region, the gas occupies the pipe cross-section over the period of time the data was acquired. This is referred by Sekoguchi and Takeishi (1989) as when huge waves are present. They added that, huge waves are greater not only in dimensions but have higher transit velocities.

The boundary for the blue line is the formation of liquid slug. This occurs upstream, close to the injection. Initially, when the huge wave regime passes by, most of the cross-section is occupied by gas core and there is a gradual but subsequent destruction of the huge waves by

the formation of liquid slugs. In contrast to the instantaneous huge wave region, here, the liquid slugs occupies nearly the whole of the pipe cross-section meaning that the void fraction decreases and liquid holdup on the other hand increases. Sekoguchi and Takeishi (1989) concluded that the huge waves have a higher velocity than the disturbance waves and the ephemeral waves they observed in annular flow. However, they did not identify the facts that within this huge wave regime, drops are being carried as per entrained fraction discussed above and identified by (Azzopardi and Wren, 2004). Nonetheless, from their work, Sekoguchi and Takeishi's Super REP probe can discriminate between bubbles, drops and waves. However, it still shows that the 'fate' of drops within this huge wave regime needs to be clearly ascertained. Sekoguchi and Takeishi (1989) added that a liquid slug moves with a nearly constant velocity giving a linear trace. In contrast, the huge waves follow a zigzag path and have varying velocities. They observed that ephemeral waves are frequently absorbed by liquid slug and huge waves and are discharged from their rear.

2.5. *Conclusion on Literature review*

This chapter discusses on the fundamentals of multiphase flow in particular two phase gas-liquid flows. For two phase gas-liquid flows in vertical pipes, the flow regimes that exist are bubble, slug, churn and annular flow regimes. It is important to note that these flow regimes are present in small diameter pipes. However, there is a direct transition from bubble to churn flow regimes in large diameter pipes where slug flow pattern has not been observed for the fluids used for experimentation.

The literature on the churn flow pattern which is the regime of interest is few. However, the observation of liquid slugs and huge waves identified by Sekoguchi and Mori (1986) has been taken into consideration and has also been identified in the chapters 4, 5 and 6. Further references can also be made to their work as observed in chapters 4, 5 and 6.

CHAPTER 3

EXPERIMENTAL ARRANGEMENTS

In this chapter, the experimental facilities used to conduct two phase upward flow experiments will be described. The experimental facilities have test section geometries of 121mm internal diameter – 5.3m in length vertical pipe (chapter 4), 127mm internal diameter – 11m in length vertical pipe in (chapters 5 and 6). Details of the rig configurations, instrumentation and operating conditions will also be discussed.

3.1. 121mm internal diameter facility

3.1.1. *Overview of experimental facility*

In this experimental facility, bubble to churn flow experiments has been carried out to find out the operation condition for the occurrence of typical churn flow. The schematic of the experimental facility is shown in Figure 3.1. The facility has a test section of 121mm internal diameter and is 5.3m in length. The operating fluids used are air and water as the dispersed and continuous phases respectively.

Compressed air was supplied through an injection device from the high-pressure laboratory line at a pressure of 8bar. A total volume of 0.45m^3 of tap water was charged into the storage tank (A). Below the storage tank, a valve was opened and this allowed the delivery of the liquid to the centrifugal pump. The pump operating at $68\text{m}^3/\text{hr}$ was started and the liquid flowed through two calibrated liquid rotameters before arriving at the main experimental section. The calibration of the liquid rotameters is shown in Figure E.1, Appendix E. The liquid phase from the pump entered two pipelines. The first line is equipped with a valve (B) and an electro-magnetic flowmeter-EMF, (C), to adjust and monitor the flowrate of the liquid while the second line has an injection device (D).

3.1.2. Start-up considerations

During the start-up of the facility, bubbles were noticed flowing through the pipe equipped with the valve (B). This was due to the fact that the air tank was open to the atmosphere. The air tank was closed to the atmosphere and the valve (B) was closed to prevent air from entering the test section.

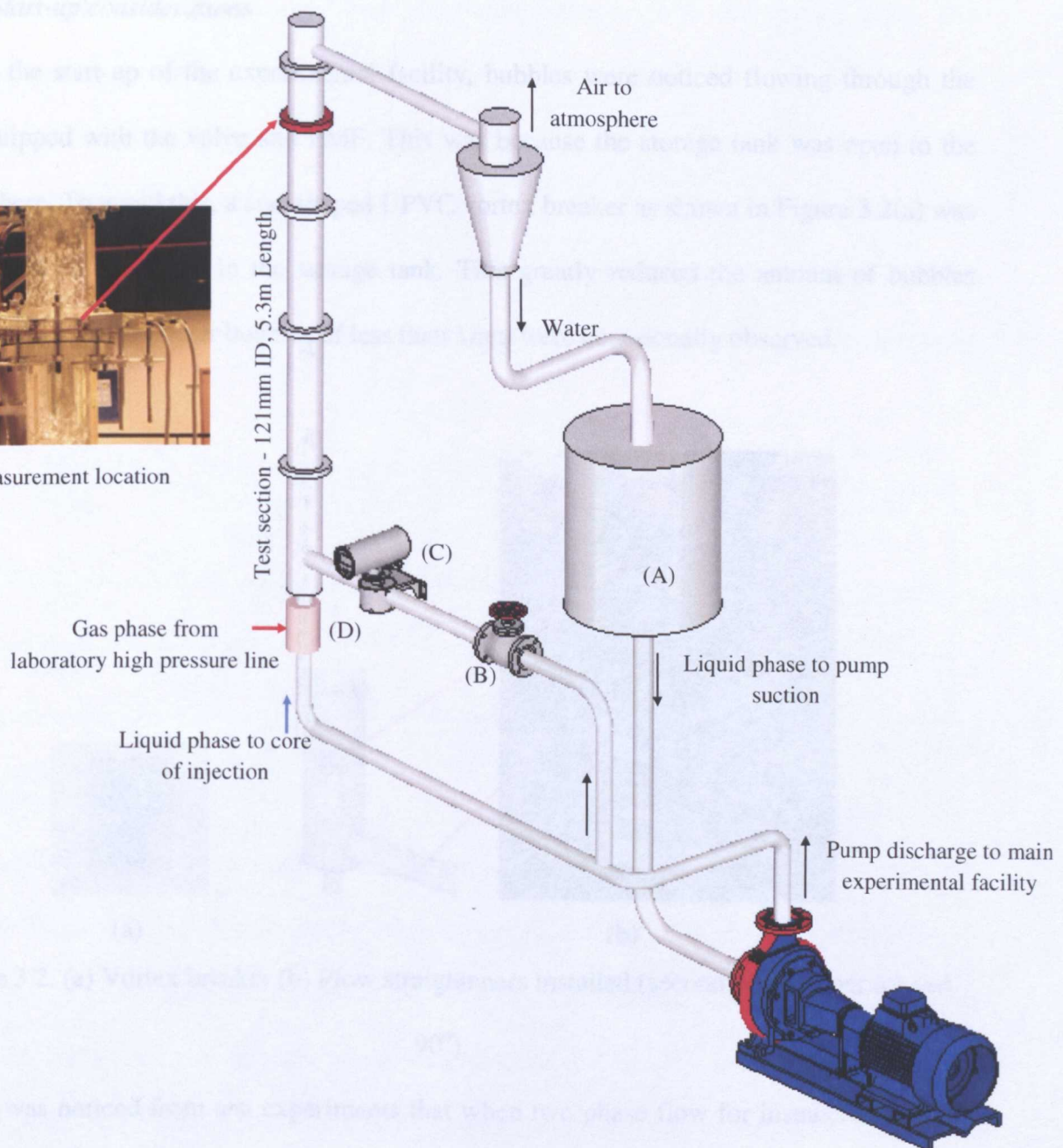
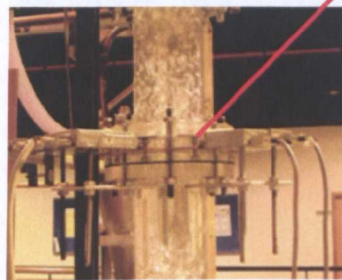


Figure 3.1. Schematic of the main parts of the 121mm internal diameter experimental facility, showing data acquisition location in red.

The orientation of valve (B) can be changed to observe the effect in the test section. However, for the present experiments, the valve was kept fully open. The compressed air from the laboratory line is supplied to the throat of the injection device while the liquid flows through the core.

3.1.2. Start-up considerations

During the start-up of the experimental facility, bubbles were noticed flowing through the line equipped with the valve and EMF. This was because the storage tank was open to the atmosphere. To avoid this, a star-shaped UPVC vortex breaker as shown in Figure 3.2(a) was constructed and installed in the storage tank. This greatly reduced the amount of bubbles formed and small diameter bubbles of less than 1mm were occasionally observed.

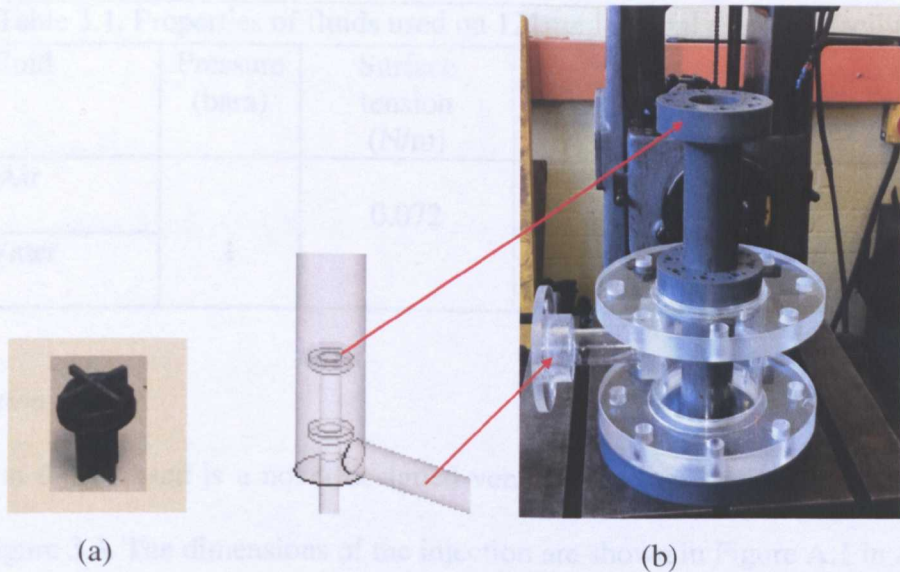


Figure 3.2. (a) Vortex breaker (b) Flow straighteners installed (second straightener rotated 90°).

Also, it was noticed from test experiments that when two phase flow for instance enters the line equipped with the (valve and EMF) into the test section, it followed a helical trajectory due to the method of injection. Therefore, two UPVC flow straighteners with a diameter of 115mm (wall spacing of 3mm taken into consideration) were designed to ensure the velocity profile was uniform. This has been shown in Figure 3.2(b). Holes were drilled in the flow straightener to enable the flow of the liquid phase. The second flow straightener was rotated 90° to the first and placed 150mm downstream. The two-phase flows downstream and enters a stainless steel cyclone separator where the gas and liquid are separated centrifugally. The

air is released to the atmosphere while the liquid flows back to the storage tank. The operating conditions for gas and liquid superficial velocities ranged from $U_{gs} = 0.21\text{m/s}$ to 3.58m/s and $U_{ls} = 0.018\text{m/s}$ to 0.13m/s respectively, at atmospheric conditions. The full experimental design can be found in Appendix B. The properties of the fluids used are shown in Table 3.1. Based on the flowrate readings acquired from calibrated rotameters and the properties of the fluids at an absolute pressure of 1bar, the gas and liquid superficial velocities were calculated.

Table 3.1. Properties of fluids used on 121mm internal diameter facility				
Fluid	Pressure (bara)	Surface tension (N/m)	Density (kg/m ³)	Viscosity (Pa.s)
Air	1	0.072	1.2	1.78×10^{-5} (0.0178cP)
Water			998	0.001 (1cP)

3.1.3. *Injection device*

The injection device used is a novel designed venturi injection device with an air chamber shown in Figure 3.3. The dimensions of the injection are shown in Figure A.1 in Appendix A. Within the air chamber, a brass piece of 30mm in height, 2mm in wall thickness and 64 x 2mm drilled holes through the walls was placed to allow air flow. Six air inlets were used and the air was introduced tangential to the brass piece placed inside the venturi injection device. The air line was equipped with a non-return valve to prevent the flow of water into the gas rotameters.

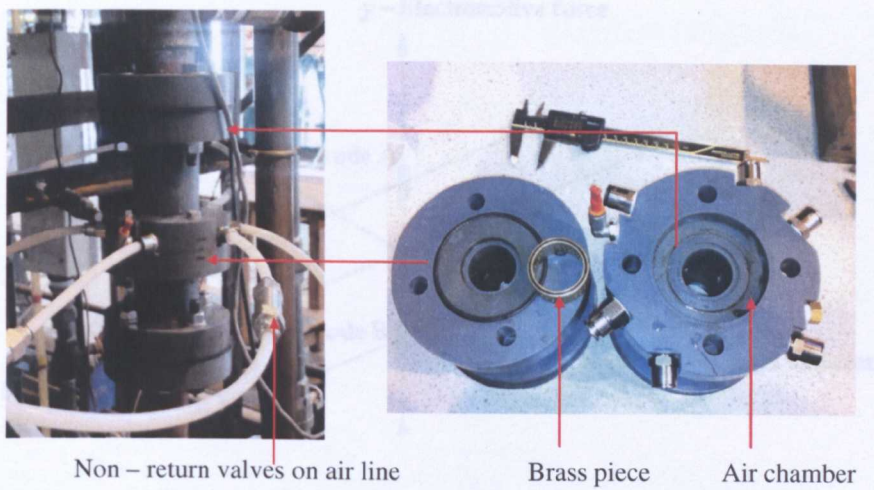


Figure 3.3. Designed venturi injection device used on the 121mm internal diameter, 5.3m in length experimental facility. The injection used is a modified venturi injection device having an air chamber to allow air flow. Schematic of injection is shown in Appendix A.

3.1.4. Electromagnetic flowmeter (EMF)

The liquid flowrate measurement on the side inlet to the test section was measured using an electromagnetic flowmeter (EMF). The conventional form of an EMF is shown in Figure 3.4. The EMF does not measure volume but velocity of the continuous phase and it is used after the valve in this study to monitor the flow of the passing fluid. Based on Faraday's law of induction an alternating magnetic field is produced with coils of copper wire. A coil current which is controlled ensures that the magnetic field strength remains constant during the measurements.

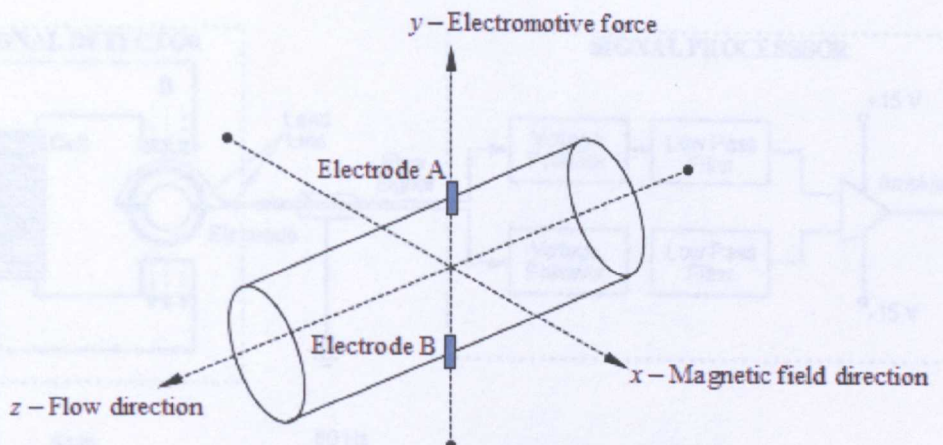


Figure 3.4. Conventional electromagnetic flowmeter (EMF) from work done by (Cha *et al.*, 2002).

The only variable based on the Faraday's equation is the velocity of the fluid passing the EMF. The voltage which is generated from AC is exactly proportional and linear to the velocity of the fluid. The electromagnet of the EMF was excited by the AC current from the mains power supply. Cha *et al.* (2002) identified the main noise sources of electromagnetic flowmeter excited by AC power and they are given as follows:

- (a) The transformer signal from the alternating magnetic field (including the effect of eddy current in the flowtube)
- (b) Noise from the capacitive and resistive coupling between signal and power circuits

In addition, the following effects that distort the flow signal corresponding to the flow rate are:

- (a) Fluctuation of the magnetic field due to fluctuation of the power input
- (b) Iron loss and hysteresis effects of the electromagnet
- (c) Amplified loading from the impedance of measuring devices

Figure 3.5 shows the block diagram for detecting and processing of signals according to (Cha *et al.*, 2002).

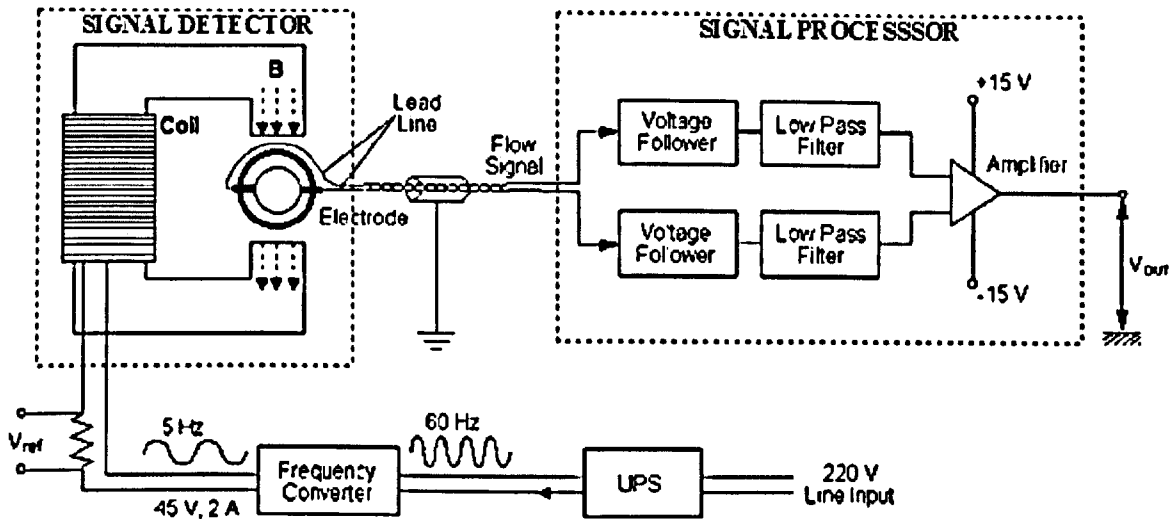


Figure 3.5. Block diagram for detecting and processing of signals, (Cha *et al.* 2002).

3.1.5. Wire mesh sensor (WMS) data acquisition electronics

The electronics used to acquire void fraction data in the above experiments was a capacitance wire mesh sensor. Details of the sensor operation have also been reported by (Thiele *et al.*, 2009). The WMS has two electrode wires stretching across the cross-sectional area of the flow. The electrode wires are on two planes designed orthogonal to each other where one set of wires serves as transmitters and the other set as receivers. The block diagram of the electronics is shown in Figure 3.6.

The transmitter electrodes are connected to a sinusoidal excitation voltage in a successive order while the other non-active transmitter electrodes are grounded. A sensing block converts the electrical currents from the activated transmitter electrode to all receiver electrodes into proportional DC voltages. All DC voltages are simultaneously analog to digital converted at the rising edge of the sample-and-hold signal and their values are stored into the RAM module of the data logger.

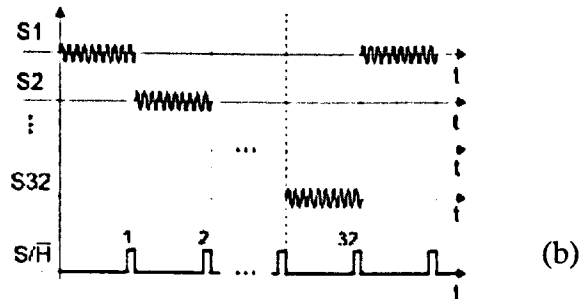
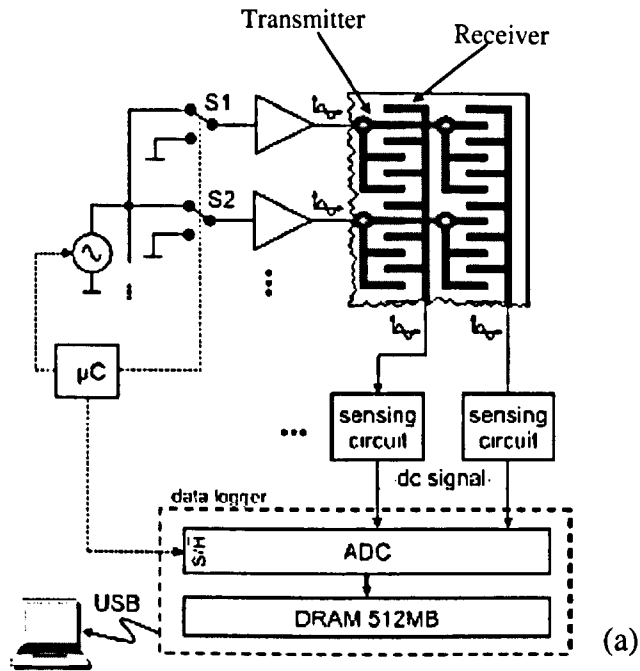


Figure 3.6. (a) Block diagram of capacitance sensor (b) Temporal excitation scheme of the transmitter electrodes with sinusoidal voltage excitation and the point of digitization with a an ADC controlled by the sample-and-hold signal, (Thiele *et al.*, 2009).

Once all 32 transmitter electrodes have been activated and all currents have been measured, a data matrix of 1024 electrical current values corresponding to the distribution of the permittivity over the sensor can be obtained. The data matrix is an instantaneous phase distribution across the sensor. A microcontroller controls the excitation and acquisition signal timing as well as the frequency of the excitation signal.

The data logger is connected to a computer through a USB wire interface, where the digitized data is reprocessed and visualized. The WMS employs the use of permittivity of fluids to infer the void fraction at crossing points of the wires. The sensor used in these set of experiments is 32 x 32 WMS with a resolution of 4mm obtained by dividing the pipe diameter by number of electrode wires.

3.1.5.1. *Permittivity measurement*

According to Thiele *et al.* (2009), the sensing circuit for the WMS is formed by three basic stages. The transmitter electrodes are excited by a sinusoidal alternating voltage. The receiver currents are converted to a voltage by a transimpedance amplifier circuit, which is then followed by a logarithmic demodulation circuit. The circuit layout for the wire mesh sensor is shown in Figure 3.7. The sensor generates a voltage V_o , which is proportional to logarithm of the root mean square value of the transmitted alternating current, which itself is proportional to the relative permittivity, ϵ_r , of the fluids present at a crossing point (Da Silva, 2007). The relative permittivity of water compared to air is in the ratio of 80 to 1. The relative permittivity is related to the output voltage as in equation (3.1):

$$V_o = a \ln(\epsilon_r) + b \quad (3.1)$$

where a and b are constants that depend on the sensor geometry and circuit parameters. The advantage is that it allows the measurement of electrical permittivity for a range of substances used in any experimental campaign.

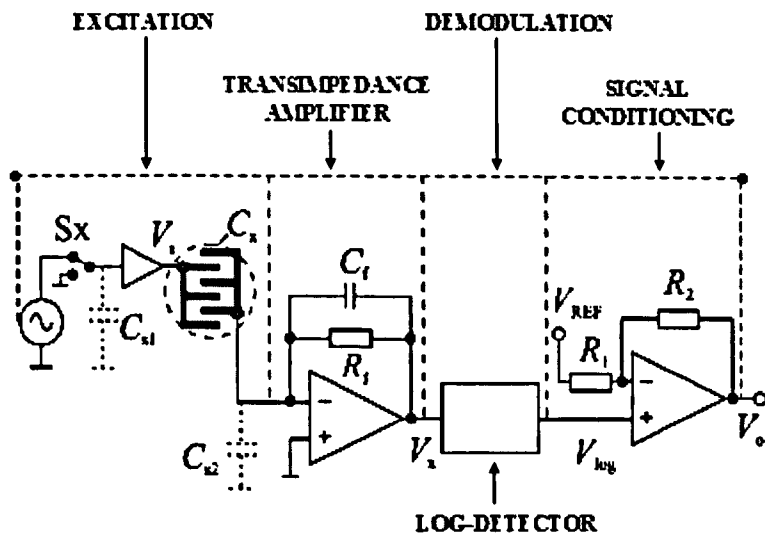


Figure 3.7. Equivalent one-channel circuit for measuring the permittivity using the Capacitance wire mesh sensor (WMS), (Thiele *et al.*, 2009).

The WMS produces sequences of cross-sectional images and voltage mappings which are further processed as a three-dimensional data matrix to permittivity values at each mesh crossing point. The permittivity distribution map is further processed to produce the void fraction image. The indices i and j are the spatial indices of the image pixels that correspond to the number of wires and k is the temporal index of each image. The above equation (3.1) holds for every crossing point in the wire mesh grid.

3.1.5.2. Calibration routine

The WMS has to be calibrated for the high and low values of permittivity that corresponds to the fluids in order to extract sensible phase fraction parameters from the raw data. The calibration routine is performed by acquiring data from measurements in conditions where the pipe is first ‘completely filled with gas’ and then then ‘completely filled with liquid’, represented by air and water respectively, (Thiele *et al.*, 2009 and Szalinski *et al.*, 2010).

In this study, the same method of calibration was applied with air and then water respectively. This is because the existence of drops on the WMS affected the calibration for

the air, that is, if the calibration for water is done prior to air. The calibration files are then saved in matrices. To obtain the void fraction a linear relationship which is known as the *parallel model* can be used. It gives the functional relationship between the void fraction $\alpha_g(i, j, k)$ and relative permittivity values according to (McKeen and Pugsley 2002).

$$\alpha_g(i, j, k) = \frac{\epsilon_{r,water} - \epsilon_{r,mix}}{\epsilon_{r,water} - \epsilon_{r,air}} \quad (3.2)$$

The measured mixture permittivity can be calculated as follows

$$\epsilon_{r,mix} = \exp\left(\frac{V_{o,mix}(i, j, k) - V_{o,air}(i, j)}{V_{o,water}(i, j, k) - V_{o,air}(i, j)} \ln(\epsilon_{r,water})\right) \quad (3.3)$$

where $V_{o,mix}(i, j, k)$ represents the voltage of the two-phase mixture, and the subscripts ‘air’ and ‘water’ indicates the values from the calibration when the pipe is empty and filled with water respectively. The three-dimensional matrix of the void fraction, axial and radial void fraction profiles can be determined by the integration of the measured data over appropriate partial volumes. The disadvantage of using this method of calibration compared to the histogram calibration Lucas *et al.* (2010) is that the conductivity of the water changes during the course of the experiments due to temperature increase from the heating pumps, which will affect the cross-sectional averaged void fraction. However, this will not have a considerable effect as such since the permittivity of the fluids is being measured not the conductivity. The phase fraction data for the experiments conducted on the 121mm internal diameter facility was acquired at L/D = 35. This was done at a frequency of 1000 Hz for 30 seconds, which gives a total number of 30,000 frames.

Overall, the WMS is a very powerful tool in acquiring cross-sectional and time averaged data due to its high resolution. However, during the experiments, a relaxation time is needed between measurements to prevent the electronics from triggering off during data acquisition

for a particular experiment. The relaxation time required in this case should be at least 20 minutes based on test experiments. This also depends on the operating conditions used.

Figure 3.8 shows the picture of a 32 x 32 WMS.



Figure 3.8. 32 x 32 Wire mesh sensor manufactured by Helmholtz-Zentrum Dresden-Rossendorf (HZDR) formerly known as Forschungszentrum Dresden-Rossendorf (FZDR).

3.1.5.3. Wire mesh sensor performance evaluation

The WMS performance evaluation addresses the issues surrounding the accuracy of the void fraction data obtained from the WMS. This was not carried out in this work but has been presented in the work of Thiele *et al.* (2009) for the same capacitance type sensor. Based on the understanding of their work, this will be briefly discussed in this sub-section.

(a) Wire mesh sensor accuracy

The experiments carried out by Thiele *et al.* (2009) as regards the WMS accuracy used five different substances and air (empty sensor) to evaluate the ability of the sensor to distinguish between various substances. Therefore, permittivity values ranging from 1 to 80 were measured. For each substance, ten frames were acquired at 10000 Hz and an average value was taken to reduce the influence of statistical signal fluctuation. The Figure 3.9 shows the measured voltage values for all substances analysed. It can be observed in Figure 3.9, that the

measured voltage values for water presents a small deviation from the expected linear relationship. However, when the calibration routine was applied, those values fall within 10% deviation lines. In other words, the nonlinear effect can be neglected.

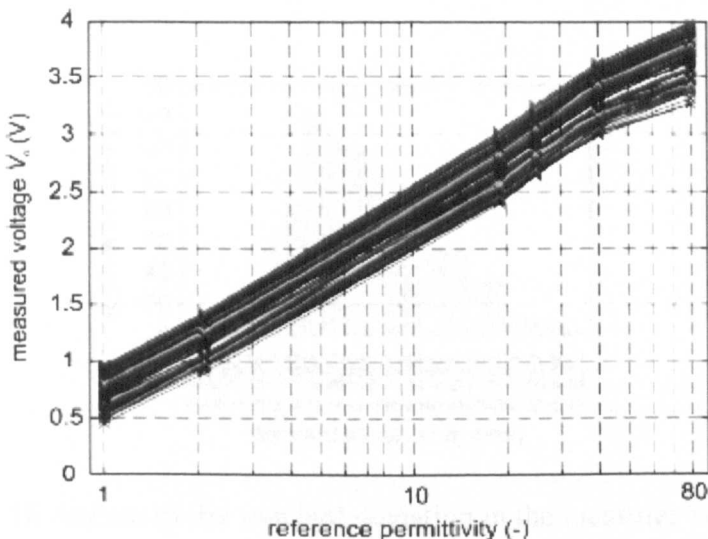


Figure 3.9. Measured voltages from the measurement of different substance in a relative permittivity range of 1 – 80 according to (Thiele *et al.*, 2009). Substances used are Air, Oil, 2-Propanol, Ethyl alcohol, Ethyl glycol and Deionized water having permittivity values of 1.0, 2.1, 20.1, 25.1, 40.3 and 79.9 respectively.

(b) Instrumental noise

To investigate for instrumental noise, the surface of the sensor was fully covered with 2-propanol solution. The standard deviation of the measured voltages over 1000 frames at a frequency of 10000 Hz was taken to estimate the instrumental noise. The histogram of the standard deviation is shown in Figure 3.10. For their experiments, they encountered a maximum value of 6.62mV. Also, using uncertainty propagation rules, they calculated the maximum noise in the permittivity measurement caused by the noise in the voltage measurement as in equation (3.4)

$$\sigma_e (\%) = \frac{\sigma_o}{a} \cdot 100\% \quad (3.4)$$

Using a value of $a = 0.57V$, they obtained a noise in the permittivity measurement of $\pm 1.16\%$.

The uncertainty value is much lower than the obtained accuracy and is negligible.

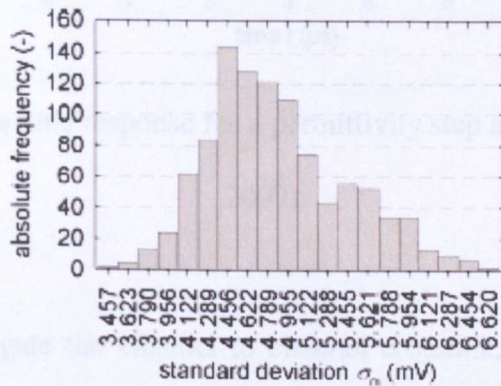


Figure 3.10. Histogram of the standard deviation in the measures voltages on each transmitter-receiver pair from 1000 frames for the evaluation of instrumental noise according to (Thiele *et al.*, 2009).

(c) Time response

The step response of the WMS was analysed to estimate the maximum achievable frame rate.

To achieve this, two transmitter electrodes were activated consecutively where one of them was covered with water the other empty (air). Figure 3.11, shows the variation of measure voltage with time response. A 1% error settling time was determined and for a 32 x 32 sensor, a maximum frame rate of 15.32 kHz is possible.

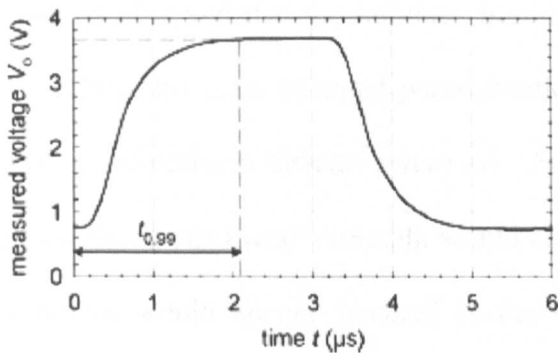


Figure 3.11. Electronics time response for a permittivity step according to (Thiele *et al.*, 2009).

(D) Cross-talk

To experimentally investigate the channel to channel crosstalk, a planar phase distribution with a well-defined phase boundary was measured. The sensor was placed in an upright position (tilted 45°) and was immersed half way inside an acrylic box with 2-propanol. The phase fraction distribution was measured at a rate of 10000 Hz and ten frames were averaged. To analyse the data, interpolated lines of equal phase fraction values (0.25, 0.5, and 0.75) were calculated. These lines represent the 2-propanol-air interface.

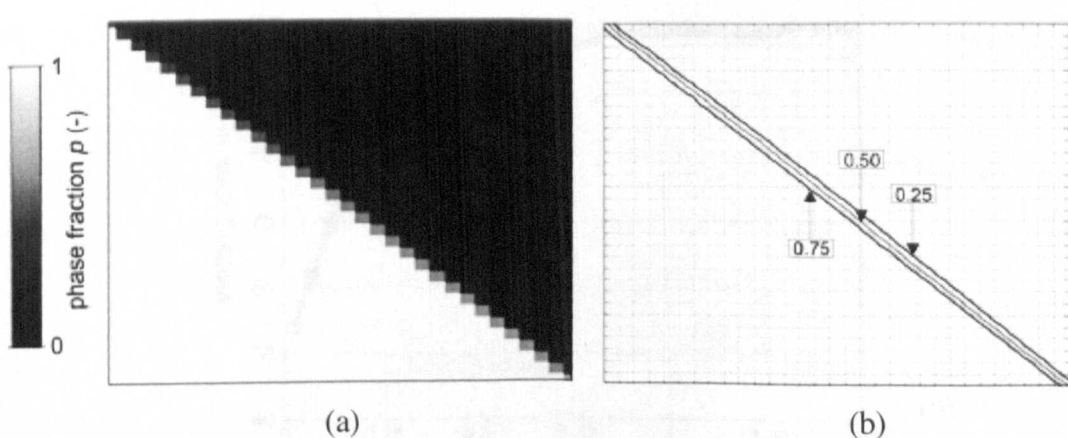


Figure 3.12. (a) Measured phase fraction distribution. (b) Calculated lines of equal phase fraction according to (Thiele *et al.*, 2009).

From Figure 3.12 (a), it can be observed that the interface is imaged abruptly without any transition layer. In Figure 3.12(b), the lines of equal phase fraction are nearly straight and distanced equally. Thus, both characteristics indicate a very low channel-to-channel crosstalk. Thiele *et al.* (2009) suggested that a significant crosstalk would cause the distortion of these lines and the phase distribution would appear smeared in the image. Therefore, images produced by the capacitance WMS are free of crosstalk artefacts.

(E) Depth Sensitivity

In addition to the above performance evaluation study, Thiele *et al.* (2009) suggests that an important parameter for the correct interpretation of the cross-sectional images generated by the WMS is the determination of depth sensitivity.

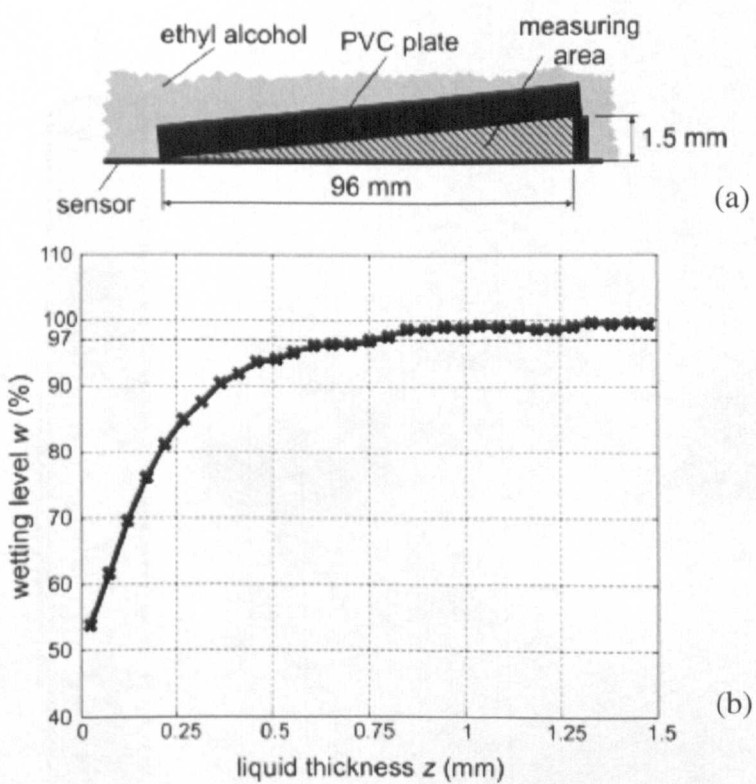


Figure 3.13. Experimental setup for the depth sensitivity estimation (b) Wetting level as a function of liquid film thickness measured in the experimental evaluation of depth sensitivity according to (Thiele *et al.*, 2009).

To investigate this, they initially placed an electrically non-conducting PVC plate over the sensor as in Figure 3.13. One of the endpoints was raised using a thin spacer and the other side was in direct contact with the sensor. This was immersed in ethyl alcohol which results into a liquid film of continuously increasing thickness over the surface of the sensor. Ten frames at 10000 Hz were acquired and averaged. They eventually obtained a maximum liquid thickness of 0.75mm that influences the measurements of the sensor. This has also been considered to be negligible.

3.1.6. High speed visualization

High speed images were acquired below the wire mesh sensor in this facility at L/D = 35. A Phantom v12.1 high speed camera at 1000 fps (frames per second) was used in this study.

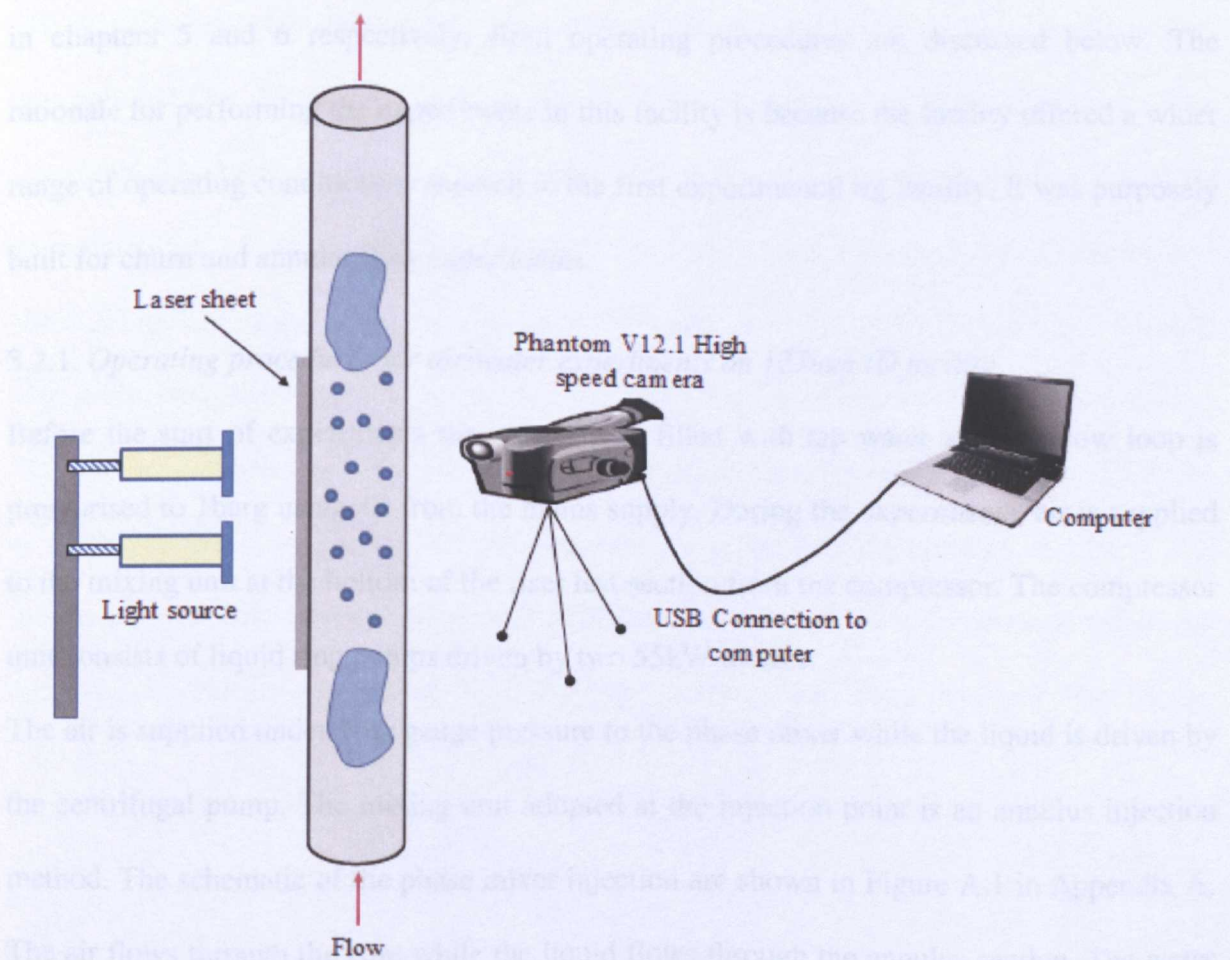


Figure 3.14. High-speed setup for the 121mm internal diameter, 5.3m in length facility

The high speed videos helped to provide additional evidence that may not be clearly ascertained from visual observations. For these experiments, a laser sheet was folded and placed on one side of the test section to reduce reflection of any rays of light that may be emitted. Spot lights were used to also provide sufficient illumination to the test section. Figure 3.14 shows the setup of the high-speed video imaging setup.

3.2. 127mm internal diameter facility

The process flow diagram of the large scale closed loop facility for churn flow development experiments is shown in Figure 3.15 and other components are shown in Figures 3.16 and 3.17. The facility was previously used by Omebere (2006) to conduct churn to annular flow transition experiments. The facility was used for air-water and air-glycerol/water experiments in chapters 5 and 6 respectively. Both operating procedures are discussed below. The rationale for performing the experiments in this facility is because the facility offered a wider range of operating conditions compared to the first experimental rig facility. It was purposely built for churn and annular flow experiments.

3.2.1. Operating procedures for air-water experiments on 127mm ID facility

Before the start of experiments the separator is filled with tap water and the flow loop is pressurised to 1 barg using air from the mains supply. During the experiments, air is supplied to the mixing unit at the bottom of the riser test section from the compressor. The compressor unit consists of liquid ring pumps driven by two 55kW motors.

The air is supplied under 1bar gauge pressure to the phase mixer while the liquid is driven by the centrifugal pump. The mixing unit adopted at the injection point is an annulus injection method. The schematic of the phase mixer injection are shown in Figure A.1 in Appendix A. The air flows through the core while the liquid flows through the annulus section. The water flowing from the periphery of the injection and air through the core form a two-phase mixture

that enters the test section. Downstream from the injection point, the two phases travel through the test section which is 11m in height and has an internal diameter of 127mm. The test section is made of UPVC but a perspex section of 700mm in length is used to observe the flow pattern present at respective axial locations from the injection point. The phase fraction data is extracted using a capacitance wire mesh sensor discussed in section 3.1.5. The location of the capacitance wire mesh sensor was varied for five axial distances from the injection position (base of test section) at $L/D = 2.4, 7.1, 30.7, 35.4$ and 82.7 .

Beyond the riser test section, the two-phase flow travels for 2.34m horizontally, through a 90° bend, a further 9.63m vertically downwards and 1.47m horizontally to the two-phase separator. The separator is a cylindrical stainless steel vessel of 1.6m^3 in volume, a diameter of 1m and height of 4m.

The liquid collected at the bottom of the separator is recycled to the test section. Therefore, this required that the liquid inventory be changed after each set of experiments has been completed. The valve located on the gas return line exiting the separator is used to control the air supply to the compressor section. This means that the gauge pressure can be increased to about 3 barg. The speed of the compressor motors can be varied up to 1500 rpm and together with associated valves just below the gas flowmeters regulate the pressure in the test section. The operating conditions for gas and liquid superficial velocities ranged from $U_{gs} = 3.26\text{m/s}$ to 17.46 m/s and $U_{ls} = 0.03$ to 0.24 m/s respectively, at an operating pressure of 1 barg. This was done to achieve churn flow regime within the test section. The full operational matrix can be found in Appendix B. Table 3.2 shows the properties of the fluids.

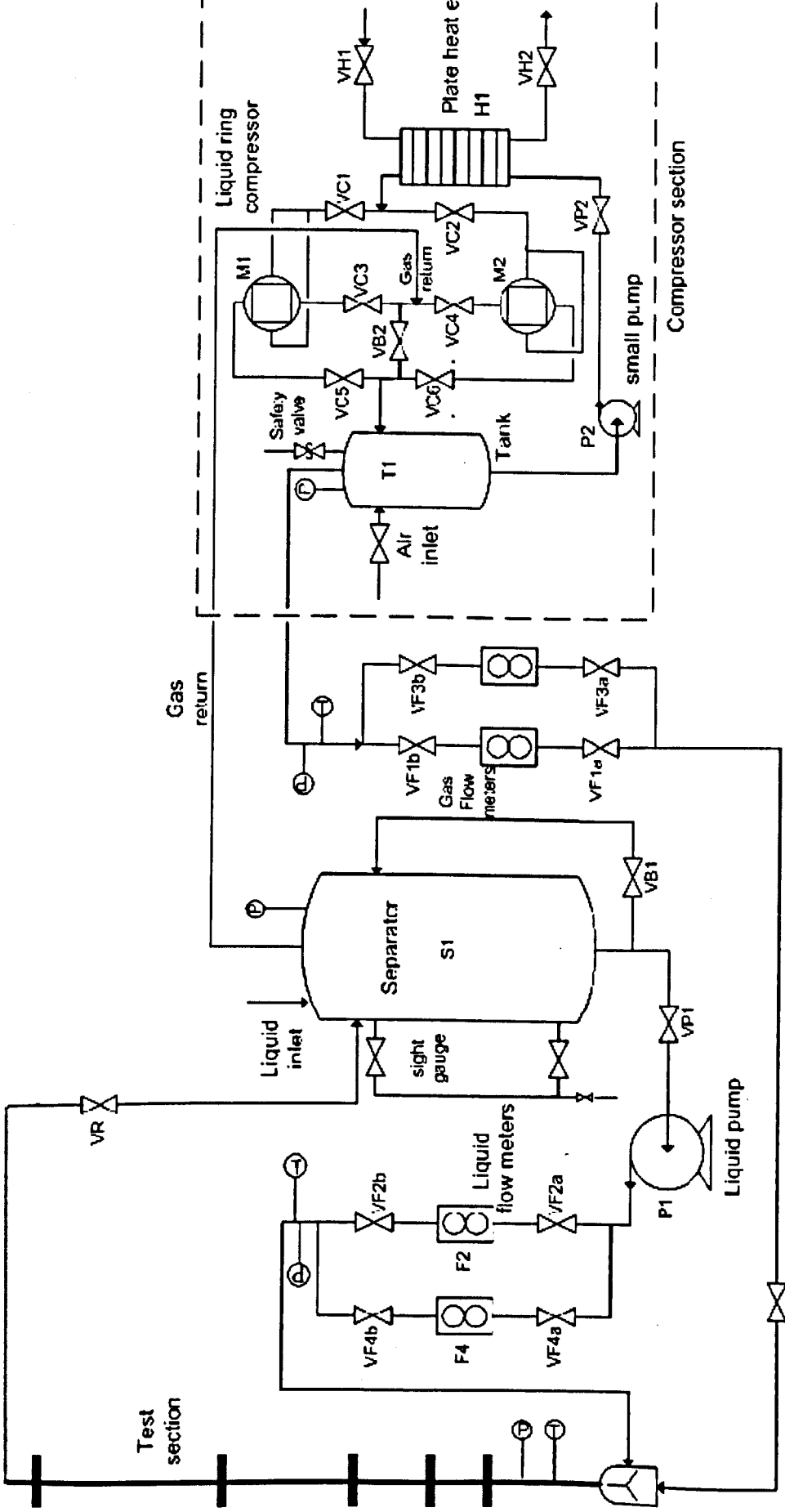


Figure 3.15. Large scale two phase flow experimental facility. Schematic originally done by Omebere (2006) who previously worked on the facility. The internal diameter of the test section is 127mm and is 11m in length. Schematic of phase mixer can be found in Appendix A. Measurement locations are indicated in red at $L/D = 2.4, 7.1, 30.7, 35.4$ and 82.7 respectively.

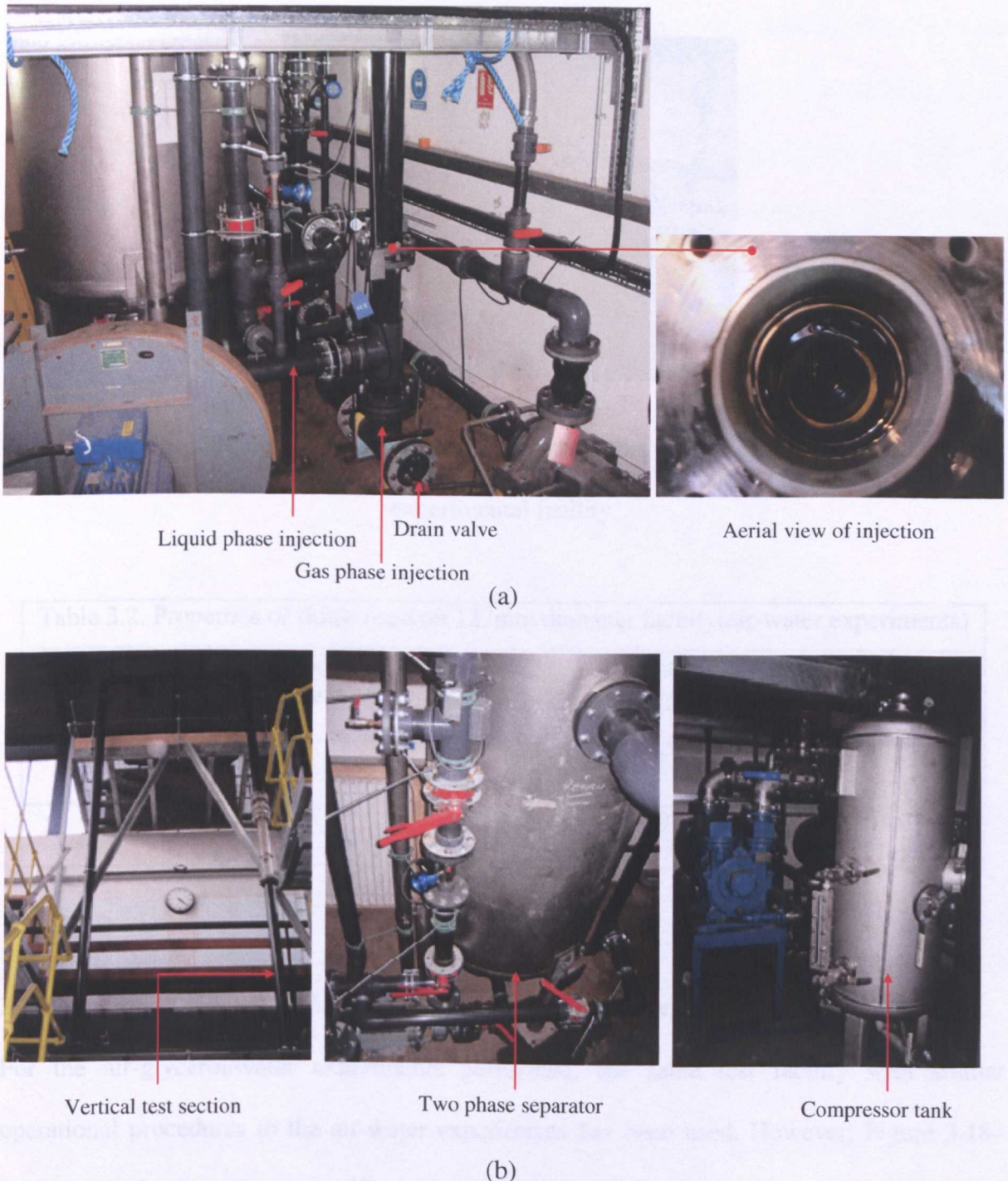


Figure 3.16. (a) Pipe-in-pipe annulus type injection (b) Other component of the 127mm internal diameter facility.



Figure 3.17. Liquid ring compressor motors as components of the 127mm internal diameter experimental facility.

Table 3.2. Properties of fluids used on 127mm diameter facility(air-water experiments)

Fluid	Pressure (bara)	Surface tension (N/m)	Density (kg/m ³)	Viscosity (Pa.s)
Air	2	0.072	2.35	1.78×10^{-5} (0.0178cP)
Water			998	0.001 (1cP)

3.2.2. Operating procedures for air-glycerol/water experiments on 127mm ID facility

For the air-glycerol/water experiments performed, the same test facility with similar operational procedures to the air-water experiments has been used. However, Figure 3.18–3.22 shows the procedures specific to the air-glycerol/water experiments. The rationale for the air-glycerol/water experiments was to investigate the effect of viscosity on the churn flow behaviour.

The separator tank was filled with tap water and the system run severally to flush out debris that may have settled in the system. This was done because when the water from separator tank was initially drained, the liquid had a black colour. Due to the fact that it is a large scale

facility, it required that the system be flushed until the inventory drained from the tank became clear water. However, this can take several runs to establish, approximately 4 – 5 hours. Eventually, clear water was obtained and the system was run again several times to check consistency. After this, the glycerol was then charged into the separator tank as shown in Figure 3.18.

From calculations, to achieve 12.2cP glycerol-water solution for instance, 0.5m^3 volume of water and 0.728m^3 pure-glycerol are needed. That is, while keeping the volume of water constant and at a reference mixture temperature of 25°C .



Figure 3.18. Procedure for charging separator tank with glycerol and water respectively.

For the large scale closed loop facility used in this work, it was rather impossible to get rid of all the water in the system. Therefore, even if proper calculations have been carried out in priori, there will still be some pockets of water trapped in the joints and elbows of the facility. Therefore, when the tank was filled with pure glycerol some of it spilled from the separator to the floor of the facility. This is because no mixing had taken place with the water that was initially charged into the tank. The spillage was taken care of, and the separator tank closed properly in order to pressurize and run the system. Figure 3.18 shows the sample from the

side of separator tank obtained at the minimum operation conditions after running for 20-30minutes. This shows a clear glycerol/water solution. It was initially assumed that efficient mixing may not take place. However, it shows that the due to the energy from the system, this gives a rather clear glycerol/water solution. A Brookfield viscometer was used to measure the viscosity of the glycerol/water mixture as shown in Figure 3.19. The nominal temperature of the mixture between experiments was kept at $27 \pm 2^{\circ}\text{C}$. The surface tension measurements were also made to obtain the surface tension of the glycerol/water solution as shown in Figure 3.20. Two glycerol/water solutions of 12.2cP and 16.2cP were used for these experiments. The summary of the fluid properties are shown in Table 3.3. The operating conditions for gas and liquid superficial velocities are 3.98m/s – 13.36m/s and 0.036m/s – 0.27m/s respectively to achieve churn flow regime. The full operational matrix can be found in Appendix B.

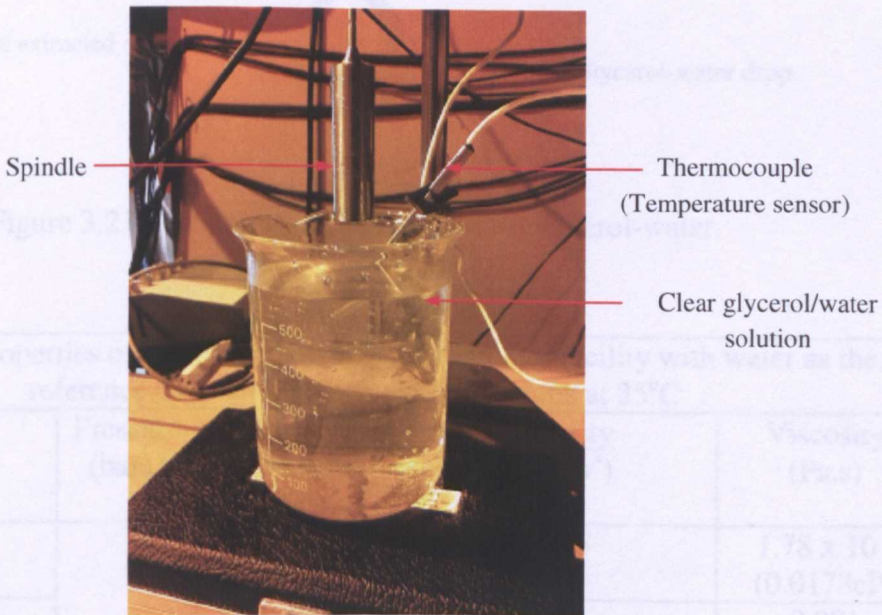


Figure 3.19. Beaker containing clear glycerol/water solution after 20-30 minutes of start-up and shutdown of test facility. System power contributes significantly to mixing of pure glycerol and water to give a clear glycerol/water solution.

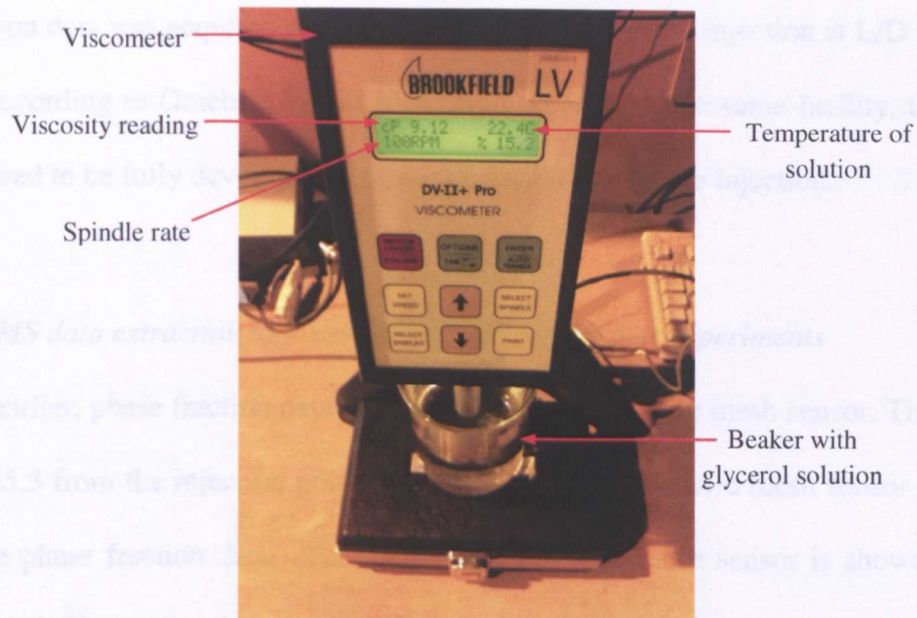


Figure 3.20. Brookfield Viscometer used in measuring viscosity.

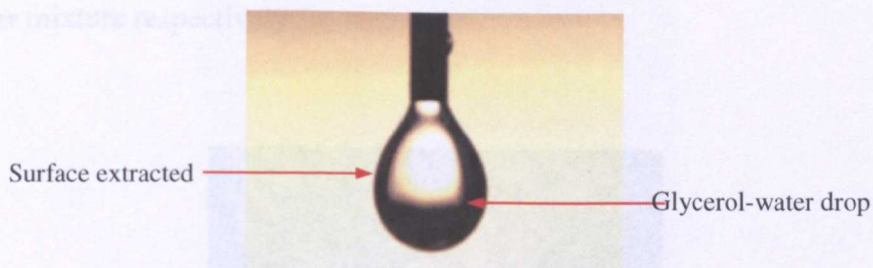


Figure 3.21. Obtaining surface tension of glycerol-water.

Table 3.3. Properties of fluids used on 127mm diameter facility with water as the reference case for glycerol-water solutions at 25°C

Fluid	Pressure (bara)	Surface tension (N/m)	Density (kg/m ³)	Viscosity (Pa.s)
Air		0.072	2.35	1.78×10^{-5} (0.0178cP)
Water	2		998	0.001 (1cP)
Glycerol- water solution		0.0635	1151.6	0.0122 (12.2cP)
Glycerol- water solution		0.0612	1166.3	0.0162 (16.2cP)

Void fraction data was acquired at a suitable axial distance from injection at $L/D = 65.5$. This because, according to Omebere-Iyari (2006) who worked on the same facility, the flow can be considered to be fully developed at this axial location from the injection.

3.2.2.1. WMS data extraction applicable to air-glycerol/water experiments

As stated earlier, phase fraction data was acquired using the wire mesh sensor. This was done at $L/D = 65.5$ from the injection point. A 32×32 capacitance wire mesh sensor was used to acquire the phase fraction data. The location of the wire mesh sensor is shown in Figures 3.22 and 3.23. The calibration specific to these set of experiments was carried out with the pipe empty representing air, and filled with glycerol-water as shown in Figure 3.21 for glycerol/water mixture respectively.

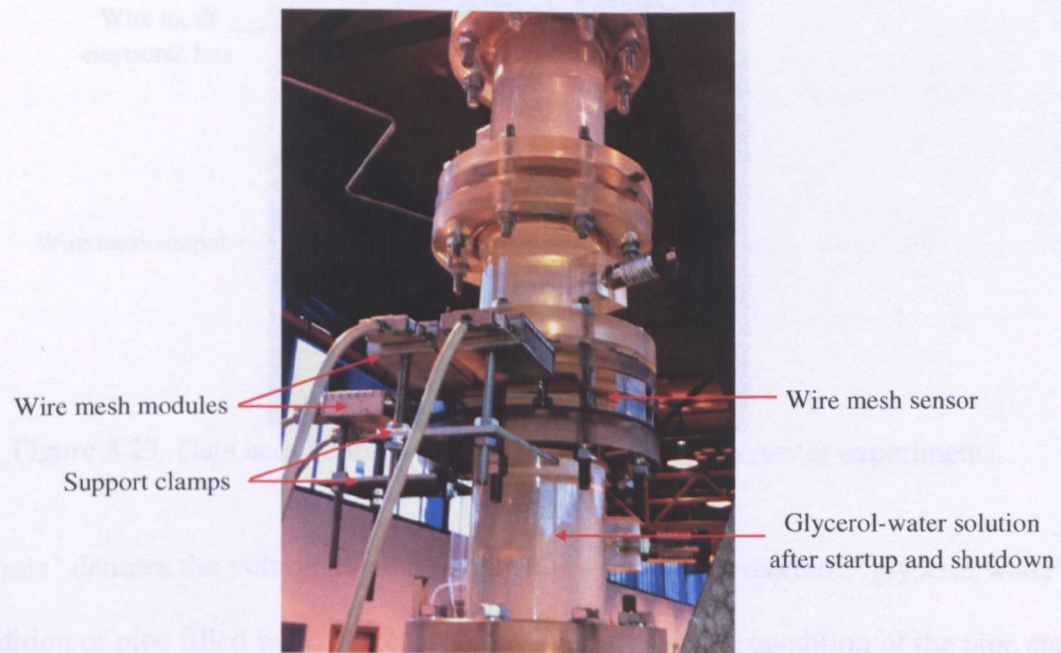


Figure 3.22. Data acquisition part of the test section showing test section clear glycerol/water solution.

The instantaneous values of void fraction as in equation(3.5) is obtained by the relating the mixture permittivity to the reference signal for the liquid phase only where the relative permittivities of the glycerol/water solutions used are 60.34 and 57.76 respectively.

$$\alpha_g = \frac{\epsilon_{r, \text{glycerol/water}} - \epsilon_{r, \text{mix}}}{\epsilon_{r, \text{glycerol/water}} - \epsilon_{r, \text{air}}} \quad (3.5)$$

$$\epsilon_{r, \text{mix}} = \exp \left(\frac{V_{\epsilon, \text{mix}}(i, j, k) - V_{\epsilon, \text{air}}(i, j)}{V_{\epsilon, \text{glycerol/water}}(i, j, k) - V_{\epsilon, \text{air}}(i, j)} \ln(\epsilon_{r, \text{glycerol/water}}) \right) \quad (3.6)$$

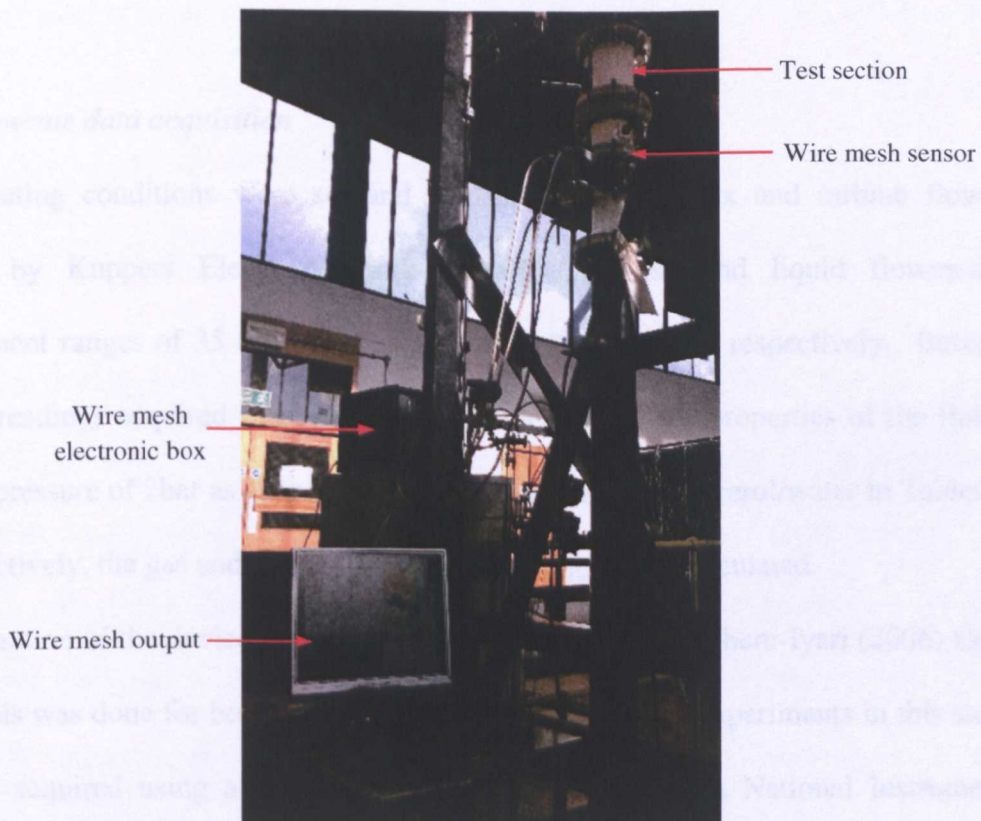


Figure 3.23. Data acquisition workstation for air-glycerol/water experiments.

where ‘mix’ denotes the voltage measurement of the two phase mixture, ‘glycerol/water’ for the condition of pipe filled with ‘glycerol/water’ and ‘air’ for the condition of the pipe empty. A three dimensional void data, (i, j, k) is acquired by reconstructing the data set at each crossing point where i and j represent the wire location and k represents the number of frames or time sequence. The acquisition rate was at 1000 Hz for a total time of 30 s.

3.2.3. Control processes for the 127mm internal diameter facility

Emergency stop buttons for the compressor and liquid ring pumps are located on the three levels of the facility. Relief valves and bursting disc are fitted on the compressor tank in the compressor section and the separator respectively for emergency pressure relief. Air and water mixtures at low pressures present no toxic hazards. Although, glycerol is flammable, care was taken to prevent large spillage from occurring during charging and discharging into separator tank. Oil absorbent granules were available to help clean up spillage.

3.2.4. Flowrate data acquisition

The operating conditions were set and measured using vortex and turbine flow meters supplied by Kppers Electromechanik GmbH. The gas and liquid flowmeter have measurement ranges of 35 to 1030m³/hr and 40 to 500litres/min respectively. Based on the flowrate readings acquired from calibrated rotameters and the properties of the fluids at an absolute pressure of 2bar as shown for both air-water and air-glycerol/water in Tables 3.2 and 3.3 respectively, the gas and liquid superficial velocities were calculated.

The calibration of the devices was previously performed by Omebere-Iyari (2006) for air and water. This was done for both air-water and air-glycerol/water experiments in this study. The data was acquired using a DAQ (Data acquisition) card from National Instruments at a frequency of 1000 Hz for a total time of 60 seconds. The relationship between the voltage output and flowrate was inputted in the Labview program in Figure E.3, Appendix E. Data was also acquired simultaneously with void fraction data.

CHAPTER 4

ESTABLISHING FLOW PATTERN TRANSITIONS FOR A CO-CURRENT AIR-WATER FLOW IN A LARGE DIAMETER VERTICAL PIPE

4.1. Introduction

A thorough understanding of the behaviour of gas-liquid flows is very important prior to the design of any industrial equipment. At low gas flowrates, bubbly flow pattern is the presiding regime and is characterized by the flow of dispersed gas bubbles in a continuous liquid. These bubbles have various sizes and their behaviours are different in small and large diameter pipes. However, in small and large diameter pipes, the bubble flow structure has been classified by its tendency to move towards the wall or core of the pipe, (Lucas *et al.*, 2005).

At higher gas flowrates, slug flow is present where the slug unit is made up of a Taylor bubble and a liquid slug. This has been found to occur only in small diameter pipes using air and water as the operating fluids, (Szalinski *et al.*, 2010, Hernandez-perez *et al.*, 2010 and Abdulkadir, 2011) in a 67mm diameter vertical pipe. In a larger diameter vertical pipe, slug flow has not been observed. Instead the presiding regime is churn turbulent, (Omebere-Iyari *et al.*, 2008 and Schlegel *et al.*, 2009) in 194mm, 102mm and 152mm diameter pipe using steam-water and air-water as the operating fluids respectively.

Taitel *et al.* (1980) earlier established a transitional criterion for the bubble to churn flow transition in small and large diameter pipes based on the following:

$$\left[\frac{\rho_l^2 g D^2}{(\rho_l - \rho_g) \sigma} \right]^{0.25} \leq 4.36 \quad (4.1)$$

where ρ_l , ρ_g , g , σ and D are the liquid density, gas density, gravitational force, surface tension and pipe diameter respectively. Ohnuki and Akimoto (2000) also reported the presence of churn flow as a dominant regime instead of slug flow when the gas flowrate is

further increased from bubbly flow for their experiments in a 200mm diameter vertical pipe.

Based on their observation they classified the regimes present into undistributed bubbly, agitated bubbly, churn bubbly, churn slug and churn froth regimes as shown in Figure 2.7.

Recently, Smith *et al.* (2012) also suggested that the fundamental changes to the flow occur when the pipe diameter is larger than the maximum bubble size formed based on the work of (Kataoka and Ishii, 1987). They suggested that slug bubbles that bridge the pipe cross-section can no longer be sustained due to Taylor instability.

Consequently, the upper surface of the bubbles formed in a large diameter vertical pipe become distorted and collapse breaking the large bubble into two or more daughter bubbles. This behaviour causes a significant change in the void fraction and results in a different behaviour compared to flows in smaller diameter pipes where Taylor bubbles are sustained. There is therefore a need to clearly predict these behaviours in large diameter vertical pipes especially where an appropriate model for CFC is required and in other cases where reactor safety is concerned.

Therefore, the present work investigates the bubble to churn transition from data acquired in the 121mm internal diameter facility that is 5.3m in length using a capacitance wire mesh sensor. Details of the experimental facility and method of data acquisition have been described in chapter 3, section 3.1. The data was acquired at 35 pipe diameters from the injection ($L/D = 35$). The operating conditions for gas and liquid superficial velocities ranged from 0.21m/s to 3.58m/s and 0.018m/s to 0.13m/s respectively, at atmospheric conditions. The results are presented and discussed in the following sections.

4.2. Results

4.2.1. Time series analysis

As indicated above, a capacitance wire mesh sensor was used to acquire void fraction data during the experiments at $L/D = 35$. Air and water were used as operating fluids indicative of the gas and liquid phases respectively. To distinguish between both phases, a calibration routine was initially carried out. The measurement/raw data acquired during the experiments were processed taking the calibration information into consideration to obtain the void fraction at each time sequence. The variation of the void fraction with time has been shown in Figure 4.1.

The black, red and green lines represent increasing gas superficial velocities of 0.21m/s, 1.03m/s and 3.58m/s respectively. This has been done for constant liquid superficial velocities of 0.018m/s, 0.041m/s, 0.075m/s and 0.13m/s from top to bottom respectively.

In reference to when the gas and liquid superficial velocities are 0.21m/s and 0.018m/s respectively, regular intervals of broad peaks can be observed having a peak void fraction of approximately 0.6. In between the broad peaks, shorter peaks can be observed with a peak void fraction at approximately 0.2. From visual observation, the flow is characterized by large bubbles that almost occupy the pipe cross-section, which flow intermittently with smaller bubbles behind them. This has a similar pattern as the slug flow in small diameter pipes as observed for instance by (Kaji *et al.*, 2010). However, the large bubbles are not as long as the Taylor bubbles in small diameter pipes and does not have a bullet-shaped nose. When the gas superficial velocity is increased to 1.03m/s, regular occurrences of bubbles such as those at lower gas superficial velocities are not present.

This is because there is a distortion in the shape of the large bubbles and more irregular sized bubbles are formed. At this operating condition, the behaviour has an oscillating nature and liquid bridging of the gas core with entrained gas bubbles in the base film flowing on the

inner walls of pipe occurs. Increasing the liquid superficial velocity for a constant gas superficial velocity causes the void fraction to decrease. For instance, when $U_{ls} = 0.13\text{m/s}$ and $U_{gs} = 0.21\text{m/s}$, the number of peaks for the 10s time interval presented increases. This is indicative of the occurrence of more small diameter bubbles compared to the same gas superficial velocity when $U_{ls} = 0.03\text{m/s}$.

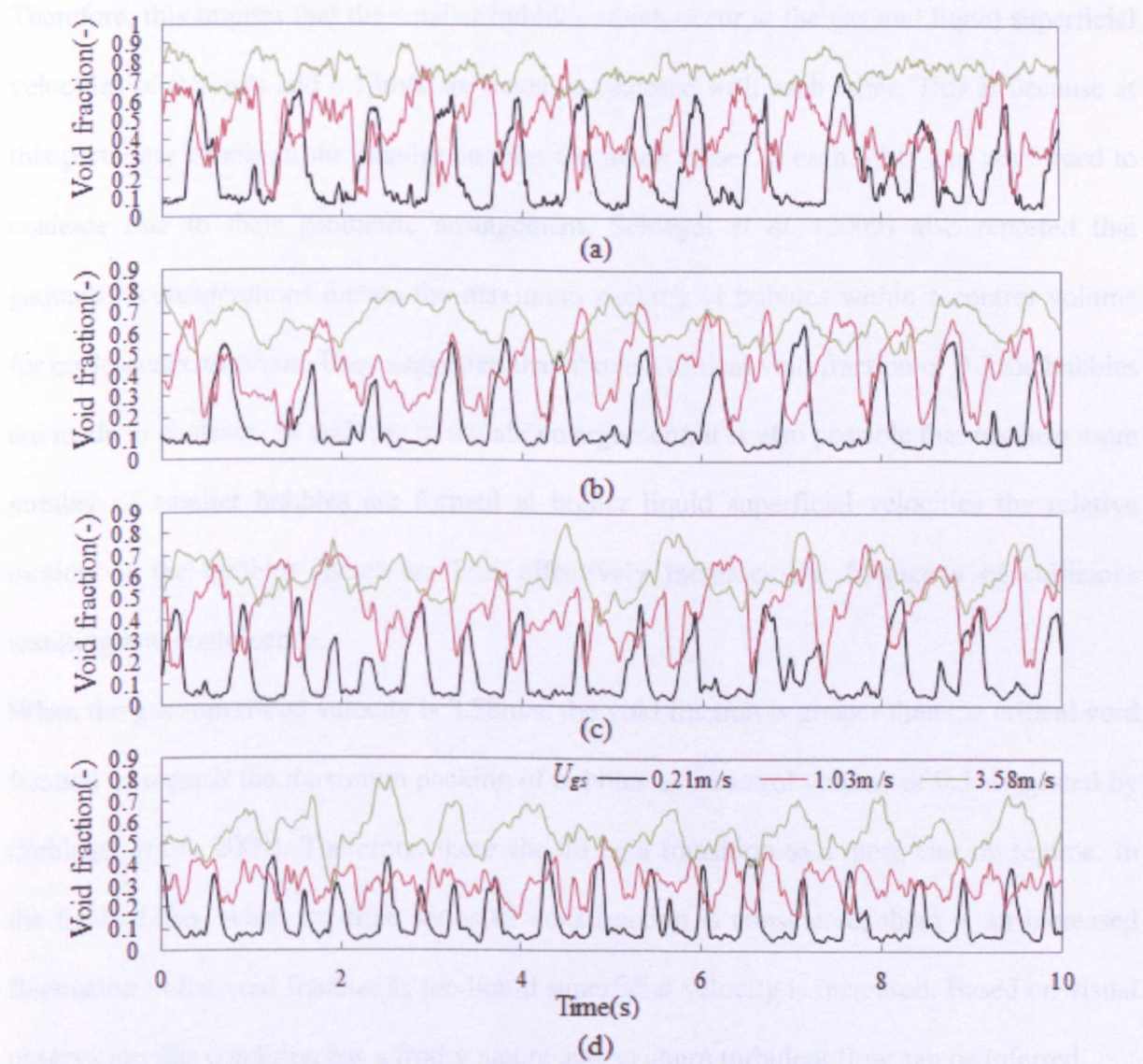


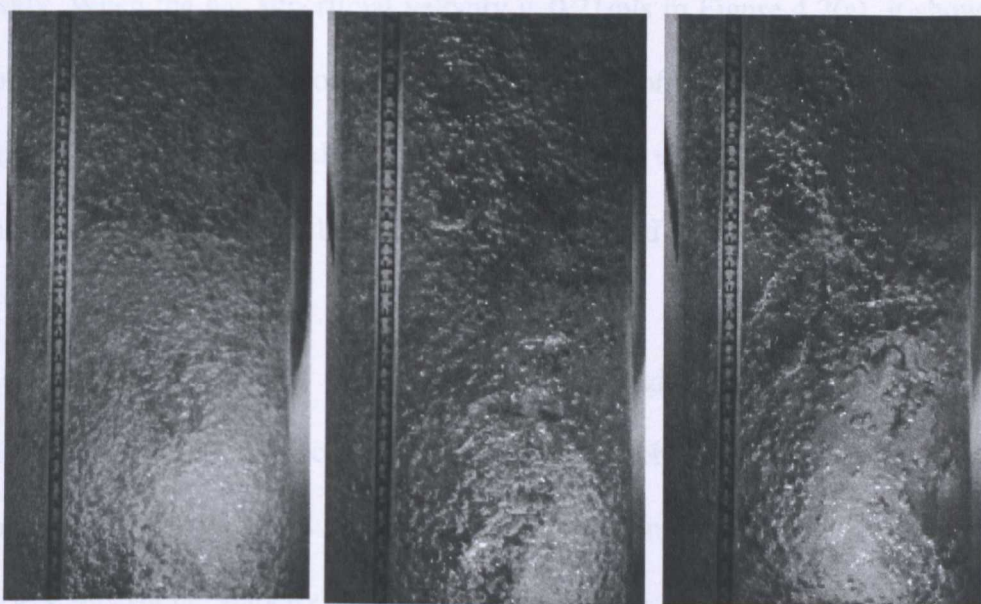
Figure 4.1. (a)-(d) Void fraction variation with time for constant liquid superficial velocities of 0.018m/s , 0.041m/s , 0.075m/s and 0.13m/s respectively. The gas superficial velocities are indicated in plot (d).

From the analysis of the graphs above, it was identified above that when the gas and liquid superficial velocities are 0.21m/s and 0.03m/s respectively, the peak at a void fraction of 0.6 is indicative of large bubbles and the smaller bubbles have a short peak at 0.2. However, when the gas and liquid superficial velocity are 0.21m/s and 0.13m/s respectively, the shorter peaks as observed for lower liquid superficial velocities cannot be observed in Figure 4.1(d). Therefore, this implies that the smaller bubbles which occur at the gas and liquid superficial velocities of 0.21m/s and 0.13m/s are made to coalesce with each other. This is because at this particular condition the smaller bubbles are much closer to each other and are forced to coalesce due to their geometric arrangement. Schlegel *et al.* (2009) also reported that geometric considerations dictate the maximum packing of bubbles within a control volume for coalescence to occur. They suggested that above a critical void fraction of 0.3 the bubbles are made to coalesce. In addition to the above argument, it is also possible that because more number of smaller bubbles are formed at higher liquid superficial velocities the relative motion of the bubbles increases. This effectively increases the frequency of collisions resulting into coalescence.

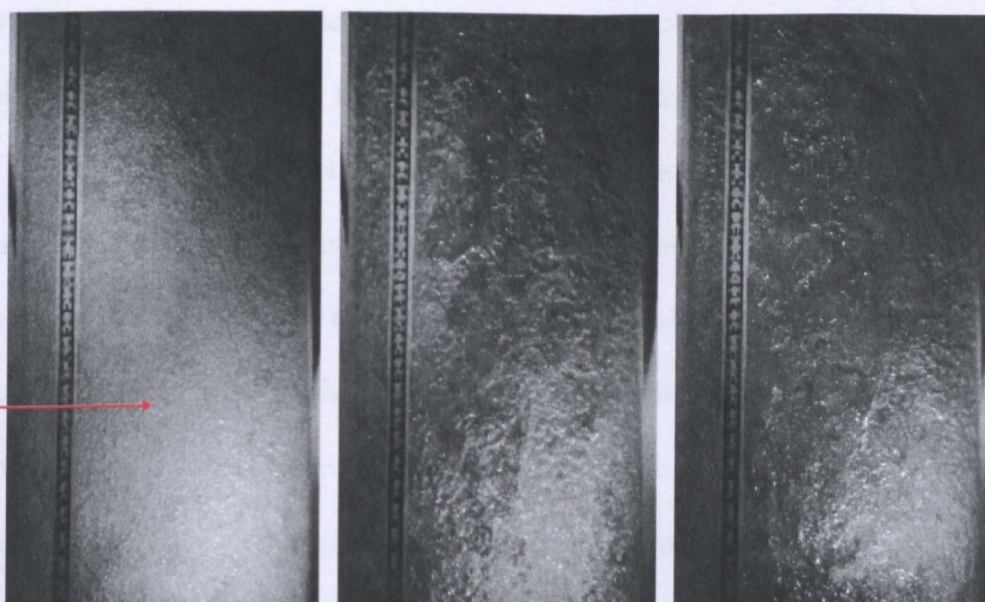
When the gas superficial velocity is 3.58m/s, the void fraction is greater than the critical void fraction as regards the maximum packing of bubbles in a control volume of 0.3 suggested by (Schlegel *et al.*, 2009). Therefore, there should be a transition to a more chaotic regime. In the light of this, when the time series of void fraction is considered, there is an increased fluctuation in the void fraction as the liquid superficial velocity is increased. Based on visual observation this condition has a frothy nature and so churn turbulent flow can be inferred.

4.2.2. Extracted high-speed images

In order to clearly clarify the nature of structures identified from the time series, high-speed videos were acquired at 1000 fps using a Phantom v12.1 high-speed camera.



(a)



(b)

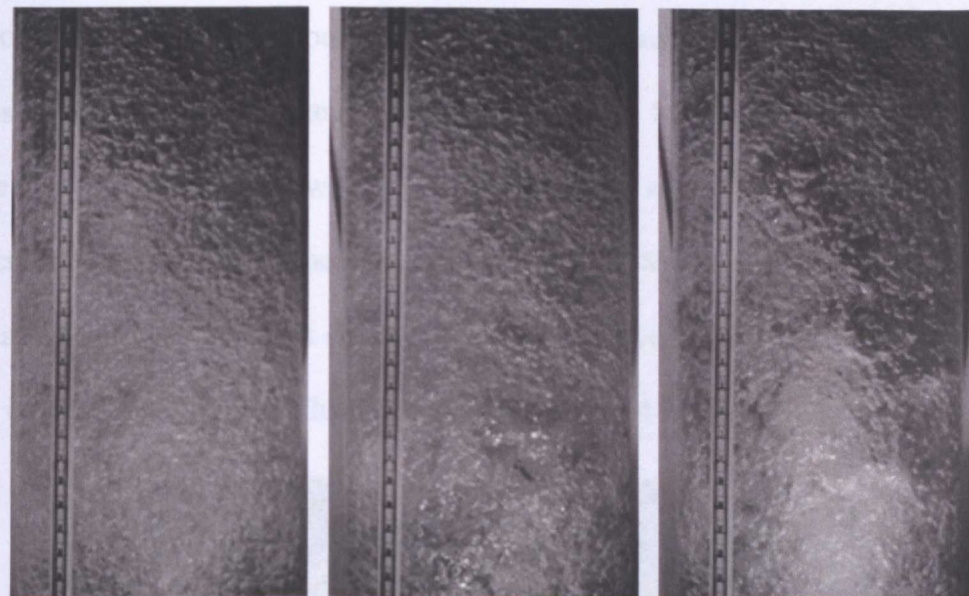
Figure 4.2. High speed images captured using a Phantom v12.1 camera for (a) $U_{gs} = 0.21\text{m/s}$

and (b) $U_{gs} = 3.58\text{m/s}$ while keeping the liquid superficial velocity constant at $U_{ls} = 0.018\text{m/s}$.

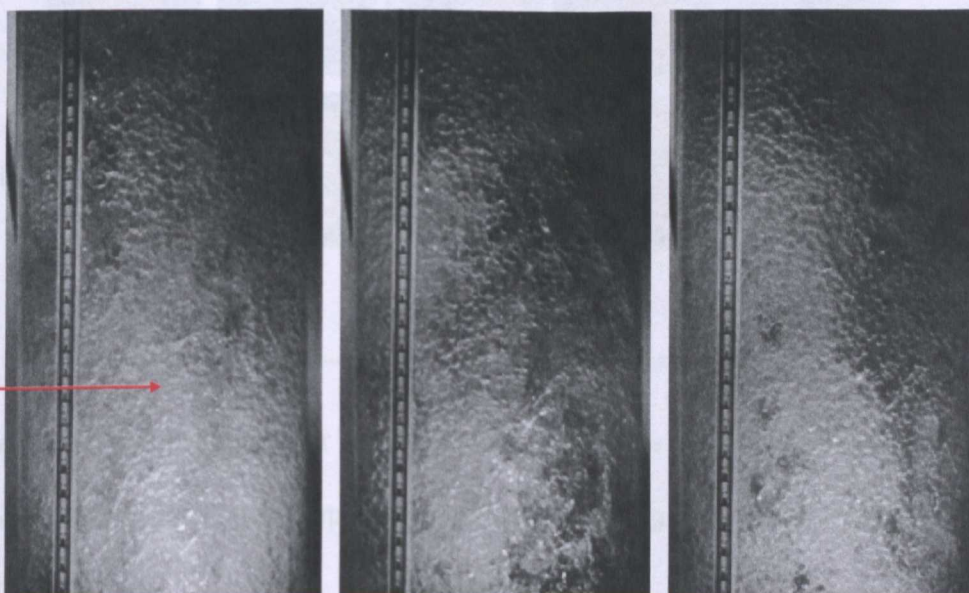
The high-speed videos were acquired below the location of the WMS at 35 pipe diameters away from the injection, $L/D = 35$. The sequence of extracted images has been shown in Figures 4.2 and 4.3 for constant liquid superficial velocities of 0.018m/s and 0.13m/s respectively. When the gas superficial velocity is 0.21m/s in Figure 4.2(a), it shows a dense cluster of bubbles (the white colour region) and a region of leaner widely spread out bubbles indicated in the figure by the darker colour. From the visual observation, the latter is a situation where a large diameter bubble passes through and pushes small bubbles to the inner walls of the pipe.

On the other hand, the former shows a liquid slug region with bubbles packed closely together. After the unit which comprises of a large bubble and liquid slug flows pass, a similar occurrence was observed at this operating condition and the pattern is intermittent. At a higher gas superficial velocity of 3.58m/s as in Figure 4.2(b), the first image shows the whole axial section of the pipe having a very white region indicative of the frothy nature of the flow. The frothy nature which is essentially a very close cluster of bubbles was also observed at the same condition in the work of (Omebere-Iyari, 2006). In the subsequent images, the close cluster of bubbles does not occupy the entire axial section of the pipe. However, some portions of the axial section of the pipe have this frothy nature while others have the cross-section of the pipe occupied mainly by gas with entrained bubbles at the walls. The effect of increasing the liquid superficial velocity to 0.13m/s is shown in Figure 4.3. It shows that the liquid slug region clearly observed in Figure 4.2(a) is less apparent in the first two sequences but can be observed in the third image/sequence. This is due to the fact that more volume of liquid is present. At this liquid superficial velocity, increasing the gas superficial velocity as in Figure 4.3(b) shows a frothier flow compared to Figure 4.2(b). This is because the degree of instability increases as the liquid superficial velocity increases. Therefore, this forms clusters of bubbles which almost occupy the axial section of the pipe.

In consideration of the high-speed images, it can be said that both Figures 4.2 and 4.3 agree with the time series of void fraction obtained from the wire mesh sensor at the respective operating conditions.



(a)



(b)

Figure 4.3. High speed images captured using a Phantom v12.1 camera for (a) $U_{gs} = 0.21\text{m/s}$ and (b) $U_{gs} = 3.58\text{m/s}$ while keeping the liquid superficial velocity constant at $U_{ls} = 0.13\text{m/s}$.

4.2.3. Cross sectional phase distribution

The cross-sectional phase distribution was extracted from the wire mesh sensor and is shown in Figure 4.4. The red and blue are indicative of gas and liquid phases respectively. This is shown for a constant liquid superficial velocity of 0.13m/s and increasing gas superficial velocities of 0.21m/s, 1.03m/s and 3.58m/s respectively for frames 1000 to 5000 or time sequence of 1-5s. Clearly, it shows that increasing the gas superficial velocity causes the pipe cross-section to be occupied more by the gas phase. More significantly, when the gas superficial velocity is 0.21m/s, it shows a large distorted bubble and small bubbles dispersed in liquid in subsequent frames. This is essentially typical of the bubbly flow behaviour.

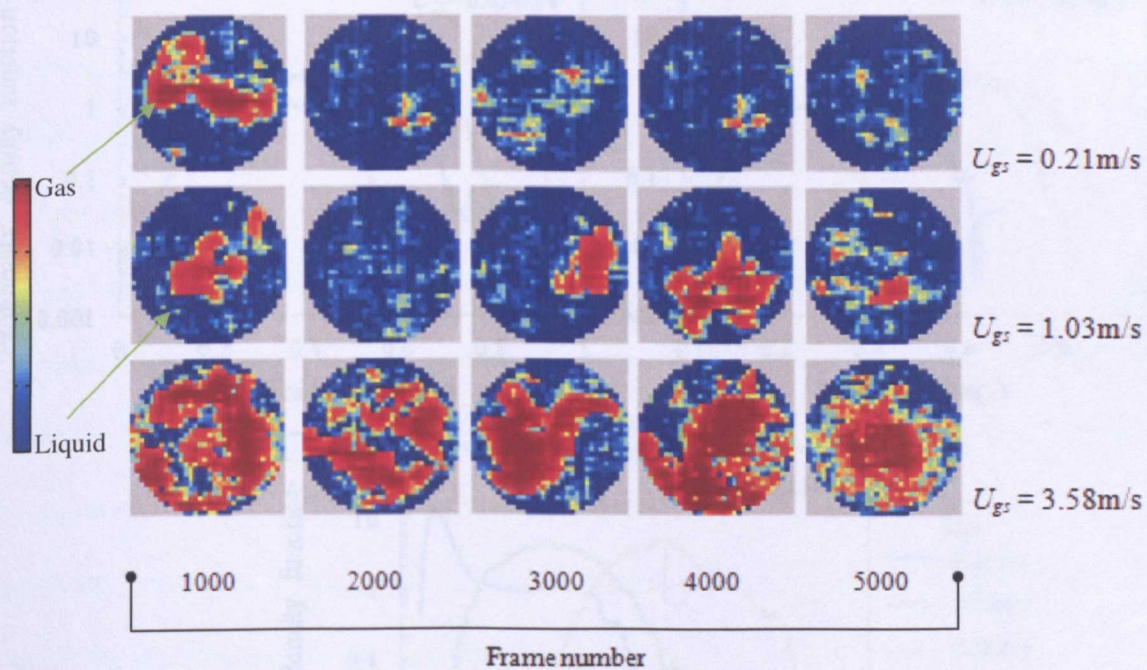


Figure 4.4. Frame sequence for $U_{gs} = 0.21\text{m/s}$, 1.03m/s and 3.58m/s from top to bottom respectively at constant liquid superficial velocity of 0.13m/s extracted from the wire mesh sensor data.

However, increasing the gas superficial velocity to 1.03m/s initially shows a distorted bubble, then dispersed bubbles in the liquid followed by large bubbles in subsequent frames. This may probably be an operating condition within the bubble to churn transition region.

Increasing the gas superficial velocity to 3.58m/s shows that the gas phase almost occupies the entire pipe cross-section. From visual observation of the flow and further clarification by the high speed image in Figure 4.3(b), this is essentially a cluster of bubbles, which has a frothy nature.

4.2.4. Statistical analysis of time series of void fraction

Statistical analysis of the time series data was carried out as a quantitative measure to distinguish between the presiding regimes present. Also, to identify whether analysing the data set statistically can reveal the transition from the bubble to churn flow regime.

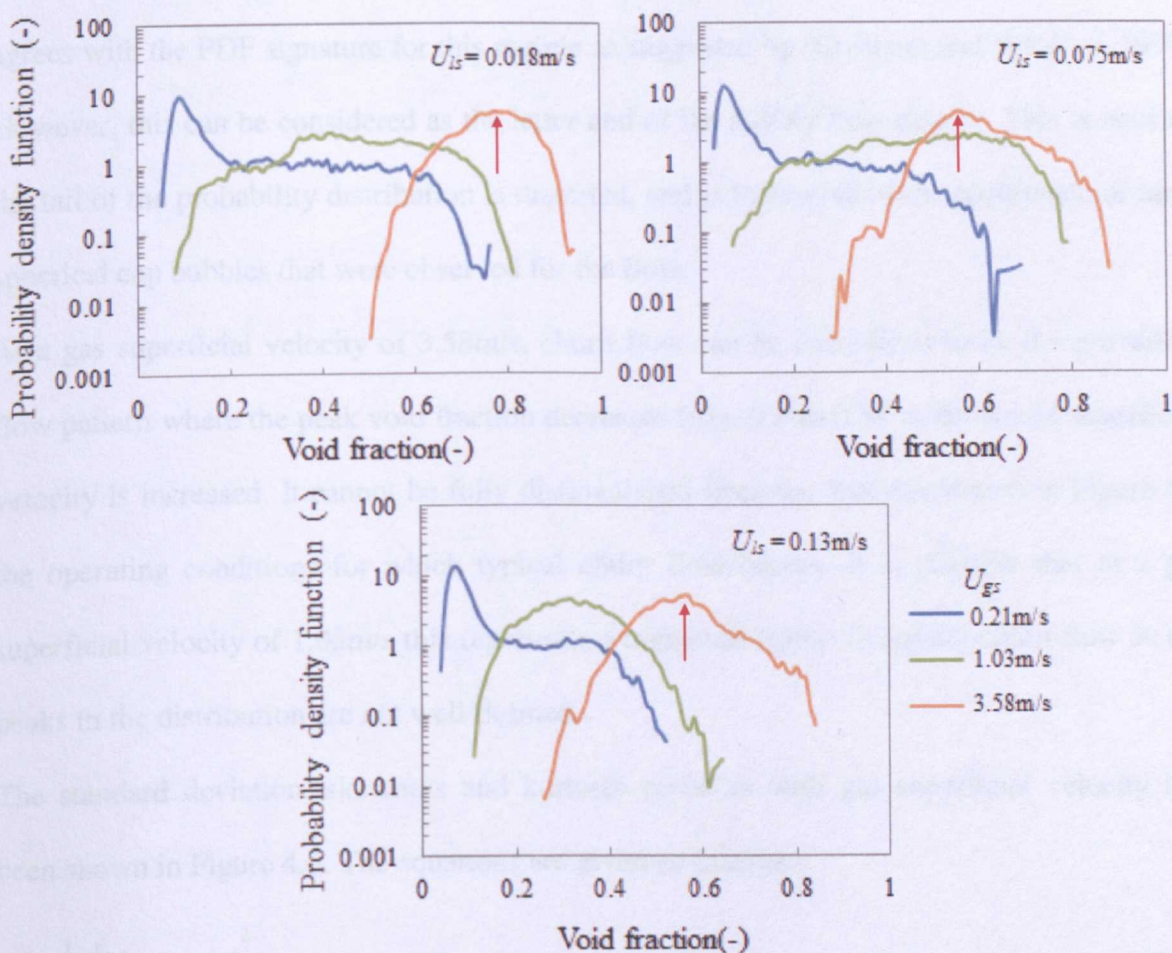


Figure 4.5. Variation of PDF with void fraction for increasing gas superficial velocities at constant liquid superficial velocity.

The probability density function (PDF), standard deviation, skewness, kurtosis and mean of time series data set have been applied as the relevant statistical tools. The probability density function of the void fraction has been shown in Figure 4.5. The PDF is the probability that the void fraction for a given data set lies within a particular range, 0 to 1. This is given as:

$$P(\alpha_g) d\alpha_g = P(0 < \alpha_g(t) \leq \alpha_g + \Delta\alpha_g) \quad (4.1)$$

From Figure 4.5, it shows that as the gas superficial velocity is increased there is a shift in peak from left to right. Increasing the liquid superficial velocity from 0.018m/s to 0.13m/s, causes a corresponding shift in probability distributions to lower void fractions. The single peak at a gas superficial velocity of 0.21m/s is indicative of bubbly flow pattern, which agrees with the PDF signature for this regime as suggested by (Costigan and Whalley, 1997). However, this can be considered as the latter end of the bubbly flow pattern. This is because the tail of the probability distribution is distorted, and is indicative of the occurrence of large spherical cap bubbles that were observed for the flow.

At a gas superficial velocity of 3.58m/s, churn flow can be considered to be the prevailing flow pattern where the peak void fraction decreases from 0.8 to 0.58 as the liquid superficial velocity is increased. It cannot be fully distinguished from the analysis shown in Figure 4.5 the operating conditions for which typical churn flow occurs. It is possible that at a gas superficial velocity of 1.03m/s this represents a transition region to typical churn flow as the peaks in the distribution are not well-defined.

The standard deviation, skewness and kurtosis variation with gas superficial velocity has been shown in Figure 4.6. The equations are given as follows:

$$\sigma = \frac{1}{n} \sum_{i=1}^n |\alpha_g - \bar{\alpha}_g|^2 \quad (4.2)$$

$$Sk = \frac{\frac{1}{n} \sum_{i=1}^n |\alpha_g - \bar{\alpha}_g|^3}{\sigma^3} \quad (4.3)$$

$$Ku = \frac{1}{n} \sum_{i=1}^n \left| \alpha_g - \bar{\alpha}_g \right|^4$$

(4.4)

As the gas superficial velocity increases the standard deviation of the void fraction decreases from 0.18 to 0.08 for bubble to churn flow. There is an initial increase, which is followed by a decrease then a constant value is more or less attained. It also shows that the profile decreases with increasing liquid superficial velocity.

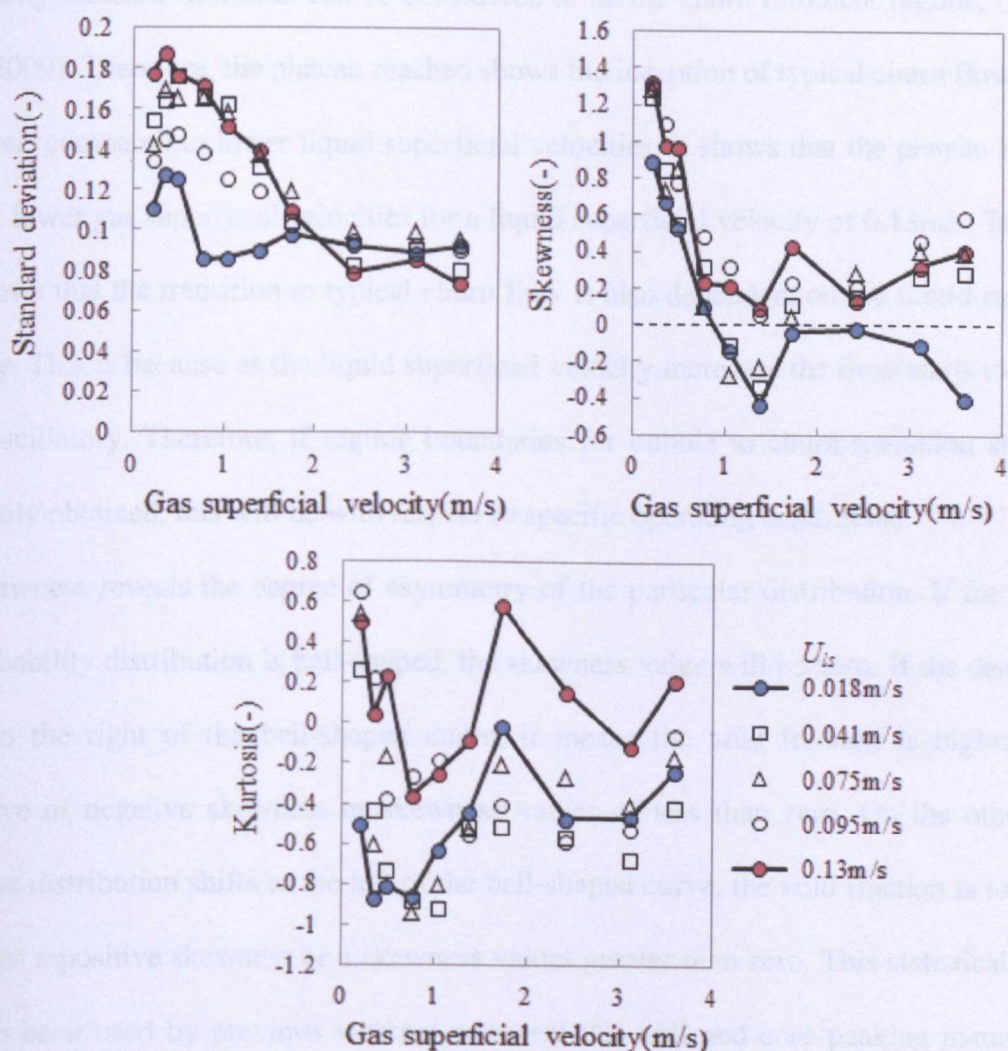


Figure 4.6. Variation of standard deviation, skewness and kurtosis of the time series data with gas superficial velocity.

From the standard deviation plot, the flow regimes present can be inferred. The region showing an initial increase is indicative of occasional occurrence of large spherical cap bubbles as shown in the time series plots. The reason for the increase is because the void fraction changes when large spherical cap bubbles and smaller bubbles that are closely packed flows pass. This regular intermittent nature leads to an increase in the standard deviation of void fraction. As the gas superficial velocity increases, the negative slope of decreasing standard deviation can be considered to be the churn turbulent regime, (Schlegel *et al.*, 2009). Therefore, the plateau reached shows the inception of typical churn flow.

However, compared to lower liquid superficial velocities, it shows that the plateau begins to form at lower gas superficial velocities for a liquid superficial velocity of 0.13m/s. Therefore, this shows that the transition to typical churn flow is also dependent on the liquid superficial velocity. This is because as the liquid superficial velocity increases the flow tends to become more oscillatory. Therefore, if regime boundaries for bubble to churn transition should be eventually obtained, this will be with respect to specific operating conditions.

The skewness reveals the degree of asymmetry of the particular distribution. If for instance the probability distribution is bell-shaped, the skewness value will be zero. If the distribution shifts to the right of the bell-shaped curve, it means the void fraction is higher and is indicative of negative skewness or skewness values of less than zero. On the other hand, when the distribution shifts to the left of the bell-shaped curve, the void fraction is lower and this gives a positive skewness or a skewness values greater than zero. This statistical method has also been used by previous workers to reveal the wall and core peaking nature of the bubbles present, (Shen *et al.*, 2005 and Qi *et al.*, 2012).

From their work, when bubbles tend towards the core of the pipe the skewness is less than zero. A wall peak profile occurs when the skewness is greater than zero and the transition from wall to core profile occurs when the skewness is equal to zero.

From both explanations given above, it shows that as the gas superficial velocity increases the bubbles formed tends more towards the core of the pipe. Since, this is also dependent on liquid superficial velocity, there is a shift towards a wall peaking behaviour when the liquid superficial velocity is increased at a constant gas superficial velocity. It is also important to note that the value of skewness decreases to a gas superficial velocity of 1.37m/s for each case of liquid superficial velocity. This may also probably indicate a transition condition to typical churn flow regime.

Further analysis of the time series data in form of kurtosis has also being investigated. The kurtosis reveals the modality of a probability distribution. This means that if the probability distribution is unimodal it has one well-defined peak whereas if it is bimodal, two peaks can be observed. For bubbly flow, the former may be the case as this can be observed in Figure 4.5. Since the flow becomes more chaotic in transiting to churn flow, bimodal or even multimodal distributions may probably be obtained. In consideration of the kurtosis variation in Figure 4.6, the profile decreases with increasing liquid superficial velocity. However there is an increase in profile when the liquid superficial velocity increases from 0.018m/s – 0.13m/s. At a constant liquid superficial velocity, increasing the gas superficial velocity causes the profile to decrease, increase to maximum and then decrease. Consequently, this gives an apparent peak occurring at a gas superficial velocity of 1.72m/s.

From the instantaneous values of void fraction at each period of acquisition, the time averaged void fraction for the whole data set was obtained. This value was varied with dimensionless gas velocity as shown in Figure 4.7 in order to make further comparisons with the data of (Szalinski *et al.*, 2010). They acquired data in 67mm internal diameter pipe, and 6m in length test section using air and water and air and silicone oil as the fluid pairs.

The dimensionless gas velocity term used in this case is given as:

$$U_g^* = U_{gs} \left[\frac{\rho_g}{gD(\rho_l - \rho_g)} \right]^{\frac{1}{2}} \quad (4.5)$$

As the gas superficial velocity increases there is a logarithmic increase in void fraction. For the experimental conditions, it shows a decrease in profile as the gas superficial velocity is increased. The air-water data from Szalinski *et al.* (2010) shows a close agreement with the experimental data when the liquid superficial velocities are 0.095m/s and 0.13m/s.

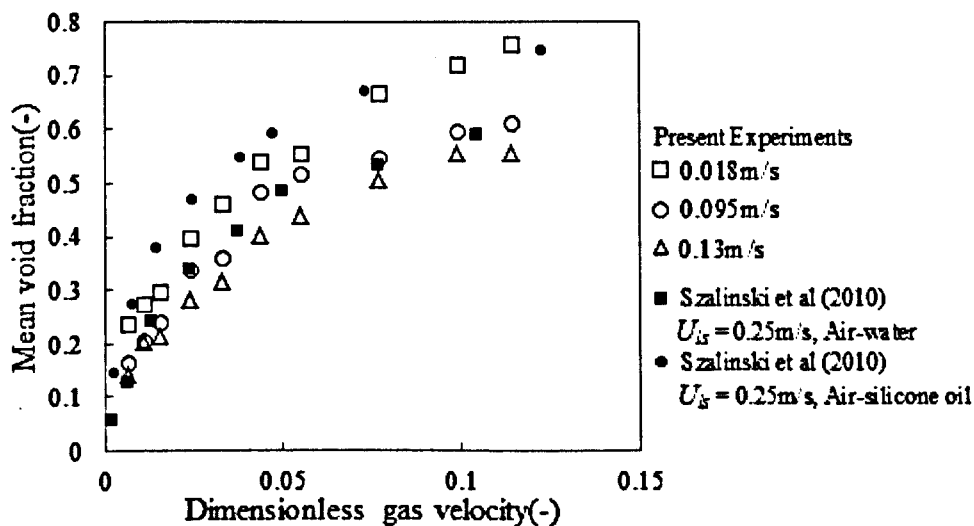


Figure 4.7. Variation of mean void fraction with dimensionless gas velocity. Further comparisons have been made to the data of Szalinski et al. (2010) where bubble, slug and churn flows were observed in a 67mm diameter pipe having a length of 6m.

Interestingly, their air-silicone oil data shows close agreement with the data from the present experiments at $U_{ls} = 0.018\text{m/s}$. Comparing both cases, the higher void fraction at lower gas superficial velocity is due to a higher viscosity of silicone oil compared to water used in the present experiments. Also, Taylor bubbles were observed in their experiments having a diameter almost equivalent to the pipe diameter. At higher gas superficial velocities the Taylor bubbles are destroyed and the churn flow pattern is present. The air-silicone oil data from Szalinski *et al.* (2010) and those for present experiment at $U_{ls} = 0.018\text{m/s}$, become

closer as the gas superficial velocity increases showing that as the churn flow pattern is entered, the void fraction does not change considerably with pipe diameter.

4.2.5. Interfacial structures

The interfacial structures have been obtained by further post processing of the three dimensional void data using a MATLAB program.

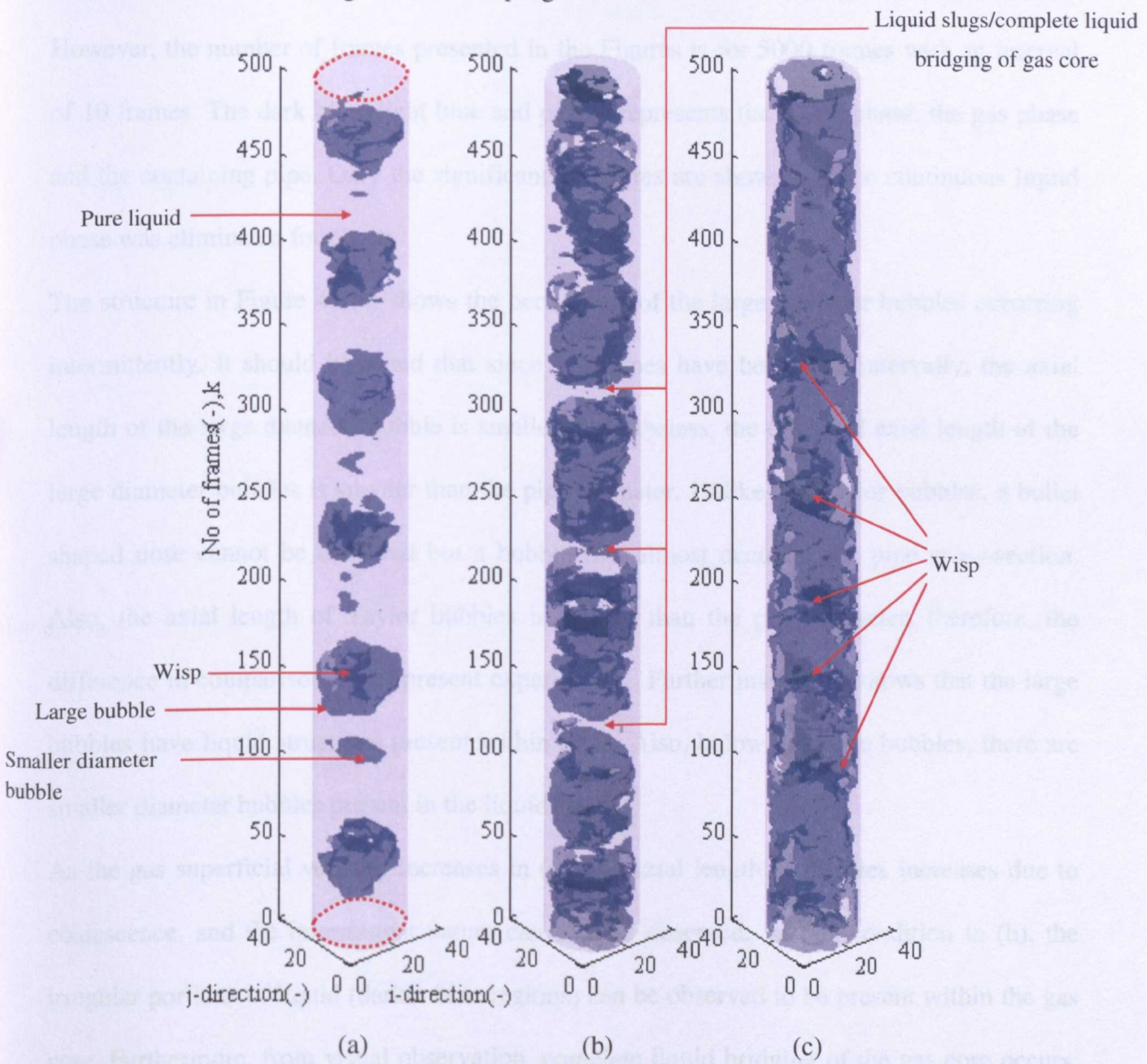


Figure 4.8. Interfacial structures at gas superficial velocities of 0.21m/s, 1.03m/s and 3.58m/s, for a constant liquid superficial velocity of 0.018m/s.

This is shown for selected gas superficial velocities with reference to previous discussions in section 4.2.1 and 4.2.3 of 0.21m/s, 1.03m/s and 3.58m/s as (a), (b) and (c) respectively. Figures 4.8, 4.9 and 4.10 represent the interfacial structures at the respective aforementioned gas superficial velocities and at constant liquid superficial velocities of 0.018m/s, 0.075m/s and 0.13m/s respectively.

Since the data was acquired at 1000Hz for 30s the total number of frames extracted is 30,000. However, the number of frames presented in the Figures is for 5000 frames with an interval of 10 frames. The dark blue, light blue and purple represents the liquid phase, the gas phase and the containing pipe. Only the significant structures are shown and the continuous liquid phase was eliminated for clarity.

The structure in Figure 4.8(a) shows the occurrence of the large diameter bubbles occurring intermittently. It should be noted that since 10 frames have been read intervally, the axial length of the large diameter bubble is smaller. Nonetheless, the observed axial length of the large diameter bubbles is smaller than the pipe diameter. Unlike the Taylor bubbles, a bullet shaped nose cannot be observed but a bubble that almost occupies the pipe cross-section. Also, the axial length of Taylor bubbles is greater than the pipe diameter, therefore, the difference in comparison to the present experiments. Further inspection shows that the large bubbles have liquid structures present within them. Also, below the large bubbles, there are smaller diameter bubbles present in the liquid phase.

As the gas superficial velocity increases in (b), the axial length of bubbles increases due to coalescence, and the intermittent nature can also be observed. At this condition in (b), the irregular portions of liquid (darker blue regions) can be observed to be present within the gas core. Furthermore, from visual observation, complete liquid bridging of the gas core occurs, which is characterised by small diameter bubbles of about 3 – 5mm in diameter entrained in the liquid. This has been shown as a pure liquid phase due to the fact that the bubbles

entrained have a small diameter. As the gas superficial velocity further increases in (c), the core is occupied by gas and more liquid structures are present within the core of the pipe. These liquid structures entrained in the gas core have been previously characterized by previous authors such as Hernandez- Perez *et al.* (2010) as *wisps*.

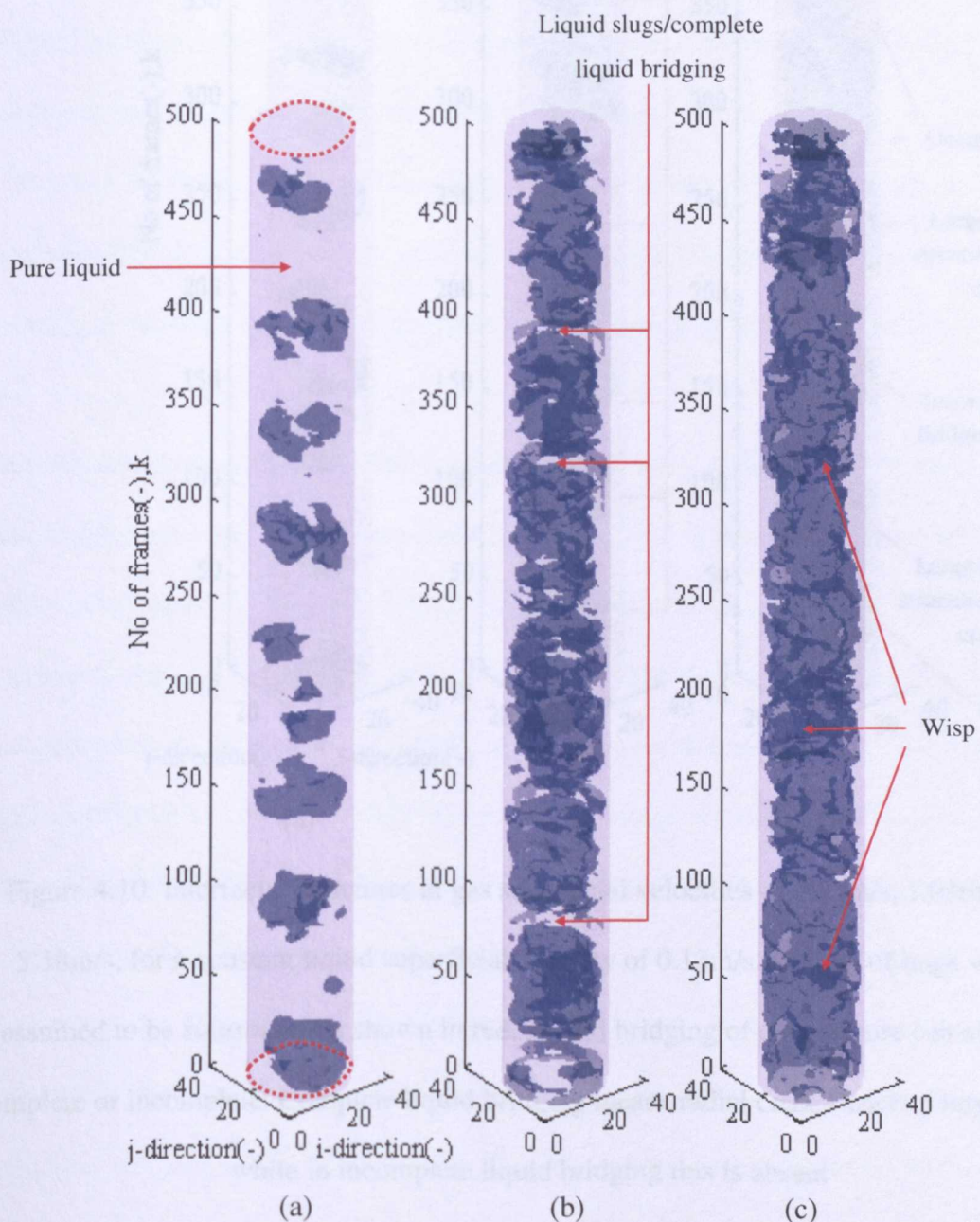


Figure 4.9. Interfacial structures at gas superficial velocities of 0.21m/s, 1.03m/s and 3.58m/s, for a constant liquid superficial velocity of 0.075m/s

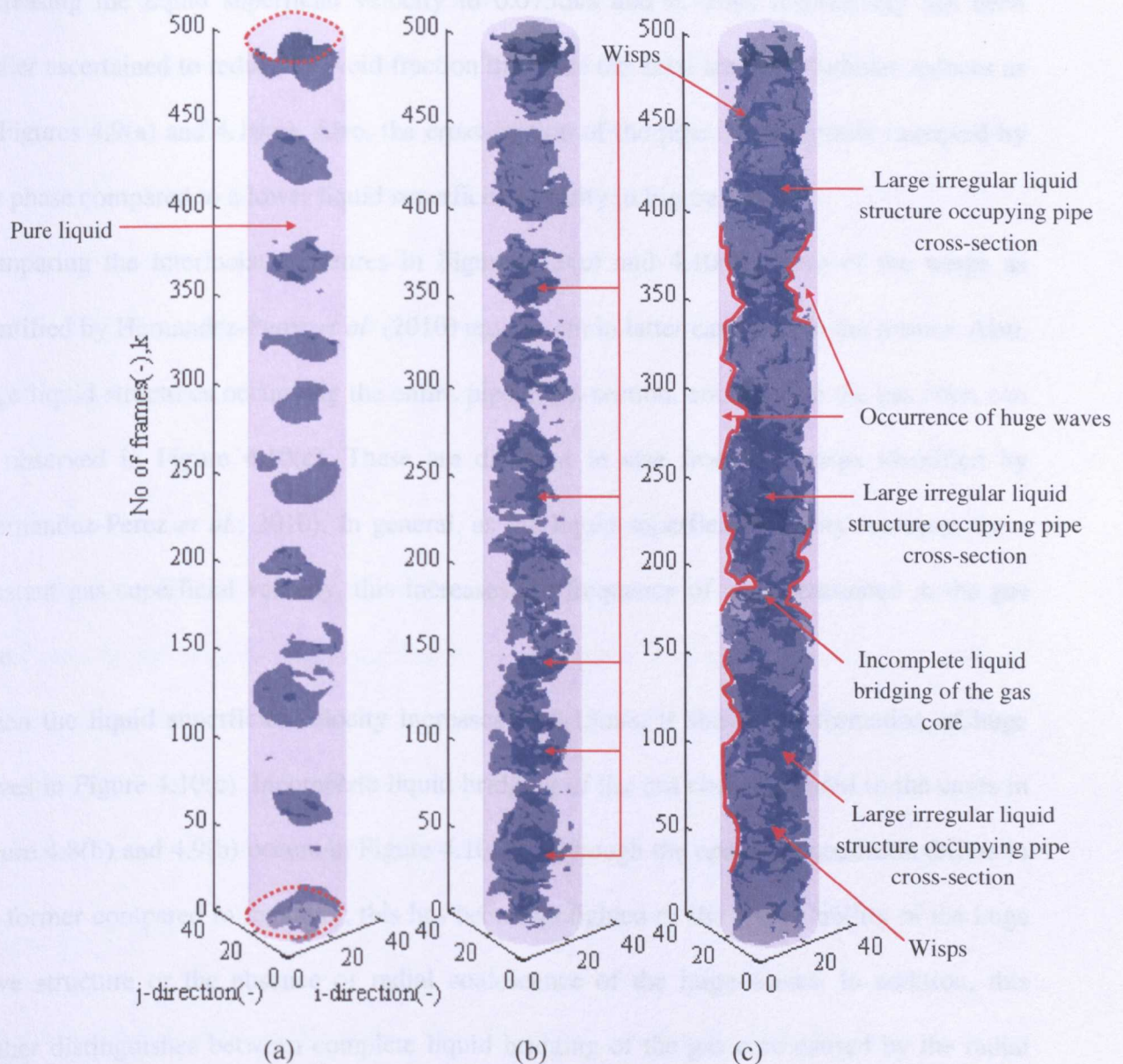


Figure 4.10. Interfacial structures at gas superficial velocities of 0.21m/s, 1.03m/s and 3.58m/s, for a constant liquid superficial velocity of 0.13m/s. Outline of huge waves (assumed to be *sinusoidal*) is shown in red. Liquid bridging of the gas core can either be complete or incomplete. Complete liquid bridging means radial coalescence of huge waves while in incomplete liquid bridging this is absent

Increasing the liquid superficial velocity to 0.075m/s and 0.13m/s respectively has been earlier ascertained to reduce the void fraction therefore the axial length of bubbles reduces as in Figures 4.9(a) and 4.10(a). Also, the cross-section of the pipe is not entirely occupied by gas phase compared to a lower liquid superficial velocity in Figure 4.8.

Comparing the interfacial structures in Figures 4.9(c) and 4.10(c), more of the wisps as identified by Hernandez-Perez *et al.* (2010) are present in latter case than in the former. Also, large liquid structures occupying the entire pipe cross-section, entrained in the gas core, can be observed in Figure 4.10(c). These are different in size from the wisps identified by (Hernandez-Perez *et al.*, 2010). In general, as the liquid superficial velocity increases for a constant gas superficial velocity, this increases the frequency of wisps entrained in the gas core.

When the liquid superficial velocity increases to 0.13m/s, it shows the formation of huge waves in Figure 4.10(c). Incomplete liquid bridging of the gas core compared to the cases in Figure 4.8(b) and 4.9(b) occurs in Figure 4.10(c). Although the operating condition differs in the former compared to the latter, this has been highlighted to show the stability of the huge wave structure or the absence of radial coalescence of the huge waves. In addition, this further distinguishes between complete liquid bridging of the gas core caused by the radial coalescence of the huge waves flowing on the inner walls of the pipe, about the pipe centre line, and incomplete liquid bridging of the gas core.

It is possible that the entrained liquid structures occupying the entire pipe cross-section are formed from the radial coalescence of huge wave propagated upwards by the gas phase inertia from an upstream location. On the other hand, the wisps are sheared off from the crest of the huge waves. In the latter, it means that the huge waves are the source of the wisps or drops entrained in the gas core and are incompletely atomised by the gas phase inertia to form them. Therefore, when huge waves are formed about the pipe centreline and the gas shears

off the crest of the huge waves, these form wisps or drops due to the absence of radial coalescence of huge waves. On other hand, when the huge waves radially coalesce, with the simultaneous occurrence of gas flowing upwards, this forms large liquid structures entrained in the gas core. From this perspective, the entrained fraction of drops in churn flow is a function of both the shedding of wisps or drops from large liquid structures as a result of complete liquid bridging(*radial coalescence of the crest of huge waves*) and incomplete liquid bridging(*absence of radial coalescence of huge waves*).

4.2.6. Spectral analysis

To further investigate the periodicity of the interfacial structures, spectral analysis of the time series data in the frequency domain has been employed. The spectral analysis in form of power spectral density (PSD) is used to quantify the strength of the time series signal across different frequency bands. To obtain the PSD, the Fourier transform of the time series signal is initially carried out and the equation is defined as:

$$F(x) = \int_{-\infty}^{\infty} \alpha_g(t) e^{(-j2\pi ft)} dt \quad (4.6)$$

The power spectral density function is then obtained by taking the Fourier transform of the auto covariance function (ACF) which is given as:

$$C_{xx}(k\Delta\tau) = \frac{1}{T-\tau} \int_0^{T-\tau} (\alpha_g(t) - \bar{\alpha}_g) \cdot (\alpha_g(t + k\Delta\tau) - \bar{\alpha}_g) dt; \tau < T \quad (4.7)$$

where T is the sampling duration $k\Delta\tau$ is the time delay τ is the interrogating time delay. The power spectrum density is then obtained as:

$$P_{xx}(f) = \Delta\tau \left(\frac{1}{2} C_{xx}(0) + \sum_{k=1}^{\tau/\Delta\tau-1} C_{xx}(k\Delta\tau) w(k\Delta\tau) \cos(2\pi f k\Delta\tau) \right) \quad (4.8)$$

A cosine windowing function in equation (4.8) $w(k\Delta\tau)$ is used to suppress the spectrum leakage similar to work of (Kaji *et al.*, 2009). This is given as:

$$w(k\Delta\tau) = \cos\left(\frac{\pi k\Delta\tau}{2\cdot\tau}\right) \quad (4.9)$$

The variation of power spectral density with frequency is shown in Figures 4.11 and 4.12. This has been done to show the effect of constant liquid and gas superficial velocities in the respective figures. In Figure 4.11, when the liquid superficial velocity is 0.018m/s, increasing the gas superficial velocity decreases the profile and no changes in the peak frequency exist. However, increasing the liquid superficial velocity to 0.075m/s shows a shift in peak frequency as the gas superficial velocity is increased. The peak in the profile increases then decreases, and this is also accompanied by a slight shift in the profile from right to left.

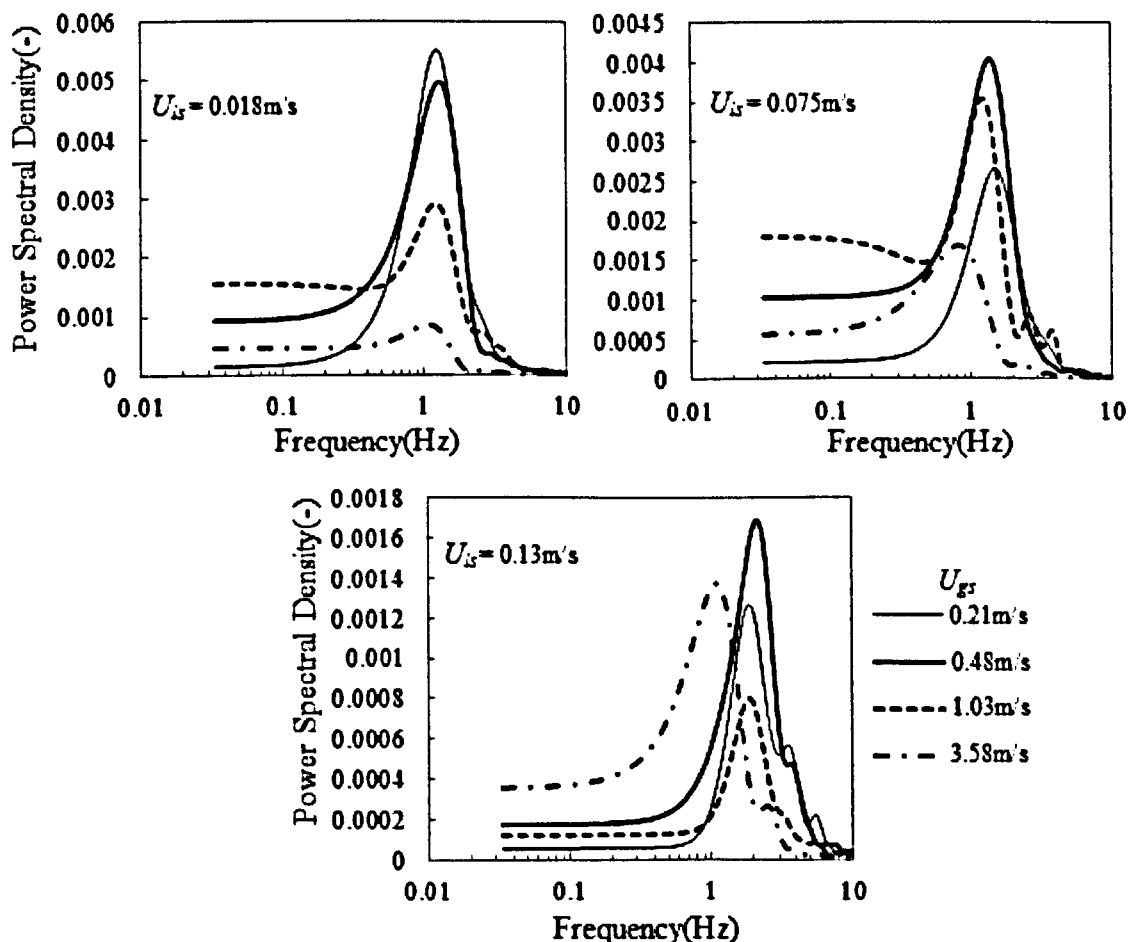


Figure 4.11. Variation of PSD with Frequency for constant liquid superficial velocity and increasing gas superficial velocity as indicated.

When the liquid superficial velocity is 0.075m/s, the flow is more oscillatory than at 0.018m/s. Therefore, it is expected that the peak increases as the gas superficial velocity increases. However this is not the case as there is a subsequent decrease in profile when the gas superficial velocity is 3.58m/s than at 1.03m/s.

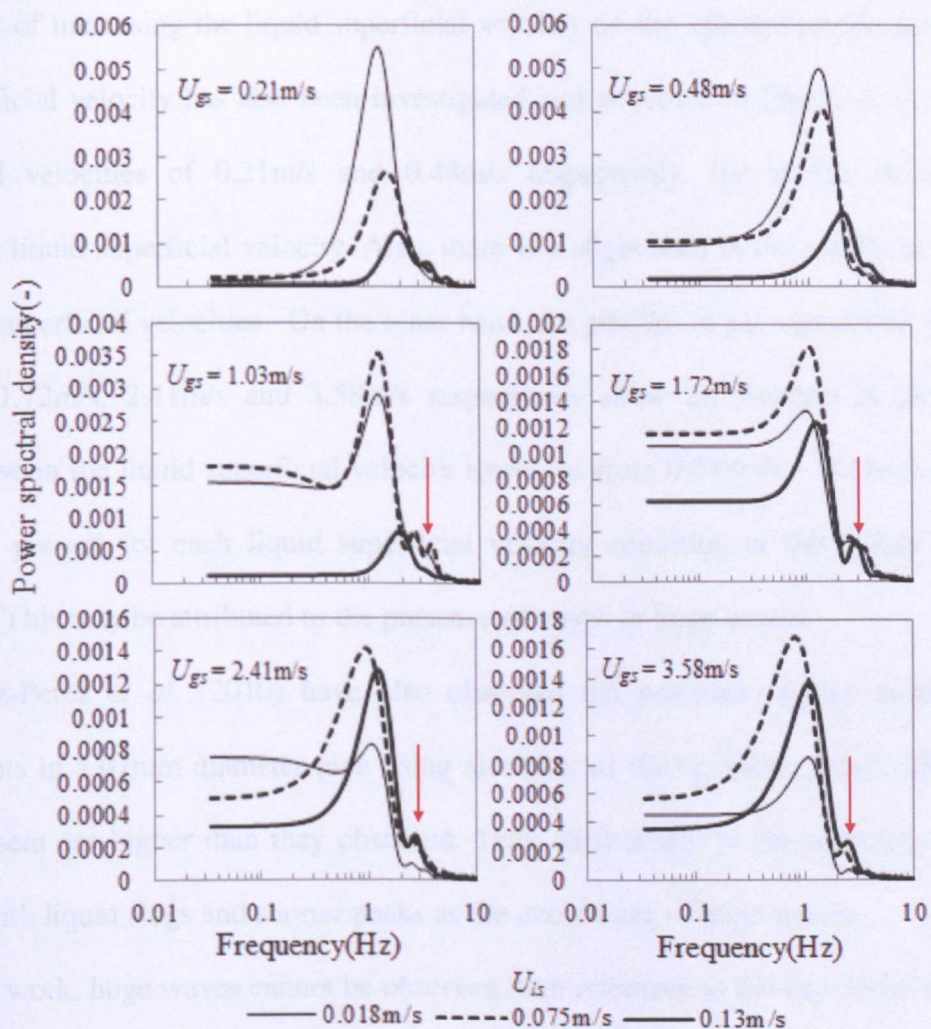


Figure 4.12. Effect of liquid superficial velocity on the variation of PSD with Frequency for constant gas superficial velocity. Two distinct peaks can be observed. The peak at higher end of the spectrum can be attributed to the formation of wisps/huge waves.

Increasing the liquid superficial velocity to 0.13m/s gives an apparent shift in profile when the gas superficial velocity is 3.58m/s. In relation to the actual flow behaviour, at this operating condition the flow is frothier as this can be observed in the high speed image in Figure 4.3. Consequently, this gives a shift in the profile to lower frequencies.

The effect of increasing the liquid superficial velocity on the spectral profile for a constant gas superficial velocity has also been investigated and is shown in Figure 4.12. At low gas superficial velocities of 0.21m/s and 0.48m/s respectively, the profile decreases with increasing liquid superficial velocity. Also, there is a slight shift in the profile to the right at these gas superficial velocities. On the other hand, the profiles at gas superficial velocities of 1.03m/s, 1.72m/s, 2.41m/s and 3.58m/s respectively show an increase in profile and a decrease when the liquid superficial velocity increases from 0.018m/s – 0.13m/s. Also short peaks are present for each liquid superficial velocity condition at the higher end of the spectrum. This may be attributed to the presence of wisps or huge waves.

Hernandez-Perez *et al.* (2010) have also observed the presence of two peaks for their experiments in a 67mm diameter pipe using air-water as the operating fluids. However, the peaks present are higher than they observed. They attributed it to the occurrence of Taylor bubbles with liquid slugs and shorter peaks as the occurrence of huge waves.

In present work, huge waves cannot be observed with reference to the interfacial structures in Figures 4.8(b), 4.9(b) and 4.10(b). This is for when the gas superficial velocity is 1.03m/s for respective liquid superficial velocities of 0.018m/s, 0.075m/s and 0.13m/s. However, what is common in all cases is the presence of wisps. At these operating conditions, huge waves may be present if the experiments were conducted in the smaller diameter pipe of 67mm as in (Hernandez-Perez *et al.*, 2010).

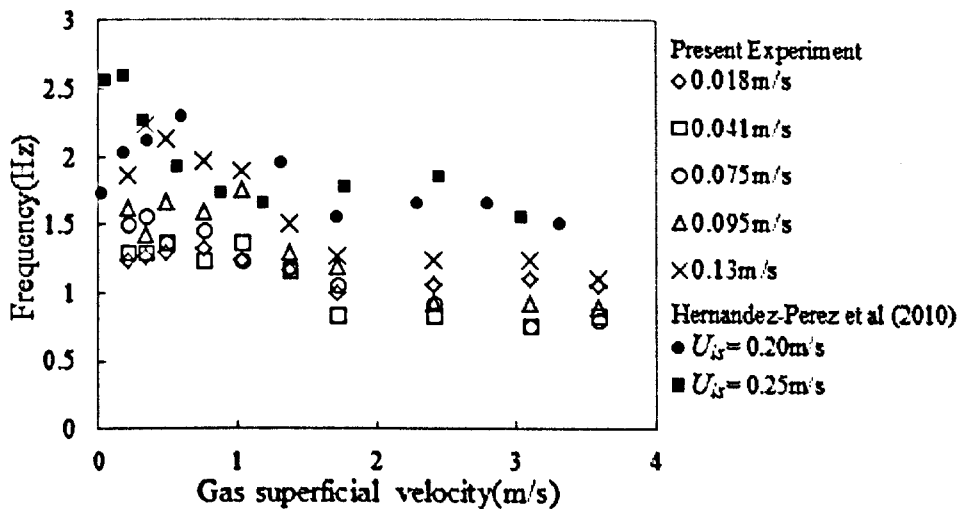


Figure 4.13. Variation of dominant frequency with gas superficial velocity. Further comparison to the work done in a 67mm internal diameter pipe of (Hernandez -Perez *et al.*, 2010).

Therefore, in their case it will be more than reasonable to attribute the second distinctive peak to huge waves. On the other hand, in Figure 4.12, the second distinctive peak at the higher end of the spectrum can only be attributed to the occurrence of wisps entrained in the gas core. This is essentially due to the transition from bubbly/spherical cap bubbly flow, of which no distinctive peak is present as shown in Figure 4.12, to churn turbulent flow (transition region) and typical churn flow, where the second peak occurs at a higher frequency than the first peak.

The dominant frequencies have been extracted from spectral plots and have been plotted against gas superficial velocity as shown in Figure 4.13. The profile is similar in trend to that obtained when the standard deviation is varied with gas superficial velocity in Figure 4.6. Therefore, similar regions identified in the standard deviation plot can be also used, namely: the bubbly, spherical cap, churn turbulent and typical churn flow regime.

Further comparison has been made to that data of (Hernandez-Perez *et al.*, 2010). The data from the present experiments at a liquid superficial velocity of 0.13m/s more or less agrees

with theirs at low gas superficial velocities where they observed bubble and slug flows. This diverges at higher gas superficial velocities and become closer to the frequency at lower liquid superficial velocities. This may probably be due to the fact that their liquid superficial condition is higher compared to the present experiments.

The degree of instability can be further examined using a dimensionless parameter, which is the Strouhal number. Azzopardi (2004) showed that the frequency of periodic structure can be correlated using the gas based Strouhal number and Lockhart-Martinelli parameter for bubbly and slug flow regimes. Both Strouhal number and Lockhart-Martinelli parameters are given in equations (4.10) and (4.11) as:

$$Str_G = \frac{fD}{U_{gs}} \quad (4.10)$$

$$X = \left[\left[\frac{\frac{dp}{dz}_L}{\frac{dp}{dz}_G} \right] \right]^{0.5} \equiv \sqrt{\frac{\rho_L}{\rho_G}} \frac{U_{ls}}{U_{gs}} \quad (4.11)$$

Slug flow has not been observed in the present experiments. Nonetheless, the above quantities have been plotted and compared with data in small diameter pipes in Figure 4.14. Also comparison has been made to the large diameter data retrieved from the work of (Hernandez *et al.*, 2010).

The data of Hernandez-Perez *et al.* (2010) in a 67mm diameter pipe and the larger diameter data are quite close to that obtained from the present experiments. However, there is a large discrepancy compared to the data with (Mao and Dukler, 1989 and Legius *et al.*, 1997). Mao and Dukler (1989) conducted their experiments in a 50.8mm diameter pipe with a length of 12.03m. On the other hand, Legius *et al.* (1997) conducted their experiments in a 50mm diameter pipe joined by a contraction to an 80mm diameter pipe section upstream with a length of 17m. Therefore, it is possible that the flow is more developed in both cases. In

addition, another reason may be that the frequency of the slug flow decays downstream, which has been previously identified by (Kaji *et al.*, 2009).

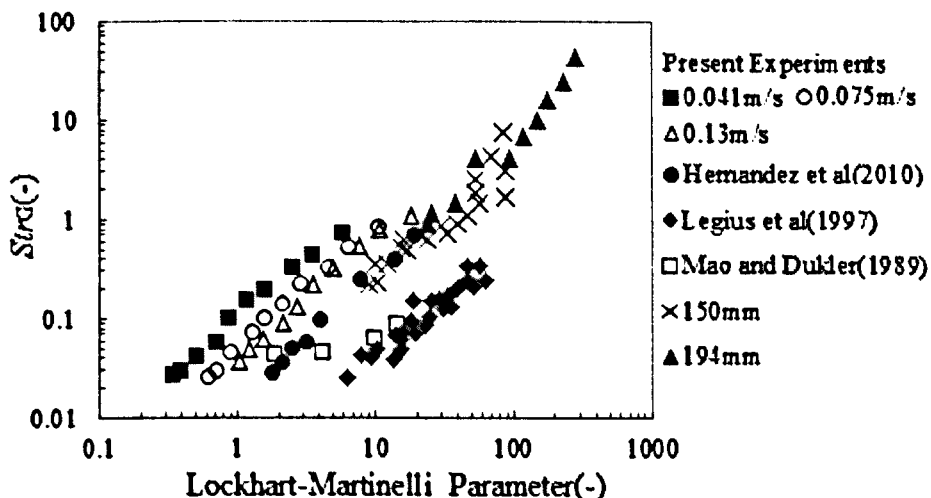


Figure 4.14. Variation of gas based Strouhal number against Lockhart –Martinelli parameter by method of Azzopardi (2004).

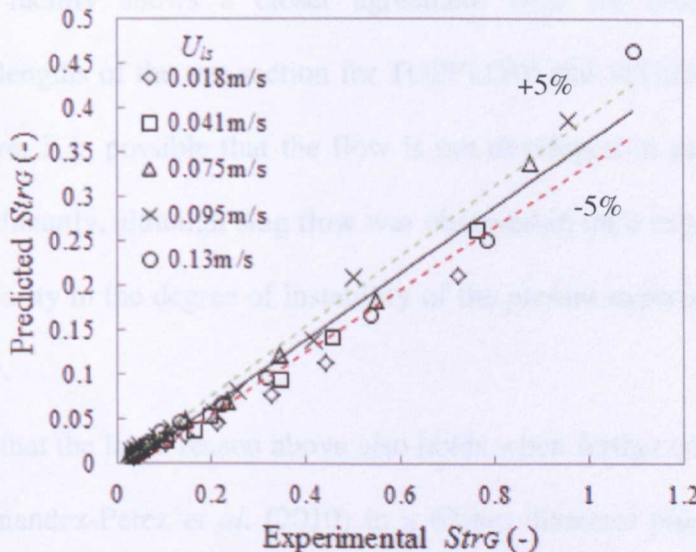
The gas based Strouhal number and the Strouhal number based on mixture velocity was further compared with the suggested Strouhal number correlations of (Kaji *et al.*, 2009). The Strouhal number based on mixture velocity is also compared with that of Kaji *et al.* (2009) as the frequency of the periodic structure decreases with increasing distance from the injection. Both quantities show quite a good agreement with experimental data in Figures 4.15 and 4.16 respectively. Their correlations are given as:

$$Str_G = AB \left(\frac{L}{D} \right)^{-0.75} \quad (4.12)$$

where the coefficients A and B are given by $A = U_{gs}^{-1.2}$ and $B = 4.94U_{ls} + 0.368$.

$$Str_m = \frac{fD}{U_m} = CE \left(\frac{L}{D} \right)^{-0.6} \quad (4.13)$$

where U_m is the mixture velocity coefficients C and D are given by $C = U_{gs}^{-0.75}$ and $E = 0.74U_{ls} + 0.53$.



to (Kaji et al., 2009).

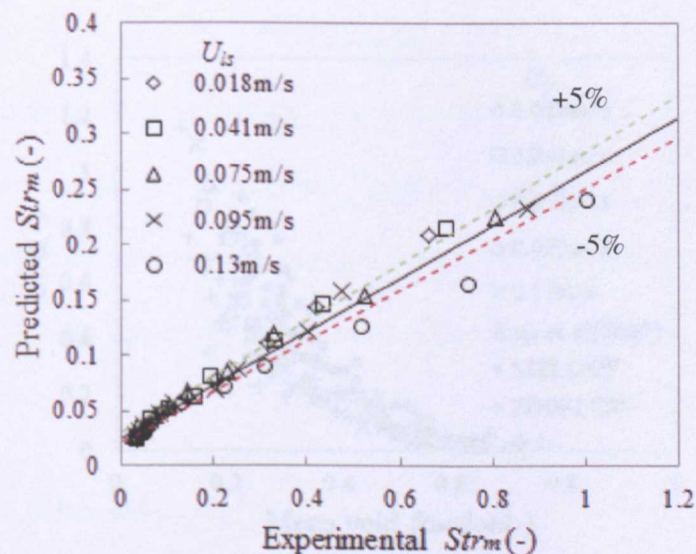


Figure 4.16. Comparison of experimental and predicted Strouhal number based on mixture velocity according to (Kaji et al., 2009).

The gas based Strouhal number variation with void fraction has been compared with the data from Kaji *et al.* (2009) in Figure 4.17. The MTLOOP and TOPFLOW facilities they conducted their experiments have diameters of 51.2mm and 52.3mm respectively. The data

from TOPFLOW facility shows a closer agreement with the data from the present experiments. The lengths of the test section for TOPFLOW and MTLOOP facilities are 9m and 3.5m. Therefore, it is possible that the flow is not developed in case of the MTLOOP facility. More significantly, although slug flow was observed in their experiments, it implies that there is a similarity in the degree of instability of the present experiment with that in the TOPFLOW facility.

Figure 4.18 shows that the latter reason above also holds when further comparisons are made to the data of Hernandez-Perez *et al.* (2010) in a 67mm diameter pipe. However, in both cases, the argument may fail as this is dependent on where the data is acquired along the test section.

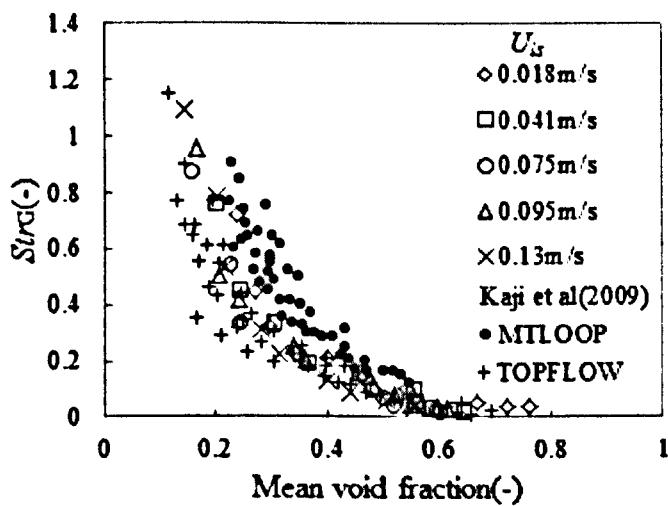


Figure 4.17. Variation of gas based Strouhal number with mean void fraction comparison with (Kaji *et al.*, 2009).

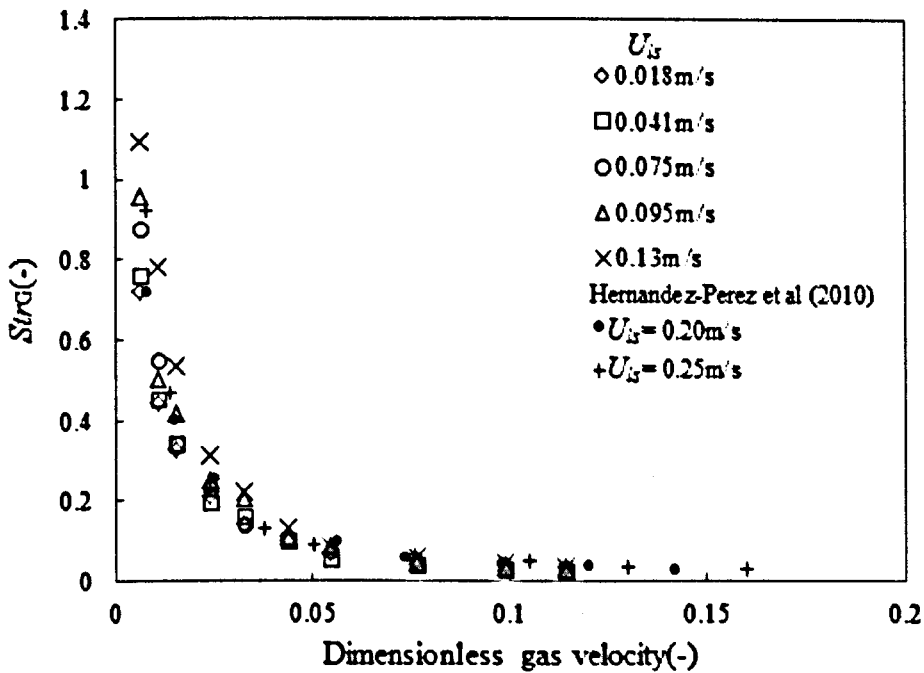


Figure 4.18. Variation of the gas based Strouhal number against dimensionless gas velocity in equation (4.5) showing comparison with (Hernandez- Perez *et al.*, 2010). The periodicity of the structures for bubbly, slug and churn flows obtained by spectral analysis for data in the 67mm internal diameter pipe of Hernandez- Perez *et al.* (2010) can be said to be similar to the periodicity of the structures in the present work for a direct transition from bubbly to churn flows when air-water are the operating fluids.

4.2.7. Radial phase distribution

Apart from the cross-sectional area averaged void fraction data, the time averaged radially resolved void fraction data can be obtained from the wire mesh sensor. The radial void fraction reveals the phase distribution from the centreline of the pipe to the walls. Also, it shows the tendency of the bubbles flowing within the cross section of the pipe to move towards the wall (wall peaking) or travel within the core (core peaking) of the pipe. A flat phase distribution profile shows a wall peak distribution while a parabolic profile a core peak distribution.

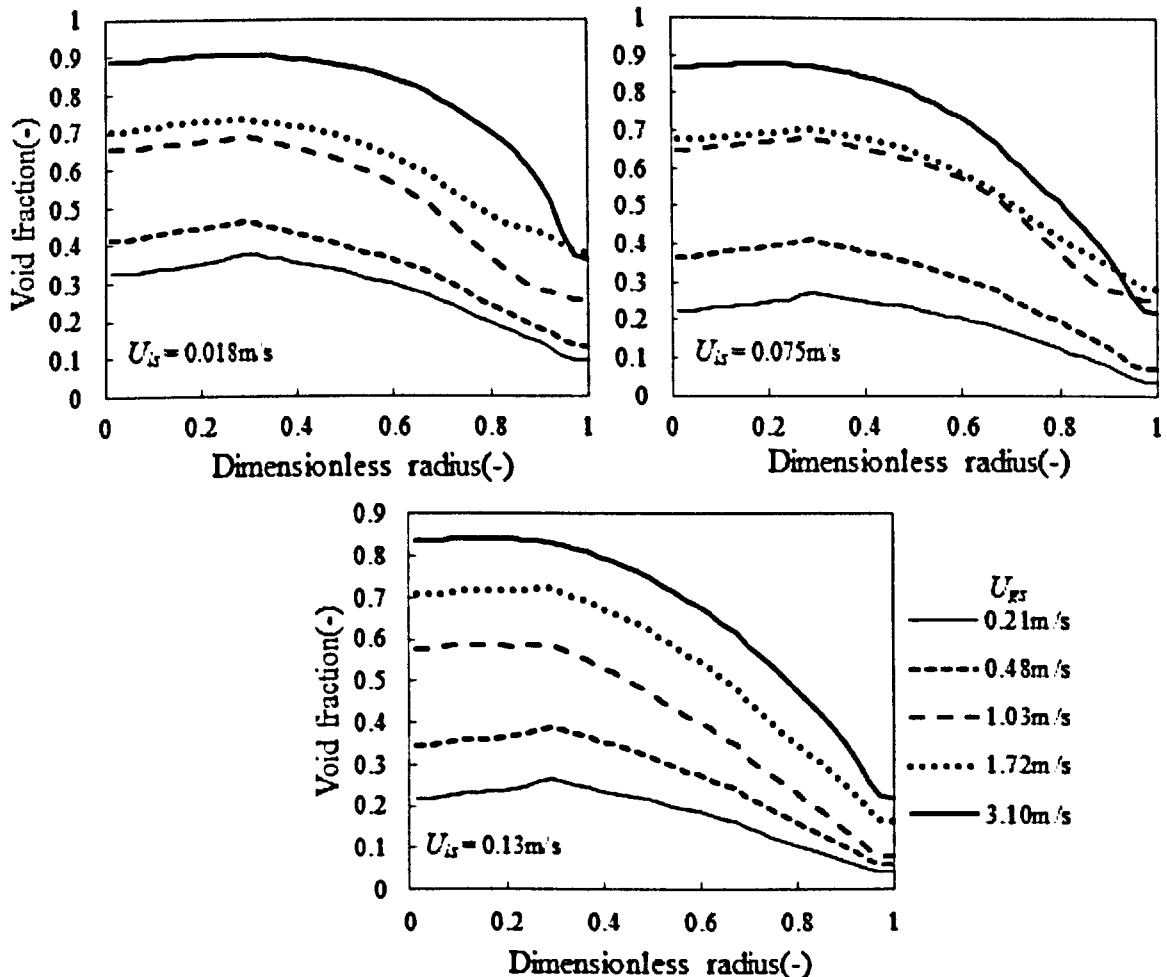


Figure 4.19. Time-average variation of radial void fraction with dimensionless radial distance
at constant liquid superficial velocities

Since the sub-regimes for bubbly to churn transitions for large diameter pipes have not been clearly defined, this analysis contributes to establishing the sub-regimes present. Figure 4.19 shows the radial phase distribution from the centre of the pipe to the wall, that is, from 0 to 1 respectively. This has been plotted against dimensionless radius, which is, the spatial distance between two successive wires in the radial direction divided by the pipe diameter (r/R) for constant liquid superficial velocities of 0.018m/s, 0.075m/s and 0.13m/s respectively.

For all cases of liquid superficial velocity presented, the void fraction profile increases towards 1 as the gas superficial velocity is increased. However, when the liquid superficial

velocity is increased, the profile becomes less parabolic which is apparent when the gas superficial velocity is 3.10m/s. Also, at low gas superficial velocities of 0.21m/s and 0.48m/s, the void fraction increases gradually to a dimensionless radial distance of 0.3 which is then followed by a decrease. This behaviour is more prominent at higher gas superficial velocities as the liquid superficial velocity increases. It is possible that this is due to the distorted shape of the large diameter bubble that almost occupies the cross-section of the pipe as earlier identified in the interfacial structures in section 4.2.5.

Further analysis on the radial phase distributions were carried out to obtain predicted radial void fraction values. The comparison of both experimental and predicted radial void fraction is shown in Figure 4.20. The equation used to predict the radial void fraction is given as:

$$\alpha_r = \bar{\alpha}_g \left(\frac{n+2}{n+2-2c} \right) \left(1 - c \left(\frac{r}{R} \right)^n \right) \quad (4.14)$$

where α_r , $\bar{\alpha}_g$ and r/R are the radial void fraction, cross sectional averaged void fraction and dimensionless radius. The other parameters n and c take into consideration the steepness of the profile and holdup close to the wall. The equation is of the same form used for bubbly flow to predict the radial profile according to (Luo and Svendsen, 1991).

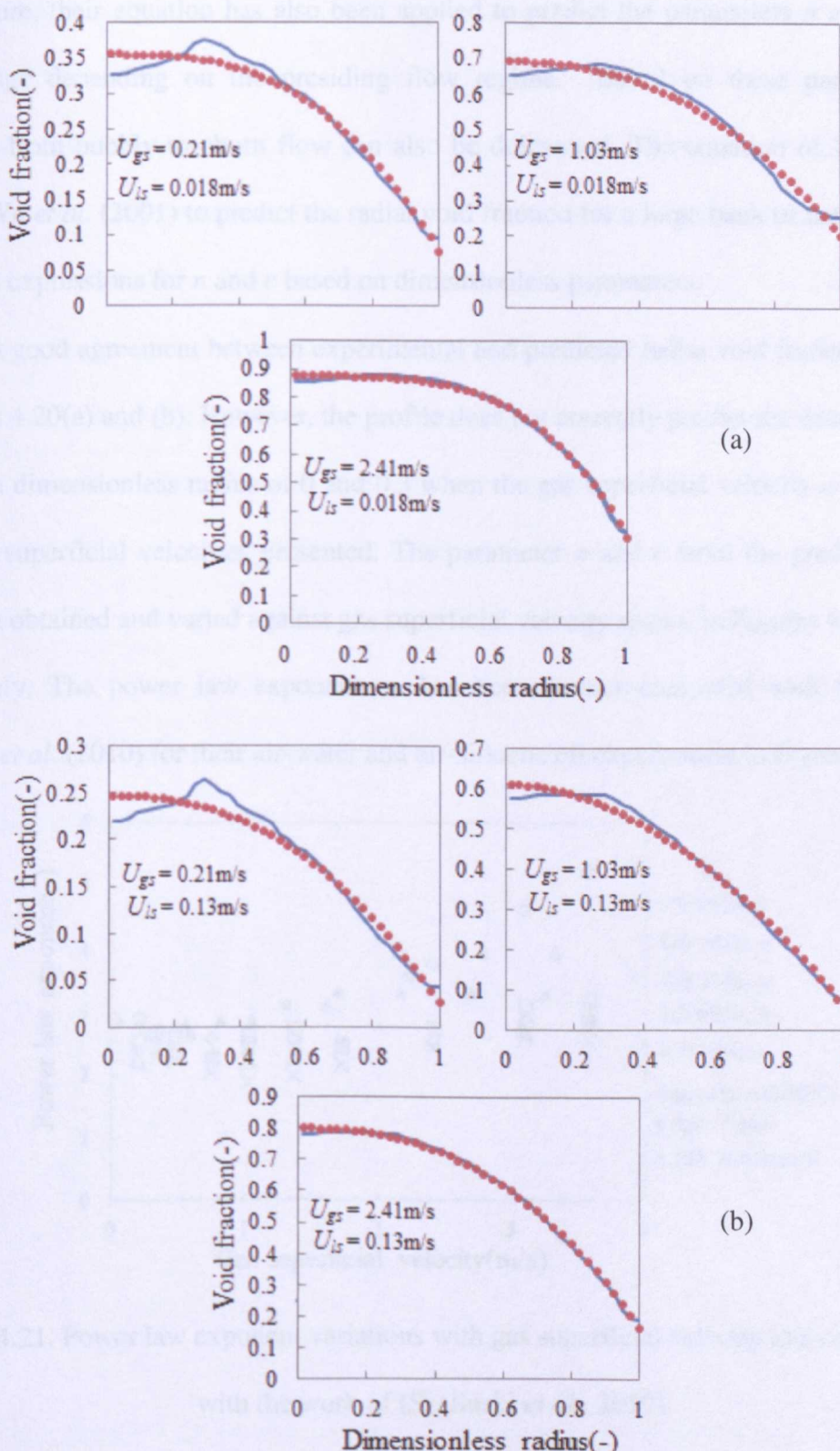


Figure 4.20. (a) and (b) Experimental and predicted radial void fraction variation with dimensionless radial distance for constant liquid superficial velocities of 0.018 m/s and 0.13 m/s respectively.

Furthermore, their equation has also been applied to predict the parameters n and c , which also change depending on the presiding flow regime. Based on these parameters the transition from bubbly to churn flow can also be delineated. The equation (4.14) has been used by Wu *et al.* (2001) to predict the radial void fraction for a large bank of data. They also suggested expressions for n and c based on dimensionless parameters.

There is a good agreement between experimental and predicted radial void fraction as shown in Figures 4.20(a) and (b). However, the profile does not correctly predict the exact behaviour between a dimensionless radius of 0 and 0.3 when the gas superficial velocity is 0.21m/s for all liquid superficial velocities presented. The parameter n and c from the predicted values have been obtained and varied against gas superficial velocity shown in Figures 4.21 and 4.22 respectively. The power law exponent, n , has been further compared with the work of Szalinski *et al.* (2010) for their air-water and air-silicone oil experiments in Figure 4.21.

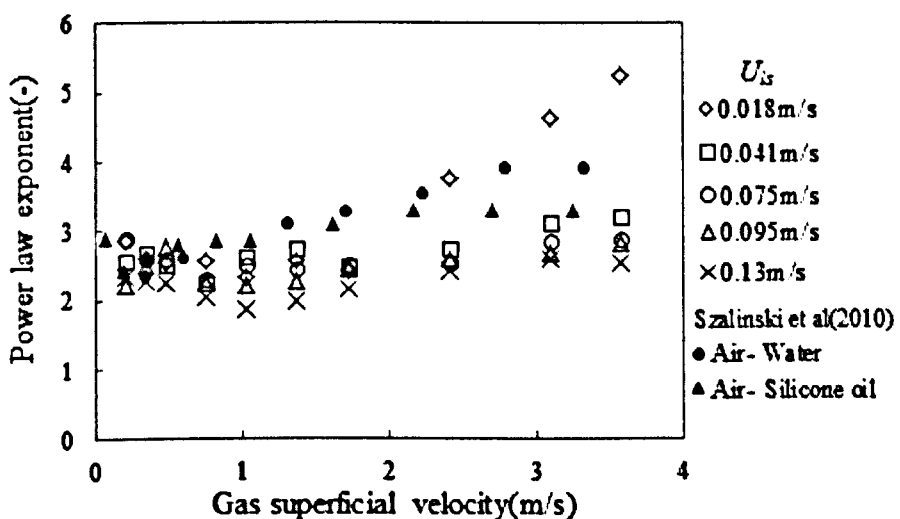


Figure 4.21. Power law exponent variations with gas superficial velocity and comparison with the work of (Szalinski *et al.*, 2010).

The data from the present experiments agrees quite well with those from (Szalinski *et al.* (2010)). As regards the data from the present experiments, there is a decrease in trend to a gas

superficial velocity of 1.03m/s followed by an increase in trend. A sharp increase in trend can be observed beyond this gas superficial velocity, for a liquid superficial velocity of 0.018m/s. This is in comparison to other liquid superficial velocities greater than this value.

In addition, there is a divergence in comparison with air-water and air-silicone oil data of Szalinski *et al.* (2010) when the gas superficial velocity is greater than 1.03m/s. However, this later converges at higher gas superficial velocities for just the air-silicone oil data of (Szalinski *et al.*, 2010). The decrease and a subsequent increase is a probable transition from bubbly to churn flow. Therefore, based on subjection and subdividing according to the trend, four regimes can be vaguely identified. The regime where values are more or less constant at low gas superficial velocity can be regarded as the bubbly regime. The spherical cap bubbly regime is associated by a decrease to a gas superficial velocity of 1.03m/s and churn flow regime after this gas superficial velocity. The churn flow regime can be further divided into churn turbulent and typical churn flow.

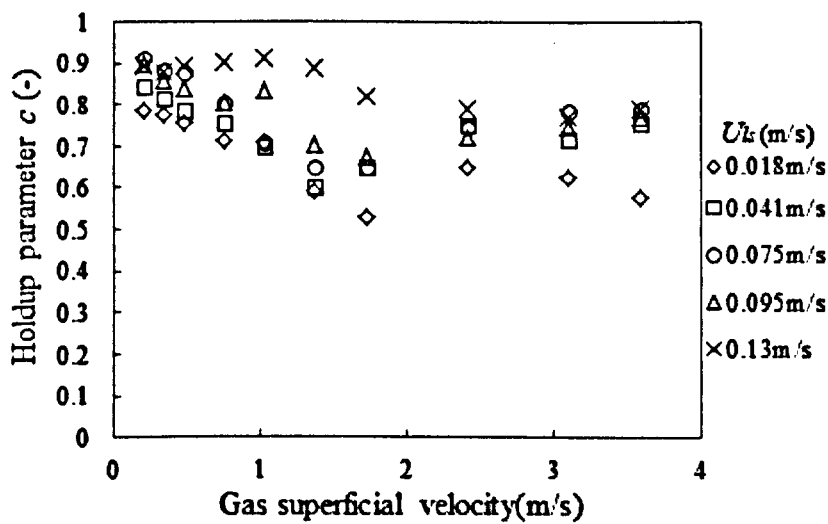


Figure 4.22. Holdup parameter against gas superficial velocity.

The churn turbulent or transition to churn flow occurs from gas superficial velocity of 1.03m/s-1.72m/s, and beyond this gas superficial velocity, a well-formed or typical churn

flow may be present. Compared to Figure 4.21, Figure 4.22 shows a transition from bubbly to churn when the holdup parameter is plotted against the gas superficial velocity, which increases in trend as the liquid superficial velocity increases. This is because the two-phase flow becomes more wall peaking as the liquid superficial velocity is increased. This has been earlier revealed by the skewness analysis of the time series data in Figure 4.6.

4.2.8. Bubble size distribution

The size distribution of bubbles has been obtained from further analysis of the 3D void data as shown in Figure 4.23. According to Prasser *et al.* (2001), using a recursive fill algorithm, bubbles are identified by extracting the contribution of each statistical bubble diameter bin to the overall void fraction.

The bubble size distribution is given as:

$$h(D_b) = \frac{d\alpha_s}{dD_b} \quad (4.15)$$

where the bubble diameter D_b is obtained as follows:

$$D_b = \sqrt[3]{\frac{6}{\pi} V_b} \quad (4.16)$$

For gas superficial velocities of 0.21m/s, 0.48m/s and 1.03m/s, bi-modal peaks can be identified having a broad and narrow area respectively. This has been shown for liquid superficial velocities of 0.018m/s, 0.075m/s and 0.13m/s from left to right respectively.

When the gas superficial velocity is 0.21m/s, increasing the liquid superficial velocity does not decrease the height of the peak for the first peak. However, there is a decrease in height for the second peak. The first peak can be classified as small bubbles that flow behind the large diameter bubble, having a narrow area. The above reason can also be applied for gas superficial velocities of 0.48m/s and 1.03m/s respectively.

When the gas superficial velocity is 3.58m/s the second peak that was identified above is not present. However, peaks appear when the liquid superficial velocity is 0.13m/s. This is because the flow behaviour had been indicated above to be more oscillatory thereby giving bubbles entrained in liquid.

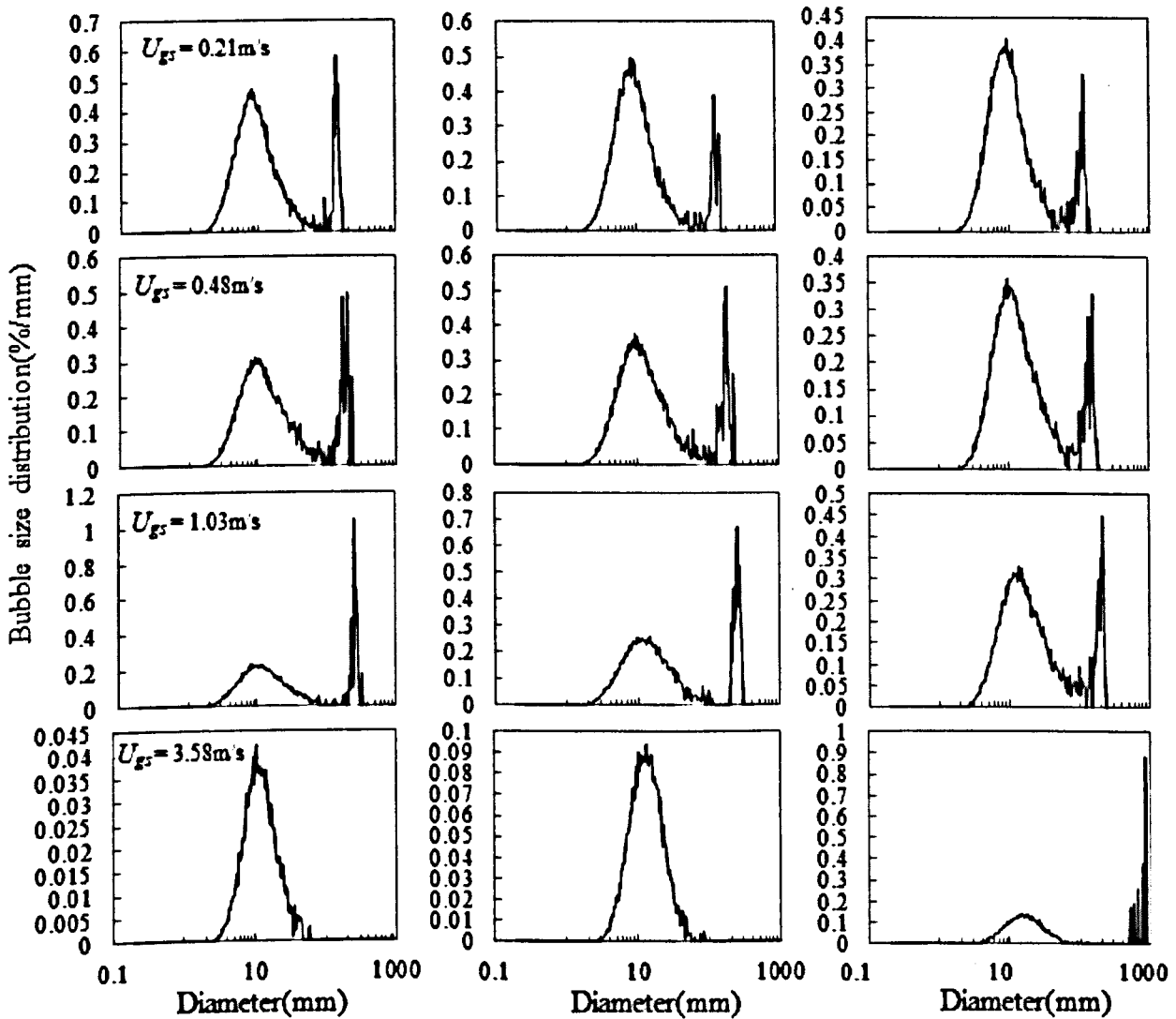


Figure 4.23. Bubble size distributions for selected gas superficial velocity and increasing liquid superficial velocity of 0.018m/s, 0.075m/s and 0.13m/s from left to right respectively.

The bubble size distribution was further compared with the air-water and air-silicone oil data of Szalinski *et al.* (2010) as shown in Figure 4.24. This size distribution has been varied with a dimensionless bubble diameter, which is divided by pipe diameter in the present

experiments of 121mm and theirs of 67mm respectively. Approximate gas superficial velocities have been compared with their liquid superficial velocity of 0.2m/s.

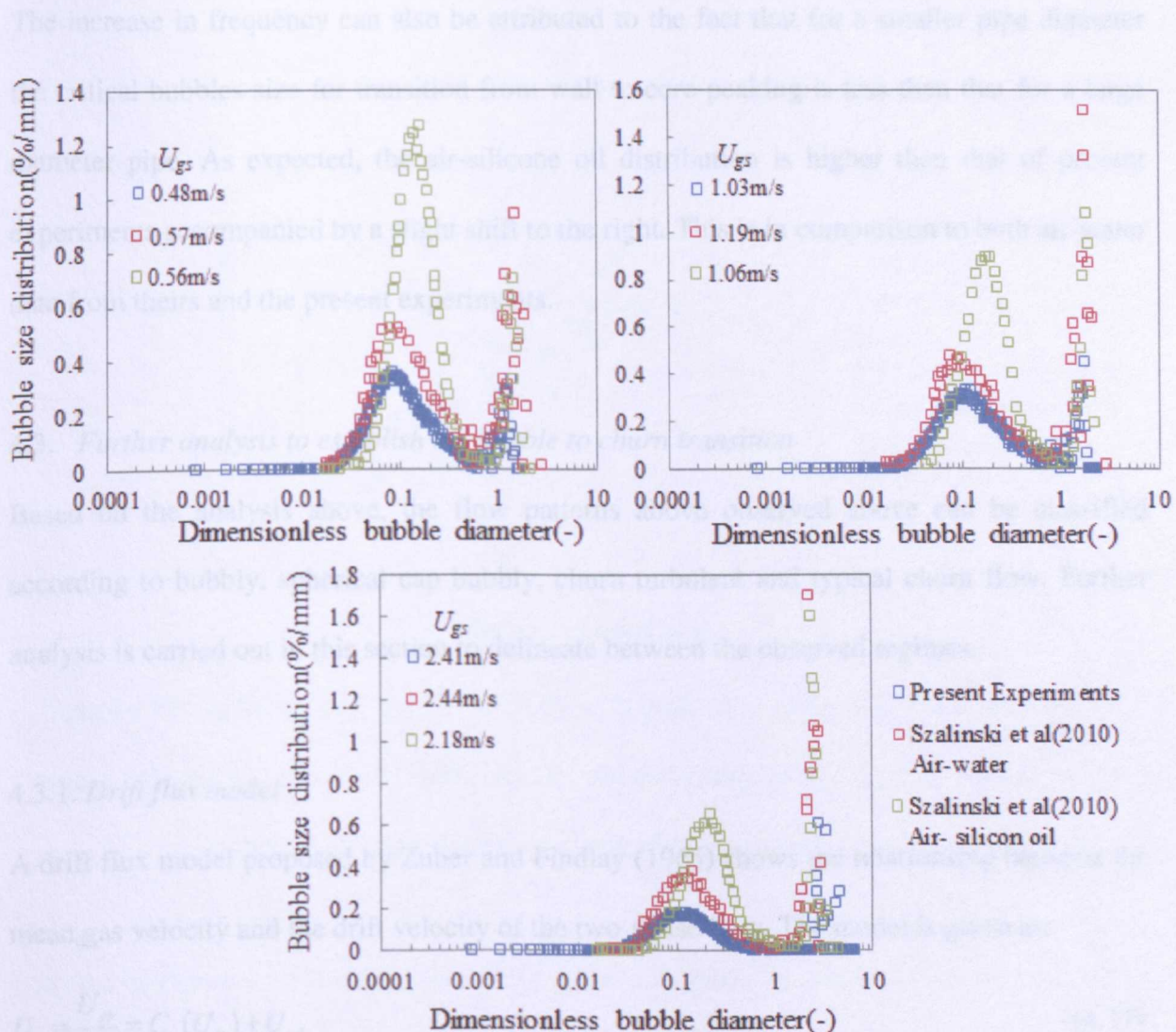


Figure 4.24. Bubble size distribution variation with dimensionless bubble diameter and comparison with (Szalinski *et al.*, 2010).

Interestingly, the distribution is slightly higher for their air-water data compared to the present experiments. However, the mean bubble diameter is approximately the same. Based on their experiments, they obtain churn flow at this condition after a slug flow pattern at a gas superficial velocity of 0.33m/s. Since the Taylor bubbles have been destroyed, large irregular shaped bubbles are present. This maybe the reason for a higher distribution compared to the

present experiment. At a gas superficial velocity of 0.48m/s in the present experiments, large bubbles have also been observed instead of churn flow.

The increase in frequency can also be attributed to the fact that for a smaller pipe diameter the critical bubbles size for transition from wall to core peaking is less than that for a large diameter pipe. As expected, the air-silicone oil distribution is higher than that of present experiments accompanied by a slight shift to the right. This is in comparison to both air-water data from theirs and the present experiments.

4.3. Further analysis to establish the bubble to churn transition

Based on the analysis above, the flow patterns above observed above can be classified according to bubbly, spherical cap bubbly, churn turbulent and typical churn flow. Further analysis is carried out in this section to delineate between the observed regimes.

4.3.1. Drift flux model

A drift flux model proposed by Zuber and Findlay (1965) shows the relationship between the mean gas velocity and the drift velocity of the two-phase flow. The model is given as:

$$U_g = \frac{U_{gs}}{\alpha_g} = C_o(U_m) + U_{gd} \quad (4.17)$$

where U_g , U_{gs} , α_g , C_o , U_m and U_{gd} are the mean gas velocity, gas superficial velocity, void fraction, distribution coefficient, mixture velocity and drift velocity respectively.

When the mean gas velocity is plotted against the mixture velocity, the distribution coefficient and drift velocity are given as the slope and intercept accordingly. The drift flux relationship from the present work has been compared with the work of (Ohnuki and Akimoto, 1996 and Omebere-Iyari *et al.*, 2008). The motivation for this comparison is based

on the fact that both carried out experiments in large diameter pipes of 480mm and 194mm using air-water and steam-water as the operating fluids respectively.

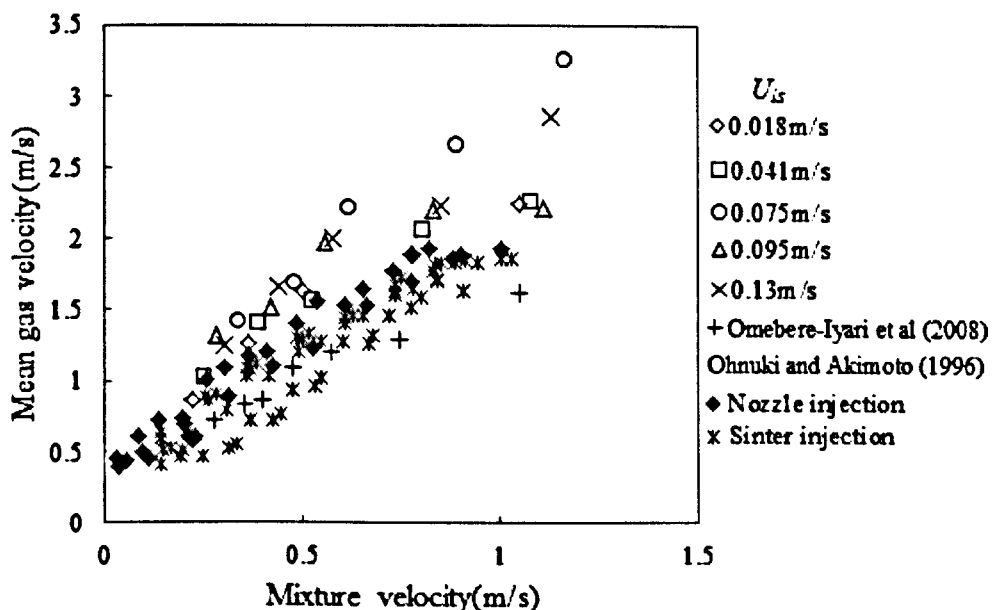


Figure 4.25. Variation of mean gas velocity with mixture velocity. Comparisons with the work of Omebere-Iyari *et al.* (2008) and Ohnuki and Akimoto (1996) from the conditions they observed bubbly flow to the churn-turbulent regime.

It shows in Figure 4.25 that there is a close agreement with the data of Ohnuki and Akimoto (1996) when they used a Nozzle type of injection compared to when they used a sinter injection. The nozzle injection is similar to the method of injection used in the present study. The data of Omebere-Iyari *et al.* (2008) agrees quite well with the data of Ohnuki and Akimoto (1996) but not the present experiments.

Ohnuki and Akimoto (1996) and Omebere-Iyari *et al.* (2008) have observed bubbly and churn turbulent regimes for the operating range shown. Therefore, if this is tallied with their experimental data, it means that the gas superficial velocity for the transition to churn turbulent regime occurs at a gas superficial velocity of 1.03m/s for the present experiments, which agrees with the analysis in the present work.

However, this also depends on the liquid superficial velocity. From the drift flux relationship in Figure 4.25, the values of the distribution parameter are 1.57, 1.46, 1.11, 1.78, and 2.20 respectively. On the other hand, the drift velocities are 0.66m/s, 0.78m/s, 1.13m/s, 0.82m/s and 0.73m/s. Kataoka and Ishii (1987) suggested a value of 1.19 and 0.45 for C_o and U_{gd} respectively based on their equations for both quantities. The value obtained in this experiment is higher than those predicted from Kataoka and Ishii (1987) which may be due to a high degree of liquid recirculation. Hibiki and Ishii (2003) suggested that the liquid recirculation is more prevalent in large diameter pipes compared to smaller ones such as that used in (Szalinski *et al.*, 2010).

4.3.2. Flow regime identification

Figure 4.26 shows the operating conditions on a flow pattern map in red markers. The blue line represents the bubble to slug transition line of Taitel *et al.* (1980) in a 50mm diameter pipe and red and green transition line of Schlegel *et al.* (2009) from 102mm diameter pipe. The red line indicates the transition from bubbly to spherical cap bubbly flow.

This agrees reasonably well with that observed in the present experiments with a critical void fraction of 0.3. The transition from spherical cap bubbly flow to churn turbulent occurs at a higher critical void fraction of 0.51 indicated by the green transition line.

Based on the experiments, the transition gas superficial velocity to the aforementioned regime has been identified to occur at 1.03m/s, which is just right of the green transition line suggested by (Schlegel *et al.*, 2009). Therefore, in this case, three regimes I, II and III can be clearly established namely bubbly, spherical cap bubbly and churn turbulent regime.

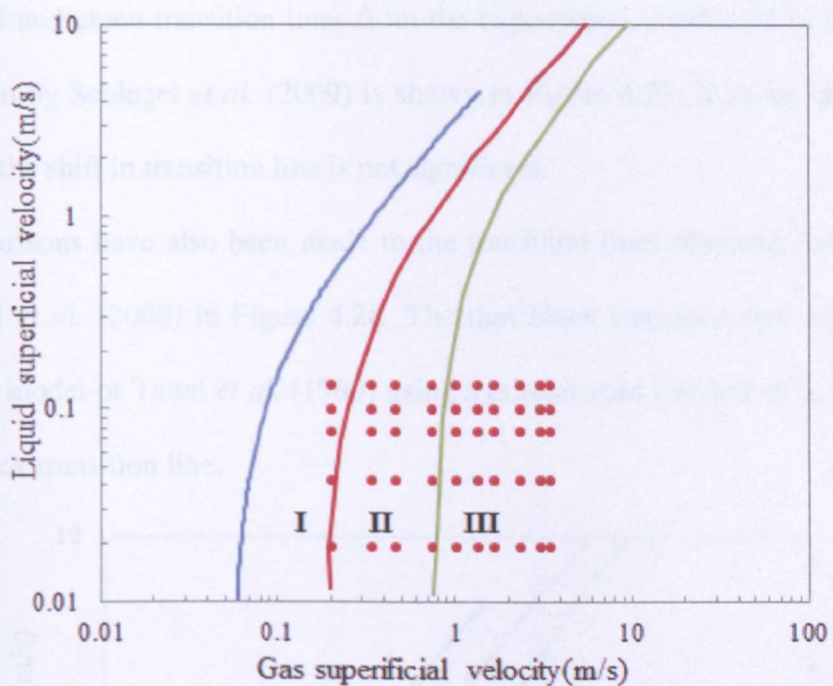


Figure 4.26. Flow regime identification with blue, red and green transition lines of Taitel *et al.* (1980) and Schlegel *et al.* (2009) in 102mm diameter pipe.

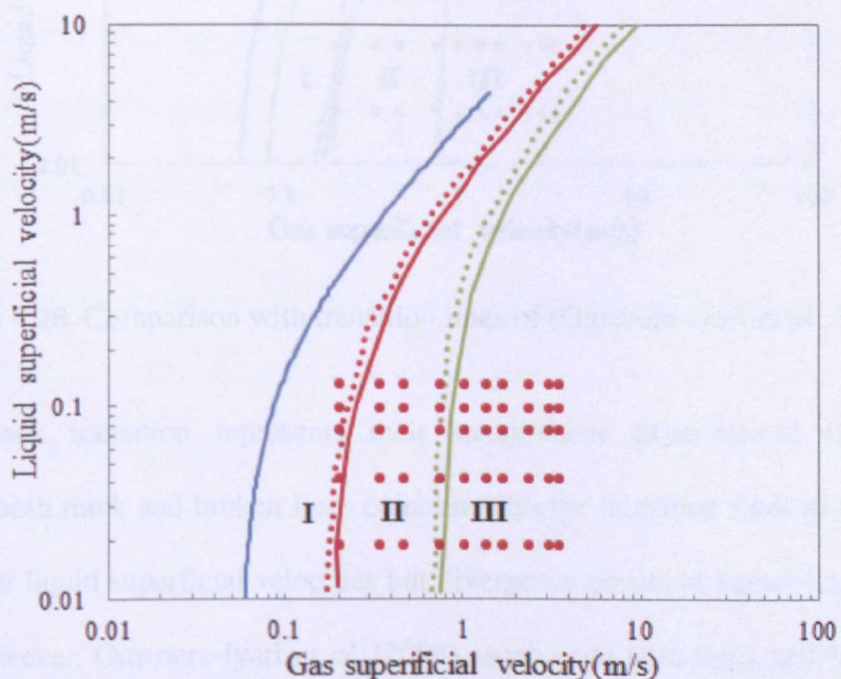


Figure 4.27. Effect of larger diameter pipe from the work of (Schlegel *et al.*, 2009) done on a 152mm internal diameter pipe.

The dotted red and green transition lines from the experiments conducted in larger diameter pipe of 152mm by Schlegel *et al.* (2009) is shown in Figure 4.27. It shows that for a larger diameter pipe the shift in transition line is not significant.

Further comparisons have also been made to the transition lines obtained from the work of Omebere-Iyari *et al.* (2008) in Figure 4.28. The thin black transition line was obtained by modifying the model of Taitel *et al.* (1980) using a critical void fraction of 0.38 and 0.68 for the broken black transition line.

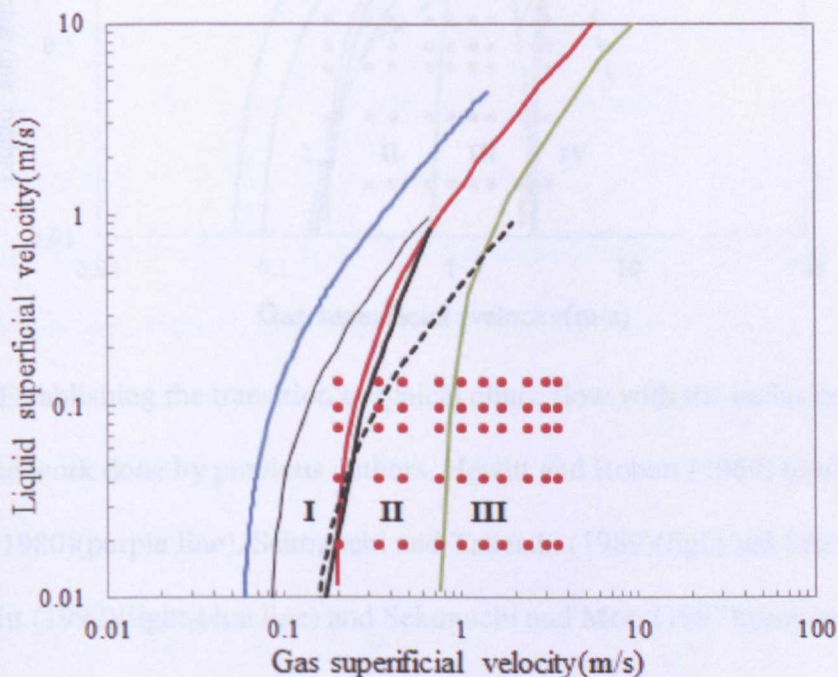


Figure 4.28. Comparison with transition lines of (Omebere-Iyari *et al.*, 2008).

The thick black transition represents their steam-water experimental transition line. Interestingly, both thick and broken lines coincide with the transition lines of Schlegel *et al.* (2009) at lower liquid superficial velocities but divergence occurs at higher liquid superficial velocities. However, Omebere-Iyari *et al.* (2008) ascertained both thick and broken lines to be a transition to churn turbulent flow. For both Omebere-Iyari *et al.* (2008) and Schlegel *et al.* (2009), the transition to typical churn flow was not clarified. Schlegel *et al* (2009)

characterized the region to the right of their green transition line as churn turbulent flow, which is essentially not the case.

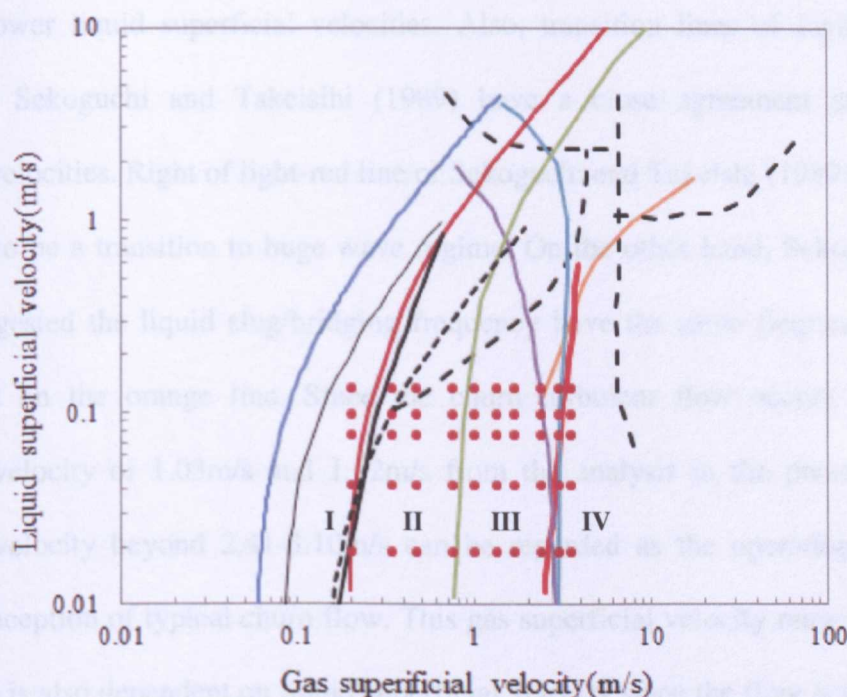


Figure 4.29. Establishing the transition to typical churn flow with the inclusion of transition lines from the work done by previous authors. Hewitt and Robert (1969) (dash black line), Taitel *et al* (1980)(purple line), Sekoguchi and Takeishi (1989)(light-red line), Jayanti and Hewitt (1992)(light-blue line) and Sekoguchi and Mori (1997)(orange line).

To further establish the conditions for which typical churn flow occurs the transition lines of Hewitt and Robert (1969), Taitel *et al* (1980)(purple line), Sekoguchi and Takeishi (1989)(light-red line), Jayanti and Hewitt (1992)(light-blue line) and Sekoguchi and Mori (1997)(orange line) have been plotted. According to Hewitt and Robert (1969) they identified four regimes based on their experiments namely the bubbly, slug, churn, wispy-annular and annular regime. The region identified by Omebere-Iyari *et al.* (2008) and Schlegel *et al.* (2009) as churn turbulent flow is within the churn flow region of (Hewitt and Robert, 1969). From the work of Taitel *et al.* (1980), they suggested that the transition from slug to churn flow is an entrance phenomenon. Their transition line at $L/D = 200$ has been plotted and

coincides with the experimental conditions for a gas superficial velocity of 2.41m/s. Their transition line agrees with lines of Jayanti and Hewitt (1992) and Sekoguchi and Takeishi (1989) at lower liquid superficial velocities. Also, transition lines of Jayanti and Hewitt (1992) and Sekoguchi and Takeishi (1989) have a close agreement at higher liquid superficial velocities. Right of light-red line of Sekoguchi and Takeishi (1989) they suggested this region to be a transition to huge wave regime. On the other hand, Sekoguchi and Mori (1997), suggested the liquid slug/bridging frequency have the same frequency as the huge wave based on the orange line. Since the churn turbulent flow occurs between a gas superficial velocity of 1.03m/s and 1.72m/s from the analysis in the present work, a gas superficial velocity beyond 2.41-3.10m/s can be regarded as the operating condition that marks the inception of typical churn flow. This gas superficial velocity range has been given because this is also dependent on liquid superficial velocity since the flow is more oscillatory when the liquid superficial velocity increases. It also means that beyond a gas superficial velocity of 3.10m/s churn flow occurs.

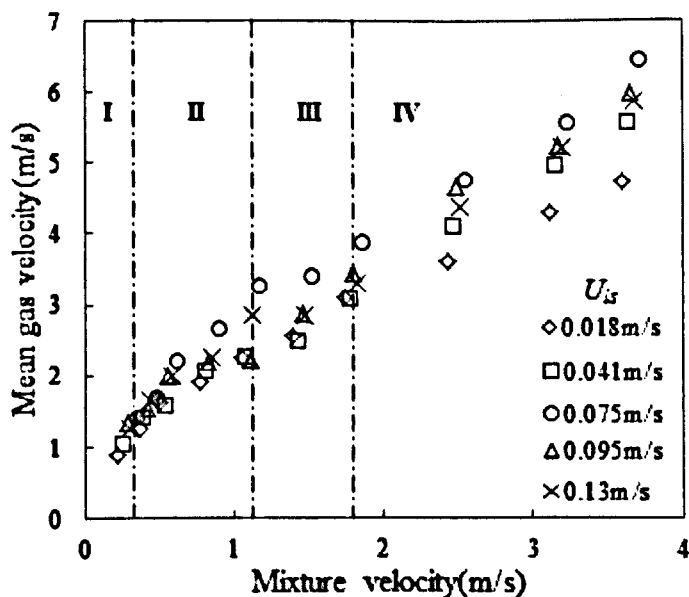


Figure 4.30. Variation of mean gas velocity with mixture velocity and identification of regimes present.

Consequently, when the drift flux relationship is again considered four regions can be identified. The bubbly, the spherical cap bubbly, churn turbulent (heterogeneous bubbly/ transition regime) and typical churn flow regimes are given as regions I, II, III and IV in Figure 4.30. The transition gas superficial velocity of 1.72m/s has been used as a benchmark to typical churn flow as it marks the absence of churn turbulent flow.

4.4. Summary

The present experiments for bubble to churn transition have been carried out in a large diameter vertical pipe of 121mm internal diameter and 5.3m in length. The operating fluids employed are air and water respectively. A wire mesh sensor has been used to acquire the phase fraction data at $L/D = 35$. Based on the analysis of the phase fraction data, the following summaries have been made:

1. At low gas superficial velocity, the presiding regime is bubbly and spherical cap bubbly flow pattern characterised by large distorted shaped bubbles almost occupying the entire cross section of the pipe. In spherical cap bubbly flow, the structure travels intermittently with smaller diameter bubbles flowing behind them. At higher gas superficial velocities, churning behaviour is present and the degree of instability increases with increasing liquid superficial velocity. Compared to the bubbly flow/spherical cap bubbly flow, it has a frothy nature depicted as clusters of closely packed small diameter bubbles.
2. The 3-D surface plots, which reveal the interfacial structures present similar to the work of Sekoguchi and Takeishi (1989) in Figure 2.26 of chapter 2, have also been used to distinguish the bubbly and churn flow patterns. For churn flow, liquid bridging of the gas core and huge waves are present. Incomplete atomisation of the huge waves gives wisps. On the other hand, coalescence of huge waves about the pipe centreline give large liquid structures entrained in the gas core, which occupy the entire cross-section of the pipe.

3. Statistical analysis such as the probability density function, standard deviation, skewness and kurtosis has proved useful in depicting the transition from the bubbly to churn flow.
4. The spectral analysis of time series was also used to ascertain the frequency of the periodic structures present. The dominant frequencies extracted have the same profile as the standard deviation profile in the statistical analysis section. However the frequencies increases with increasing liquid superficial velocity while the reverse is the case in the standard deviation profiles.
5. The gas based Strouhal number and Lockhart-Martinelli parameter initially correlated by Azzopardi (2004) for bubbly and slug flows, shows a close agreement with the data of Hernandez-perez *et al.* (2010) in a small diameter pipe. Further comparison of both gas and mixture based Strouhal number was made with data of Kaji *et al.* (2010), in small diameter pipes. Also, the variation of gas based Strouhal number with void fraction showed good agreement with (Kaji *et al.*, 2009).
6. Four enduring regimes are present based on comparison made with respect to small and larger diameter pipes. These are bubbly, spherical cap bubbly, churn-turbulent flow and typical churn flow.

In consideration of the present work, the operating condition for the inception of typical churn flow has been delineated. Churn flow has a frothy nature and is also characterised by liquid bridging of the gas core and formation of huge waves. Wisps and large liquid structures entrained in the gas core are also present. The large liquid structures entrained in the gas core that occupies most of the pipe cross-section and the frothy nature of the flow is the desirable condition for the downstream GLCC. However, it is necessary to know the operating conditions that give a high degree of frothing as well as a high frequency of large liquid structures entrained in the gas core. These will be further investigated for a wider range of conditions in chapter 5 at different axial distances from the injection for a longer pipe.

CHAPTER 5

BEHAVIOUR OF CHURN FLOW AND INSIGHTS INTO FLOW REGIME PHENOMENON

5.1. Introduction

The churn flow regime has been found to be the required flow regime for the coalescence of liquid structures entrained in the core in order to achieve downstream purity in the GLCC separator gas-leg. The fact is that the two-phase flow pattern present in offshore vertical risers is due to the conditions from the well-head. However, in most cases it is possible to divert the flow from the well-head into a particular riser or manifold of pipelines using a valve or T-junction.

At higher gas flowrates than the churn flow, the flow pattern present is annular flow. According to Hewitt and Hall-Taylor (1970), the annular flow pattern as discussed in chapter 2, is characterised by the presence of a thin liquid film flowing on the pipe wall and a continuous gas core flowing in the centre. Therefore, one may probably suggest operating within the annular flow regime since it is more stable than the churn flow regime. However, large liquid structures that exist in churn flow, which are easily separated in downstream GLCC separators are not present in annular flow.

Within the churn flow regime, two enduring phenomena are present, namely: liquid bridging of the gas core (liquid slugs) and huge waves. Both liquid slugs and huge waves have been observed by (Sekoguchi and Takeishi, 1989 and Sekoguchi and Mori, 1997). According to Sekoguchi and Takeishi (1989), the liquid slugs have the same nature and form as the liquid slugs in slug flow. The liquid slugs bridge the pipe cross section and travel almost equal to those present in slug flow. They suggested that huge waves are present when the gas core is fully formed. It has been termed huge waves because the waves have larger amplitudes compared to those in annular flow.

Therefore, it is in the remit of this work to study the behaviour of liquid slugs and huge waves, and where they occur more frequently along a vertical pipe. The experiments were carried out in the large scale closed loop facility described in chapter 3 having a vertical test section that is 127mm in internal diameter and 11m in length. Air and water were used as the operating fluids and the phase fraction data was acquired using high-resolution capacitance wire mesh sensor instrumentation. The sensor was placed at different locations to acquire void fraction data at these locations. In effect, the present study is based on churn flow development.

The experiments performed in chapter 4 established the conditions when typical churn flow occurs in large diameter pipes. It has paved way for in-depth churn flow studies to be conducted in this work. The gas and liquid superficial velocities ranged from $U_{gs} = 3.26\text{m/s}$ to 17.46m/s and $U_{ls} = 0.03\text{m/s}$ to 0.24m/s respectively, at an operating pressure of 1 barg. The full operational matrix is found in Appendix B. Since the experimental facility is a closed system, the gas superficial velocities at the respective liquid superficial velocity conditions are not exactly the same.

By carrying out churn flow development experiments in this work, this will provide further insights into the flow regime phenomenon and provide a fulcrum for the development of the CFC model in the subsequent chapter.

5.2. Results

The wire mesh sensor gives a three dimensional volume data from which further processing of the data reveals the inherent nature of the flow. The wire mesh sensor was placed at five locations from the injection, $L/D = 2.4, 7.1, 30.7, 35.4$ and 82.7 . In most cases, the analysis of data from two or three of the five locations will be presented, for instance, $L/D = 7.1, 35.4$ and 82.7 , as they represent bottom, middle and top of the test section respectively.

5.2.1. Time Series of void fraction

Figures 5.1(a), 5.1(b) and 5.2 show the variation of the void fraction with time using a moving average. The moving average is obtained by taking the average of sub-sets of the overall data set. The data was acquired at a frequency of 1000Hz and total time of 30s. This gives 30000 void fraction values from which 15 sub-sets of 2000 values from the total data set were extracted and averaged.

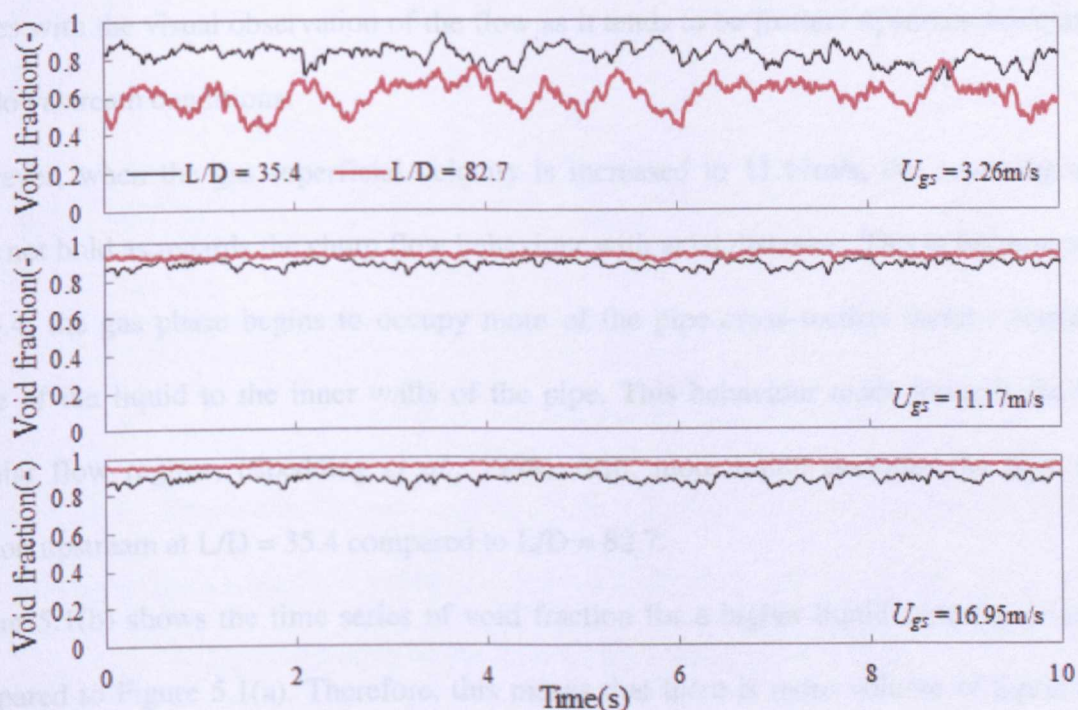


Figure 5.1(a). Time series of void fraction at $L/D = 35.4$ and 82.7 axial distance from the injection for a liquid superficial velocity of 0.03m/s .

The essence of applying this method is because the test section vibrated considerably due to the chaotic nature of the flow. Thus, the application of this method was to eliminate the background noise and effectively provide clarity in the presented time series data.

The Figure 5.1(a) gives the time series of void fraction comparing the data acquired at two axial distances from the injection. These are at $L/D = 35.4$ and 82.7 respectively for a liquid superficial velocity of 0.03m/s . When the gas superficial velocity is 3.26m/s , from visual

observation the behaviour has a clear-cut churning motion. Therefore, this results into the presence of fluctuations in time series of void fraction as shown above.

Also, at $L/D = 35.4$, the overall void fraction is higher compared to the void fraction downstream at $L/D = 82.7$. This is because at this condition, the gravitational forces from the liquid phase have a larger effect compared to the inertia forces from the gas phase. In other words, there is more liquid accumulation upstream than downstream for this condition. This agrees with the visual observation of the flow as it tends to be frothier upstream compared to the downstream conditions.

However, when the gas superficial velocity is increased to 11.17m/s, the reasoning above does not hold as regards the churn flow behaviour with axial distance. This is because at $L/D = 35.4$, the gas phase begins to occupy more of the pipe cross-section thereby restraining some of the liquid to the inner walls of the pipe. This behaviour tends towards the semi-annular flow regime, (Spedding *et al.*, 1998). Still, more liquid occupies the pipe cross-section upstream at $L/D = 35.4$ compared to $L/D = 82.7$.

Figure 5.1(b) shows the time series of void fraction for a higher liquid superficial velocity compared to Figure 5.1(a). Therefore, this means that there is more volume of liquid in the test section. As a result, the frequency of churning motion increases, which was also visually observed. For all three plots shown in Figure 5.1(b), when the gas superficial velocity is increased there is a near superimposition of void traces from the data acquired upstream and downstream of the test section.

At $L/D = 35.4$, it seems that it takes less time for the pipe cross-section to be occupied by the gas phase. On the other hand, the gas phase occupies the pipe cross-section for a longer period of time downstream at $L/D = 82.7$. It may probably be that the frequency of liquid bridging of the gas core decreases downstream when the liquid superficial velocity is increased beyond a critical liquid superficial velocity compared to that in Figure 5.1(a).

This occurrence is very apparent when the gas superficial velocity is increased to 13.39m/s in

Figure 5.1(b)

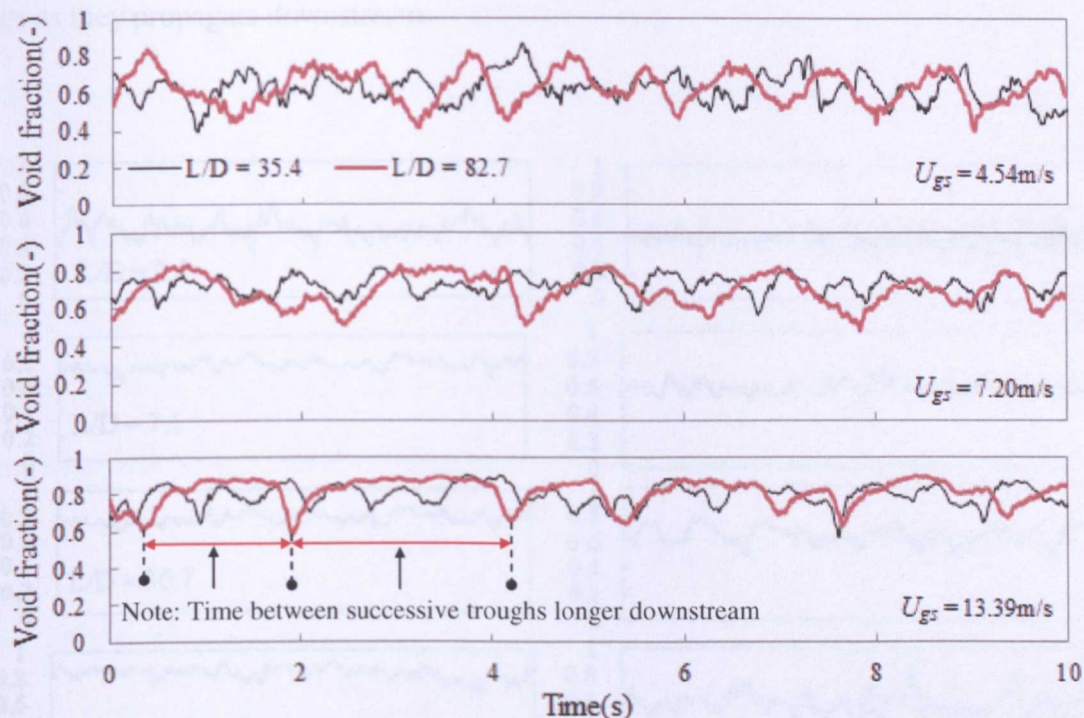


Figure 5.1(b). Time series of void fraction at $L/D = 35.4$ and 82.7 axial distance from the injection for a liquid superficial velocity of 0.24 m/s . The dash line represents the occurrence of liquid bridging or the time between successive troughs.

Furthermore, the time series of the void fraction at this condition shows that the gas occupies the pipe cross-section for a longer period of time before liquid bridging of the gas core takes place. As regards flow development, this condition means that the gas phase occupies the pipe cross-section for approximately twice the time it does upstream than downstream of the test section.

The time between successive troughs is longer downstream than upstream. This has also been indicated in Figure 5.1(b). This is a possible indication that *axial coalescence*¹ of huge waves occurs as they propagate downstream.

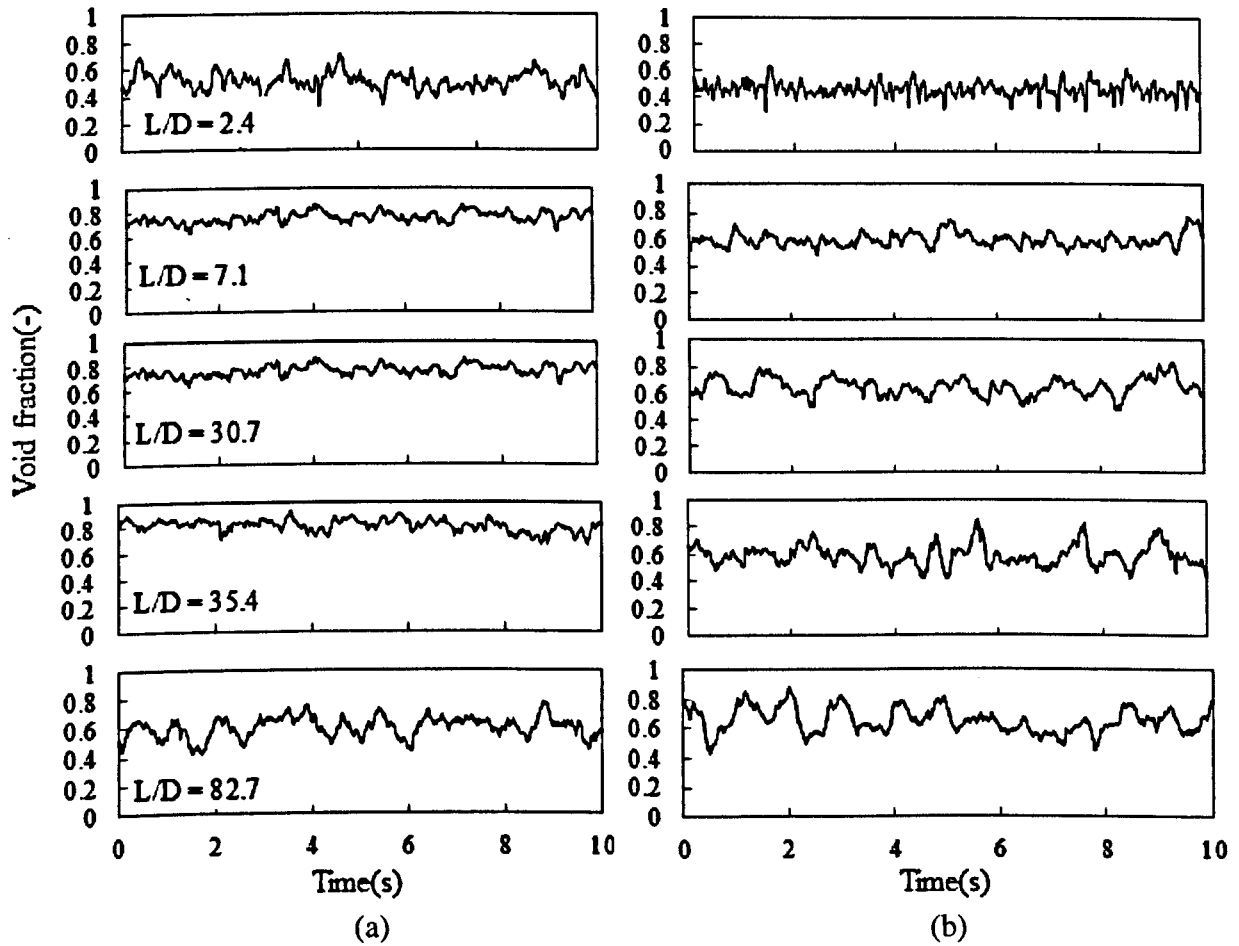


Figure 5.2. Time series of void fraction at each axial distance shown in the graph(left) from the injection point for constant superficial gas velocity $U_{gs} = 3.26\text{m/s}$ for (a) $U_{ls} = 0.03\text{m/s}$ (b)

$$U_{ls} = 0.24\text{m/s.}$$

The void fraction variation with time at each axial distance as shown in Figure 5.2 has a different behaviour at low liquid superficial velocity in Figure 5.2(a) than at high liquid

¹ Please note that *Radial coalescence* of huge waves has been identified in chapter 4, Figure 4.10(c) at $L/D = 35$ for the experiments in the 121mm internal diameter, 5.3 in length facility.

superficial velocity in Figure 5.2(b). Towards the bottom of test section, at $L/D = 2.4$, this is in close proximity to the injection point and as indicated in the time series of void fraction, there are more oscillations compared to downstream conditions due to turbulence. This turbulence is caused as a result of the injection of gas and liquid into the test section, which can be visually observed as vibrations close to the base of the test section.

In Figure 5.2(b), when the liquid superficial velocity increases to 0.24m/s, the void fraction is lower as the liquid holdup or the amount of liquid present increases. However, the inception of liquid bridging of the gas core begins to take effect at $L/D = 30.7$ and increases downstream which is typical of condition when the gas superficial velocity is low, in this case 3.26m/s.

5.2.2. Interfacial structures present

From the wire mesh sensor data, the interfacial structures present can be obtained. These interfacial structures have been presented in subsequent Figures in form of surface plots from post processing of the wire mesh sensor three dimensional data in MATLAB. From this data, surfaces can be made by patching and interfacial surfaces/structures can be distinguished.

In the Figures below, the dark blue patch represents liquid, light blue patch represents gas and the purple colour is the containing pipe. The method is applied to reveal the interfaces present for 5000 frames. Since the data was acquired at 1000Hz this represents a time scale of 5 seconds. An interval of 10 frames was used in this case thus a total number of 500 frames have been read and presented in the following Figures. The interfacial structures shown below are at dimensionless axial distances of $L/D = 7.1, 35.4$ and 82.7 respectively. These axial distances have been selected as they represent the bottom, middle and top of test section, hence an overall axial insight can be obtained. Further reference of the interfacial structures can be made to those obtained in chapter 4, section 4.2.5.

5.2.2.1. Interfacial structures at $L/D = 7.1$

Figures 5.3 – 5.5 shows the interfacial structures with increasing liquid superficial velocity close to the injection, at $L/D = 7.1$.

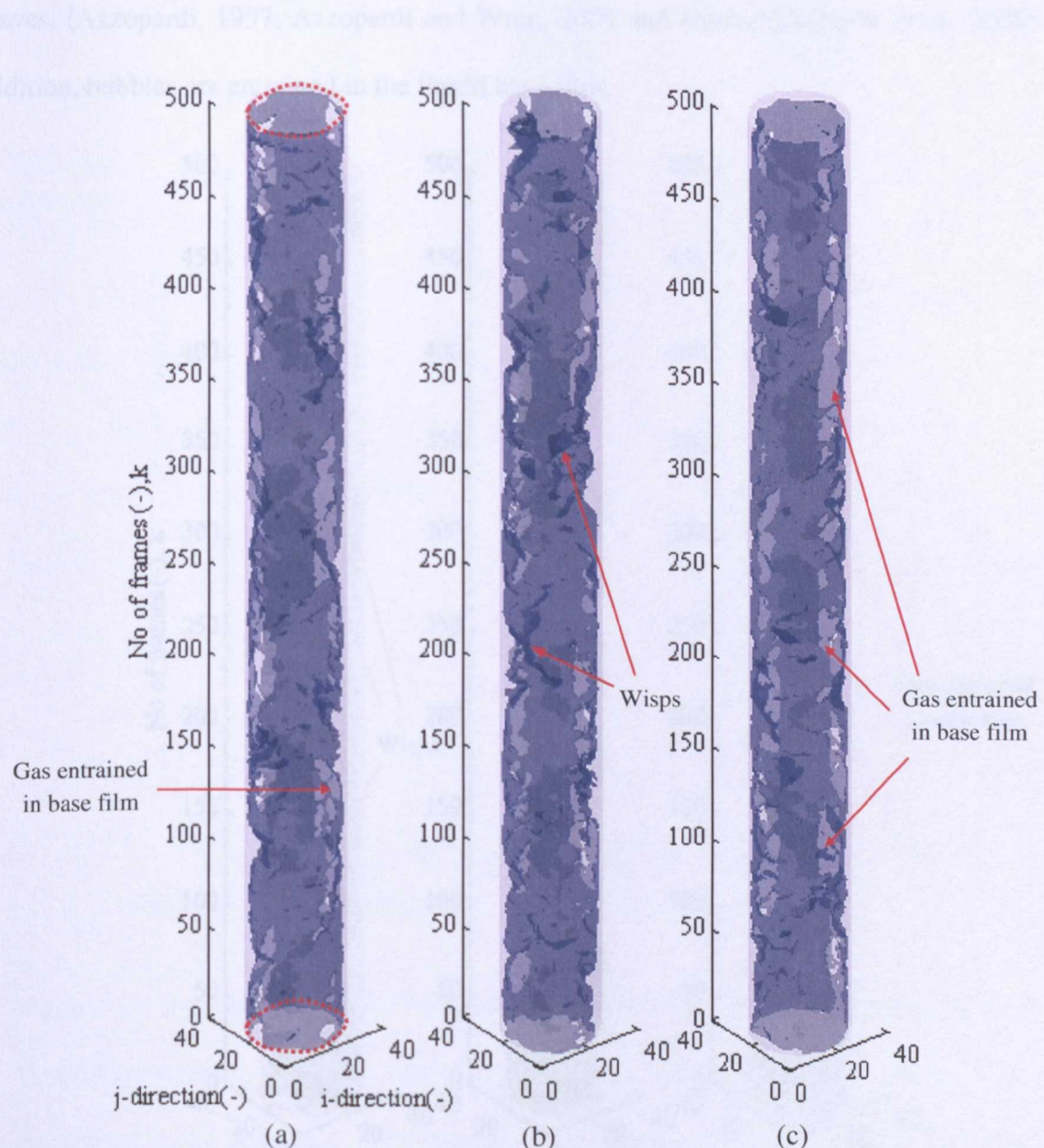


Figure 5.3. Interfacial structure of operating conditions at $L/D = 7.1$ for constant liquid superficial velocity of 0.03m/s , (a) $U_{gs} = 3.70\text{m/s}$ (b) 6.59m/s (c) 8.81m/s (Dark blue – suspended liquid, light blue – gas and purple – containing pipe) and the continuous phases were removed for clarity.

At a liquid superficial velocity of 0.03 m/s and at this axial distance from the injection, it shows that liquid bridging of the gas core does not occur. However, there is the formation of wisps similar to those observed in chapter 4, section 4.2.5, due to incomplete atomisation of waves, (Azzopardi, 1997, Azzopardi and Wren, 2004 and Hernandez-Perez *et al.*, 2010). In addition, bubbles are entrained in the liquid base film.

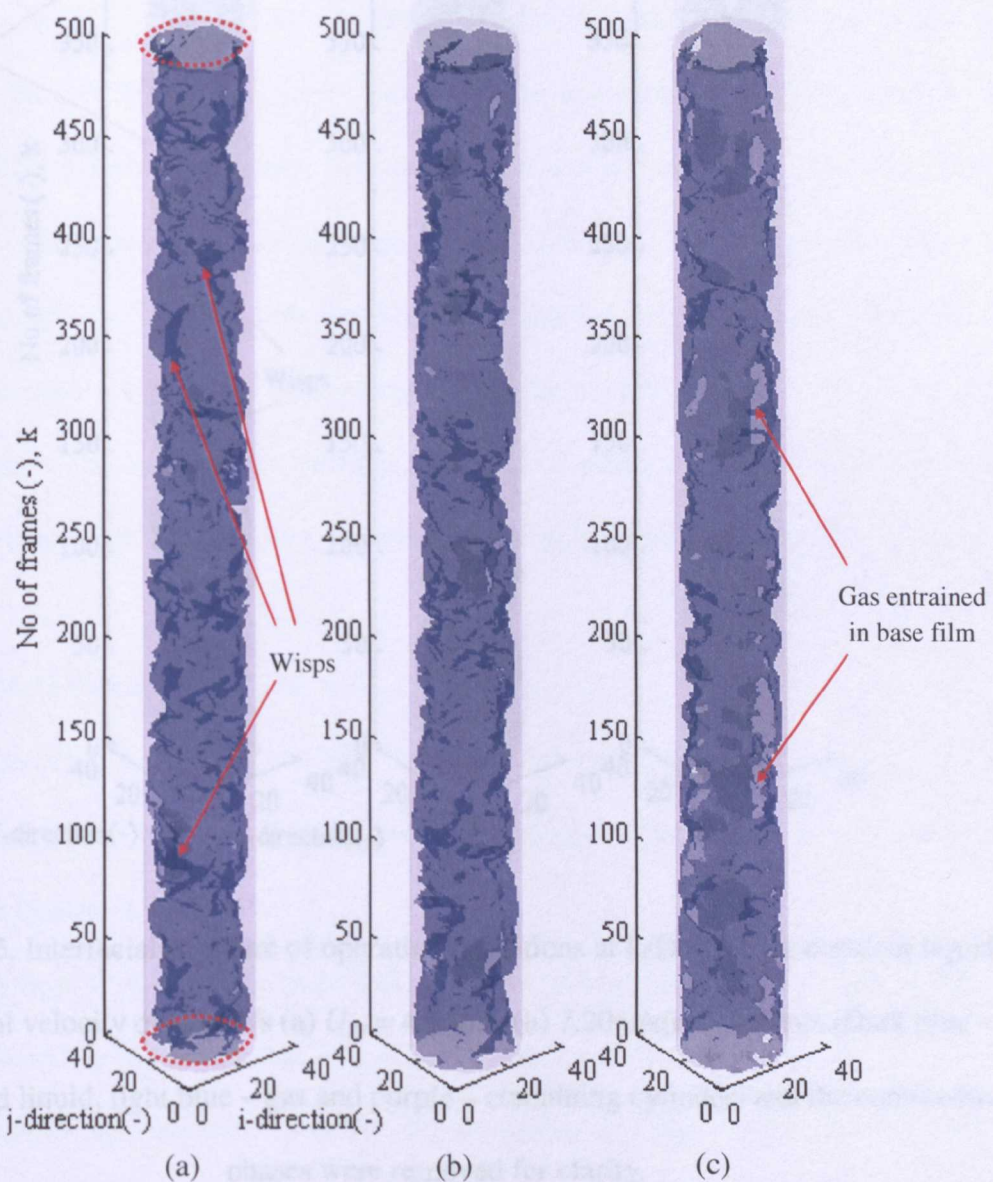


Figure 5.4. Interfacial structure of operating conditions at $L/D = 7.1$ for constant liquid superficial velocity of 0.13m/s (a) 5.28m/s (b) 7.08m/s(c) 10.58m/s. (Dark blue – suspended liquid, light blue – gas and purple – containing cylinder) and the continuous phases were removed for clarity.

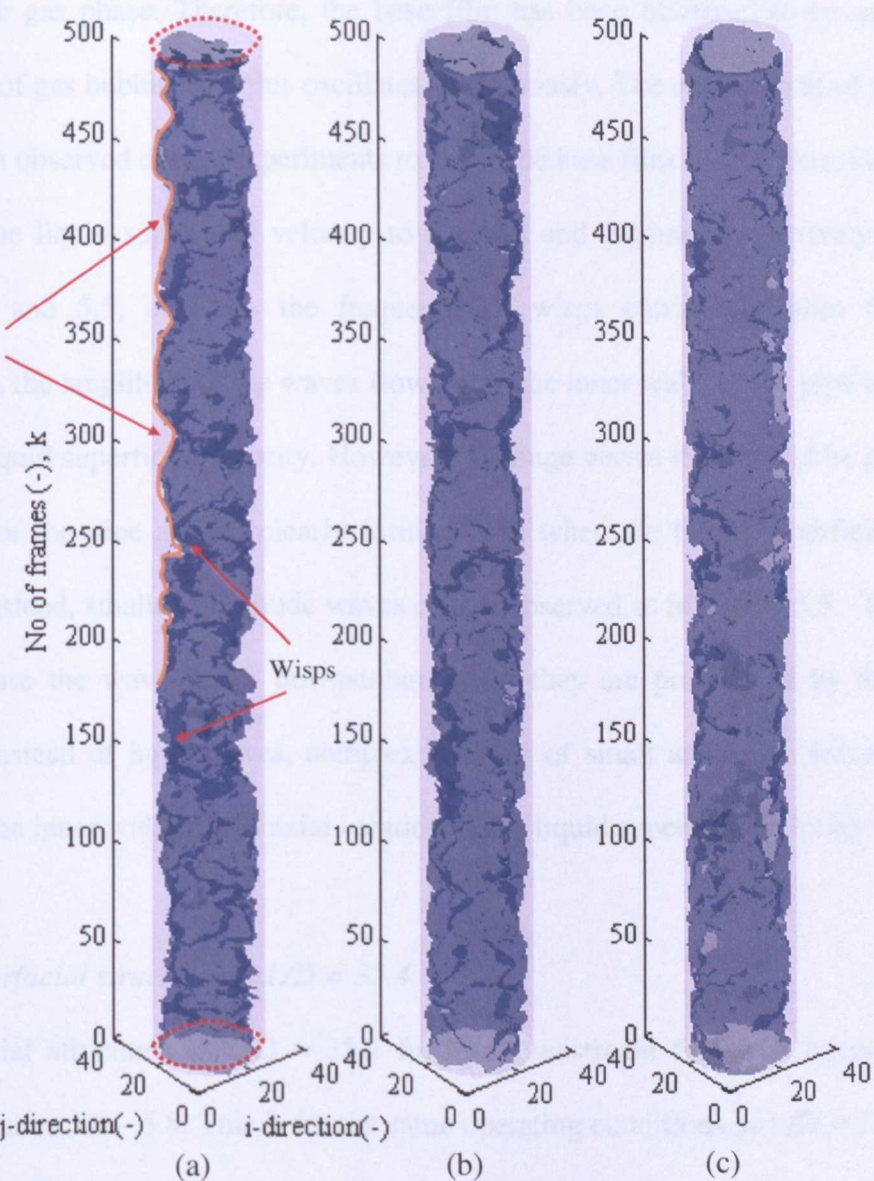


Figure 5.5. Interfacial structure of operating conditions at $L/D = 7.1$ for constant liquid superficial velocity of 0.24m/s (a) $U_{gs} = 4.54\text{m/s}$ (b) 7.20m/s (c) 11.42m/s (Dark blue – suspended liquid, light blue – gas and purple – containing cylinder) and the continuous phases were removed for clarity.

Entrainment occurs when the gas is forced into the liquid base film as a result of the high inertia of the gas phase. Therefore, the base film has been observed to be aerated due to entrainment of gas bubbles and this oscillates continuously. The entrainment of these bubbles has also been observed during experiments to cause the base film to flow downwards.

Increasing the liquid superficial velocity to 0.13m/s and 0.24m/s respectively as shown in Figures 5.4 and 5.5, increases the frequency of wisps entrained within the gas core. Furthermore, the amplitude of the waves flowing on the inner walls of the pipe increases with increasing liquid superficial velocity. However, the huge waves that should be present on the inner walls of the pipe are not clearly formed even when the liquid superficial velocity is increased. Instead, smaller amplitude waves can be observed as in Figure 5.5. The reason for this is because the waves grow downstream when they are propagated by the gas phase. Therefore, instead of huge waves, complex patterns of small amplitude waves are formed flowing on the inner walls at this axial location as the liquid superficial velocity increases.

5.2.2.2. Interfacial structures at L/D = 35.4

The interfacial structures at $L/D = 35.4$ further downstream from the injection has been shown in Figures 5.6 – 5.8. This is for the same operating conditions as $L/D = 7.1$, and also at $L/D = 82.7$ in Figures 5.9 – 5.11.

In Figure 5.6(a), it shows that there are bubbles entrained in the base film. The presence of bubbles entrained in the base film increases as the gas superficial velocity increases in subsequent interfacial structures. However, the frequency of wisps within the core decreases at this operating condition and at this axial distance from the injection. It also shows that at low liquid superficial velocity, the pipe cross-section begins to be properly occupied by the gas phase indicative of flow development.

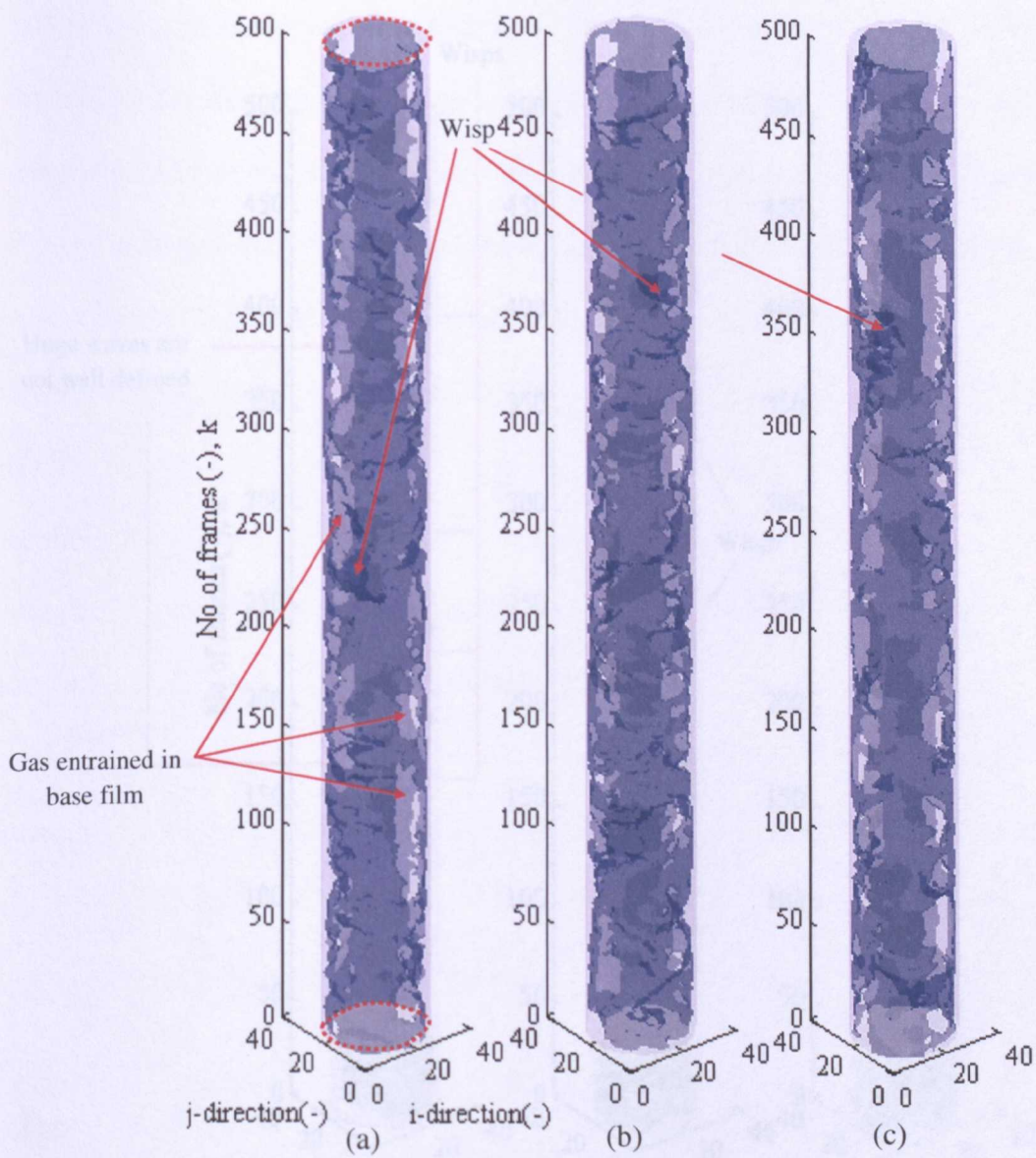


Figure 5.6. Interfacial structure of operating conditions at $L/D = 35.4$ for constant liquid superficial velocity of 0.03m/s (a) 3.70m/s (b) 6.59m/s (c) 8.81m/s (Dark blue – suspended liquid, light blue – gas and purple – containing cylinder) and the continuous phases were removed for clarity.

When the liquid superficial velocity is sufficient as in Figure 5.7, liquid entrainment of the gas

is not well defined and the entrainment of bubbles is dominant. The

further increase in liquid superficial velocity leads to the formation of

large-scale structures such as wisps and waves.

The interfacial structure at different liquid superficial velocities is shown in Figure 5.7.

Huge waves are
not well defined

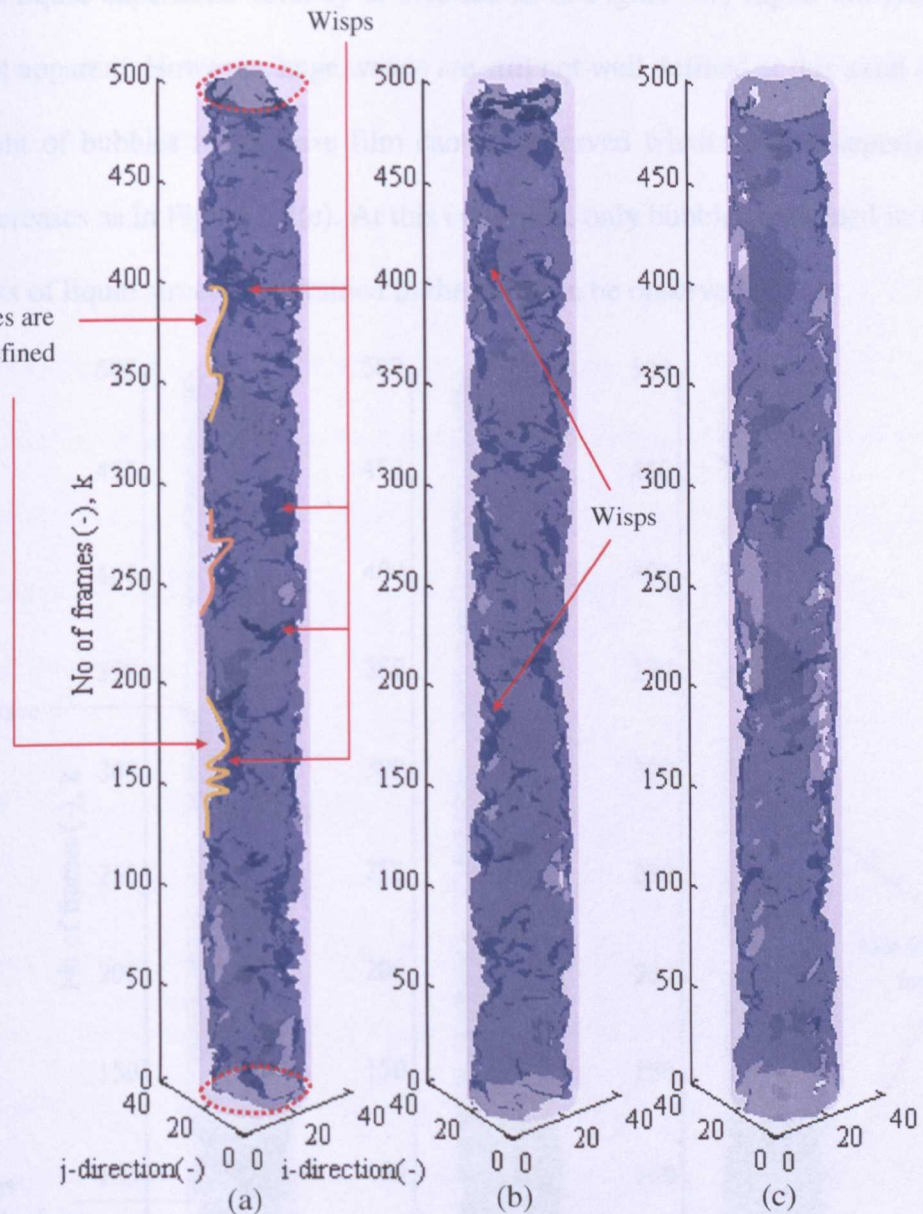


Figure 5.7. Interfacial structure of operating conditions at $L/D = 35.4$ for constant liquid superficial velocity of 0.13m/s (a) 5.28m/s (b) 7.08m/s (c) 10.58m/s (Dark blue – suspended liquid, light blue – gas and purple – containing cylinder) and the continuous phases were removed for clarity. Outline of huge waves indicated in red.

When the liquid superficial velocity is 0.13m/s as in Figure 5.7, liquid bridging of the gas core is not apparent. However, huge waves are still not well defined at this axial location. The entrainment of bubbles in the base film can be observed when the gas superficial velocity further increases as in Figure 5.7(c). At this condition, only bubbles entrained in the base film and streaks of liquid structure entrained in the core can be observed.

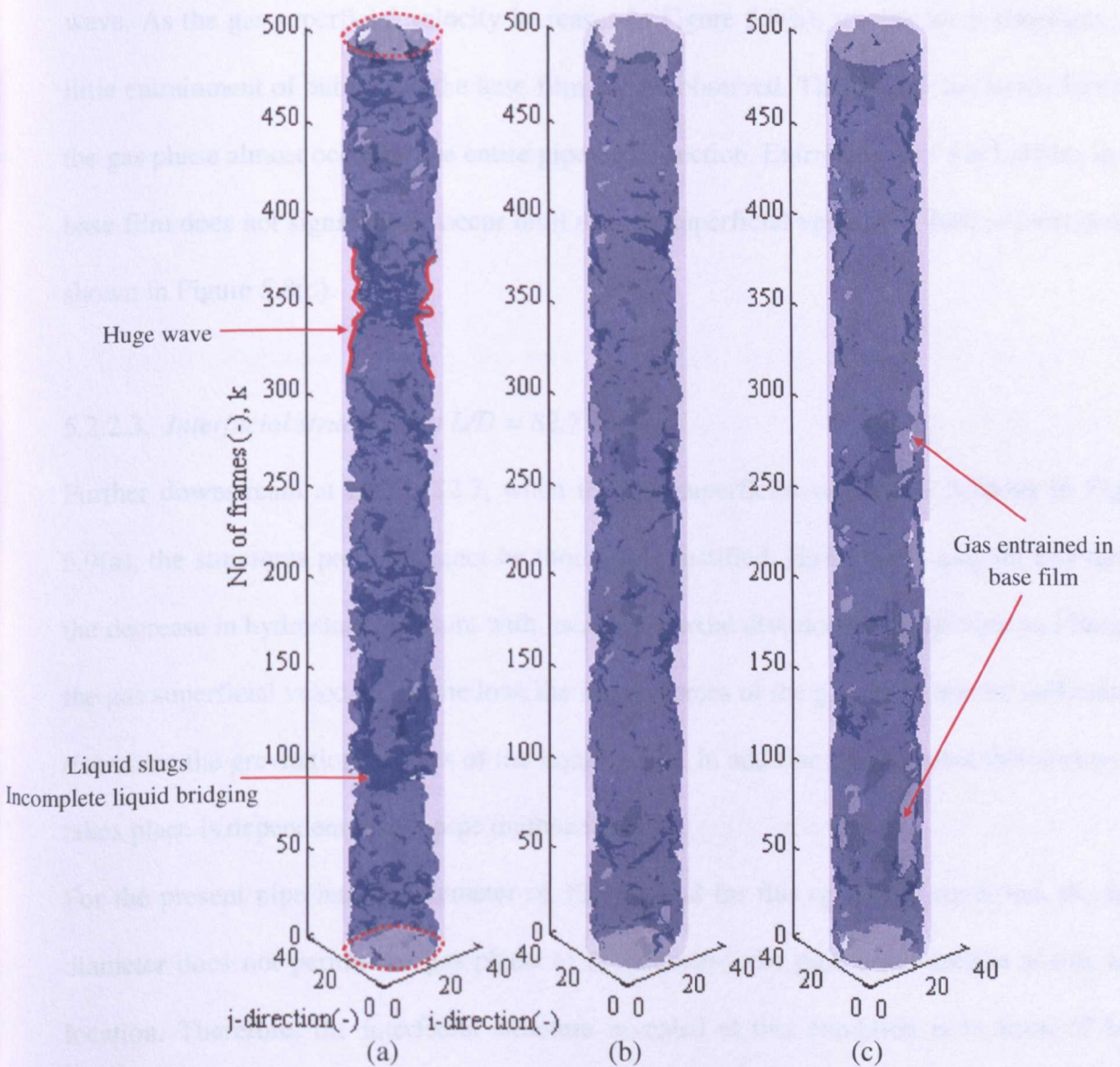


Figure 5.8. Interfacial structure of operating conditions at $L/D = 35.4$ for constant liquid superficial velocity of 0.24m/s (a) 4.54m/s (b) 7.20m/s(c) 11.42m/s. (Dark blue – suspended liquid, light blue – gas and purple – containing cylinder) and the continuous phases were removed for clarity.

When the liquid superficial velocity is increased to 0.24m/s as in Figure 5.8(a), complete liquid bridging as a result of radial coalescence of huge waves occurs to form what may be a section of liquid slug. From the visual observation at this condition, the liquid slug is characterised as small diameter bubbles entrained in the liquid and they have a frothy nature. In addition, the interfacial structure in frame 300 of Figure 5.8(a) may be classified as a huge wave. As the gas superficial velocity increases in Figure 5.8(b), smaller wisp structures and little entrainment of bubbles in the base film can be observed. This is still due to the fact that the gas phase almost occupies the entire pipe cross-section. Entrainment of gas bubbles in the base film does not significantly occur until the gas superficial velocity is further increased as shown in Figure 5.8(c).

5.2.2.3. *Interfacial structures at L/D = 82.7*

Further downstream at $L/D = 82.7$, when the gas superficial velocity is 3.70m/s in Figure 5.9(a), the structures present cannot be thoroughly justified. However, it may be that due to the decrease in hydrostatic pressure with increase in axial distance from injection and because the gas superficial velocity is quite low, the inertia forces of the gas phase are not sufficient to overcome the gravitational forces of the liquid phase. In addition, the fact that this occurrence takes place is dependent on the pipe diameter.

For the present pipe internal diameter of 127mm and for this operating condition, the large diameter does not permit the gas phase to fully occupy the pipe cross-section at this axial location. Therefore, the interfacial structure revealed at this condition is in form of large liquid structures that occupy the entire pipe cross-section as observed in Figure 5.9(a).

The reason behind this argument is because for the same condition and almost the same length of pipe of 9.5m, Sekoguchi and Takeishi (1989) have not reported the occurrence of this sort of structures in their experiments in a smaller pipe diameter of 25.8mm. Further references can be made to their work or as discussed in section 2.4.3 in chapter 2.

When the gas superficial velocity is increased as shown in Figure 5.9 (b), there is mostly the formation of wisps as well as bubbles entrained in the base film. In Figure 5.9(c), wisps and long segments of gas can be observed on the wall of the pipe. The long segments of gas are different from when the pipe walls have entrained bubbles in the liquid base film. This is because the segment on the wall will be shorter such as in Figure 5.9(b). However, as observed visually, it is possible to have a situation where there are bubbles entrained in the liquid film on the wall as well as “dry patches”. From visual observation, the latter is when there is an absence of liquid on the inner walls of the pipe occurring momentarily. This should be expected at the walls when examining the interfacial structure for annular flow regime.

In terms of the precedence of which comes before the other, that is, base film with entrained gas bubble or “dry patch”, this depends on the gas and liquid superficial velocities. Generally, a single phase liquid will flow quickly downwards under gravity. This will effectively have a higher velocity than gas bubbles entrained in the base film flowing downwards. When gas bubbles are entrained in the base film and flowing downwards, this will experience an opposite buoyancy force. The bubbles entrained in the base film at the walls behave like those in bubbly flow, (Barnea, 1986). Therefore, the presence of gas bubbles reduces the downward base film velocity. Also the non-drag lift force, which has a radial resultant force towards the core of the pipe, will affect the velocity of the downward moving base film.

In Figure 5.10, these show the interfacial structures when the liquid superficial velocity is increased to 0.13m/s at respective gas superficial velocities. In Figure 5.10(a), larger liquid structures entrained in the gas core can be observed at higher frequencies compared to the interfacial structures obtained upstream for the same condition.

As earlier stated, they are formed due to the radial coalescence of the huge wave structure. When the gas superficial velocity is increased in Figure 5.10(b), the frequency of these entrained liquid structures decreases compared to Figure 5.10(a). Furthermore, there is the

presence of wisps within the core and bubbles entrained in the base film. Huge waves cannot be observed in Figure 5.10(c) but entrained bubbles in the liquid base film. However, increasing the liquid superficial velocity to 0.24m/s as in Figure 5.11(a) increases the appearance frequency of huge waves. As the gas superficial velocity increases, the dominant occurrence is the entrainment of bubbles in the base film.

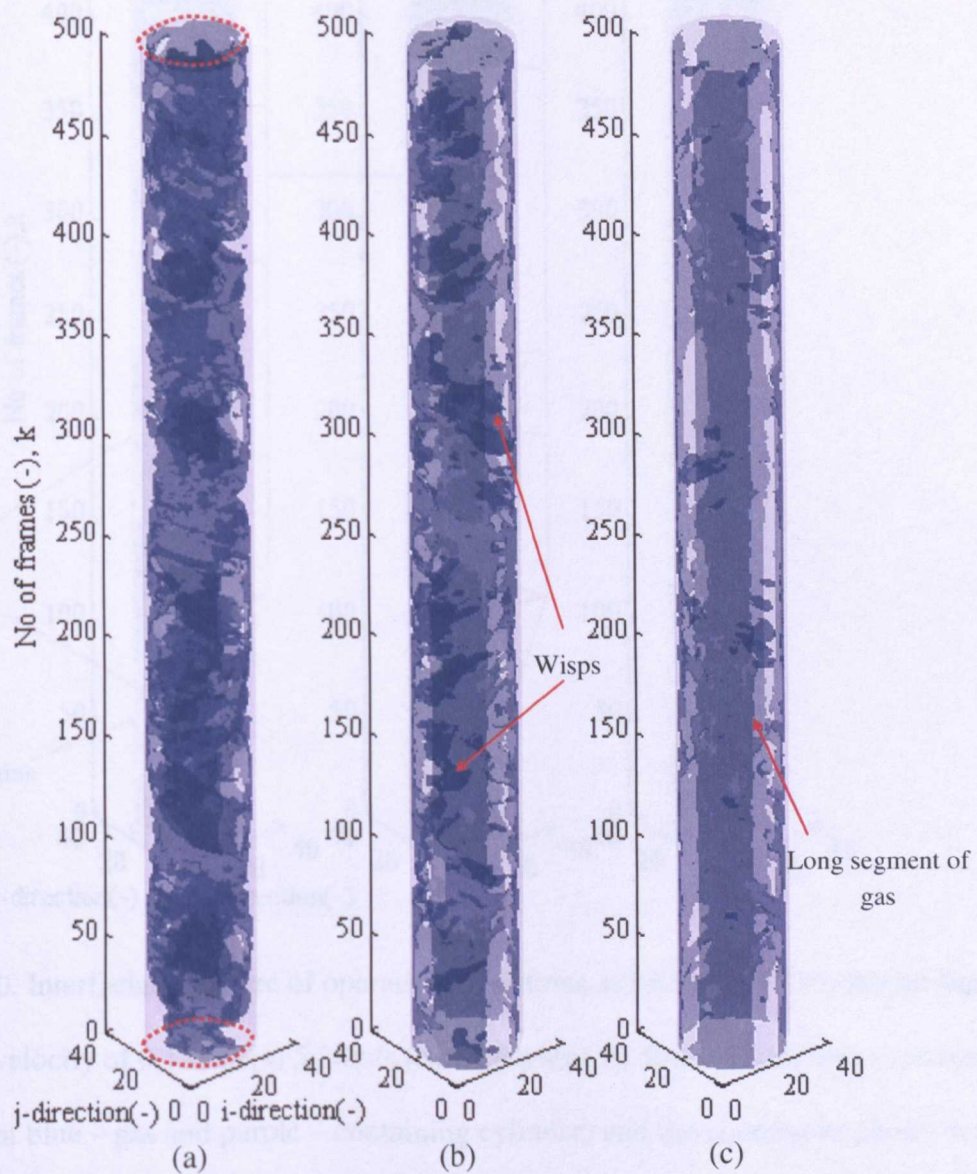


Figure 5.9. Interfacial structure of operating conditions at $L/D = 82.7$ for constant liquid superficial velocity of 0.03m/s (a) 3.70m/s (b) 6.59m/s (c) 8.81m/s (Dark blue – suspended liquid, light blue – gas and purple – containing cylinder) and the continuous phases were removed for clarity.

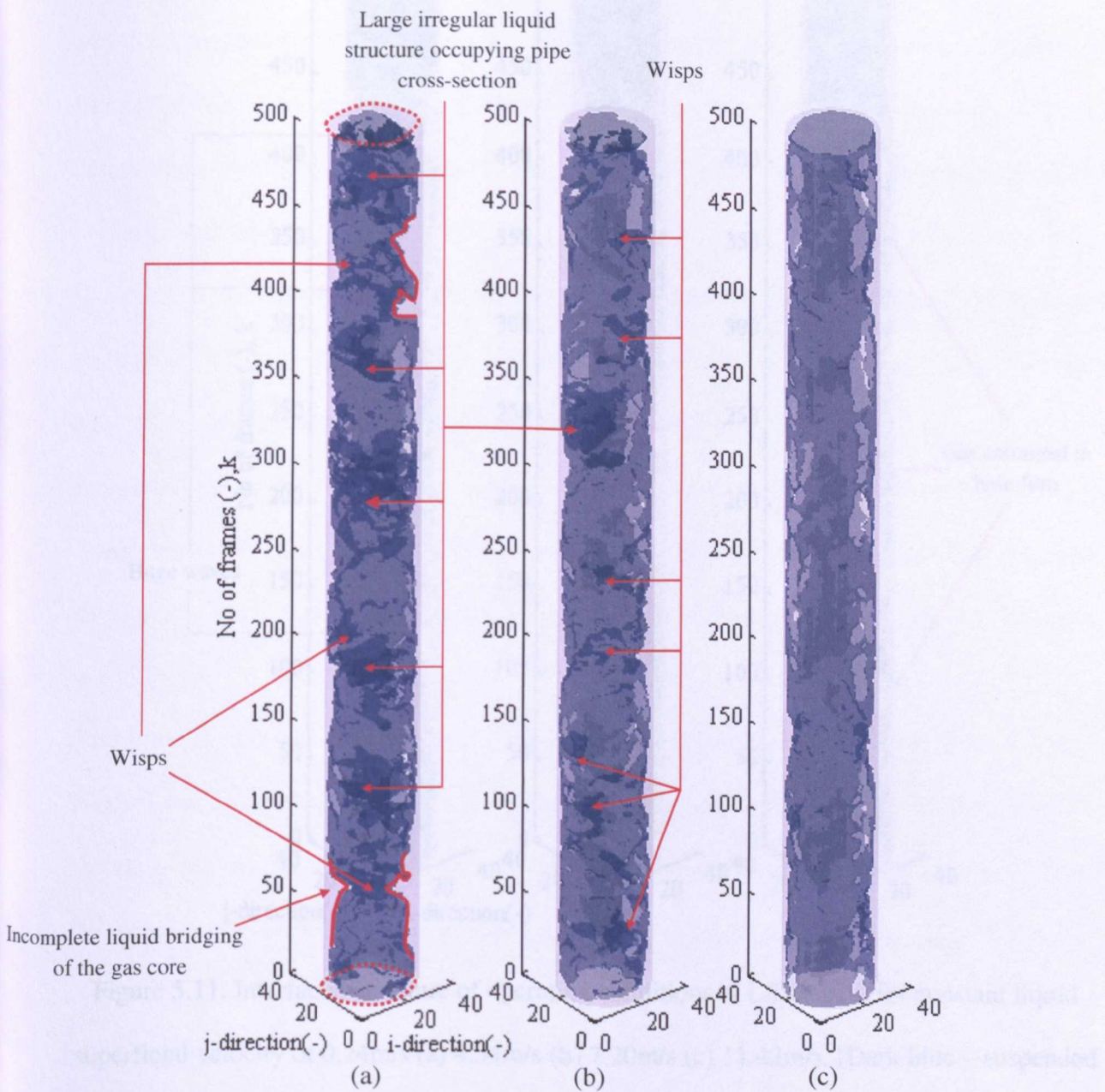


Figure 5.10. Interfacial structure of operating conditions at $L/D = 82.7$ for constant liquid

superficial velocity of 0.13m/s (a) 5.28m/s (b) 7.08m/s (c) 10.58m/s (Dark blue – suspended

liquid, light blue – gas and purple – containing cylinder) and the continuous phases were

removed for clarity.

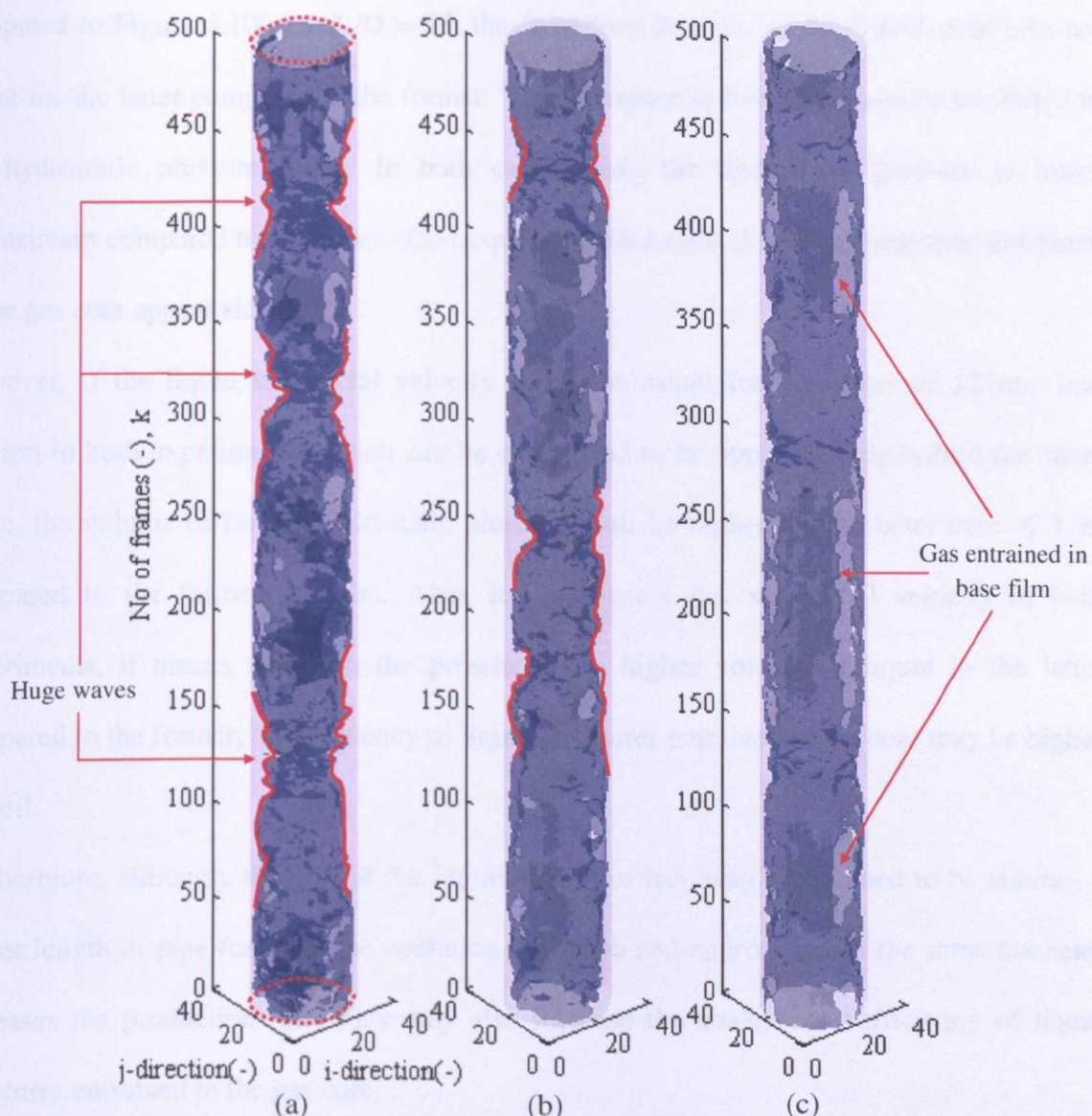


Figure 5.11. Interfacial structure of operating conditions at $L/D = 82.7$ for constant liquid superficial velocity of 0.24m/s (a) 4.54m/s (b) 7.20m/s (c) 11.42m/s . (Dark blue – suspended liquid, light blue – gas and purple – containing cylinder) and the continuous phases were removed for clarity.

also been shown in Figure 5.12 as time evolution of droplets and huge waves in (a). From the interfacial structures presented above, it can be said that the frequency of huge waves and liquid structures entrained in the gas core increases downstream. In comparison to the interfacial structures obtained for the 121mm internal diameter experiments at $L/D = 35$, in reference to Figure 4.10(c), it shows that the large liquid structures entrained in the gas core have the same size as in the present study at $L/D = 82.7$. Also, when comparisons are made to the liquid structures entrained in the gas core for the present study at $L/D = 35.4$

compared to Figure 4.10(c) at L/D = 35, the frequency and size of the liquid structures are larger for the latter compared to the former. The difference in both cases can be attributed to the hydrostatic pressure effect. In both experiments the hydrostatic pressure is lower downstream compared to upstream. Consequently, this makes the liquid structures entrained in the gas core appear similar.

However, if the liquid superficial velocity is kept constant for diameters of 121mm and 127mm in both experiments, which can be considered to be approximately within the same range, the volume of liquid (hydrostatic pressure) will be higher for the latter case of 11m compared to the former of 5.3m. Also, for a constant gas superficial velocity in both experiments, it means that with the presence of a higher volume of liquid in the latter compared to the former, the frequency of liquid structures entrained in the core may be higher as well.

Furthermore, although, the size of the liquid structures has been ascertained to be similar, a longer length of pipe for the same operating condition and approximately the same diameter increases the production rate. This may also increase the coalescence efficiency of liquid structures entrained in the gas core.

5.2.3. Qualitative assessment on the cross section phase distribution

Similar to the work of Sekoguchi and Takeishi (1989) shown in Figure 2.27, the behaviour or stability of the interfacial structures per number of frames can also be elucidated. This has also been shown in Figure 5.12 as cross sectional phase distribution with huge waves in (a) and liquid slugs in (b). The frames were selected just to distinguish between the phenomena present.

In corroboration with Sekoguchi and Takeishi (1989), huge waves are formed when the gas phase occupies most of the pipe cross-section. As shown in Figure 5.12(a) and (b), huge

waves have a higher transit velocity than liquid slugs based on the number of frames before the inception of the liquid slugs.

When liquid slugs occur, the gas phase becomes entrained in liquid, thereby forming clusters of closely packed bubbles of various sizes within the liquid mass as shown especially in frame 895. This has been presented to clarify the sub-regimes within the churn flow pattern.

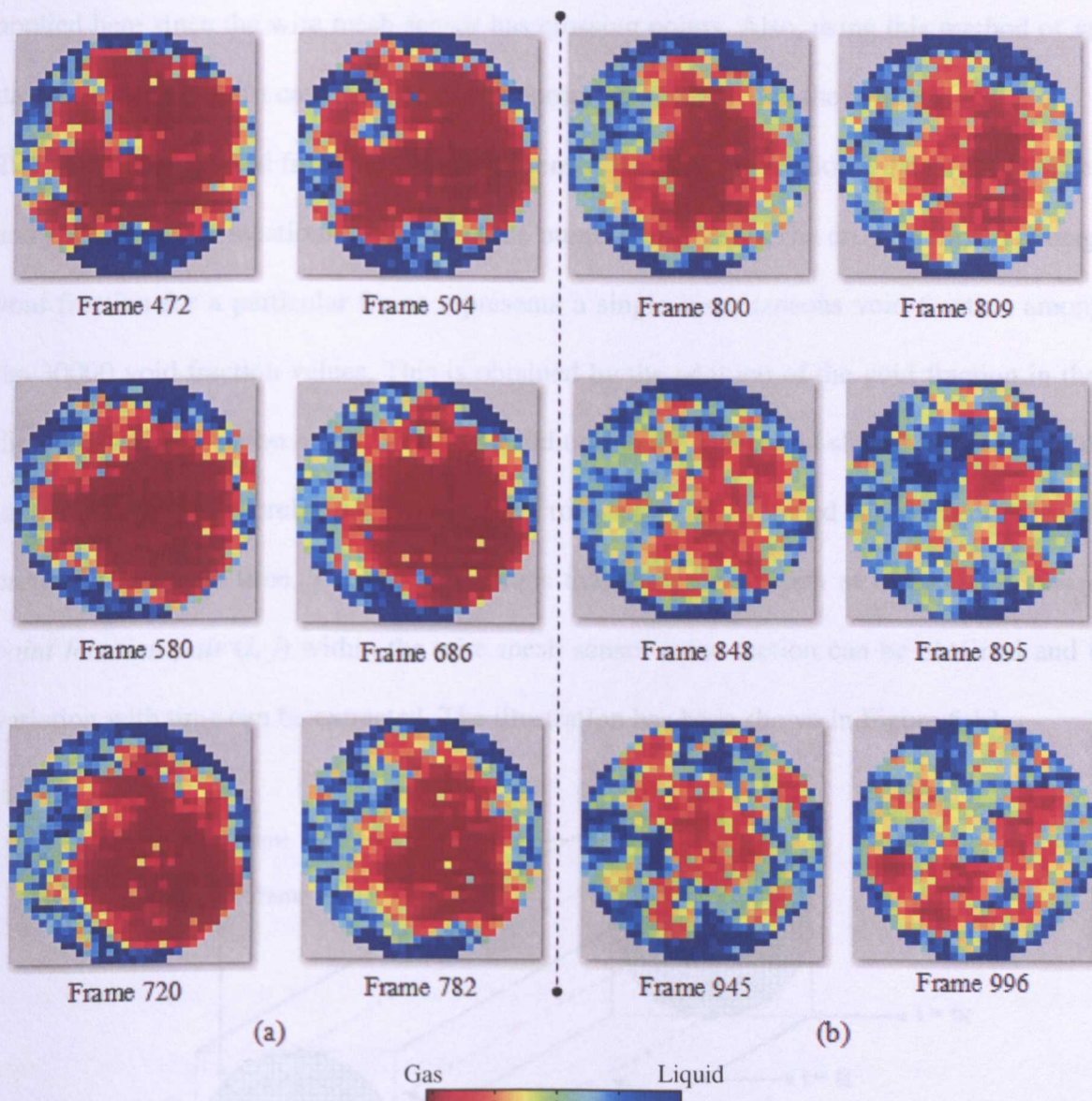


Figure 5.12. Stability of Huge waves and Liquid slugs within pipe cross-section in (a) and (b) respectively. Selected frame were extracted from the data at $L/D = 35.4$.

5.2.4. Extraction of chordal data

There are two methods of distinguishing the interfacial structures above obtained from the time series data. The widely used approach method is by applying a void fraction threshold to the time series data and identifying the relevant structures. However, a more interesting method is to extract the chordal void fraction data or point values. The latter method has been applied here since the wire mesh sensor has crossing points. Also, using this method of void data extraction in most cases can be more appropriate compared to the former. The void data obtained from the wire mesh sensor is a three dimensional data, (i, j, k) . The (i, j) are the wire locations while (k) is the number of frames. The cross-sectional averaged void fraction for a particular frame represents a single instantaneous void fraction amongst the 30000 void fraction values. This is obtained by the addition of the void fraction in the i -direction and j -direction respectively. The addition in the i -direction should be similar to that in the j -direction, thereby confirming the cross-sectional averaged void fraction for that particular frame or time. Therefore, it means that the void fraction at a particular *crossing point location pair* (i, j) within the wire mesh sensor cross-section can be obtained and the variation with time can be extracted. The illustration has been shown in Figure 5.13.

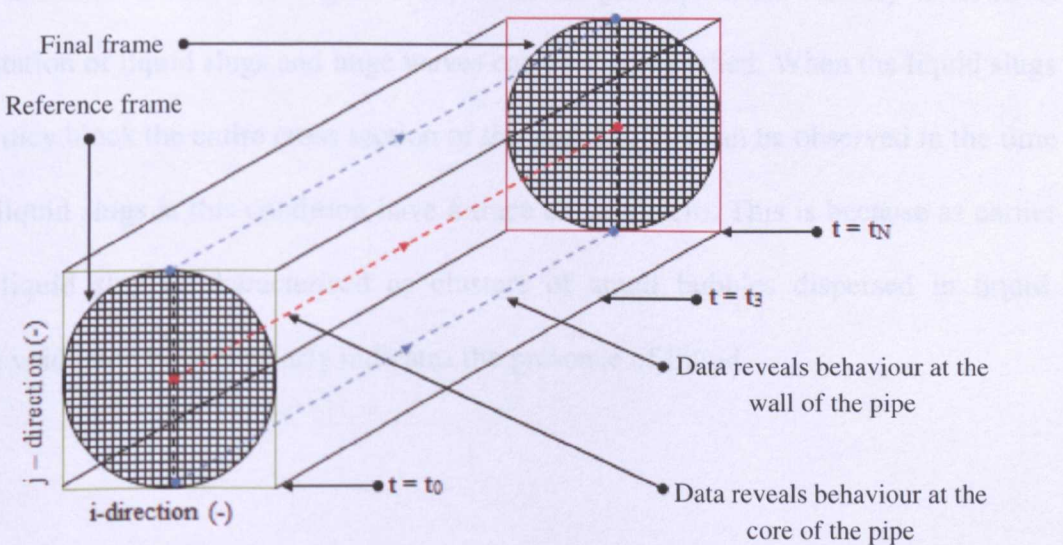


Figure 5.13. Illustration of chordal void fraction extraction from wire mesh sensor data.

It is important to note that the void fraction at a particular crossing point location or point values has a lower value than the overall cross-sectional void fraction and also the time averaged void fraction in comparison to Figures 5.1 and 5.2.

In Figures 5.14 and 5.15, it shows the extracted void fraction time series data for gas superficial velocities of 4.54m/s, 5.76m/s 7.20m/s, 8.11m/s and 11.42m/s respectively at constant liquid superficial velocity of 0.24m/s. The data was extracted at location $i = 16$ and $j = 16$ (centre location) with reference to the cross sectional illustration shown on the right of both plots. This is shown for the data acquired at $L/D = 7.1$ and 35.4 in Figures 5.14 and 5.15 respectively.

In Figure 5.14, the interfacial structures on the left hand side of the time series plots show the presence of wisps structures and the corresponding time series plot gives peaks that tend towards zero. It is important to note that the presence of dense peaks in the chordal time series data is because of the different sizes of wisp structures present. These are formed due to the fact that the flow is very unstable close to the injection. In general, there is a high entrainment of liquid structures within the gas core but the liquid structures formed are not large enough to occupy the entire pipe cross-section.

Further downstream, as shown in Figure 5.15, when the gas superficial velocity is 4.54m/s, the representation of liquid slugs and huge waves can be distinguished. When the liquid slugs are present, they block the entire cross section of the pipe and this can be observed in the time series. The liquid slugs at this condition have a trace close to zero. This is because as earlier stated, the liquid slug is characterised as clusters of small bubbles dispersed in liquid. Therefore, a void trace of zero clearly indicates the presence of liquid.

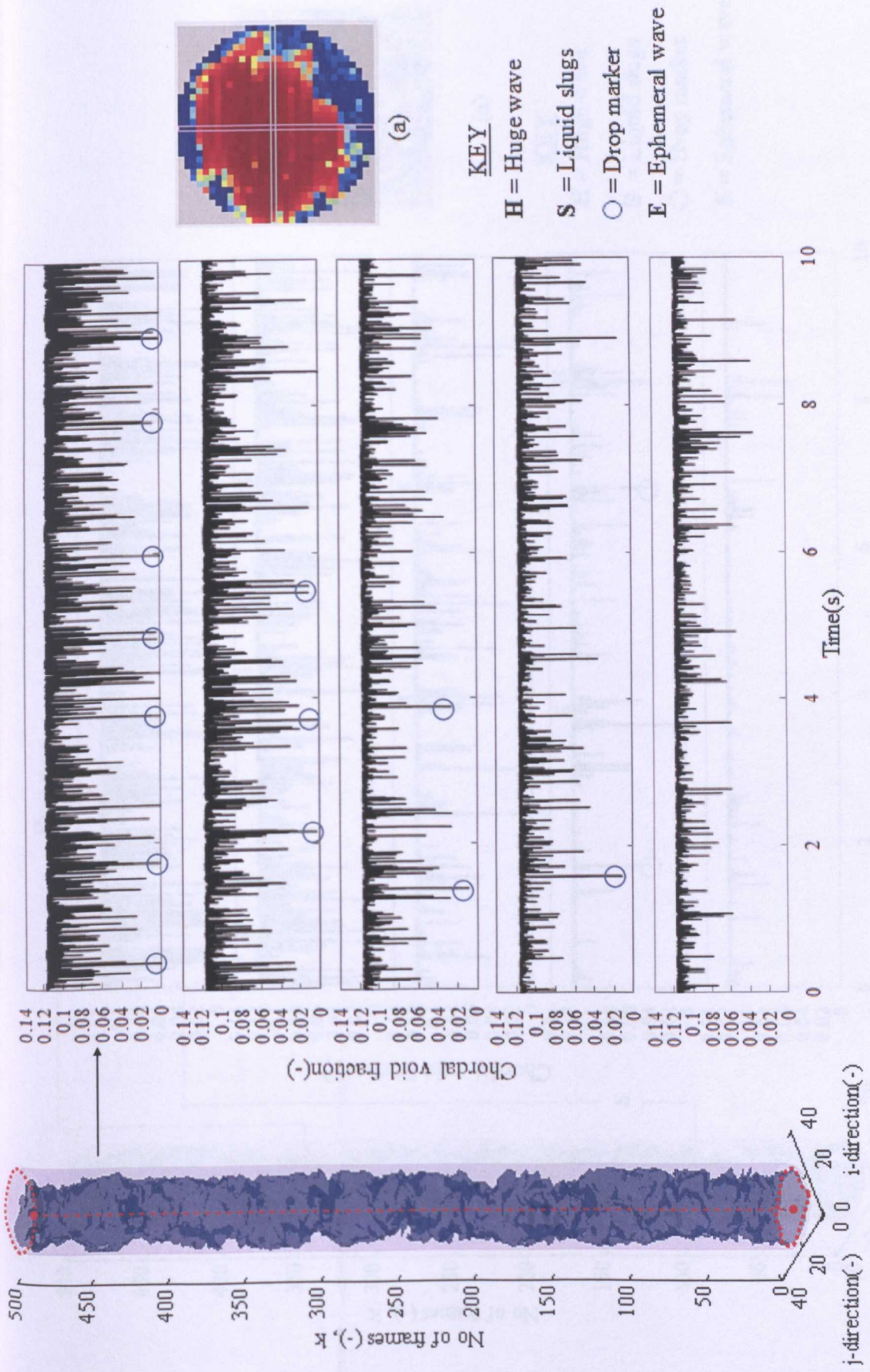


Figure 5.14. Time series of chordal void fraction at $L/D = 7.1$ (a) $X = 16$, $Y = 16$, (b) and (c) represent interfacial structures for a constant liquid superficial velocity of 0.24m/s and for gas superficial velocities of 4.54m/s, 5.76m/s, 7.20m/s, 8.11m/s and 11.42m/s from top to bottom respectively.

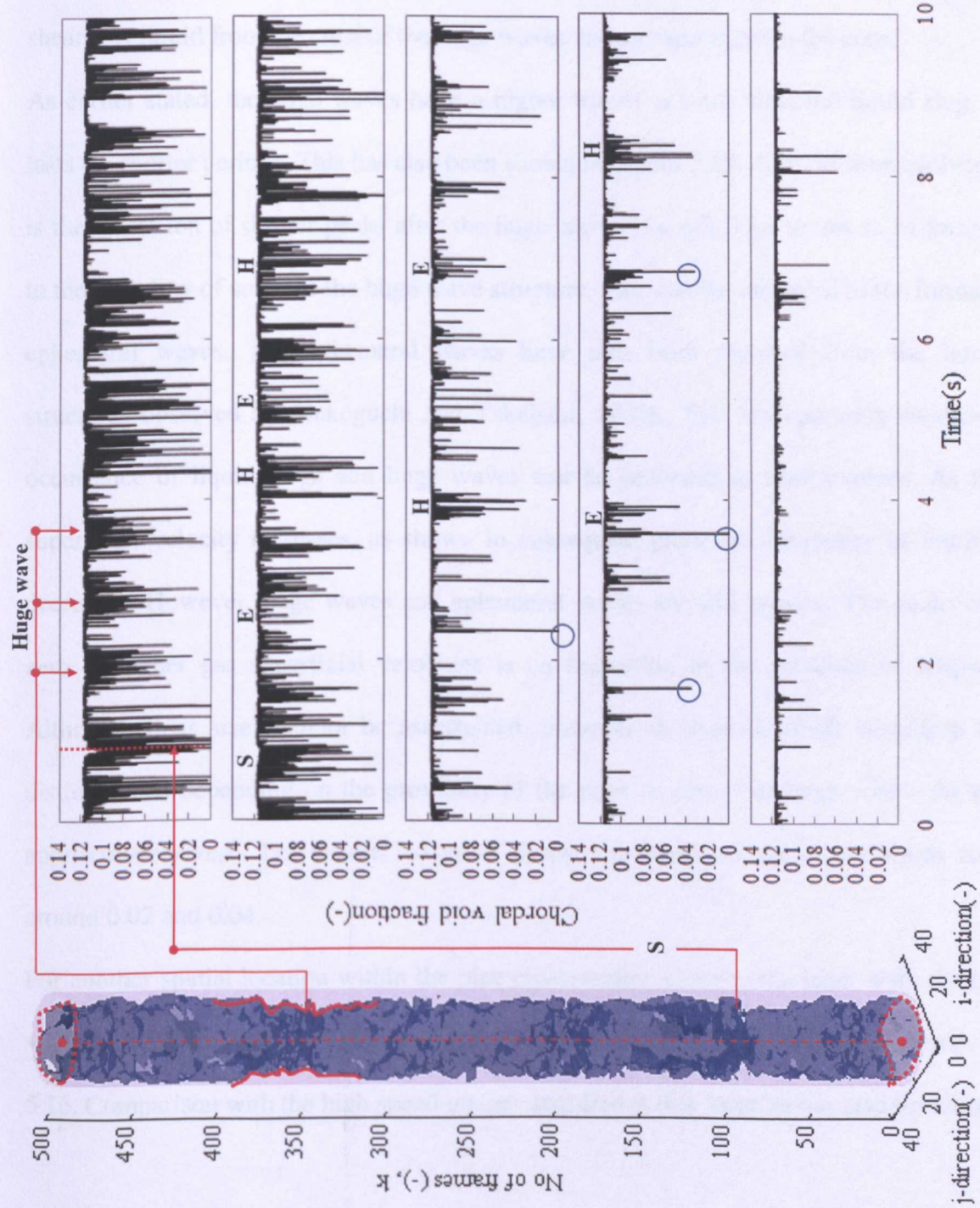
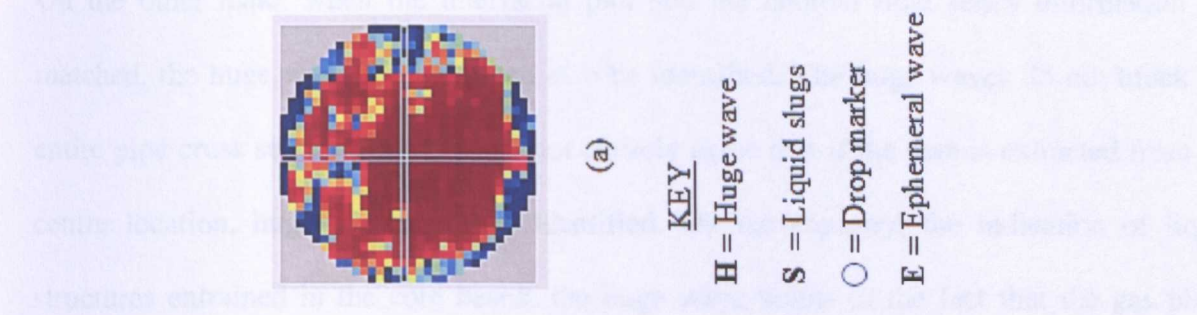


Figure 5.15. Time series of chordal void fraction at $L/D = 35.4$ (a) $X = 16$, $Y = 16$, (b) and(c) represent interfacial structures for a constant liquid superficial velocity of 0.24m/s and for gas superficial velocities of 4.54m/s , 5.76m/s , 7.20m/s , 8.11m/s and 11.42m/s from top to bottom respectively.

On the other hand, when the interfacial plot and the chordal time series information are matched, the huge wave signature can also be identified. The huge waves do not block the entire pipe cross section and one may not entirely agree that if the data is extracted from the centre location, huge waves can be identified. On the contrary, the indication of liquid structures entrained in the core beside the huge wave points to the fact that the gas phase shears off liquid from the crest of the huge waves and entrains them in the core.

As earlier stated, the huge waves have a higher transit velocity than the liquid slug, which lasts for shorter periods. This has also been shown in Figure 5.15. Also, as time evolves, there is the formation of shorter peaks after the huge waves ($t = 4\text{s}$). This seems to be formed due to the shedding of some of the huge wave structure. This can be attributed to the formation of ephemeral waves. The ephemeral waves have also been reported from the interfacial structures observed by (Sekoguchi and Takeishihi, 1989). For this operating condition, the occurrence of liquid slugs and huge waves can be observed as time evolves. As the gas superficial velocity increases, as shown in subsequent plots, the frequency of liquid slugs decreases. However, huge waves and ephemeral waves are still present. The peaks close to zero at higher gas superficial velocities is an indication of the presence of wisps/drops. Although, their sizes cannot be ascertained, however, a large or small wisp/drop can be distinguished depending on the proximity of the peak to zero. For large wisps, the peak is approximately zero. For smaller wisps or drops, the peaks do not tend towards zero but around 0.02 and 0.04.

For another spatial location within the pipe cross-section close to the inner wall, the chordal void fraction data was also extracted from the data acquired at $L/D = 82.7$ as shown in Figure 5.16. Comparison with the high speed images acquired at this location has also been made.

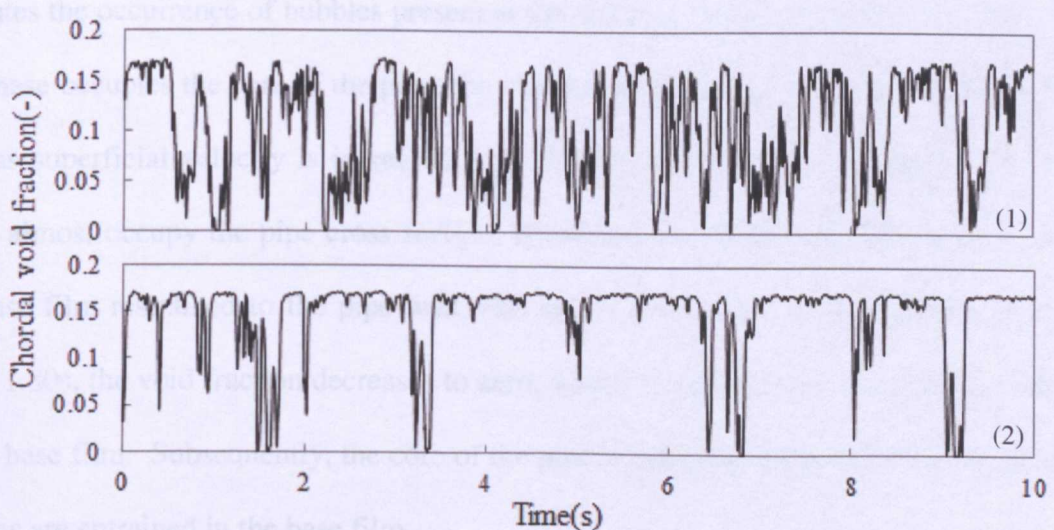
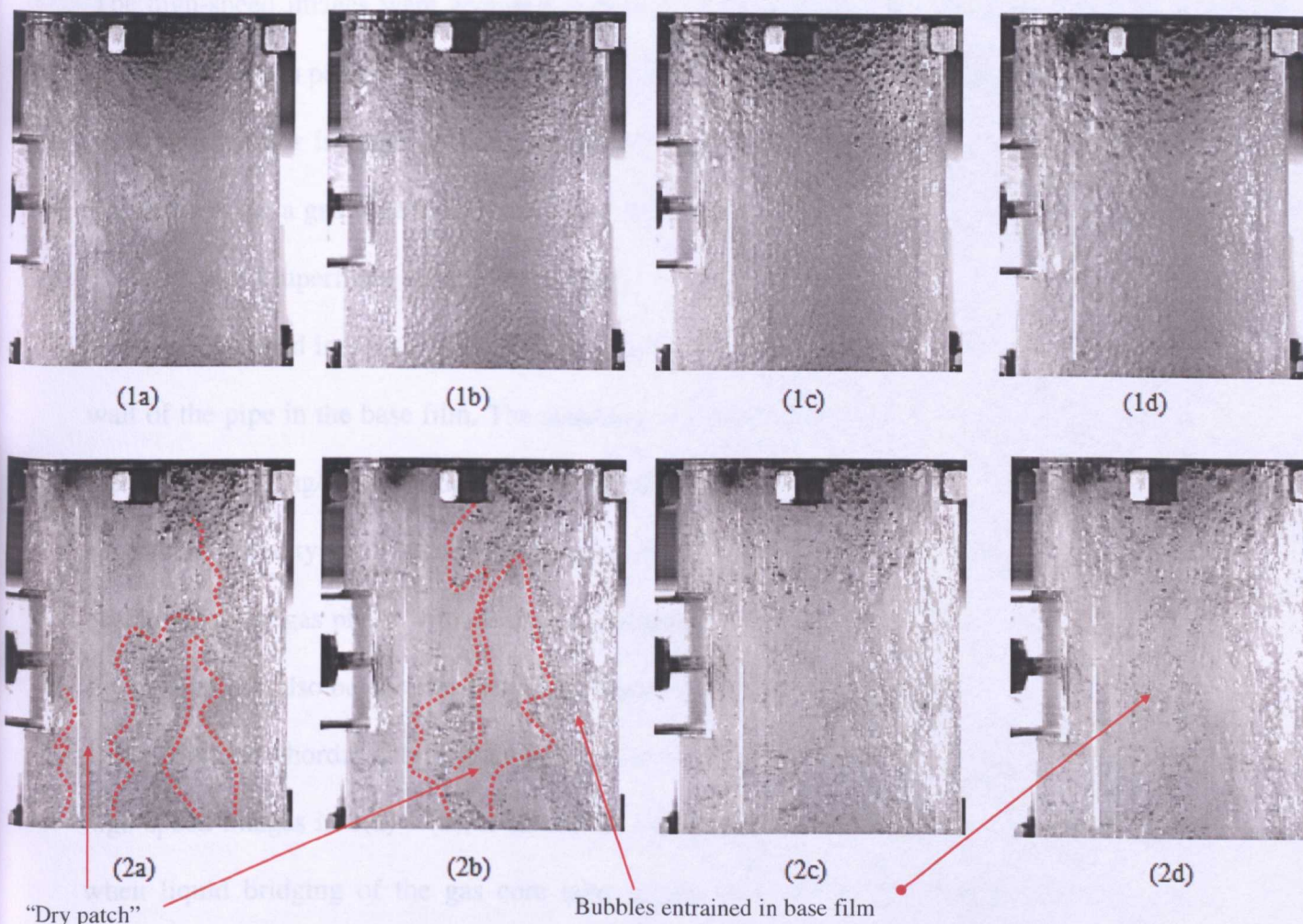


Figure 5.16. (1a-d) High speed images at gas superficial velocity of 3.26m/s and 11.42m/s for constant liquid superficial velocity of 0.24 at L/D = 82.7.

The high-speed images were acquired at each axial distance location below the wire mesh sensor acquisition point at 1000 frames per second (fps). The acquisition rate is similar to the wire mesh sensor in order to make necessary comparisons. The first set of image frames presented is for a gas superficial velocity of 3.26m/s while the second set is at 11.42m/s at a constant liquid superficial velocity of 0.24m/s.

It can be observed in 1(a)-(d) that the nature of the flow is made up of bubbles enriching the wall of the pipe in the base film. The sequence of images presented shows the dominance of the liquid slugging/liquid bridging phenomena at this operating condition. At a higher gas superficial velocity of 11.42m/s in 2(a)-(d) the pipe cross section can be observed to be occupied by the gas phase with definite entrainment of bubbles in the liquid base film. Also, dry patches can also be observed and these have been indicated in Figure 5.16.

Comparing the chordal data extracted from the wire mesh sensor at $i = 1$ and $j = 16$ to the high speed images in 1(a) – (d), it shows the oscillating nature of the flow close to the wall when liquid bridging of the gas core takes place. A chordal void fraction value of 0.05 indicates the occurrence of bubbles present at the walls of the pipe. On the other hand, as the gas phase occupies the core of the pipe, the chordal void fraction value increases to 0.15. As the gas superficial velocity is increased from 3.26m/s to 11.42m/s in Figure 5.16, the gas phase almost occupy the pipe cross-section. However, because gas bubbles are entrained in the base film restrained to the pipe wall, this shows a decrease in void fraction to 0.05. At about 1.80s, the void fraction decreases to zero, which is indicative of the absence of bubbles in the base film. Subsequently, the core of the pipe is completely occupied by gas phase and bubbles are entrained in the base film.

Based on the above analysis, the characteristic natures of huge waves and liquid slugs have been identified. However, to extract finer details from the void data, it is necessary that

further analysis of the void fraction data should be carried out. This has been presented in the subsequent sections.

5.2.5. Statistical analysis of time series data

As a means of distinguishing the occurrence of both liquid slugs and huge waves, statistical analysis has been carried out. From the cross sectional averaged void fractions, time averaged values can be obtained. The mean void fraction values are obtained by taking the average of the instantaneous void fraction values over the total time. The standard deviation on the other hand, reveals the deviation from mean void fraction.

Figure 5.17 shows the mean void fraction variation with axial distance. At a liquid superficial velocity of 0.03m/s, the mean void fraction does not change considerably. This is with respect to higher gas superficial velocities than 3.26m/s. When the liquid superficial velocity increases to 0.13m/s, 0.18m/s and 0.24m/s respectively, there is general increase in void fraction with increasing gas superficial velocity and axial distance from the injection. The variation of mean void fraction with axial distance gives a logarithmic increase. It also shows that the void fraction values obtained at $L/D = 35.4$ and $L/D = 82.7$ are of approximately the same magnitude. However, this does not mean that the flow is developed at $L/D = 35.4$ because other flow phenomena such as the frequency of liquid bridging of the gas core, huge waves and entrained liquid structures change with increasing axial distance from the injection.

The standard deviation and skewness variation are shown in Figure 5.18. The standard deviation of the time series data generally increases with axial distance from the injection. On the other hand, the skewness increases then decreases with axial distance from the injection.

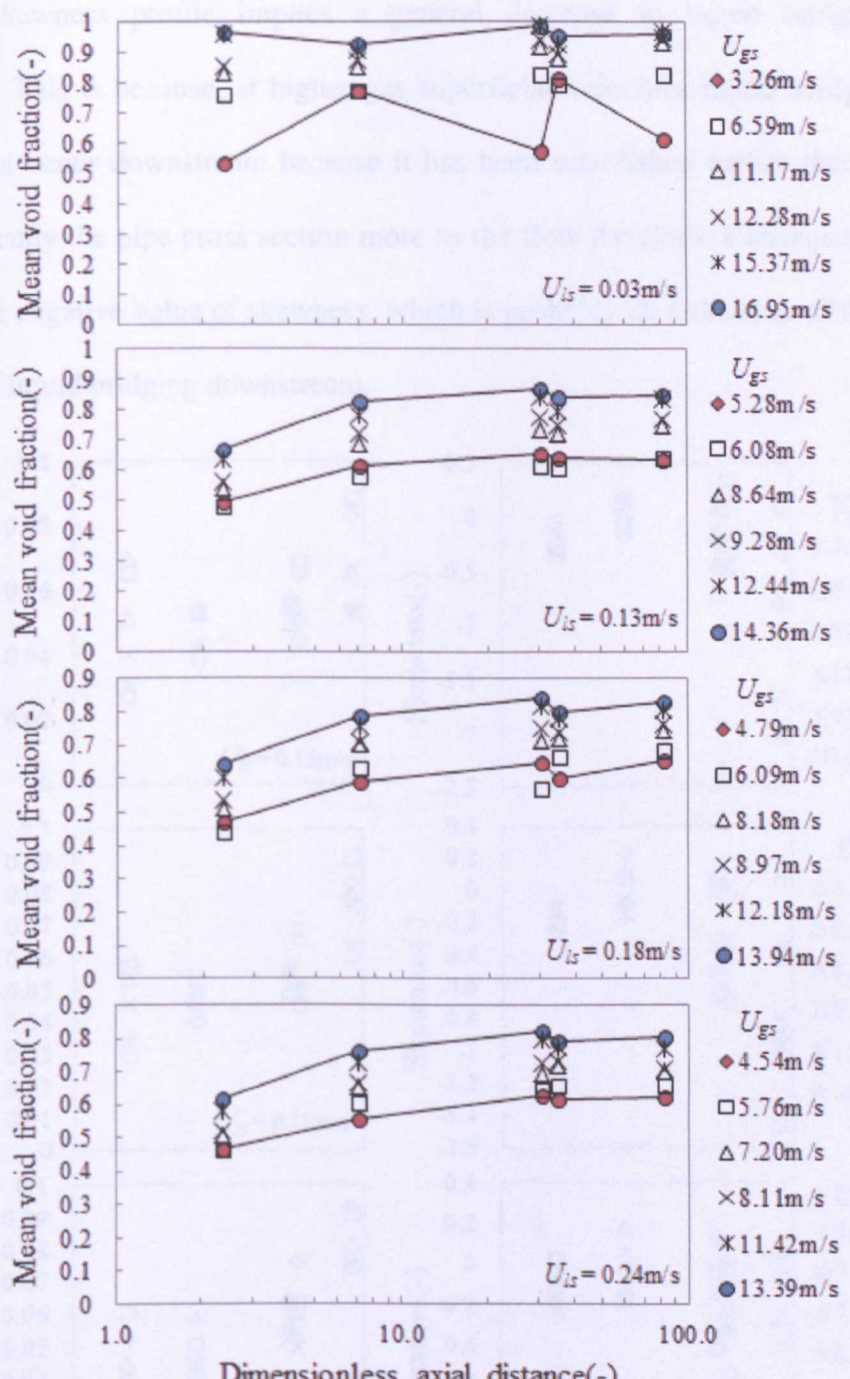


Figure 5.17. Variation of mean void fraction with axial distance from injection for liquid superficial velocities of 0.03m/s, 0.13m/s, 0.18m/s and 0.24m/s as indicated in the respective plots.

It is possible that the increasing trend of the standard deviation with dimensionless axial distance is related to the increase in the frequency of huge waves downstream. On the other

hand, the skewness profile implies a general decrease in liquid bridging frequency downstream. This is because, at higher gas superficial velocities liquid bridging of the gas core does not occur downstream because it has been established earlier that the gas phase begins to occupy the pipe cross section more as the flow develops. Consequently, this gives an increasing negative value of skewness, which is probably an indication of the reduction in frequency of liquid bridging downstream.

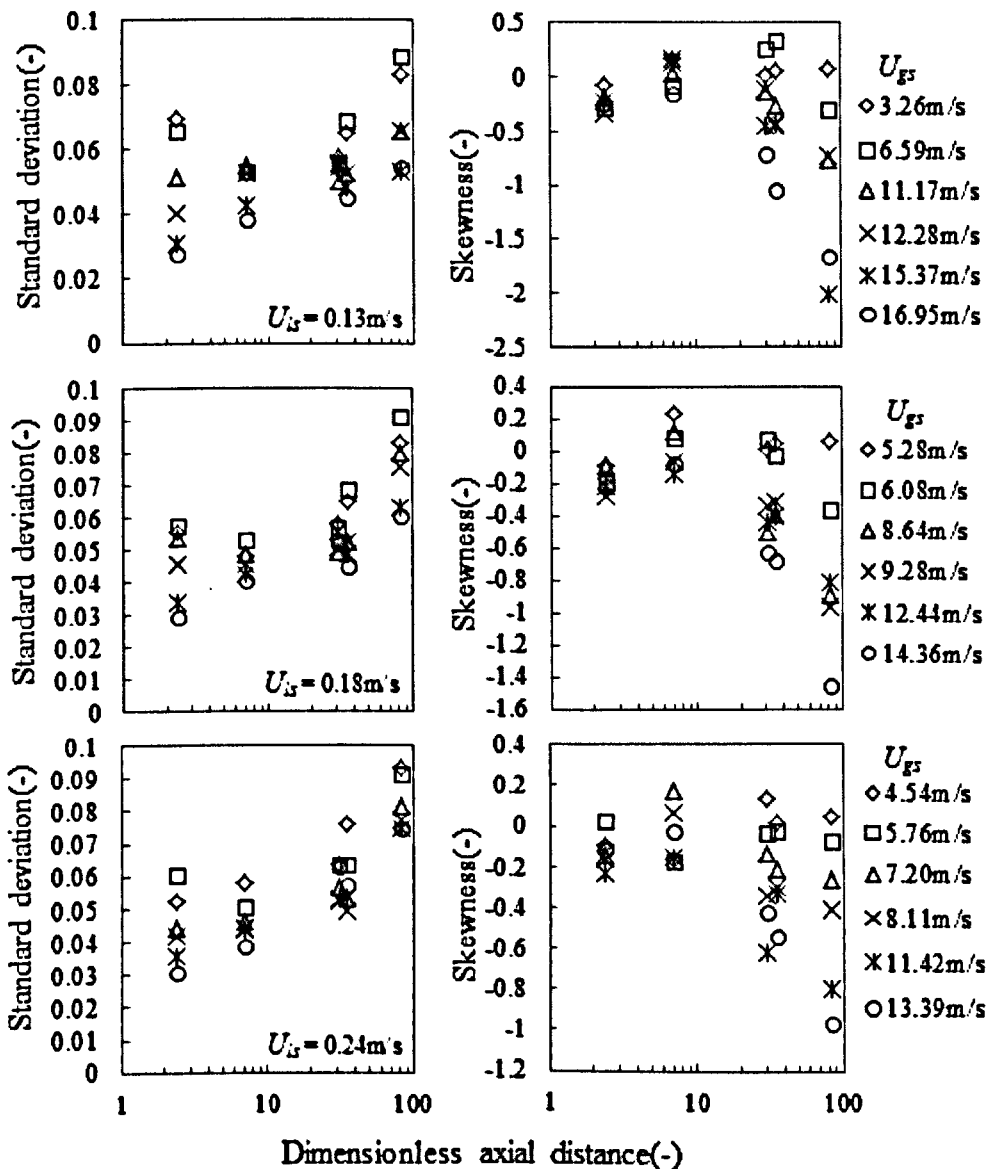


Figure 5.18. Variation of standard deviation and skewness of void fraction with

dimensionless axial distance at liquid superficial velocities of 0.13m/s, 0.18m/s and 0.24m/s respectively.

5.2.6. Spectral analysis of time series data

The spectral analysis in terms of power spectral density (PSD) has been used as a measure of analysing the time series data in the frequency domain. This has been done to obtain the dominant frequency of the structures present. The PSD is essentially the Fast Fourier transform (FFT) of the auto covariance function (ACF) as explained in section 4.2.6. The power spectrum variation with frequency is shown in Figure 5.19 for a constant liquid superficial velocity of 0.18m/s at $L/D = 35.4$ and 82.7 respectively.

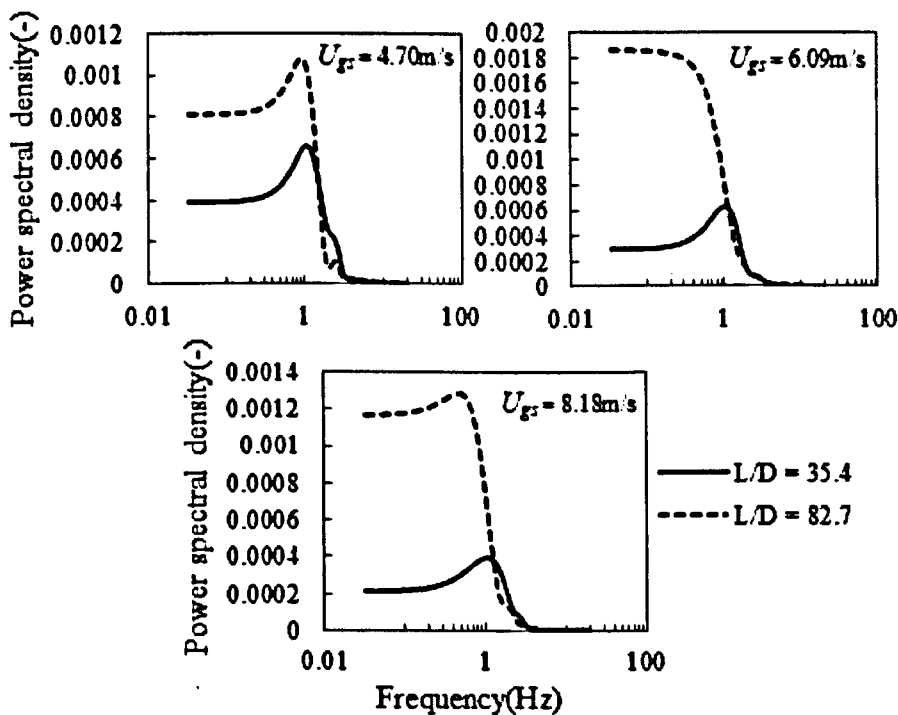


Figure 5.19. Power spectral density variation with frequency at a constant liquid superficial velocity of 0.18m/s.

It shows that when the gas superficial velocity is 4.70m/s , well-defined peaks can be observed. The peaks at both axial distances from the injection occur at about the same frequency but the profile downstream is higher. As the gas superficial velocity is increased, the profile for $L/D = 35.4$ gradually decreases. On the other hand, although the profile is higher downstream at $L/D = 82.7$, there is a slight shift to lower frequencies.

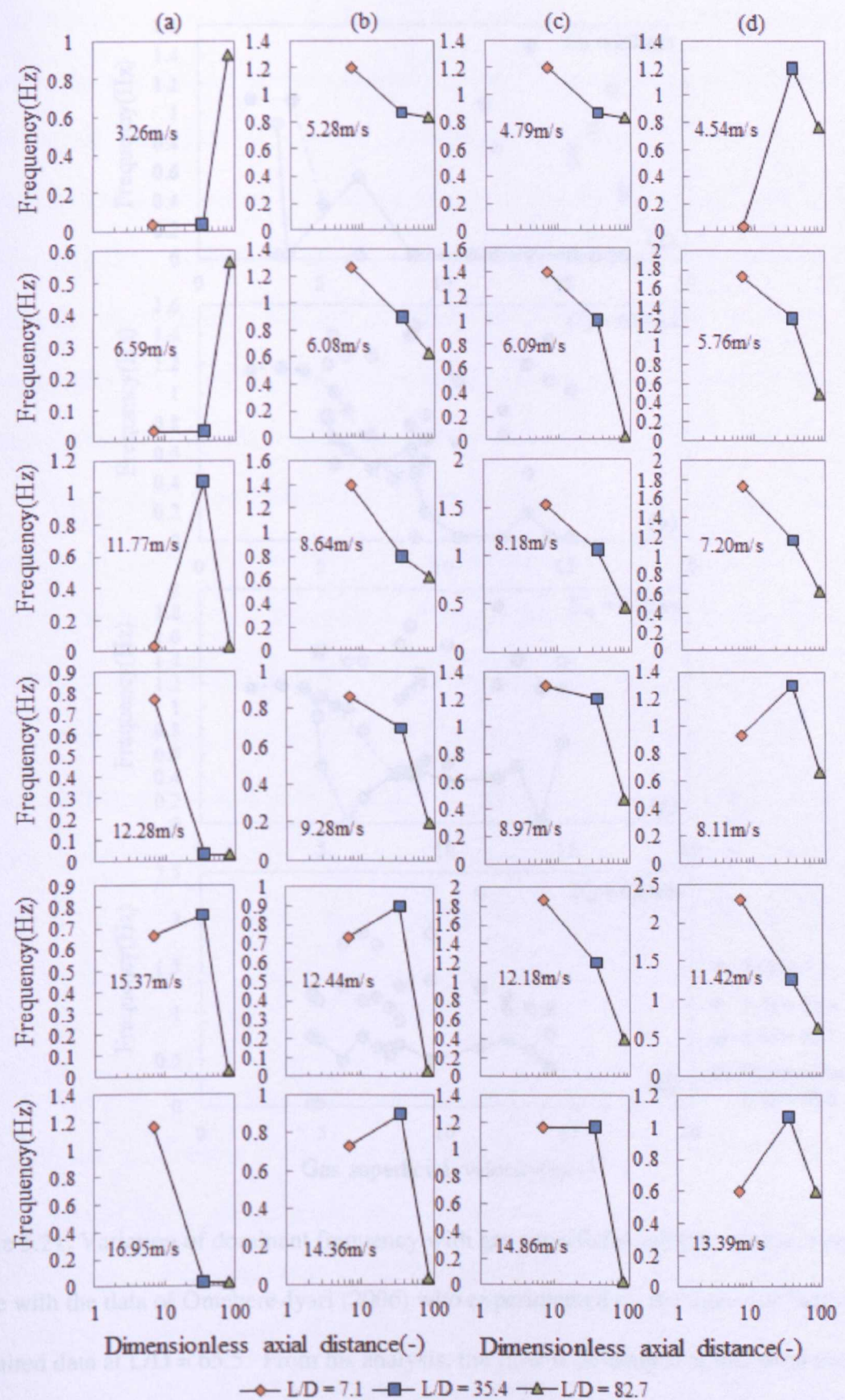


Figure 5.20. Variation of dominant frequency with dimensionless axial distance at liquid superficial velocities of 0.03m/s, 0.13m/s, 0.18m/s and 0.24m/s in (a)-(d) respectively.

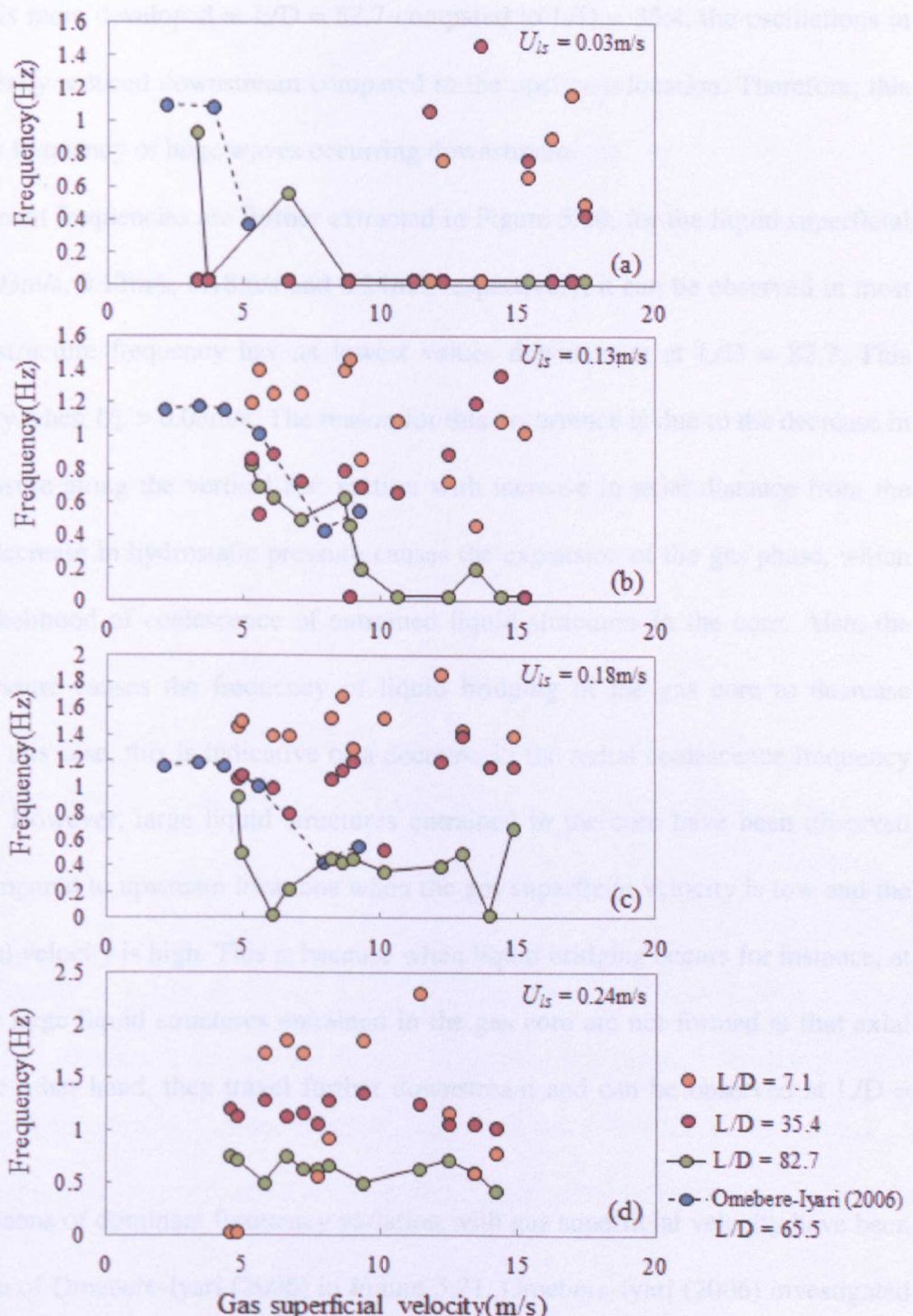


Figure 5.21. Variation of dominant frequency with gas superficial velocity with comparisons made with the data of Omebere-Iyari (2006) who experimented on the same test facility and acquired data at $L/D = 65.5$. From his analysis, the flow is developed at this axial distance from the injection .The liquid superficial velocities for his cases are 0.05m/s in (a) and 0.1m/s in (b) and (c) respectively.

Since the flow is more developed at $L/D = 82.7$ compared to $L/D = 35.4$, the oscillations in the flow are greatly reduced downstream compared to the upstream location. Therefore, this implies a higher frequency of huge waves occurring downstream.

When the dominant frequencies are further extracted in Figure 5.20, for the liquid superficial velocities of 0.03m/s, 0.13m/s, 0.18m/s and 0.24m/s respectively, it can be observed in most cases that the structure frequency has its lowest values downstream at $L/D = 82.7$. This occurs especially when $U_{ls} > 0.03\text{m/s}$. The reason for this occurrence is due to the decrease in hydrostatic pressure along the vertical test section with increase in axial distance from the injection. The decrease in hydrostatic pressure causes the expansion of the gas phase, which increases the likelihood of coalescence of entrained liquid structures in the core. Also, the decrease in pressure causes the frequency of liquid bridging of the gas core to decrease downstream. In this case, this is indicative of a decrease in the radial coalescence frequency of huge waves. However, large liquid structures entrained in the core have been observed downstream compared to upstream locations when the gas superficial velocity is low and the liquid superficial velocity is high. This is because when liquid bridging occurs for instance, at $L/D = 35.4$, the large liquid structures entrained in the gas core are not formed at that axial location. On the other hand, they travel further downstream and can be observed at $L/D = 82.7$.

Further comparisons of dominant frequency variation with gas superficial velocity have been made to the data of Omebere-Iyari (2006) in Figure 5.21. Omebere-Iyari (2006) investigated the churn-annular regime transition and acquired void fraction data using conductance probes at axial distances of $L/D = 3.5, 30.9, 62.7, 63.8$ and 65.5 . Necessary Comparisons have been made to the frequency data obtained from the time series of the void fraction at $L/D = 65.5$. From Figure 5.21, this shows that at low liquid superficial velocity of 0.03m/s there is no particular trend. However, when the liquid superficial velocity is increased, the trend

becomes more apparent as there is a decrease in the structure frequency with increase in axial distance from the injection. A further decrease in frequency can also be observed at L/D = 82.7, compared to L/D = 65.5, where Omebere-Iyari (2006) suggested that the flow with respect to the void fraction is developed. Therefore, it can be said at this point that the rate of coalescence of liquid structures entrained in the core increases downstream.

A dimensionless frequency known as the Strouhal number has been used to characterize the degree of instability in the flow. This encapsulates the frequency of periodic structures identified above (Azzopardi (2004), Kaji *et al.*, (2009) and Hernandez-Perez *et al.*, 2010).

The gas based Strouhal number is given as:

$$Str_G = \frac{fD}{U_{gs}} \quad (5.1)$$

where f is the frequency, D is the diameter and U_{gs} is the gas superficial velocity.

Kaji *et al.* (2009) predicted another form of gas based Strouhal number which is given as:

$$Str_G = AB\left(\frac{L}{D}\right)^{-0.75} \quad (5.2)$$

where the coefficients A and B are given by $A = U_{gs}^{-1.2}$ and $B = 4.94U_{ls} + 0.368$. Also, the dimensionless axial distance is represented as L/D. They used this form of Strouhal number to obtain a good correlation having a coefficient of determination of 97.3%. Both forms of Strouhal number in equations (5.1) and (5.2) have been varied with liquid holdup as shown in Figure 5.22.

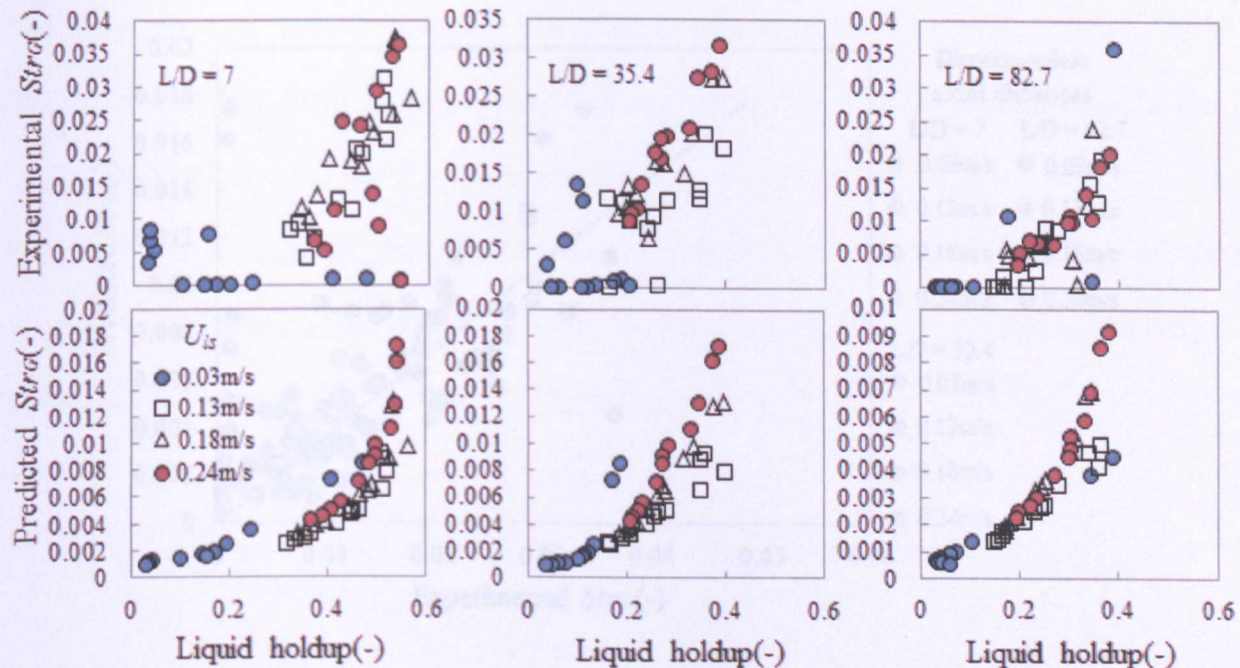


Figure 5.22. Comparison of experimental and predicted gas-based Strouhal number according to Kaji *et al.* (2009) against liquid holdup.

For both experimental and predicted Strouhal number variations, when the liquid holdup increases, there is an increasing trend with the Strouhal number at each axial distance from the injection. Also, there is a shift in the data for each liquid superficial velocity from right of a liquid holdup of 0.4 to the left. This is essentially because of flow development. The profiles at higher liquid superficial velocities are almost the same at $L/D = 82.7$. Compared to the experimental Strouhal number variation with liquid holdup, the predicted values shows a better defined exponentially increasing trend as the liquid holdup increases. In general, it shows that for churn flow regime when the liquid holdup increases, the periodicity of the structures present exponentially increases.

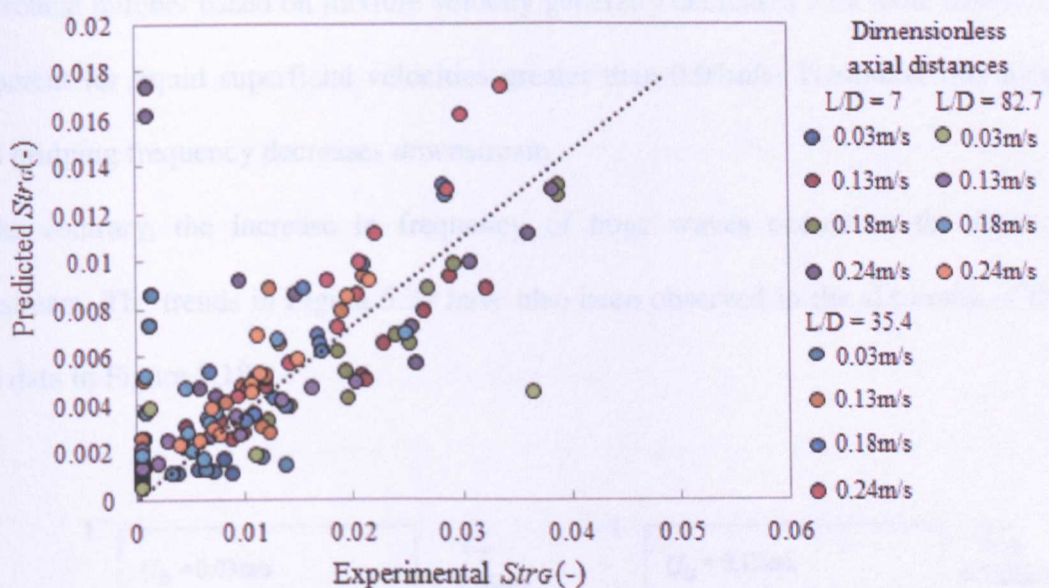


Figure 5.23. Comparison of experimental and predicted gas based Strouhal number according to (Kaji *et al.*, 2009).

Both experimental and predicted Strouhal number has been compared as shown in Figure 5.23. It shows that there is a good agreement when the liquid superficial velocity is greater than 0.03m/s.

The Strouhal number in terms of mixture velocity has also been used to characterise the liquid bridging behaviour or frequency of liquid slugs with increase in axial distance, (Kaji *et al.*, 2009). The predicted form of the Strouhal number based on mixture velocity according to Kaji *et al.* (2009) is given as:

$$Str_m = CE \left(\frac{L}{D} \right)^{-0.6} \quad (5.3)$$

where $C = U_{gs}^{-0.75}$ and $E = 0.74U_{ls} + 0.53$ respectively. The variation of the Strouhal number based on mixture velocity with dimensionless axial distance is shown in Figure 5.24 at respective liquid superficial velocities.

When the liquid superficial velocity is 0.03m/s, the profile can be observed to increase with axial distance for gas superficial velocities of 3.26m/s and 6.59m/s respectively. However,

the Strouhal number based on mixture velocity generally decreases with axial distance. This is apparent for liquid superficial velocities greater than 0.03m/s. Therefore, this means the liquid bridging frequency decreases downstream.

On the contrary, the increase in frequency of huge waves occurs as the flow travels downstream. The trends in Figure 5.24 have also been observed in the skewness of the time series data in Figure 5.18.

Barnes (1986) suggested that when the liquid films were broken up, the frequency of wave breaking

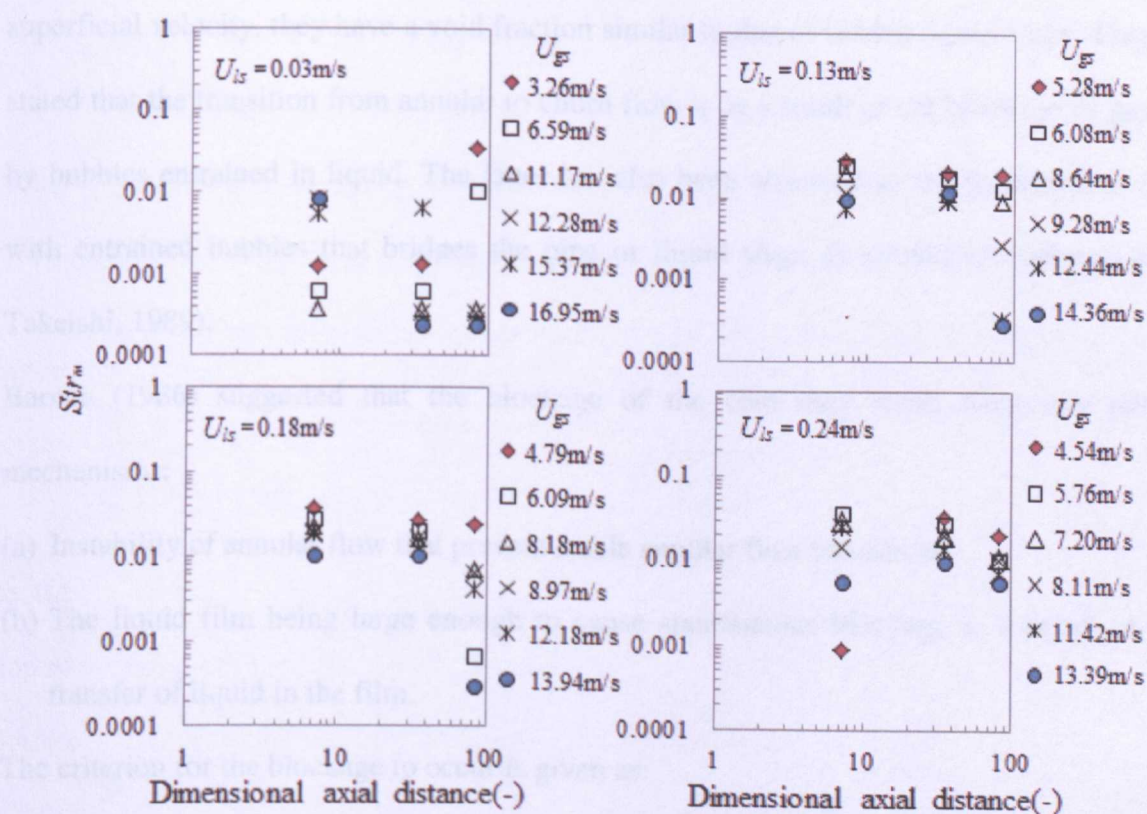


Figure 5.24. Variation of Strouhal number based on mixture velocity with dimensionless axial distance (compared to the skewness variation with axial distance in Figure 5.18)

is the minimal liquid holding within the liquid bridge to be able to hold it. The transition to churning flow occurs when the liquid holding is removed from the liquid bridge. This occurs when the liquid holding is removed from the wave trough to the crest. The transition to churning flow occurs at the wave trough to the crest, the transition to churning flow occurs at the wave trough to the crest.

5.2.7. Stability analysis by method of Barnea (1986)

Barnea (1986) obtained a criterion for the transition from annular flow to intermittent flow. They classified intermittent flow as either slug or churn flow. Slug flow has not been observed in the present experiments. Also, this is the case in previous large diameter pipe experiments by (Omebere-iyari 2006, Omebere-iyari *et al.*, 2008 and Ali 2009). Therefore, this can be considered as the transition to churn flow.

Barnea (1986) suggested that when the liquid films are thick as a result of an increased liquid superficial velocity, they have a void fraction similar to that of bubbly liquid slugs. They also stated that the transition from annular to churn flow is as a result of the blockage of gas core by bubbles entrained in liquid. The latter has also been observed as the formation of liquid with entrained bubbles that bridges the pipe or liquid slugs as termed by (Sekoguchi and Takeishi, 1989).

Barnea (1986) suggested that the blockage of the core may result from two possible mechanisms:

- (a) Instability of annular flow that prevent stable annular flow conditions
- (b) The liquid film being large enough to cause spontaneous blockage as a result of axial transfer of liquid in the film.

The criterion for the blockage to occur is given as:

$$\frac{A_l}{A_c R_{sm}} = \frac{\alpha_L}{R_{sm}} \geq 0.5 \quad (5.4)$$

where A_l is the area occupied by the liquid phase, A_c is the pipe cross sectional area and R_{sm} is the minimal liquid holdup within the liquid slug that will allow complete blockage of the gas passage. Since there is the presence of waves on the interface, the fluid is transferred axially from the wave trough to the crest. Therefore, when sufficient liquid is accumulated at the crest, the transition to churn flow occurs. The accumulation of sufficient liquid at the crest

as observed by Barnea (1986) is similar to the occurrence of huge waves. She came up with a dimensionless parameter, given as:

$$Y = \frac{1 + 75\alpha_L}{(1 - \alpha_L)^{2.5}} - \frac{1}{\alpha_L^3} X^2 \quad (5.5)$$

$$X^2 = \frac{\frac{4C_L}{D} \left(\frac{U_{ls} D}{V_L} \right)^{-n} \frac{\rho_L U_{ls}}{2}}{\frac{4C_G}{D} \left(\frac{U_{gs} D}{V_L} \right)^{-m} \frac{\rho_G U_{gs}}{2}} = \frac{\left(\frac{dp}{dz} \right)_{LS}}{\left(\frac{dp}{dz} \right)_{GS}} \quad (5.6)$$

where the parameter X^2 is the Lockhart-Martinelli parameter.

Based on the phenomenon of (a) and (b) outlined above, Barnea (1986) developed a dimensionless map by plotting the parameter Y against X, which is the Lockhart-Martinelli parameter. The data at these axial distances from the injection is shown in Figures 5.25-5.27. The curve represents the stability line according to the mechanisms (a) and (b) respectively.

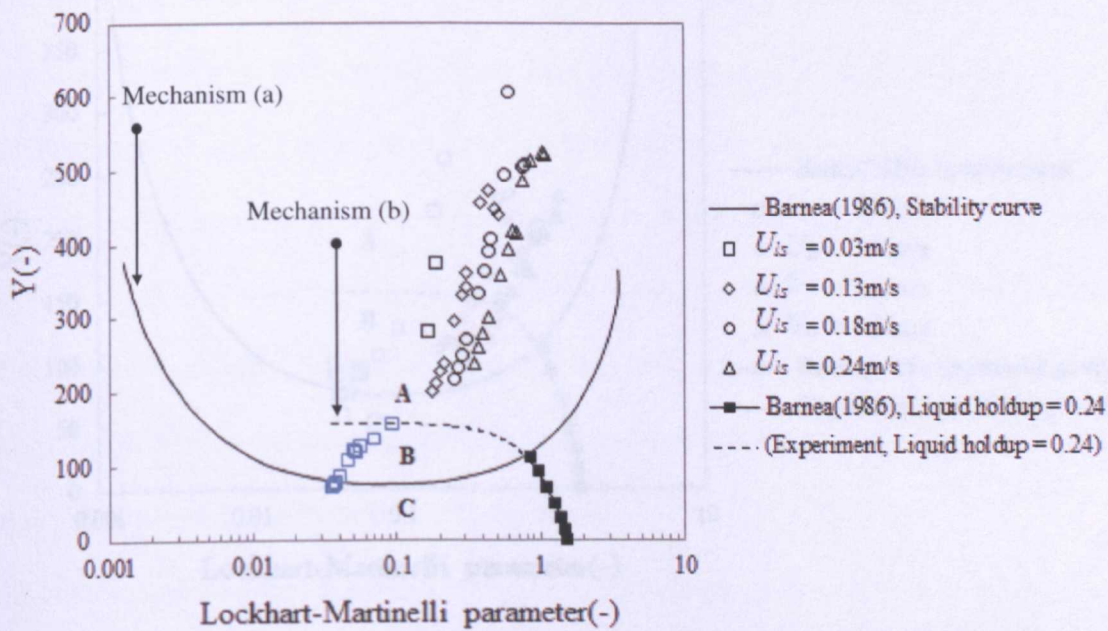


Figure 5.25. Variation of dimensionless parameter with Lockhart-Martinelli parameter by method of (Barnea, 1986) for data acquired at L/D = 7.1.

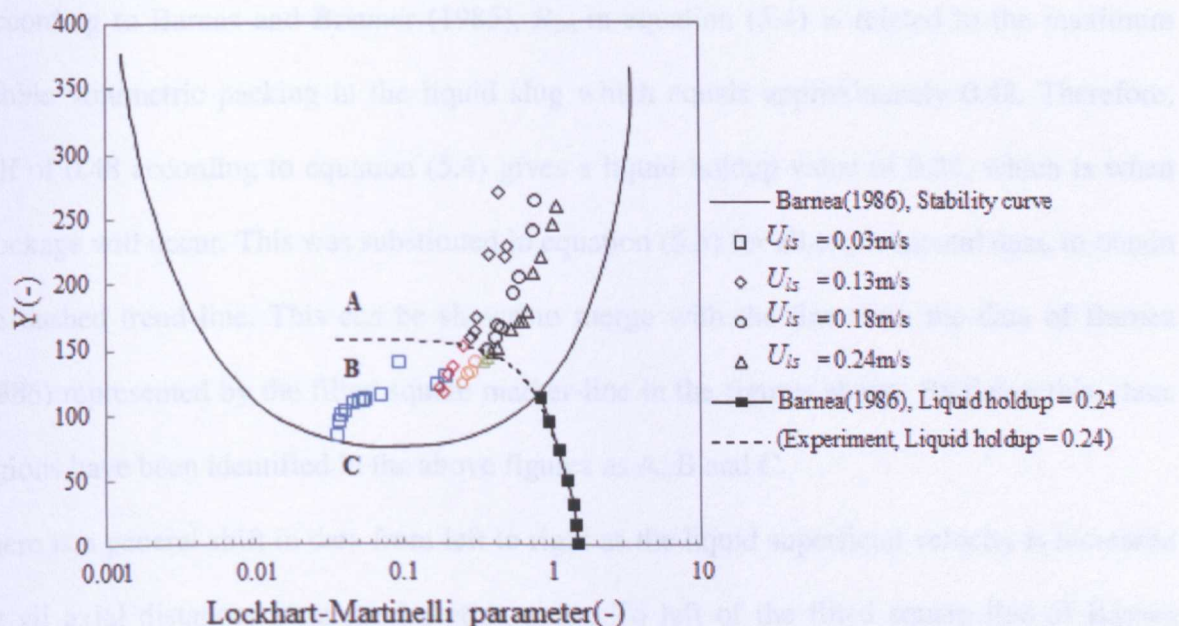


Figure 5.26. Variation of dimensionless parameter with Lockhart-Martinelli parameter by method of (Barnea, 1986) for data acquired at $L/D = 35.4$.

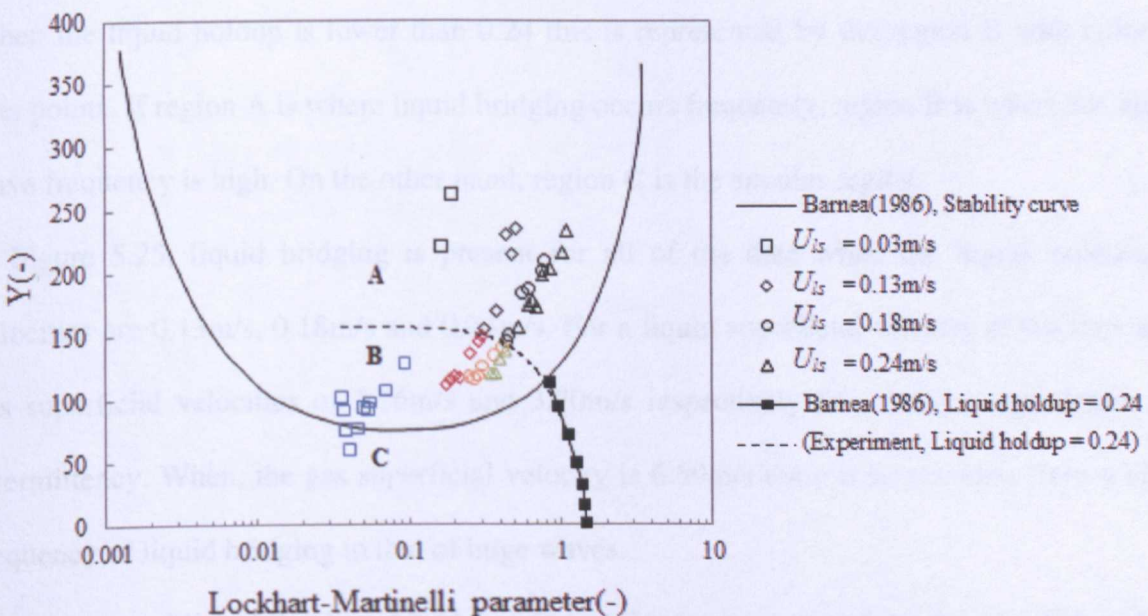


Figure 5.27. Variation of dimensionless parameter with Lockhart-Martinelli parameter by method of (Barnea, 1986) for data acquired at $L/D = 82.7$.

According to Barnea and Brauner (1985), R_{sm} in equation (5.4) is related to the maximum bubble volumetric packing in the liquid slug which equals approximately 0.48. Therefore, half of 0.48 according to equation (5.4) gives a liquid holdup value of 0.24, which is when blockage will occur. This was substituted in equation (5.5) for all experimental data, to obtain the dashed trend line. This can be shown to merge with the line from the data of Barnea (1986) represented by the filled square marker-line in the figures above. By doing this, three regions have been identified in the above figures as A, B and C.

There is a general shift in data from left to right as the liquid superficial velocity is increased for all axial distances from the injection point. To left of the filled square line of Barnea (1986), namely in region C, is the stable annular flow whereas to the right, annular flow is not present. The region to the right of the dashed trend line given as region A, has liquid holdup values greater than 0.24.

When the liquid holdup is lower than 0.24 this is represented by the region B with colored data points. If region A is where liquid bridging occurs frequently, region B is where the huge wave frequency is high. On the other hand, region C is the annular region.

In Figure 5.25, liquid bridging is present for all of the data when the liquid superficial velocities are 0.13m/s, 0.18m/s and 0.24m/s. For a liquid superficial velocity of 0.03m/s and gas superficial velocities of 3.26m/s and 3.70m/s respectively this show a high degree of intermittency. When, the gas superficial velocity is 6.59m/s there is a transition from a high frequency of liquid bridging to that of huge waves.

It has been established that liquid bridging decays downstream, therefore, there is shift in data points from region A- liquid bridging dominant regime, to B-huge wave dominant regime. This also agrees with the analysis that the huge wave frequency increases downstream.

At $L/D = 35.4$ and 82.7 in Figures 5.26 and 5.27, it shows that when the liquid superficial velocity is 0.03m/s, all the data points are present in the region B. In Figure 5.27, there are

more data points at higher liquid superficial velocities as result of high frequency of huge waves. However, when the liquid superficial velocity is 0.03m/s and gas superficial velocities are 3.26m/s and 3.70m/s, the data points are present within the liquid bridging regime since the inertia forces are not sufficient enough compared to the gravitational forces. Interestingly, at higher gas superficial velocities some data points are present within region C. This is the annular flow region as indicated by (Barnea, 1986). However, based on visual observation this is not the existing regime present.

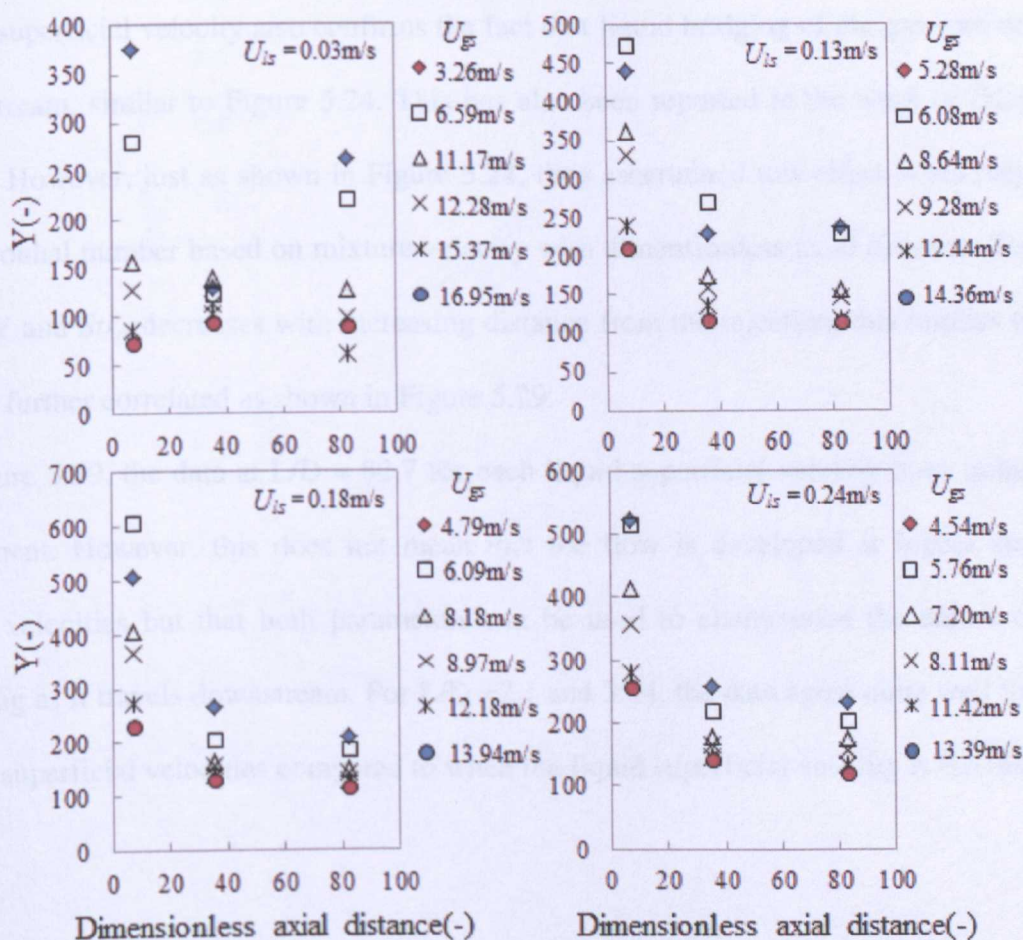


Figure 5.28. Variation of dimensionless parameter suggested by Barnea (1986) against dimensionless axial distance for constant liquid superficial velocities.

It shows that for data points within this region there is a tendency for the flow pattern to be annular or semi-annular as the liquid superficial velocity is low and the gas superficial velocity is high. This also ascertains the fact that at $L/D = 82.7$ when the liquid superficial velocity is 0.03m/s and the gas superficial velocity is 17.46m/s, the flow is fully developed. The values of dimensionless parameter, Y , at each axial distance from the injection have been obtained to clarify its variation with axial distance as shown in Figure 5.28.

It shows from Figure 5.28 that for higher liquid superficial velocities than 0.03m/s, there is a decreasing trend with increasing axial distance from the injection. The profiles at higher liquid superficial velocity also confirms the fact that liquid bridging of the gas core decreases downstream, similar to Figure 5.24. This has also been reported in the work of (Kaji *et al.*, 2009). However, just as shown in Figure 5.24, they ascertained this effect when they varied the Strouhal number based on mixture velocity with dimensionless axial distance. Therefore, since Y and Str_m decreases with increasing distance from the injection, this implies that they can be further correlated as shown in Figure 5.29.

In Figure 5.29, the data at $L/D = 82.7$ for each liquid superficial velocity have quite a good agreement. However, this does not mean that the flow is developed at higher superficial liquid velocities but that both parameters can be used to characterize the nature of liquid bridging as it travels downstream. For $L/D = 7.1$ and 35.4, the data agree quite well for higher liquid superficial velocities compared to when the liquid superficial velocity is 0.03m/s.

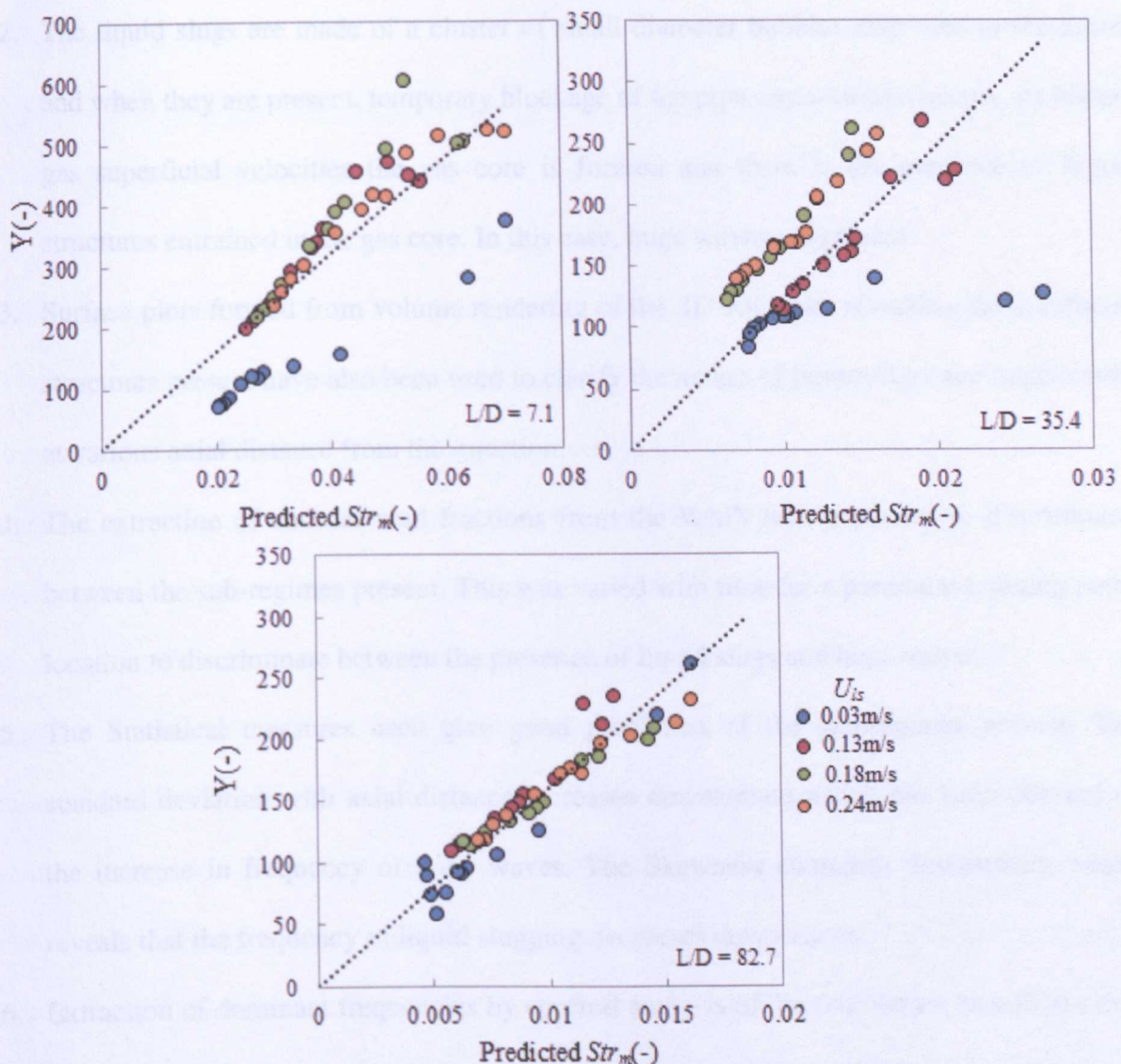


Figure 5.29. Variation of dimensionless parameter according to Barnea (1986) against predicted Strouhal number based on mixture velocity according to (Kaji *et al.*, 2009). The data seems to be well correlated at $L/D = 82.7$ for the liquid superficial velocities.

5.3. Summary

This study examined the spatio-temporal evolution of churn flow with increasing axial distance from the injection. The results obtained can be summarised as follows:

1. Churn flow regime is made up of two sub regimes namely: the formation of liquid slugs and huge waves. The transit velocities of the liquid slugs are lower than the huge waves.

2. The liquid slugs are made of a cluster of small diameter bubbles dispersed in the liquid and when they are present, temporary blockage of the pipe cross-section occurs. At higher gas superficial velocities the gas core is formed and there is the presence of liquid structures entrained in the gas core. In this case, huge waves are present.
3. Surface plots formed from volume rendering of the 3D void data revealing the interfacial structures present have also been used to clarify the nature of liquid slugs and huge waves at various axial distance from the injection.
4. The extraction of chordal void fractions from the WMS data was used to discriminate between the sub-regimes present. This was varied with time for a particular crossing point location to discriminate between the presence of liquid slugs and huge waves.
5. The Statistical measures used give good prediction of the sub-regimes present. The standard deviation with axial distance increases downstream which has been denoted as the increase in frequency of huge waves. The Skewness decreases downstream which reveals that the frequency of liquid slugging decreases downstream.
6. Extraction of dominant frequencies by spectral analysis of the time series data shows that the dominant frequency decreases with axial distance, which is clearly an indication of the decay of liquid slugging downstream.
7. Further analysis using prediction of Kaji *et al.* (2009) and Barnea (1986) have been used to show the dominance of both liquid slugging and huge waves. The Strouhal number predicted by Kaji *et al.* (2009) and the dimensionless parameter by Barnea are well correlated further downstream from the injection at $L/D = 82.7$.

From the above result and analysis, the nature of both liquid slugs and huge waves has been ascertained for air-water experiments. The effect of viscosity will be investigated in chapter 6 using air-glycerol/water as the fluid phases and making necessary comparisons to air-water experiments. Based on the subsequent comparative study, the CFC model has been proposed.

CHAPTER 6

EFFECT OF LIQUID VISCOSITY ON CHURN FLOW PATTERN IN VERTICAL UPWARD GAS-LIQUID FLOW

6.1. Introduction

Most of the research carried out on two phase flow studies use air-water as the operating fluids. Both have been the most appropriate fluid pair to use for experimentation. However, engineers dealing with fluids typical of industrial applications observe that water has inappropriate values of physical properties especially with reference to a surface tension that is much higher than many of the materials they deal with, (Szalinski *et al.*, 2010). This is because water is cheap and harmless to the environment even when large volumes of spillage occur. On the other hand, air is mostly released into the atmosphere as can be observed for the experiments in chapter 4. Szalinski *et al.* (2010) indicated that electrical resistance methods can be employed on water but non-conducting organic liquids would have to employ the more difficult capacitive approach.

There is a need to carry out research on fluids that have similar properties to those used in the oil and gas industries. This is not only to ensure that the data banks for the experiments are filled for further reference, but to draw conclusions taking into consideration the effect of fluid properties. Thus, this is the reason for investigating the effect of liquid viscosity in this study, especially as regards churn flow.

Studies on the effect of liquid viscosity on the two phase flow have been carried out by few workers, (Furukawa and Fukano, 2001 and Szalinski *et al.*, 2010). Consequently, there is a dearth of data when necessary comparisons are to be made with literature. From the work of Furukawa and Fukano (2001), they compared their air-water data to air-glycerol/water data. Their glycerol/water solutions had viscosities of 6cP and 17cP respectively. Szalinski *et al.*

(2001) also carried out a comparative study for their air-water and air-silicone oil data, where the viscosity of continuous phase for the latter was 5cP. Both workers performed their experiments on what can be considered as small diameter pipes of internal diameters of 19.2mm and 67mm respectively. In the work of Furukawa and Fukano (2001), when the liquid viscosity increased, the void fraction was higher for their air-water data compared to air-glycerol/water in the case of bubbly to slug flow transition. As a result, this led to them plotting a transition line that was to the right hand side of their air-glycerol/water data based on high speed video observation and further analysis of their liquid holdup data. The reverse occurred for slug to churn and churn to annular flows as they observed a higher void fraction for air-glycerol/water compared to air-water.

They further examined the applicability of the Baker (1954) parameters that takes into consideration the fluid properties that were obtained for horizontal flows, in their vertical upflow experiments. They found out that irrespective of the pipe orientation using the Baker parameters give good predictions for the slug to churn and churn to annular flows. Conversely, the Baker parameters give poor prediction for bubbly to slug flows. On the other hand, the experiments conducted by Szalinski *et al.* (2001) gives a higher void fraction for air-silicone oil experiments compared to air-water experiments. This was observed for the transition from bubble to churn flows. The experiments performed above investigate the effect of viscosity on the transition between subsequent two phase flow regimes. The question arises as to the effect of viscosity on the behaviour of the two phase flow within a specific flow regime.

Therefore, the work presented investigates the effect of liquid viscosity within the two phase churn flow regime. The experiments were performed in the same facility used in chapter 5 of 127mm internal diameter and 11m in length test section. Detailed description of the operating procedures is given in chapter 3. The operating conditions for gas and liquid superficial

velocities are 3.98m/s – 13.36m/s and 0.036m/s – 0.27m/s respectively. The full operational matrix can be found in Appendix B. Comparisons of the void fraction data was made to the air-water experiments (chapter 5). Based on this, the CFC model has also been presented.

6.2. Results

From the wire mesh sensor, the three-dimensional volume data can be extracted, which is essentially the void fraction data set. The time series of the void fraction or the void fraction variation with time is shown in Figures 6.1 – 6.3. The comparisons are made for air-water (black line) and air-glycerol/water solutions of 12.2cP and 16.2cP indicated as green and red lines respectively. The plots in Figure 6.1 – 6.3 are at an average constant liquid superficial velocity of 0.11m/s, 0.17m/s and 0.26m/s respectively. It was not possible to set the gas and liquid superficial velocities to be the same for both experimental campaigns since the experiments were carried out on a closed loop test facility. Therefore, approximate range value comparisons are made and maintained throughout the present work to draw necessary conclusions.

6.2.1. *Comparison of time series data for air-water and air-glycerol/water*

In Figures 6.1(a)-(c), the time series of the void fraction overlap each other for both glycerol/water viscosities. In Figure 6.1(a), for about 0-3s, the void fraction does not change considerably for the 16.2cP data compared to 12.2cP glycerol-water data. This behaviour can also be observed around 5-10s and 10-15s. This probably means that the core is occupied more by gas phase when the viscosity is 16.2cP compared to when it is 12.2cP.

The addition of pure glycerol to water certainly increases the viscosity of the resultant mixture but this reduces its surface tension. A lower surface tension means that the liquid holdup decreases when the viscosity increases. In comparison to the air-water data, this is probably the reason for a lower time series of void fraction.

However, the increased viscosity from air-water as the base case probably increases the stability of the interfacial wave. Therefore, from this explanation, the interfacial wave should be thinner when the viscosity is increased before incipient breakdown of the two phase flow structure occurs. As can also be observed, this seems to be more frequent for the air-water compared to air-glycerol/water data in Figures 6.1 – 6.3.

It should be noted that the moving average technique of averaging sub-sets of data has not been applied to the glycerol/water data but to the air-water data. This means that there is less dissipation of energy as the viscosity increases.

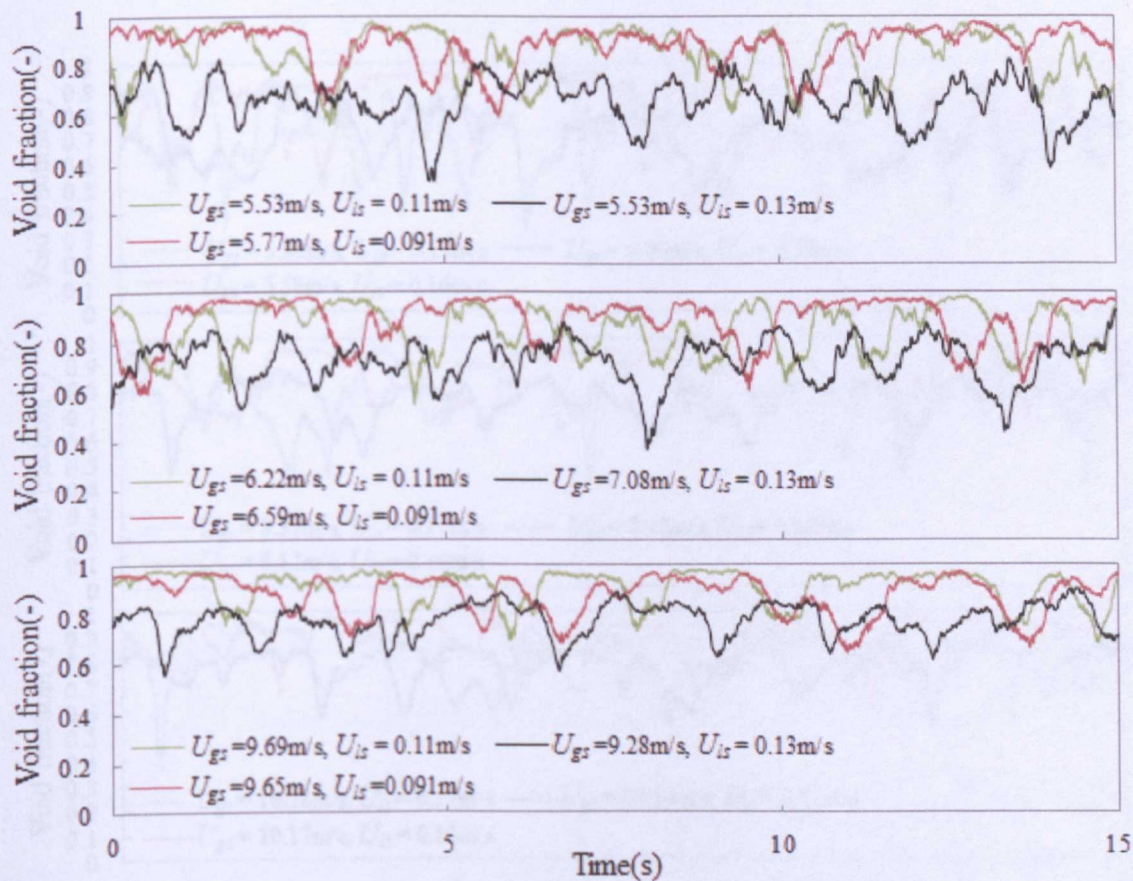


Figure 6.1. Variation of void fraction with time showing comparison of the air-water data (black line) with air-glycerol/water data at 12.2cP (green line) and 16.2cP (red line) at an average liquid superficial velocity of 0.11m/s.

Hewitt and Hall-Taylor (1970) explained the effect of an increase in viscosity from the understanding of the behaviour around the critical layer. Far from the gas-liquid interface, the gas moves faster than the wave. On the other hand, close to the gas-liquid interface, the wave moves faster than the gas. A point is reached away from the wall where the velocity is zero. This point or interface is known as the critical layer. They stated that due to an increase in viscosity sufficient energy is needed to overcome the vortices created in the critical layer. In relation to the present scenario, the abstraction of energy causes the interface to be more stable as the viscosity increases from air-water. Therefore, this leads to a higher time series of void fraction.

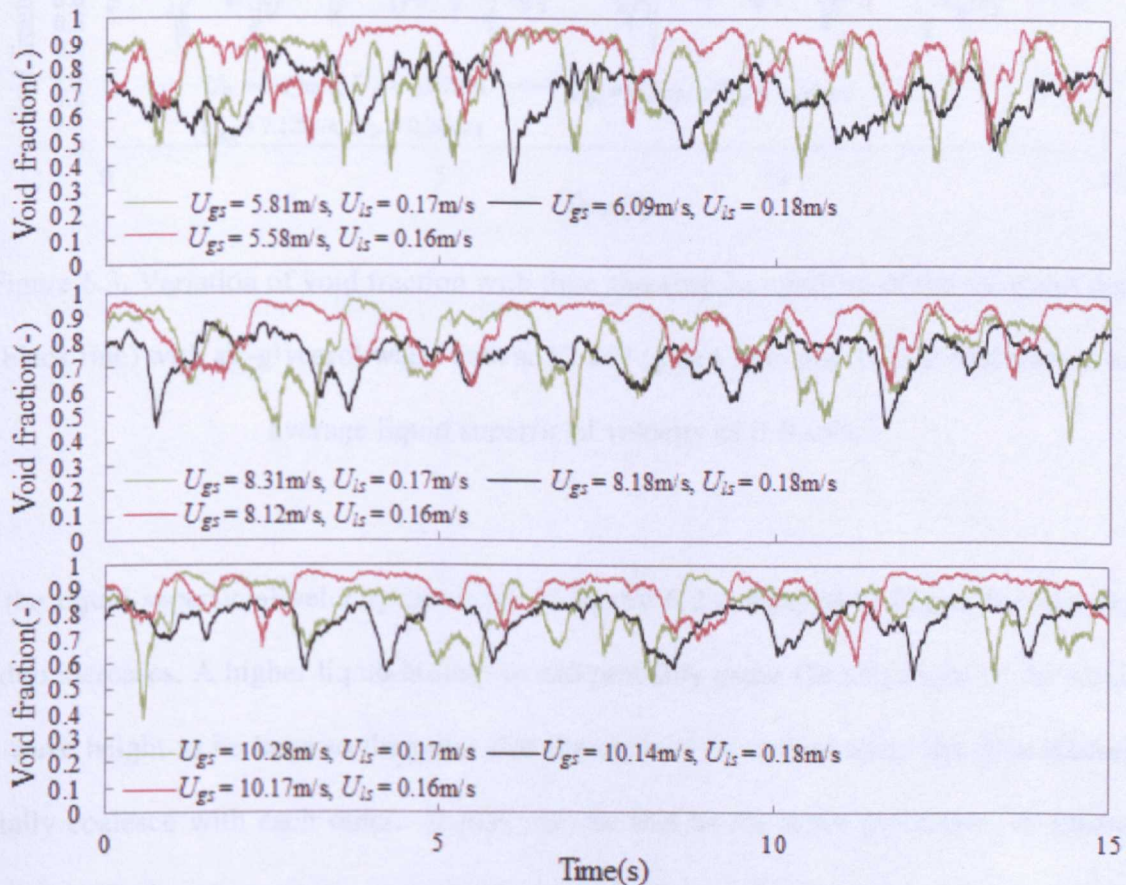


Figure 6.2. Variation of void fraction with time showing comparison of the air-water data (black line) with air-glycerol/water data at 12.2cP (green line) and 16.2cP (red line) at an average liquid superficial velocity of 0.17m/s.

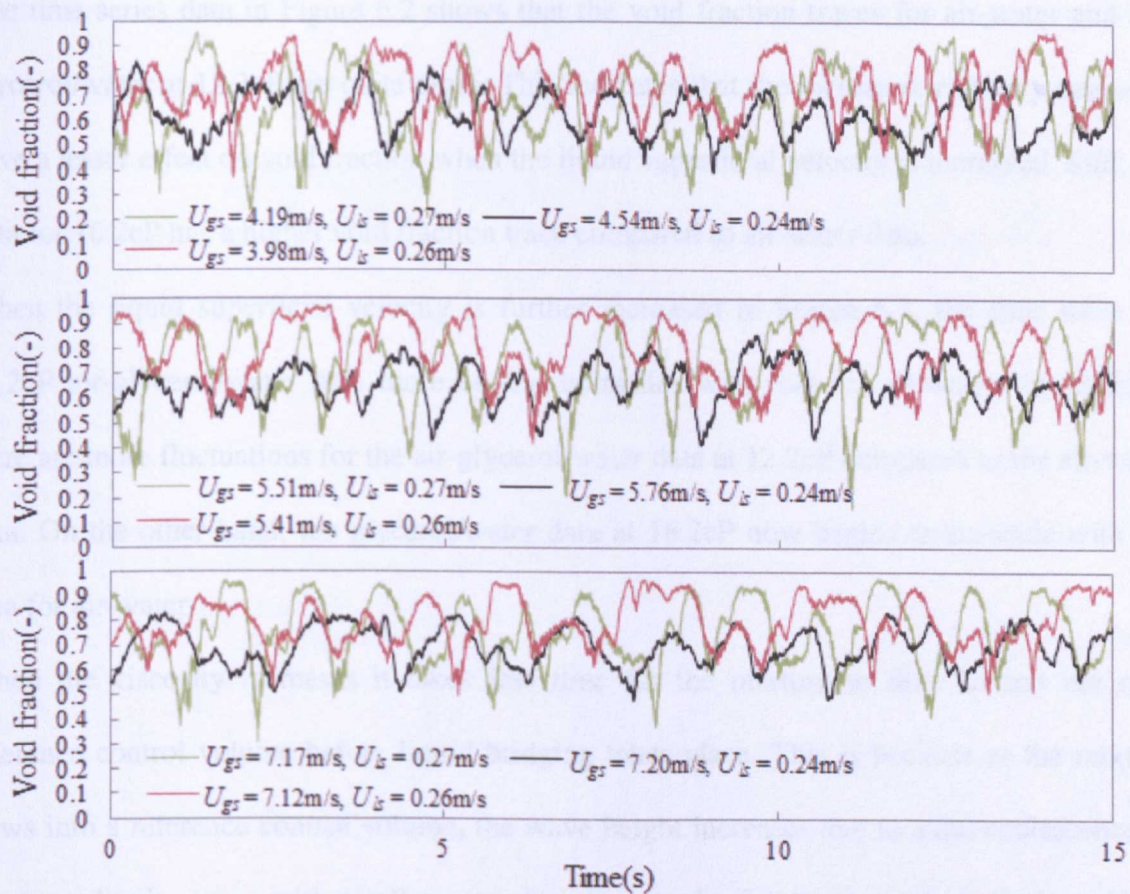


Figure 6.3. Variation of void fraction with time showing comparison of the air-water data (black line) with air-glycerol/water data at 12.2cP (green line) and 16.2cP (red line) at an average liquid superficial velocity of 0.26m/s.

As the liquid superficial velocity increases in Figure 6.2 compared to Figure 6.1, the liquid holdup increases. A higher liquid holdup would probably cause the amplitude of the wave or the wave height to be large to the point that the crest of the waves about the pipe centreline radially coalesce with each other. It may also be that as the wave propagates downstream from the injection they grow over and above a critical wave height due to axial coalescence. Therefore, the effect of gravity on the wave can be considered to be higher for air-water than air-glycerol/water data. In addition, this means there will be higher drag force acting on the wave in the case of air-water compared to air-glycerol/water.

The time series data in Figure 6.2 shows that the void fraction traces for air-water and air-glycerol/water at 12.2cP are quite close. This indicates that the increased viscosity begins to have a lesser effect on void fraction when the liquid superficial velocity is increased. Still, the data for 16.2cP has a higher void fraction trace compared to air-water data.

When the liquid superficial velocity is further increased in Figure 6.3, the time trace for 12.2cP air-glycerol/water data more or less coincides with that for air-water. In addition, there are more fluctuations for the air-glycerol/water data at 12.2cP compared to the air-water data. On the other hand, the glycerol/water data at 16.2cP now begins to coincide with the data for air-water.

When the viscosity increases it takes less time for the mixture to flow in and out of a reference control volume before liquid bridging takes place. This is because as the mixture flows into a reference control volume, the wave height increases due to axial coalescence of large amplitude waves with smaller ones. In other words, due to an increase in viscosity, it takes more time for the amplitude of the wave to grow to eventually result into the liquid bridging of the gas core.

Figure 6.4 gives the variation of mean void fraction with gas superficial velocity with comparisons made to the air-water data. The plots shown in (a)-(d) of Figure 6.4 are at constant average liquid superficial velocities of 0.03m/s, 0.11m/s, 0.17m/s and 0.26m/s respectively. Comparisons are made to mean void fraction from the air-water data acquired at two axial distances from the injection, $L/D = 35.4$ and $L/D = 82.7$. The blue filled diamond represents the former while the orange filled circle is for the latter case. The glycerol-water data of 12.2cP and 16.2cP acquired at $L/D = 65.5$, are given as square and triangle respectively.

For each liquid superficial velocity, the mean void fraction obtained from the air-water data at both axial distances does not change considerably. In further comparison with the glycerol-

water data, a higher profile can be observed. However, the data seems to be close together as the liquid superficial velocity increase, which is reflected in (c) and (d).

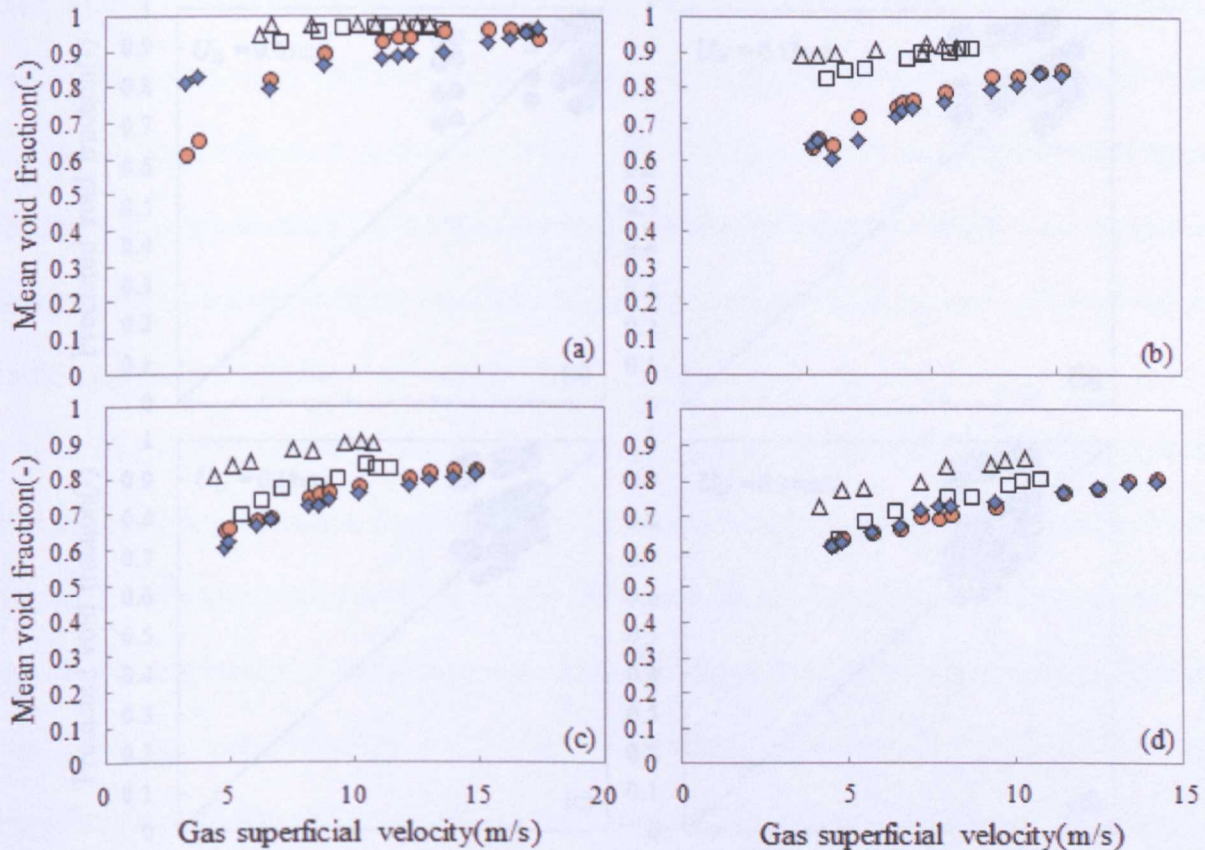


Figure 6.4. Variation of mean void fraction with gas superficial velocity for 12.2cP glycerol solution (\square) and 16.2cP glycerol solution (Δ) with comparisons made with air-water data at $L/D = 35.4$ (\blacklozenge) and 82.7 (\bullet) respectively. (a)-(d) represent constant average liquid superficial velocities of 0.03m/s , 0.11m/s , 0.17m/s and 0.26m/s respectively.

6.2.2. Comparison glycerol-water data with void fraction correlations

Apart from the comparative study of the time spatial maps of air-water and air-glycerol/water carried out by Furukawa and Fukano (2001) for bubbly to annular flows, the experimental mean void fraction data have not been compared to predicted values. In this sub-section, the

experimental void fraction values have been compared to predicted values as shown in Figures 6.5.

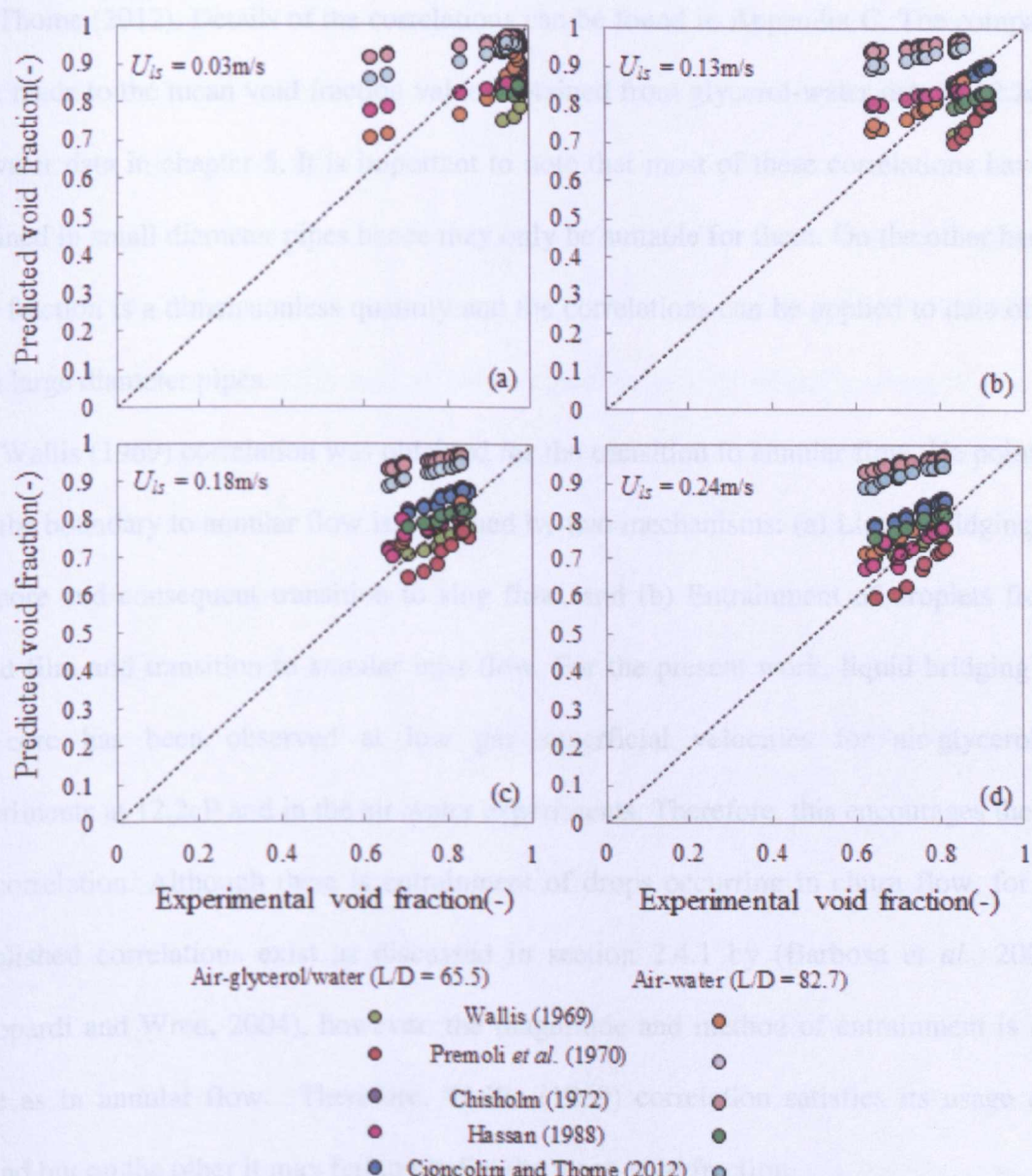


Figure 6.5. Comparison of experimental void fraction for air-glycerol/water at 12.2cP and air-water with predicted void fraction values obtained from correlations proposed by Wallis (1969), Premoli *et al.* (1970), Chisholm (1972), Hassan (1988) and Cioncolini and Thome (2012) respectively. The correlation proposed by these workers can be found in Appendix C. Average liquid superficial velocities have been indicated in plots (a) – (d) respectively.

The correlations used from the oldest to the most recent ones are: Wallis (1969), CISE correlation given by Premoli *et al.* (1970), Chisholm (1972), Hassan (1988) and Cioncolini and Thome (2012). Details of the correlations can be found in Appendix C. The comparisons were made to the mean void fraction values obtained from glycerol-water data at 12.2cP and air-water data in chapter 5. It is important to note that most of these correlations have been obtained in small diameter pipes hence may only be suitable for them. On the other hand, the void fraction is a dimensionless quantity and the correlations can be applied to data obtained from large diameter pipes.

The Wallis (1969) correlation was obtained for the transition to annular flow. He pointed out that the boundary to annular flow is governed by two mechanisms: (a) Liquid bridging of the gas core and consequent transition to slug flow, and (b) Entrainment of droplets from the liquid film and transition to annular mist flow. For the present work, liquid bridging of the gas core has been observed at low gas superficial velocities for air-glycerol/water experiments at 12.2cP and in the air-water experiments. Therefore, this encourages the use of the correlation. Although there is entrainment of drops occurring in churn flow, for which established correlations exist as discussed in section 2.4.1 by (Barbosa *et al.*, 2002 and Azzopardi and Wren, 2004), however, the magnitude and method of entrainment is not the same as in annular flow. Therefore, Wallis (1969) correlation satisfies its usage on one ground but on the other it may fail to predict the mean void fraction.

It shows in Figure 6.5 that the predicted void fraction values does not agree well with the experimental void fraction value for the air-glycerol/water data when the liquid superficial velocities are 0.03m/s and 0.13m/s respectively. However, the predicted void fraction values begins to agree well with the experimental void fraction values when $U_{ls} > 0.13\text{m/s}$. In the case of the air-water predicted void fraction values, the Wallis (1969) correlation agrees quite well for liquid superficial velocities of 0.13m/s, 0.18m/s and 0.24m/s respectively. The main

difference between both cases is that at a liquid superficial velocity of 0.13m/s, liquid bridging of the gas core was not observed for the air-glycerol/water experiments compared to the air-water experiments.

The Premoli *et al.* (1970) correlation also known as the CISE does not properly predict the void fraction for both air-glycerol/water and air-water experiments at respective liquid superficial velocities. Szalinski *et al.* (2010) also showed that this correlation over predicts the void fraction when used in their case for air-water and air-silicone oil. The Chisholm (1972) correlation agrees quite well at lower liquid superficial velocities, that is, at 0.03m/s and 0.13m/s for air-glycerol/water. When the liquid superficial velocity is increased, the correlation over predicts the void fraction. The prediction of void fraction by the Chisholm (1972) for air-water is not successful for each respective liquid superficial velocity. The correlation of Hassan (1988) agrees quite well with the experimental void fraction for both air-glycerol/water and air-water for $U_{ls} > 0.03\text{m/s}$. This equation was retrieved from the work of (Wang *et al.*, 2012). They used it to predict the total pressure drop.

Interestingly, the correlation of Cioncolini and Thome (2012) used in predicting the void fraction, follows the same trend to the simple correlation of Chisholm (1972) for both air-water and air-glycerol/water. The correlation of Chisholm (1972) used a slip ratio, which is substituted in the homogenous void fraction equation to obtain a predicted mean void fraction. On the other hand, the correlation of Cioncolini and Thome (2012) uses the Hill function to predict the void fraction. The void fraction correlation developed by Cioncolini and Thome (2012) is specifically designed for cases where annular flow is the presiding flow pattern. Therefore, this agrees with the data when the liquid superficial velocity is low. In fact, they suggested the correlation works well when the void fraction is between 0.7-1.

In consideration of the established correlation above, there may not be any one correlation that can predict the void fraction in churn flow, even when the liquid viscosity is taken into

consideration. However, one thing is certain, which is that some predicted correlations work well at low liquid superficial velocity but not at high liquid superficial velocity and vice versa. This is because as the liquid superficial velocity in churn flow increases, the flow is more oscillatory and has a chaotic nature.

From work of Azzopardi (2012), he stated that churn flow fits into the Edward Lorenz definition of chaos “it is not random but looks random”. Using Lorenz (1963) approach, a reasonable void fraction model may probably be obtained that predicts the void fraction under churn flow operating conditions. However, based on Figure 6.5, the equation of Wallis (1969) and Hassan (1988) give good prediction of the void fraction in churn flow.

6.2.3. Probability density function (PDF) of time series data

In addition to the mean void fraction of the time series data set earlier obtained, the probability density distribution of the void fraction has also been used as a quantitative measure. This shows that the probability of the void fraction is within a specific range, in this case, 0 – 1.

Comparisons were made with the air-water data on the same plot in Figures 6.6 and 6.7. Since it has been clarified above that increasing the viscosity increases the void fraction, there is a shift in the probability distribution from left to right. The proximity to a void fraction value of 1 at low liquid superficial velocity is indicative of an annular flow pattern distribution as suggested by (Costigan and Whalley, 1997). The characteristic of the annular flow pattern PDF has the void fraction tending to 1 and a short tail towards low void fraction. Therefore, it can be said that the second and third plots at low liquid superficial velocity, although within the churn flow, have a probability distribution typical of annular flow. However, this is in reference to glycerol/water data. From visual observation, the flow is not

annular, that is, the film does not move continuously upwards as the gas inertia is not sufficient to cause this to occur.

Increasing the liquid superficial velocity in (1b) and (1c) increases the area under the probability distribution respectively. For the glycerol/water data, one will expect that the distribution will have the same shape as that of air-water with a shift to the right. However, this is not the case as another distinct peak apart from the peak at the mean value can be observed. The other peak appears under the air-water probability distribution for (1b) and (1c).

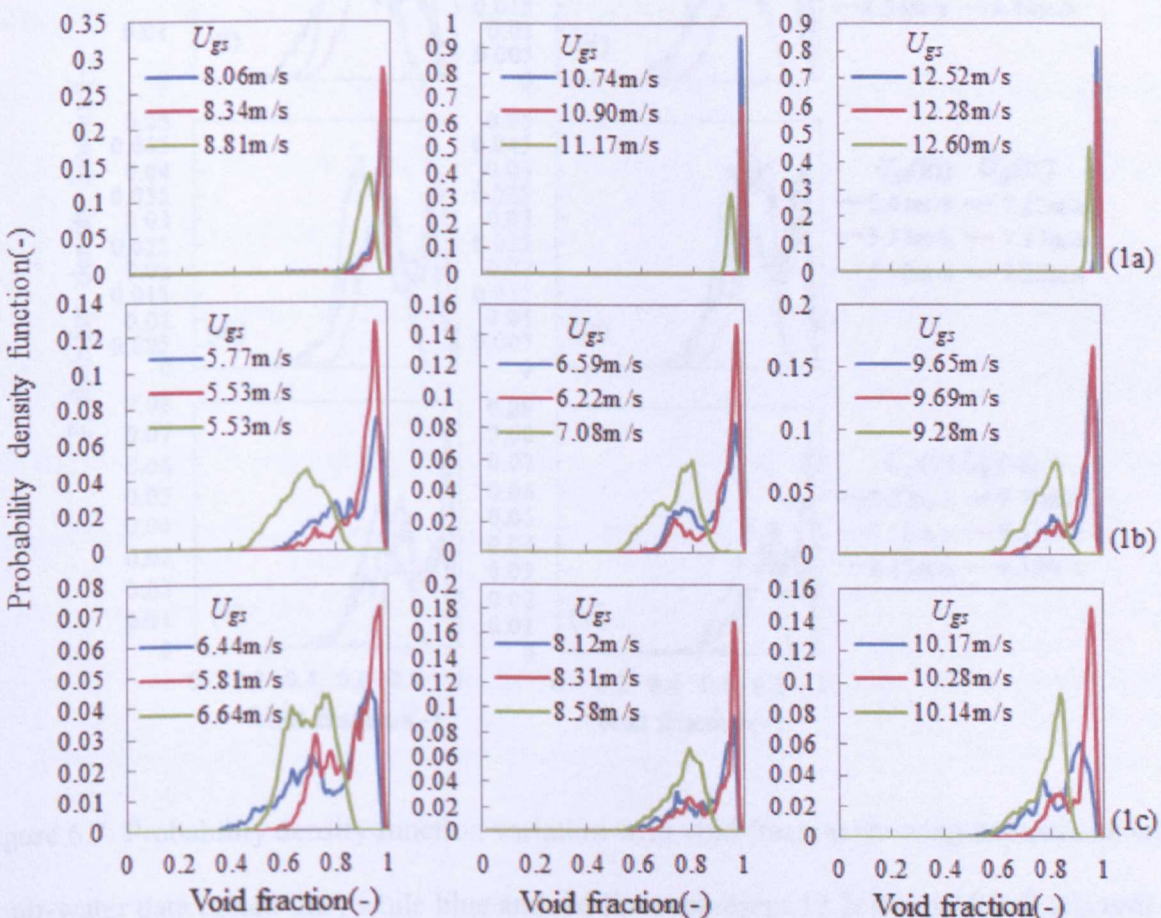


Figure 6.6. Probability density function variation with void fraction showing comparison with air-water data (green line) while blue and red lines represent 12.2cP and 16.2cP glycerol solutions respectively. (1a)-(1c) represent average constant liquid superficial velocity of 0.03m/s, 0.11m/s and 0.18m/s respectively.

For a higher liquid superficial velocity in Figure 6.7, more comparisons can be found between operating conditions utilized. Compared to the air-water, two peaks can be clearly identified. This is because for air-glycerol-water, the frequency and size of the liquid strictures entrained in the core increases. Therefore, this gives a second peak at lower void fractions.

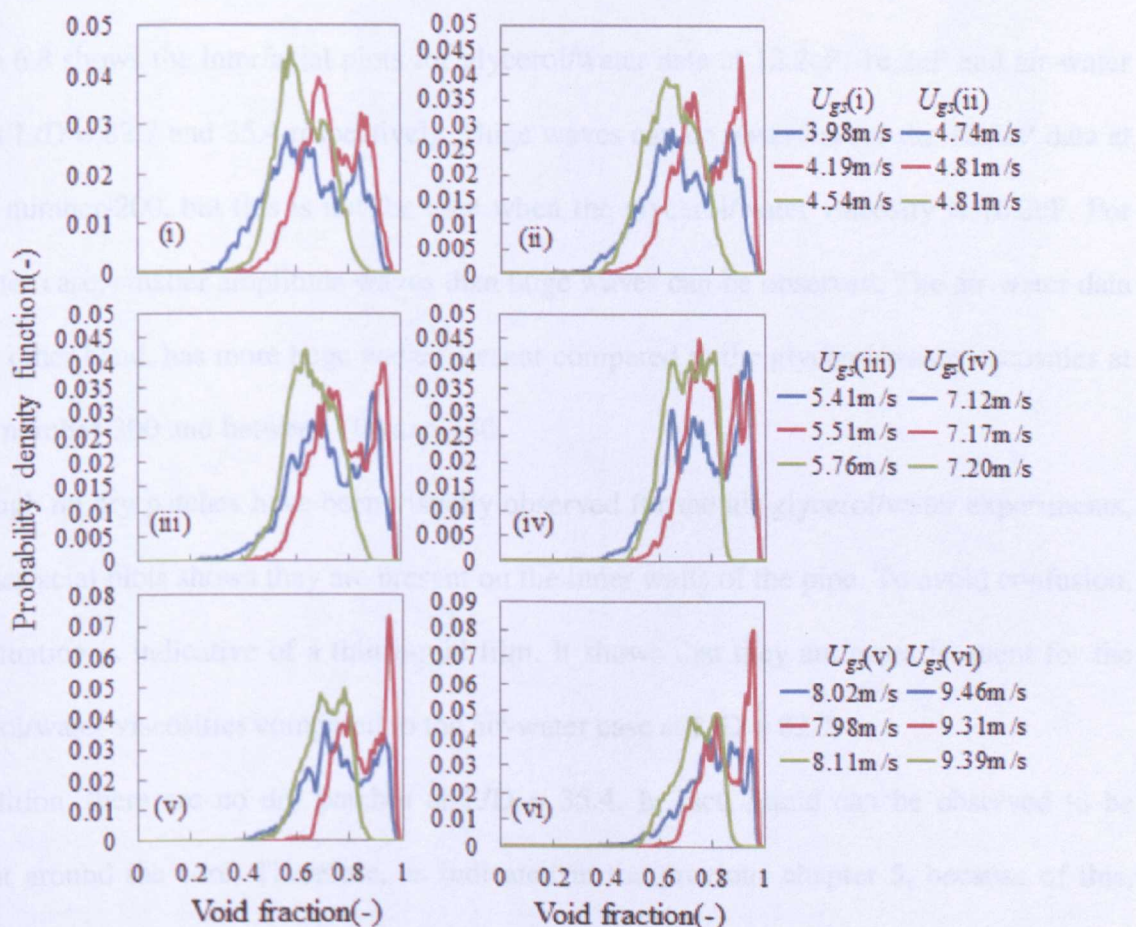


Figure 6.7. Probability density function variation with void fraction showing comparison with air-water data (green line) while blue and red lines represent 12.2cP and 16.2cP glycerol solutions respectively for an average constant liquid superficial velocity of 0.26m/s. More comparisons can be made at this liquid superficial velocity.

6.2.4. Comparison of interfacial structures for air-glycerol/water and air-water

The interfacial structures represent the formation of structures that are present within the pipe cross-section for a particular gas and liquid superficial velocity. The reason for the presence of structures in the core is because there is a competition between flow field forces that give rise to them. The interfacial plots have been obtained from the three dimensional void fraction data.

Figure 6.8 shows the interfacial plots for glycerol/water data at 12.2cP, 16.2cP and air-water data at $L/D = 82.7$ and 35.4 respectively. Huge waves can be observed for the 12.2cP data at frame number-200, but this is not the case when the glycerol/water viscosity is 16.2cP. For the latter case, smaller amplitude waves than huge waves can be observed. The air-water data on the other hand, has more huge waves present compared to the glycerol/water viscosities at frame number-300 and between 100 and 150.

Although no dry patches have been visually observed for the air-glycerol/water experiments, the interfacial plots shows they are present on the inner walls of the pipe. To avoid confusion, this situation is indicative of a thin liquid film. It shows that they are more frequent for the glycerol/water viscosities compared to the air-water case at $L/D = 82.7$.

In addition, there are no dry patches at $L/D = 35.4$. In fact, liquid can be observed to be present around the core. Therefore, as indicated in the previous chapter 5, because of this, liquid bridging of the gas core becomes frequent at this location. Small amplitude waves are present for all cases and there are also entrained liquid structures present. However, the frequency of the entrained liquid structures is lowest for air-water at $L/D = 35.4$. This confirms the fact that when the liquid viscosity increases, the liquid structures entrained in the core are larger for air-glycerol/water compared to the air-water case because less energy is being dissipated. This is the reason for the other distinct peak at a lower void fraction for the air-glycerol/water cases in the PDF plots in Figure 6.6 and 6.7.

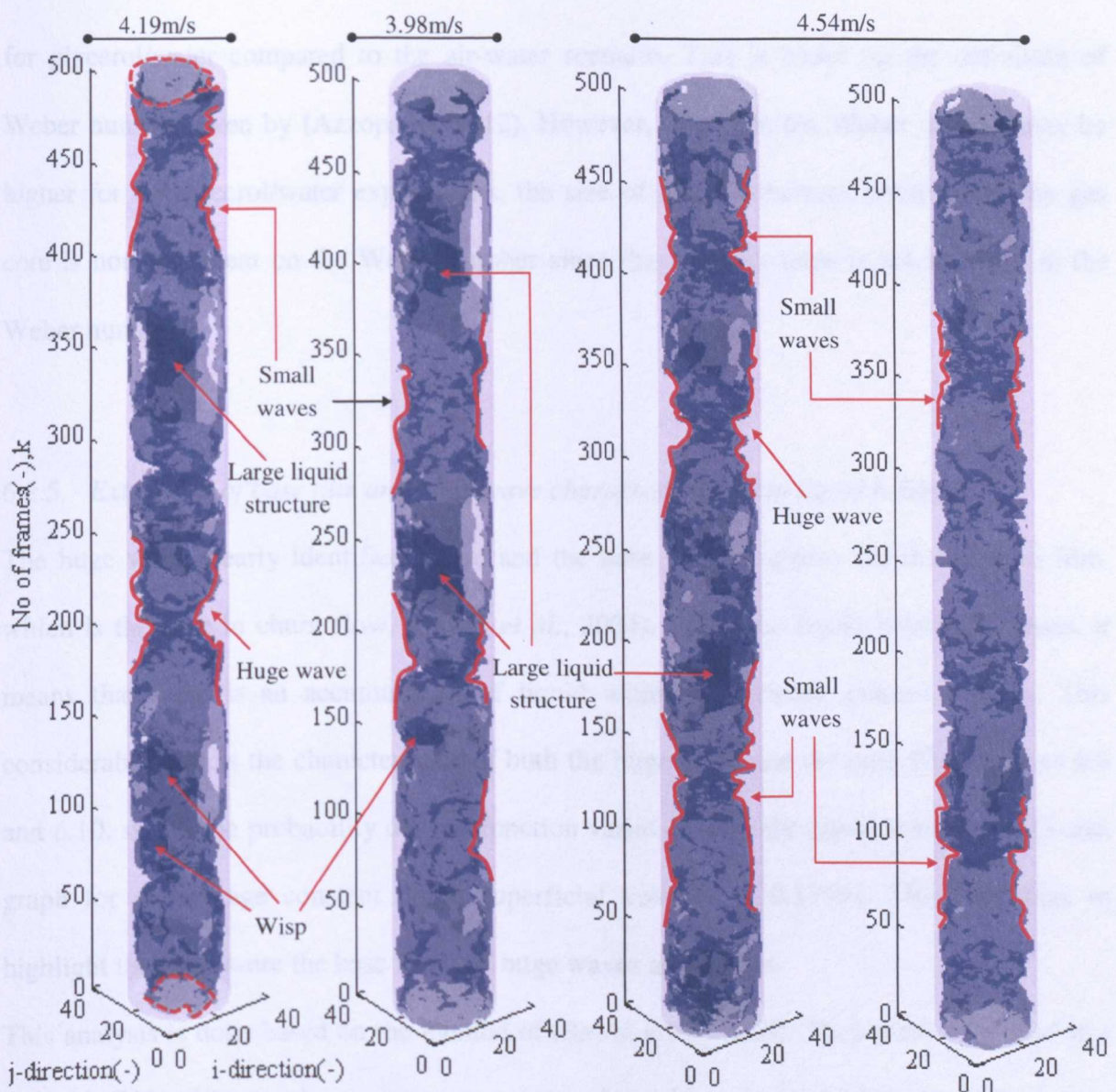


Figure 6.8. Comparison of interfacial structures for 12.2cP, 16.2cP glycerol solutions and air-water data at $L/D = 82.7$ and 35.4 respectively for an average constant liquid superficial of 0.24m/s . Gas superficial velocity are indicated atop structures. The small waves that have been identified have smaller amplitudes than huge waves.

On the other hand, when the liquid viscosity is increased, the liquid holdup decreases. Therefore, this makes the film thinner having a similar behaviour to annular flow. Since in annular flow the wave velocity is low, (Azzopardi, 1997), this also gives a low wave velocity for the air-glycerol/water experiments. Therefore, a higher Weber number may be obtained

for glycerol/water compared to the air-water scenario. This is based on the definition of Weber number given by (Azzopardi, 2012). However, although, the Weber number may be higher for air-glycerol/water experiments, the size of liquid structures entrained in the gas core is not dependent on the Weber number since the viscosity term is not included in the Weber number.

6.2.5. Extraction of base film and huge wave characteristics from liquid holdup

The huge wave clearly identified above and the base film comprises the thick liquid film, which is the case in churn flow, (Sawai *et al.*, 2004). When the liquid holdup increases, it means that there is an accumulation of liquid within a reference control volume. This considerably affects the characteristics of both the huge wave and the base film. Figures 6.9 and 6.10, shows the probability density function variation with the liquid holdup in 2-D area graph for an average constant liquid superficial velocity of 0.17m/s. This was done to highlight the areas where the base film and huge waves are present.

This analysis is done based on the method of (Sawai *et al.*, 2004). They previously used this method of identification by assuming symmetry about the mean liquid holdup. In their case, the pipe diameter was 25.8mm and air and water were used as the fluid phases. The probability distribution of the liquid holdup in their work did not have distortions to the peak. Therefore, it was easier to assume symmetry around the mean liquid holdup. However, this is not the case in the present work as can be observed in Figures 6.9 and 6.10.

To overcome this problem, two peaks occurring at low liquid holdup were identified. The base film liquid holdup may not be the same as the overall liquid holdup as proposed by (Sawai *et al.*, 2004). However in corroboration with their work and as a method of simplification, the base film symmetry has been assumed. The symmetry in the base film means that the structures of the base film about the pipe centre line, flowing below the huge

wave are the same. As expected, the area for the huge waves is larger for the 12.2cP glycerol/water data compared to 16.2cP glycerol/water data. The huge wave area is indicated as green and purple respectively for both glycerol/water probability distributions were the demarcated areas decreases with increasing gas superficial velocity.

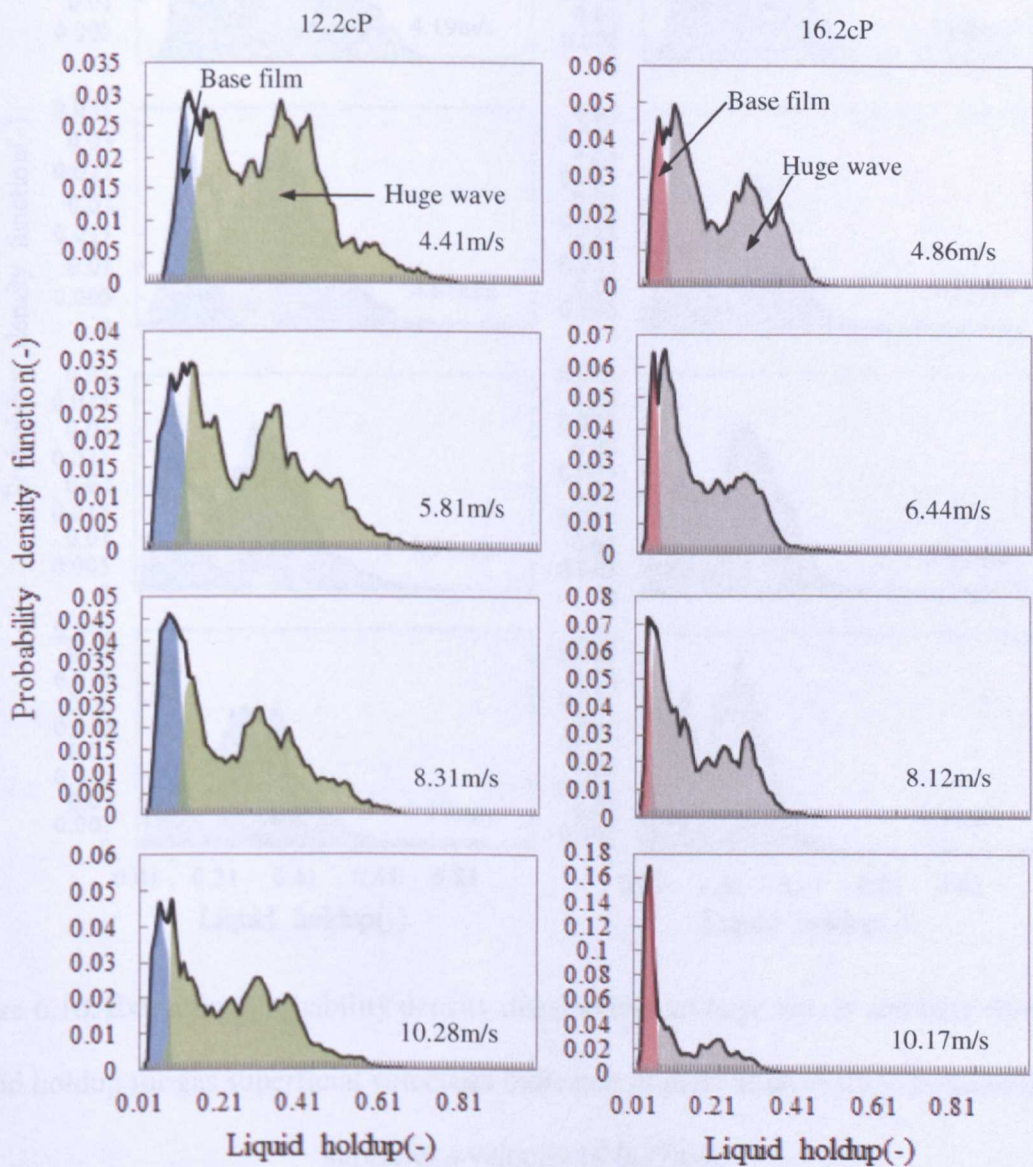


Figure 6.9. Extracting probability density distributions of huge waves and base film from liquid holdup for gas superficial velocities indicated in plots at an average constant liquid superficial velocity of 0.17m/s.

huge wave rather than a separate entity. In other words, the well-defined peaks on the density function are associated with liquid holdup values corresponding to different liquid structures.

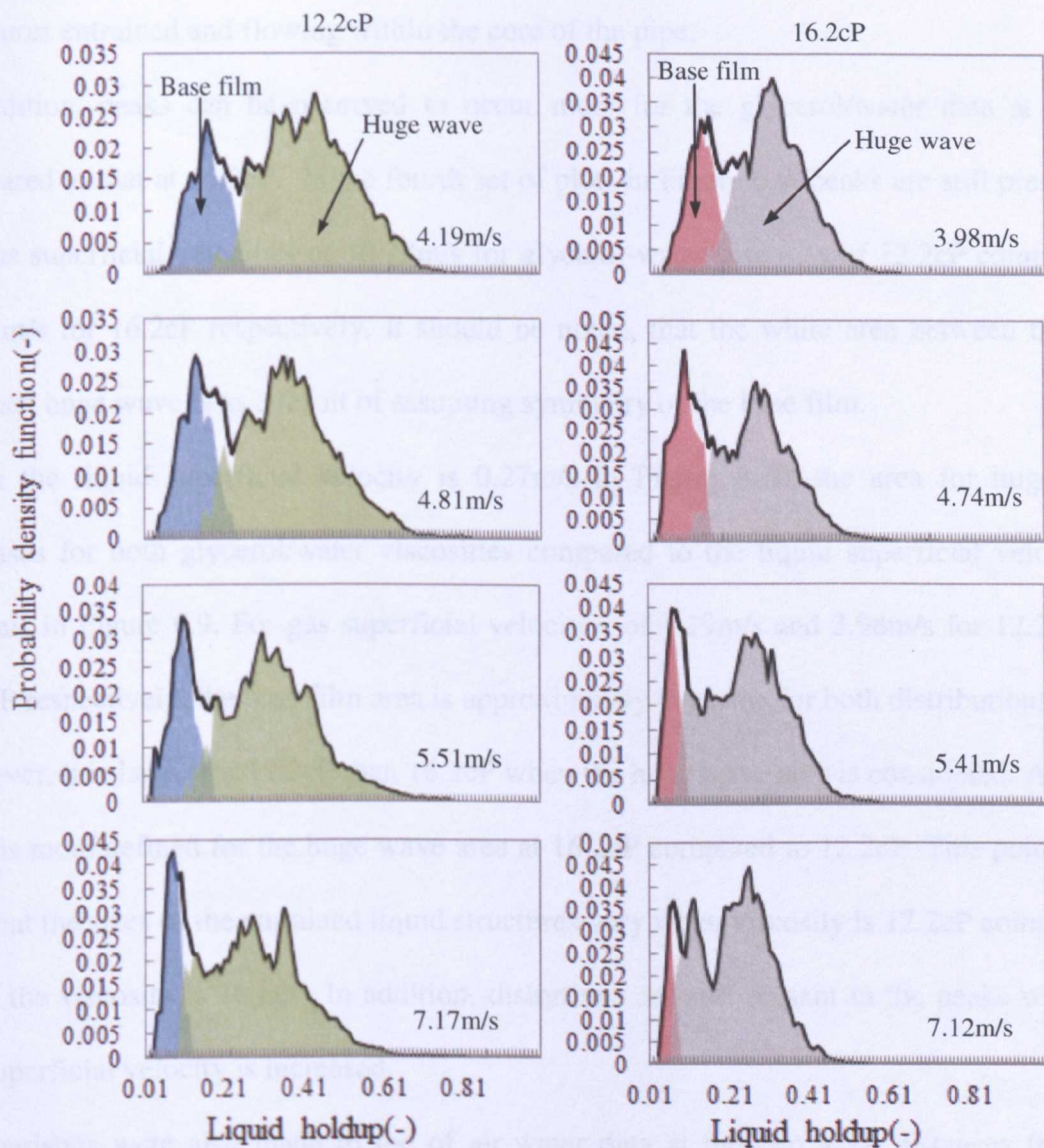


Figure 6.10. Extracting Probability density distributions of huge waves and base film from liquid holdup for gas superficial velocities indicated in plots at an average constant liquid superficial velocity of 0.27m/s.

The probability distribution for the huge wave has various peaks. This is indicative of large liquid structures formed from the huge waves. It also means that the probability distribution of the liquid structures may not be successfully extracted. Therefore, it is probably better to approach it from the perspective that the wisps/large liquid structures are formed from the

huge wave rather than a separate entity. In other words, the well-defined peaks on the demarcated huge wave region at high liquid holdup refer to the presence of large liquid structures entrained and flowing within the core of the pipe.

In addition, peaks can be observed to occur more for the glycerol/water data at 12.2cP compared to that at 16.2cP. In the fourth set of plots in Figure 6.9, peaks are still present for the gas superficial velocities of 10.28m/s for glycerol-water viscosity of 12.2cP compared to 10.17m/s for 16.2cP respectively. It should be noted, that the white area between the base film and huge wave is as a result of assuming symmetry of the base film.

When the liquid superficial velocity is 0.27m/s in Figure 6.10, the area for huge wave increases for both glycerol/water viscosities compared to the liquid superficial velocity of 0.17m/s in Figure 6.9. For gas superficial velocities of 4.19m/s and 3.98m/s for 12.2cP and 16.2cP respectively, the base film area is approximately the same for both distributions.

However, it is larger for 12.2cP than 16.2cP when the huge wave area is considered. Also, the peak is more defined for the huge wave area at 16.2cP compared to 12.2cP. This point to the fact that the sizes of the entrained liquid structures vary when viscosity is 12.2cP compared to when the viscosity is 16.2cP. In addition, distortions are still present in the peaks when the gas superficial velocity is increased.

Comparisons were also made to the air-water data at the two axial distances from the injection where data was acquired. This has been shown in Figures 6.11 and 6.12. The blue, red, green and purple distributions are for air-water two axial distances (upstream- $L/D = 35.4$ and downstream- $L/D = 82.7$) and glycerol-water viscosity of 12.2cP and 16.2cP respectively at $L/D = 65.5$. The operating condition used in the previous plots above is the same here with approximate conditions for air-water. The shift in probability distribution from right to left is in the direction of lower liquid holdup. Clearly, this means that the liquid holdup is highest for air-water at $L/D = 35.4$ than at $L/D = 82.7$ and glycerol-water data.

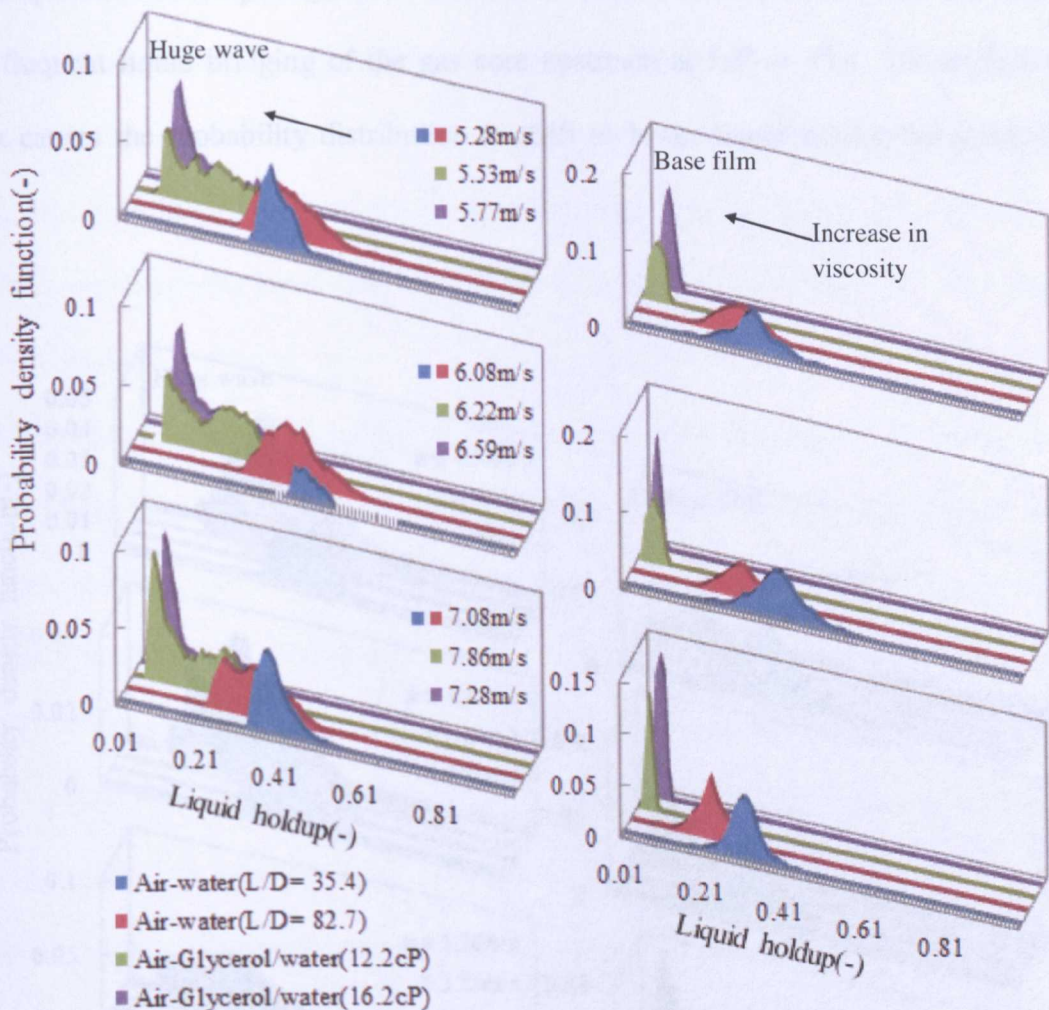


Figure 6.11. Area plot of huge wave and base film showing comparison with glycerol-water solutions and air-water data with gas superficial velocities indicated in plots for an average constant liquid superficial velocity of 0.11m/s.

In comparing both air-water data, the area under the huge wave probability distribution is larger downstream than upstream. From visual observation and the analysis carried out in chapter 5, the frequency of liquid bridging of the gas core is higher upstream than downstream. Since the hydrostatic pressure increases with height, there is more volume of liquid accumulated upstream. Therefore, the gas flowing upwards encounters more volume of

liquid upstream. Consequently, this induces the formation of huge waves, which coalesces to give frequent liquid bridging of the gas core upstream at $L/D = 35.4$. The surface tension effect causes the probability distribution to shift to lower liquid holdup for glycerol-water cases. As liquid holdup is low, the peak of the huge wave distribution is shifted towards the right.

16.2.1. Comparison of the other data. This is a clear indication of a sharp transition in the

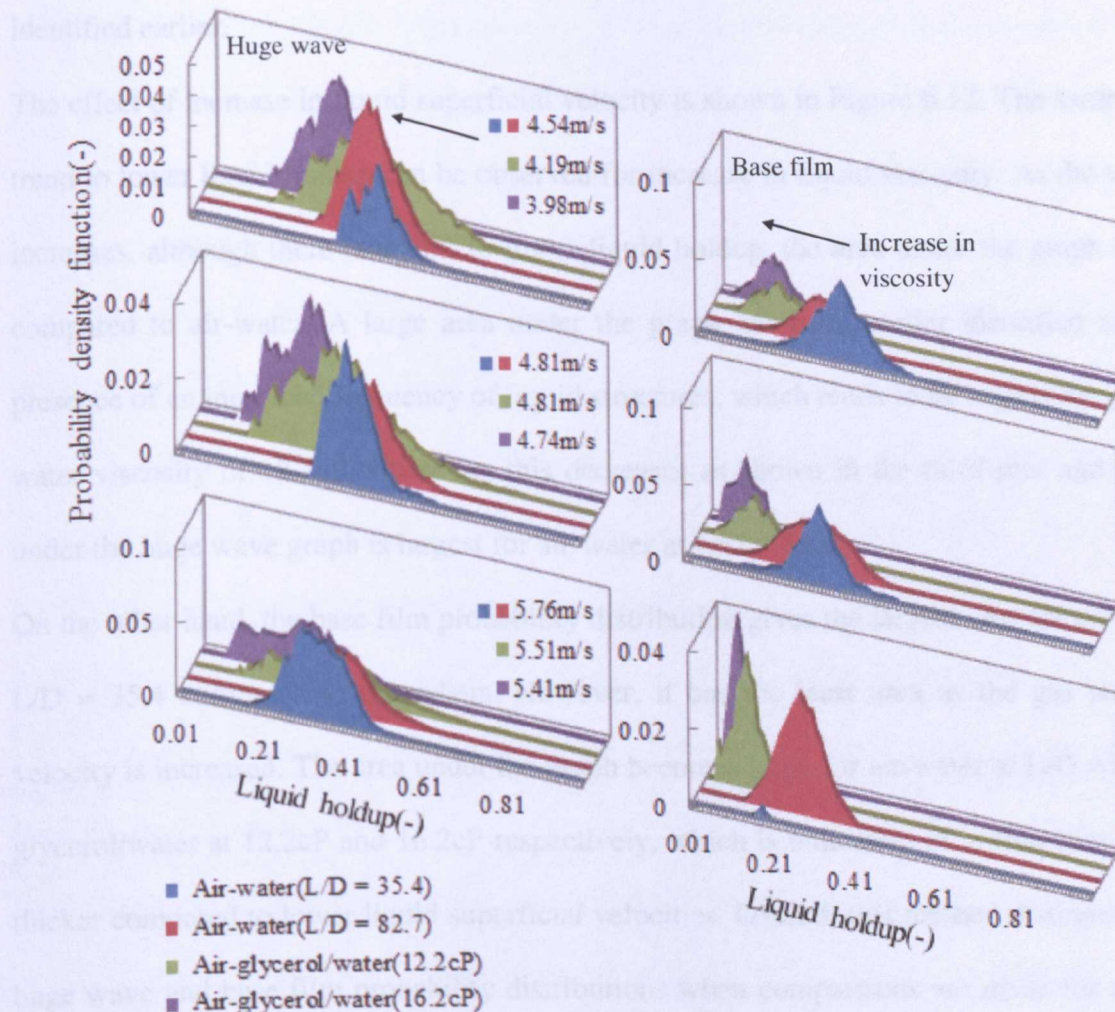


Figure 6.12. Area plots of huge wave and base film showing comparison with glycerol-water solutions and air-water data with gas superficial velocities indicated in plots for an average constant liquid superficial velocity of 0.27m/s.

On the other hand, as regards the base film probability distribution, bubble entrainment in the base film should cause the base film to depart from the form of pure liquid. The area under the base film is larger for the air-water data compared to both glycerol/water data. Although, when the liquid holdup is low, the peak of the base film is highest for glycerol/water at 16.2cP compared to the other data. This is a clear indication of a thin base film, which was identified earlier.

The effect of increase in liquid superficial velocity is shown in Figure 6.12. The same shift in trend to lower liquid holdup can be observed for increase in liquid viscosity. As the viscosity increases, although there is a shift to lower liquid holdup, the area under the graph is larger compared to air-water. A large area under the graph has been earlier identified to be the presence of an increased frequency of liquid structures, which tends to be largest for glycerol-water viscosity of 12.2cP. However, this decreases as shown in the third plot and the area under the huge wave graph is largest for air-water at $L/D = 35.4$.

On the other hand, the base film probability distribution gives the largest area for air-water at $L/D = 35.4$ compared to the others. However, it has the least area as the gas superficial velocity is increased. The area under the graph becomes large for air-water at $L/D = 82.7$ and glycerol/water at 12.2cP and 16.2cP respectively, which is indicative of a thin base film but thicker compared to lower liquid superficial velocities. Overall, this method distinguishes the huge wave and base film probability distributions when comparisons are made for air-water and air-glycerol/water.

6.2.6. Analysis of time series in frequency domain

In churn flow, the flow is inherently chaotic and has this behaviour to the highest degree compared to other flow regimes: bubbly, slug and annular. Spectral analysis of the time series data in the frequency domain reveals the inherent chaotic flow behaviour. Auto-correlation function has been initially used as a method of revealing this behaviour by correlating the time series signal with itself. It can be referred to as the normalized auto-covariance function given below with reference to equation (4.7) in chapter 4:

$$c_{xx}(k\Delta\tau) = \frac{C_{xx}(k\Delta\tau)}{C_{xx}(0)} \quad (6.1)$$

According to Cai *et al.* (1995), for a chaotic time series data such as in the case of churn flow, information about its past is lost. Therefore, the signal is only correlated with its recent past. The importance of calculating the auto-correlation function is to have knowledge of the optimum time delay. This value is estimated to be the smallest time at which the first minimum in the auto-correlation function occurs. Also, calculating the auto-correlation function enables dominant periods to be identified. The auto-correlation has been carried out and presented in the subsequent plots for air-glycerol/water and further comparisons have been made to air-water.

In Figure 6.13, the auto-correlation is varied with delay time for the glycerol/water viscosity of 12.2cP and a liquid superficial velocity of 0.17m/s. When the gas superficial velocity is increased from 4.19m/s, a large dip in the profile can be observed. Also, there a shift in the profile to a higher delay time when the gas superficial velocity is 7.17m/s. An increase to a gas superficial velocity of 7.98m/s gives the same delay time but with an increase in profile. This shows that the periodicity of the structures present decreases at higher gas superficial velocities. In relation to the physical nature of the flow, this can be interpreted to be the occurrence of liquid bridging of the gas core and the presence of entrained liquid structures.

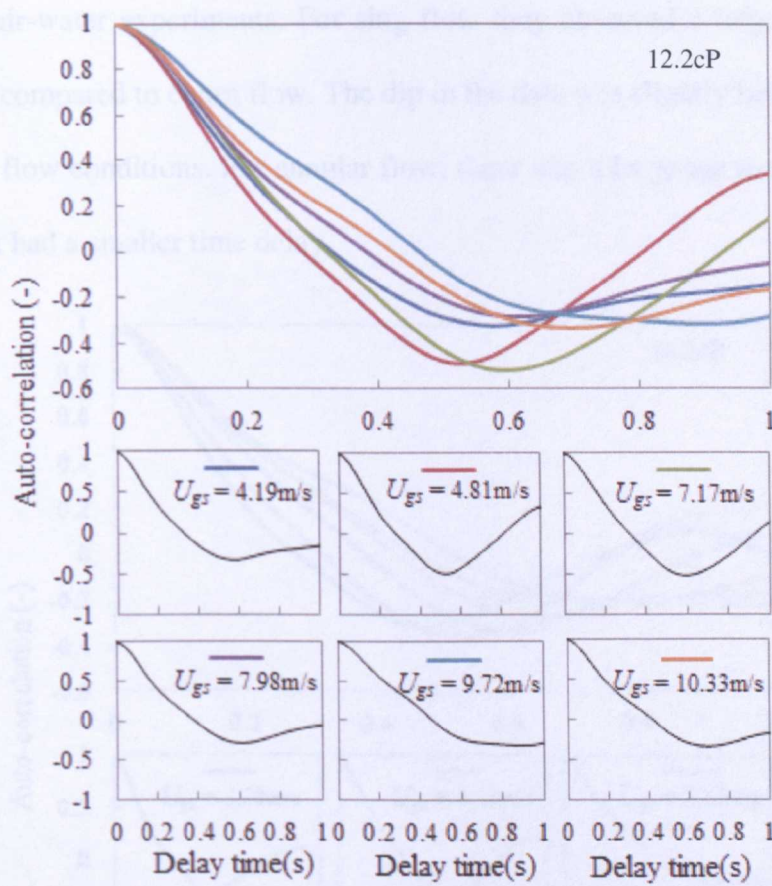


Figure 6.13. Autocorrelation variations with delay time at liquid superficial velocity of 0.27m/s for glycerol-water solution of 12.2cP. Auto-correlation of the time series data is carried out since we are dealing with a chaotic time series data.

Liquid bridging has been observed to have lower transit velocities compared to huge waves from the air-water experiments in chapter 5, section 5.2.3. Therefore, it is possible that the lower time lag with a dip at a gas superficial velocity of 4.81m/s is indicative of liquid bridging and simultaneous entrainment of liquid structures, while the higher time lag with the absence of a dip is for the occurrence of only liquid structures entrained in the core. The same behaviour of delay time shift can also be observed when the viscosity is increased to 16.2cP in Figure 6.14. Kaji (2008) also calculated the auto-correlation from their void fraction data and used it to distinguish between slug, slug-churn transition, churn and annular

flows for their air-water experiments. For slug flow they observed a large dip of negative auto-correlation compared to churn flow. The dip in the data was slightly beyond the negative x -axis for churn flow conditions. For annular flow, there was a large dip in their data such as for slug flow but had a smaller time delay.

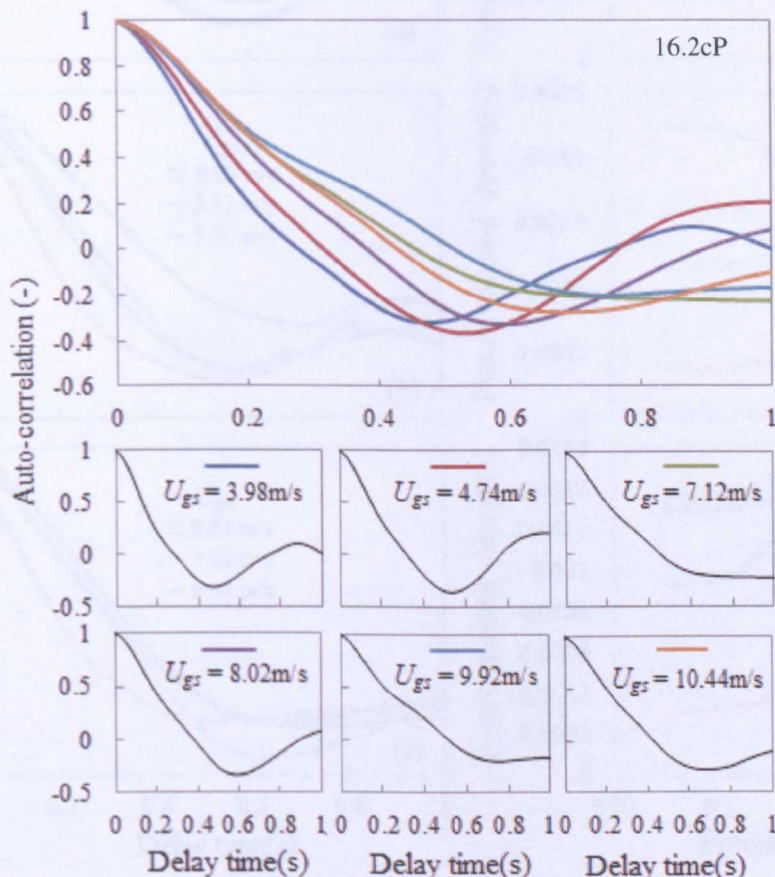


Figure 6.14. Autocorrelation variations with delay time at liquid superficial velocity of 0.26m/s for glycerol-water solution of 16.2cP. Auto-correlation of the time series data is carried out since we are dealing with a chaotic time series data.

In comparison to Kaji's air-water ACF plots, it shows that there is a discrepancy between the periodicity of churn flow in their experiment and the present case. This is because the delay time is larger for the present work compared to his. It is important to note that his data was obtained in a 19mm internal diameter pipe, thus could be a plausible reason for the marked difference.

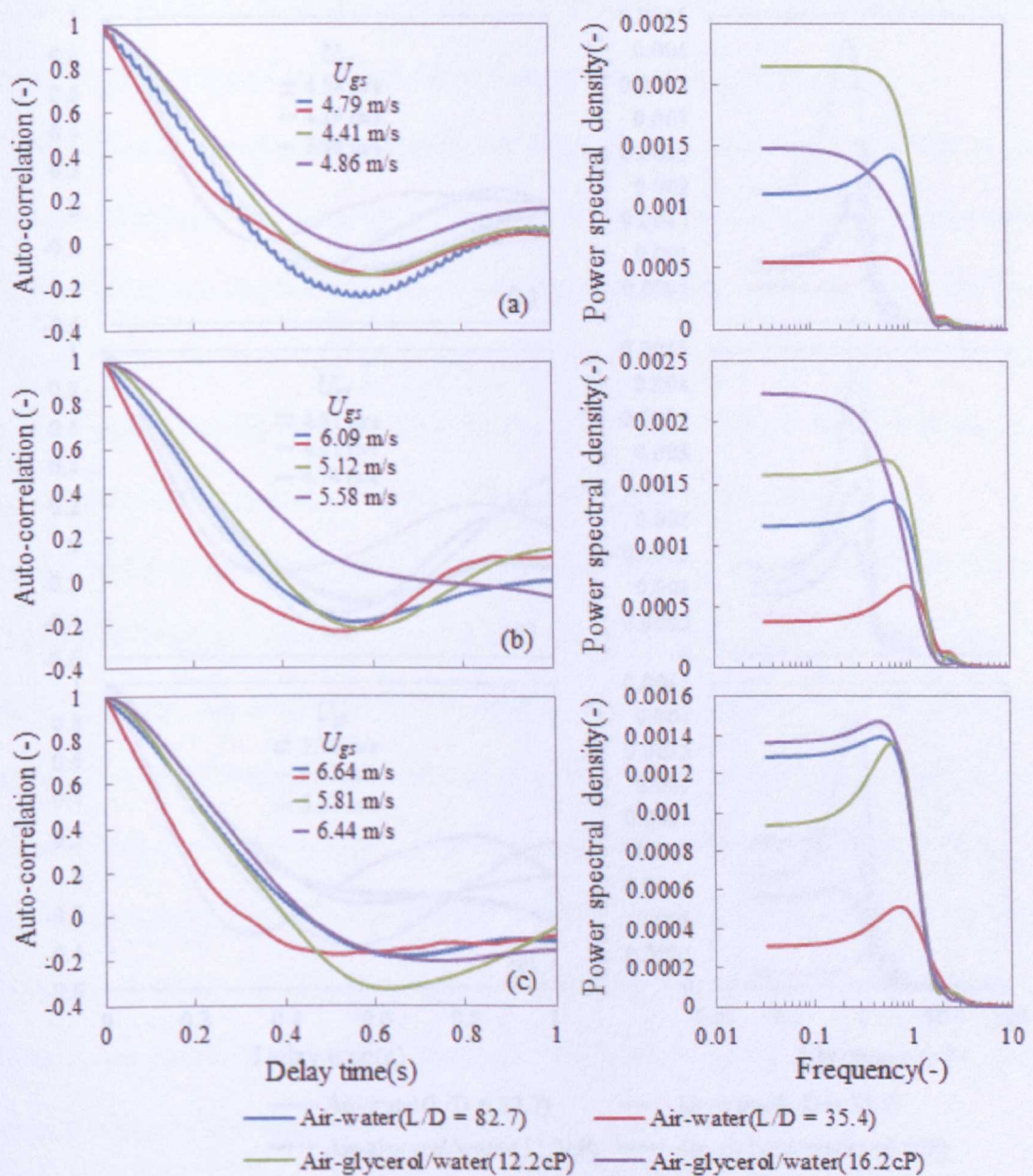


Figure 6.15. Autocorrelation variation with time and power spectral density against frequency placed side by side for glycerol-water solutions and air-water data at axial distances of $L/D = 35.4$ and 82.7 for average constant liquid superficial velocity in (a)-(c) of 0.11m/s .

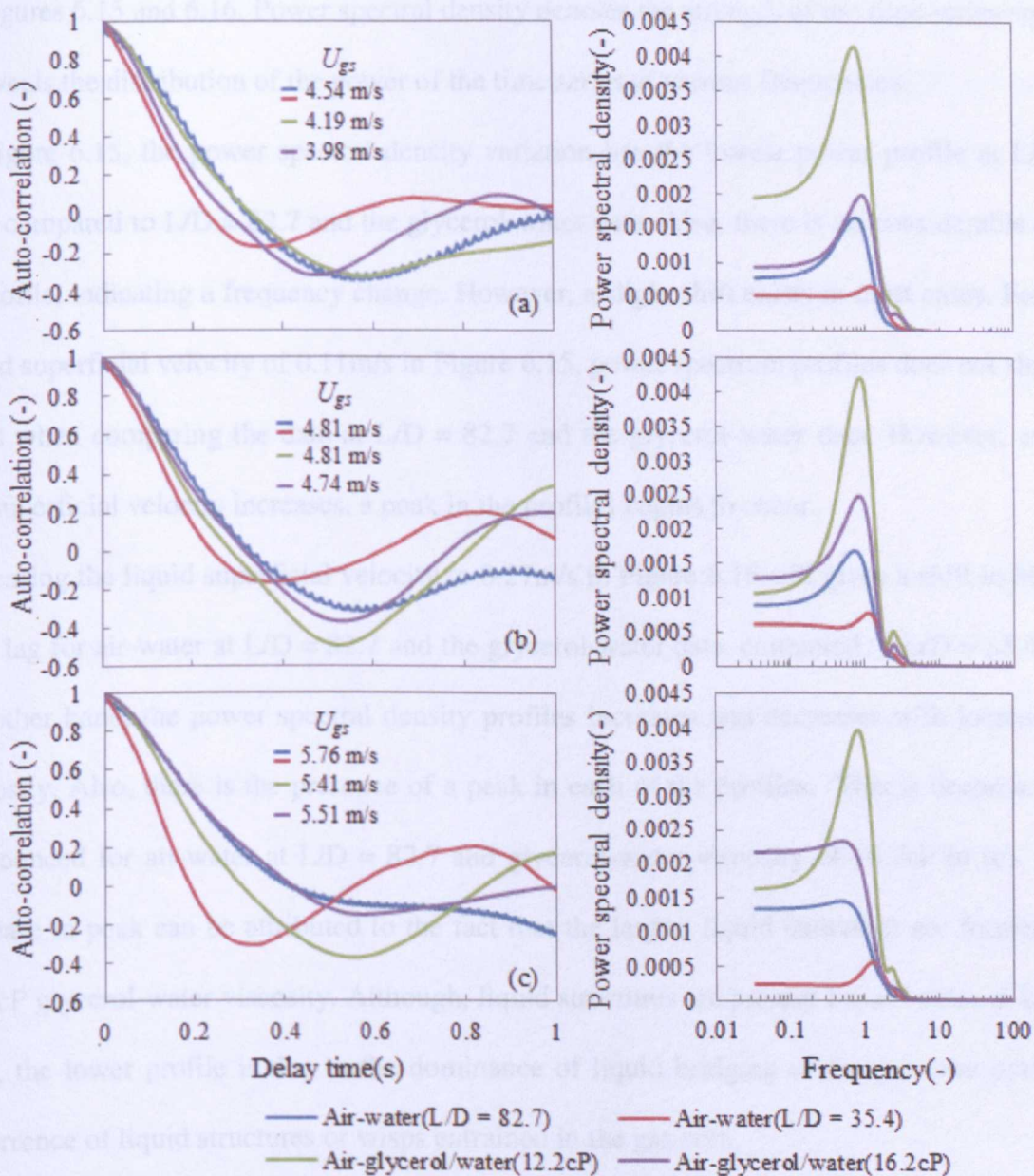


Figure 6.16. Autocorrelation variation with time and power spectral density against frequency placed side by side for glycerol-water solutions and air-water data at axial distances of $L/D = 35.4$ and 82.7 for constant liquid superficial velocity of 0.27 m/s .

Figure 6.15 and 6.16, shows the comparison of the auto-correlation functions with data for air-water at $L/D = 35.4$ and 82.7 . Increasing the viscosity leads to an increase in the profile of the auto-correlation function. Also there is a shift to the right to a higher time delays. Fourier transform of the auto-covariance function was also used to obtain the power spectral density

in Figures 6.15 and 6.16. Power spectral density denotes the strength of the time series signal.

It reveals the distribution of the power of the time series at various frequencies.

In Figure 6.15, the power spectral density variation has the lowest power profile at $L/D = 35.4$ compared to $L/D = 82.7$ and the glycerol-water data. Also, there is no considerable shift in profile, indicating a frequency change. However, a slight shift exists in most cases. For the liquid superficial velocity of 0.11m/s in Figure 6.15, power spectrum profiles does not show a trend when comparing the data at $L/D = 82.7$ and the glycerol-water data. However, as the gas superficial velocity increases, a peak in the profiles begins to occur.

Increasing the liquid superficial velocity to 0.27m/s in Figure 6.16 still gives a shift to higher time lag for air-water at $L/D = 82.7$ and the glycerol-water data, compared to $L/D = 35.4$. On the other hand, the power spectral density profiles increases and decreases with increase in viscosity. Also, there is the presence of a peak in each of the profiles. This becomes less pronounced for air-water at $L/D = 82.7$ and glycerol-water viscosity of 16.2cP in (c). The increase in peak can be attributed to the fact that the largest liquid structures are formed for 12.2cP glycerol-water viscosity. Although, liquid structures are present for air-water at $L/D = 35.4$, the lower profile is due to the dominance of liquid bridging of the gas core over the occurrence of liquid structures or wisps entrained in the gas core.

The dominant frequencies from the power spectral densities in each case above can also be obtained. Firstly, that of air-glycerol/water case is shown in Figure 6.17. The dominant frequency variation with gas superficial velocity does not have a particular trend. However, when comparing the red lines on both plots for the highest liquid superficial velocity used in both glycerol-water experiments, the dominant frequency generally decreases and increases. Since, liquid bridging of the gas core does not occur at the point of a sudden increase in the dominant frequency, this is probably the occurrence of huge waves or wisps. At lower liquid superficial velocities, indicated by the green line in both plots, the dominant frequency

decreases. This is because the flow becomes less oscillatory as the liquid superficial velocity decreases. Interestingly, the dominant frequency gives a high value at a low liquid superficial velocity and high gas superficial velocity. This may probably be the occurrence of smaller amplitude waves than huge waves previously identified in the interfacial plots in Figure 6.8.

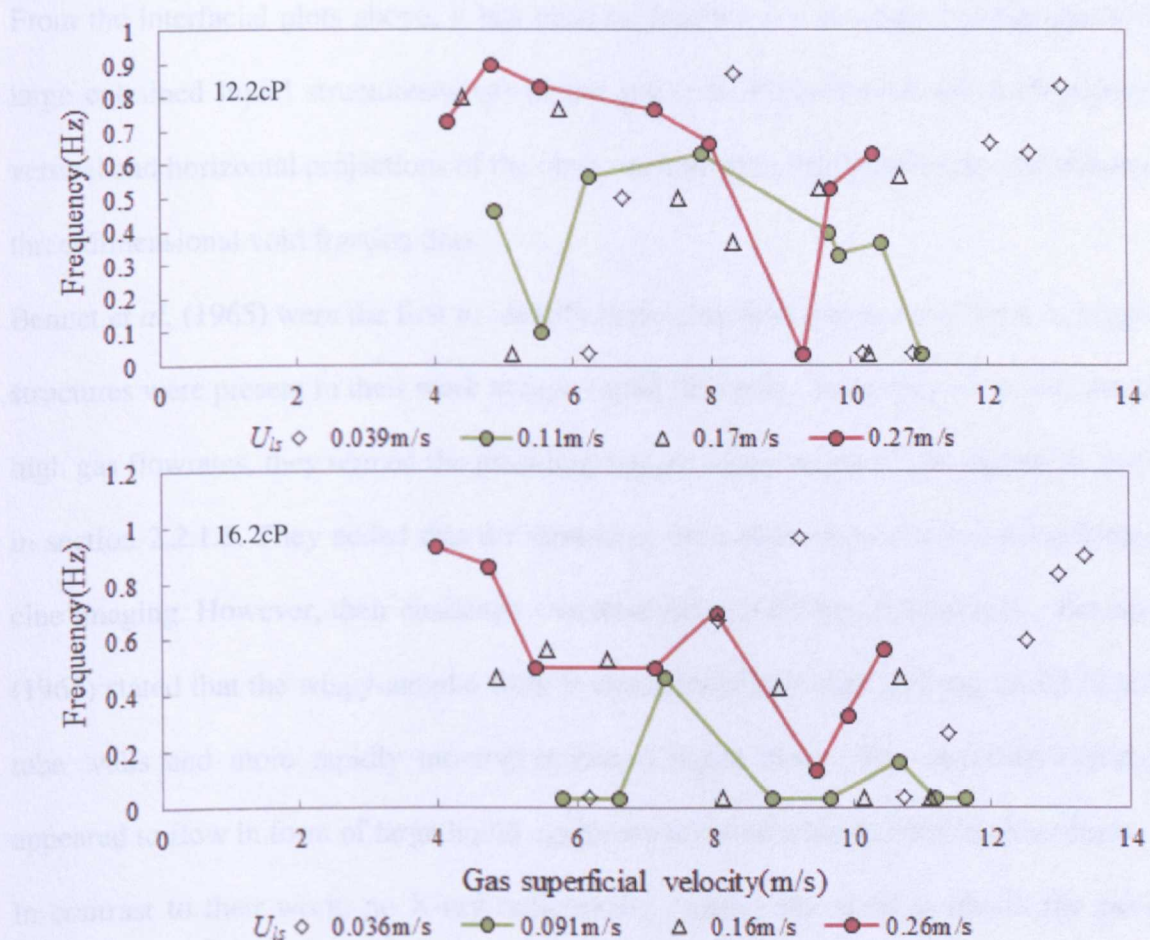


Figure 6.17. Dominant frequency against gas superficial velocity for glycerol-water solutions indicated in plots.

To be able to further distinguish the occurrence of liquid bridging, huge waves and the occurrence of liquid structures, the threshold method to the time series data needs to be applied. Establishing a threshold will enable distinguishing the structures present with reference to the dominant frequency plot. However, before going further to address this issue,

qualitative assessment of liquid structures entrained in the gas core is carried out in the subsection below.

6.2.6.1. Qualitative assessment of entrained liquid structures

From the interfacial plots above, it has been ascertained that the liquid phase also flows as large entrained liquid structures/wisps in the gas core. Figures 6.18 and 6.19 presents the vertical and horizontal projections of the cross-section obtained from the reconstruction of the three-dimensional void fraction data.

Bennet *et al.* (1965) were the first to identify these structures and classify them as wisps. The structures were present in their work at high liquid flowrates. Since they were also working at high gas flowrates, they termed the presiding regime wispy-annular flow regime as discussed in section 2.2.1.5. They added that the structures were difficult to observe using high-speed cine imaging. However, their challenge was resolved using X-ray radiography. Bennet *et al.* (1965) stated that the wispy-annular flow is characterized by slow moving liquid film on the tube walls and more rapidly moving entrained liquid phase. The entrained liquid phase appeared to flow in form of large liquid agglomerates somewhat resembling ectoplasm.

In contrast to their work, no X-ray radiography method was used to obtain the gas-liquid phase distribution with respect to showing the entrained liquid structures as in Figures 6.18 and 6.19. This has been done similar to work of (Hernandez-Perez *et al.*, 2010). From the void data, vertical and horizontal projections of the entire cross section can be obtained. Random frame numbers have been selected that show the entrained liquid structures.

The vertical and horizontal projections are shown on the left and right respectively for each frame number at a 4s time interval. Also, the cross-sectional projection is shown below the vertical and horizontal projections. The view of the cross section X-X is shown for each frame. This has been done for glycerol-water viscosities of 12.2cP and 16.2cP at approximate

gas and liquid superficial velocities respectively. For the frames shown in Figure 6.18, the core is mostly occupied by the gas phase with entrained liquid structures. This has the same form as those observed for wispy-annular flows by (Bennet *et al.*, 1965).

The structures present are irregular and do not have a definite shape. Furthermore, if the frequency should be obtained to ascertain the contribution to the overall dominant frequency in Figure 6.17, they have to be grouped into different sizes. Estimating the size of liquid structures according to its major/minor dimensions and classifying them into probably small, medium and large, could give a more realistic value to the wisp frequency. Wisps greater than a particular threshold size can be considered to be an agglomeration of wisps and should be termed differently. The effect of the increase of liquid viscosity on the size of liquid structures present is shown in Figure 6.19. The sizes of the entrained liquid structures are smaller compared to the 12.2cP phase distributions.

A method of estimating the entrained liquid structures cross-sectionally can be shown in Figure 6.20. The void data of frames 3547 and 10843 in Figure 6.18 were extracted and converted into contour filled plots in MATLAB as shown in Figure 6.20. The gas is indicated as orange while the liquid is blue. This method ensures that a grid is applied to the data thereby giving an estimate of the cross-sectional dimension. This also enables better classification of the entrained liquid structures.

In view of the gas-liquid phase distributions in Figure 6.18 and 6.19 respectively, Figure 6.21 shows the projections of the gas-liquid phase distribution for the same operating conditions in Figure 6.18. The essence of presenting the gas-liquid phase distribution in Figure 6.21 in this manner is to elucidate the behaviour of the liquid film that causes the entrainment of large liquid structures in the gas core. It was earlier ascertained that less energy is dissipated as the viscosity increases. As a result of this, the liquid film becomes more stable.

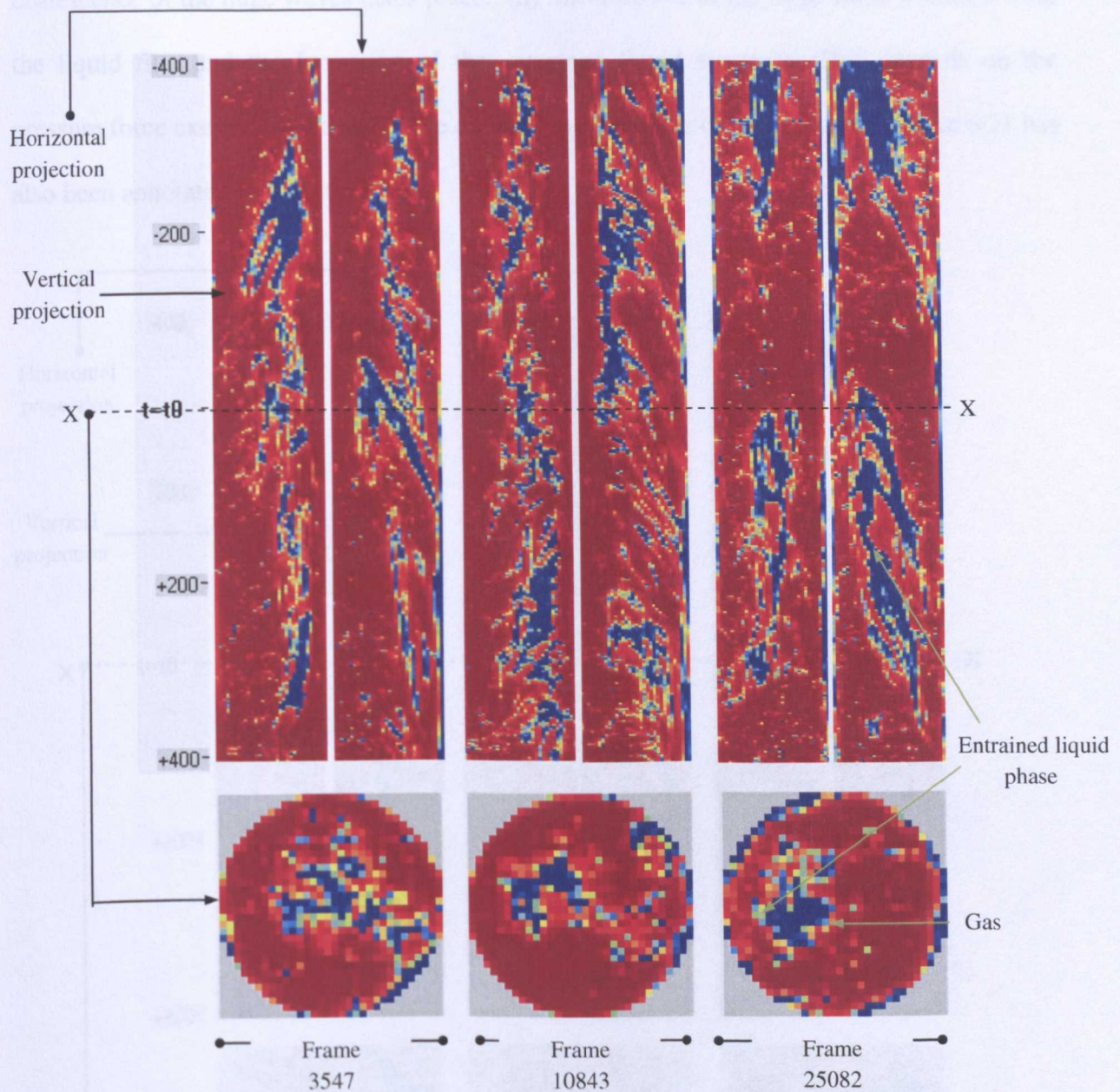


Figure 6.18. Assessment of the wisp structures from selected frames of 12.2cP glycerol-water data. Gas and liquid superficial velocity are given as of 4.19m/s and 0.27m/s respectively.

The processes that give rise to the entrained liquid phase in the gas core can be summarized as follows: (a) Peaking of the liquid film into the gas core (b) Coalescence of propagating huge waves from an upstream location to augment the amplitude of the wave within a reference control volume. (c) Protrusion of the augmented huge wave structure into the gas core after a critical wave amplitude/height has been attained. This is also where radial

coalescence of the huge waves takes place. (d) Shearing-off of the huge wave structure from the liquid film and the formation of the entrained liquid structure. This depends on the pressure force exerted by the gas phase on the windward side of the structure. Figure 6.21 has also been annotated for clarity.

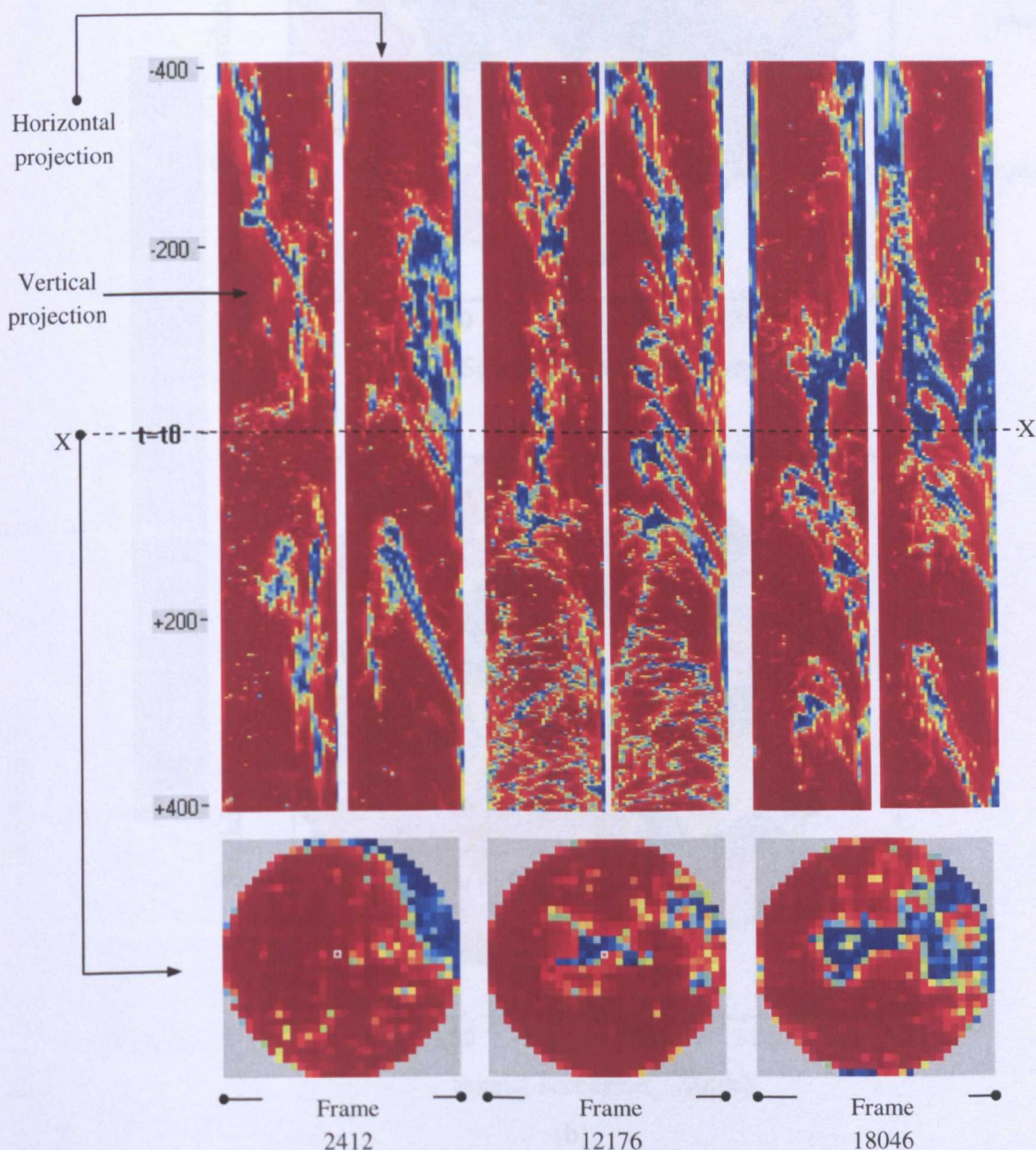
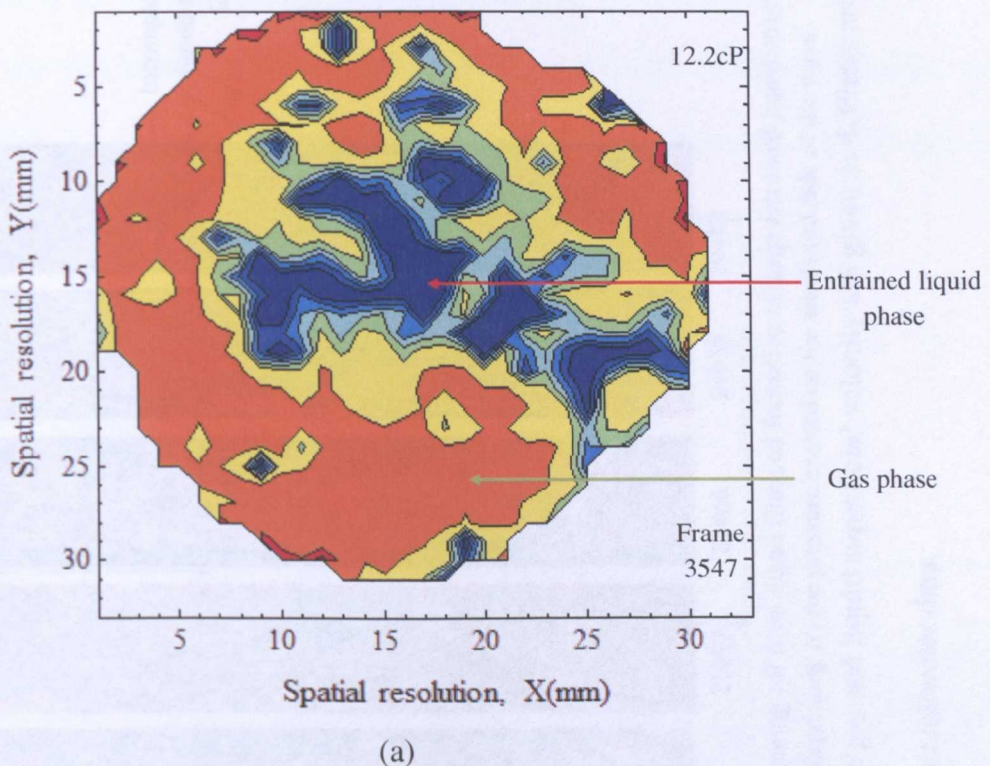
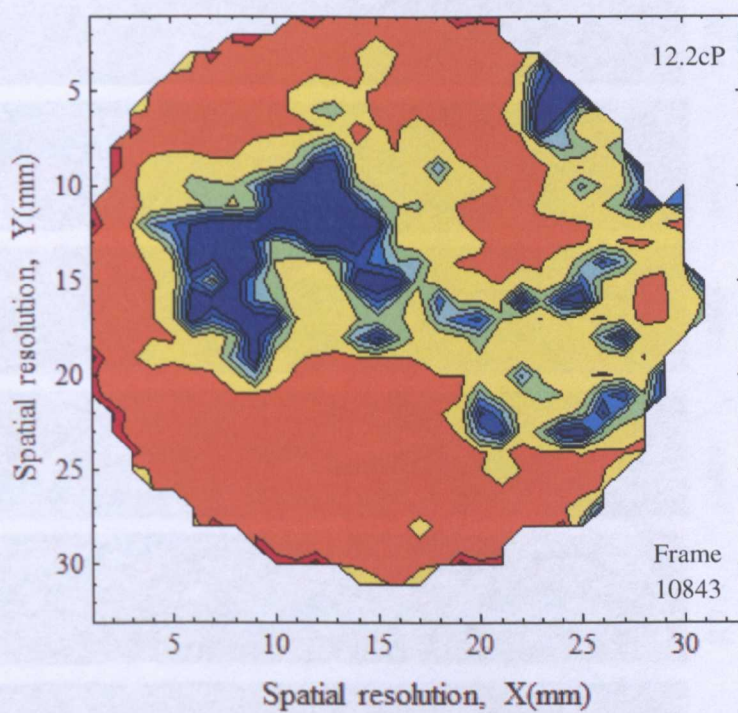


Figure 6.19. Assessing the wisp structures from selected frames of 16.2cP glycerol-water data. Gas and liquid superficial velocity are given as of 3.98m/s and 0.26m/s respectively.



(a)



(b)

Figure 6.20. Contour filled plots of cross sectional area according to Figure 6.18 for frames 3547 and 10843 respectively. This method is proposed for calculating wisp size cross-sectionally.

IMAGING SERVICES NORTH

Boston Spa, Wetherby
West Yorkshire, LS23 7BQ
www.bl.uk

**TEXT BOUND CLOSE TO
THE SPINE IN THE
ORIGINAL THESIS**

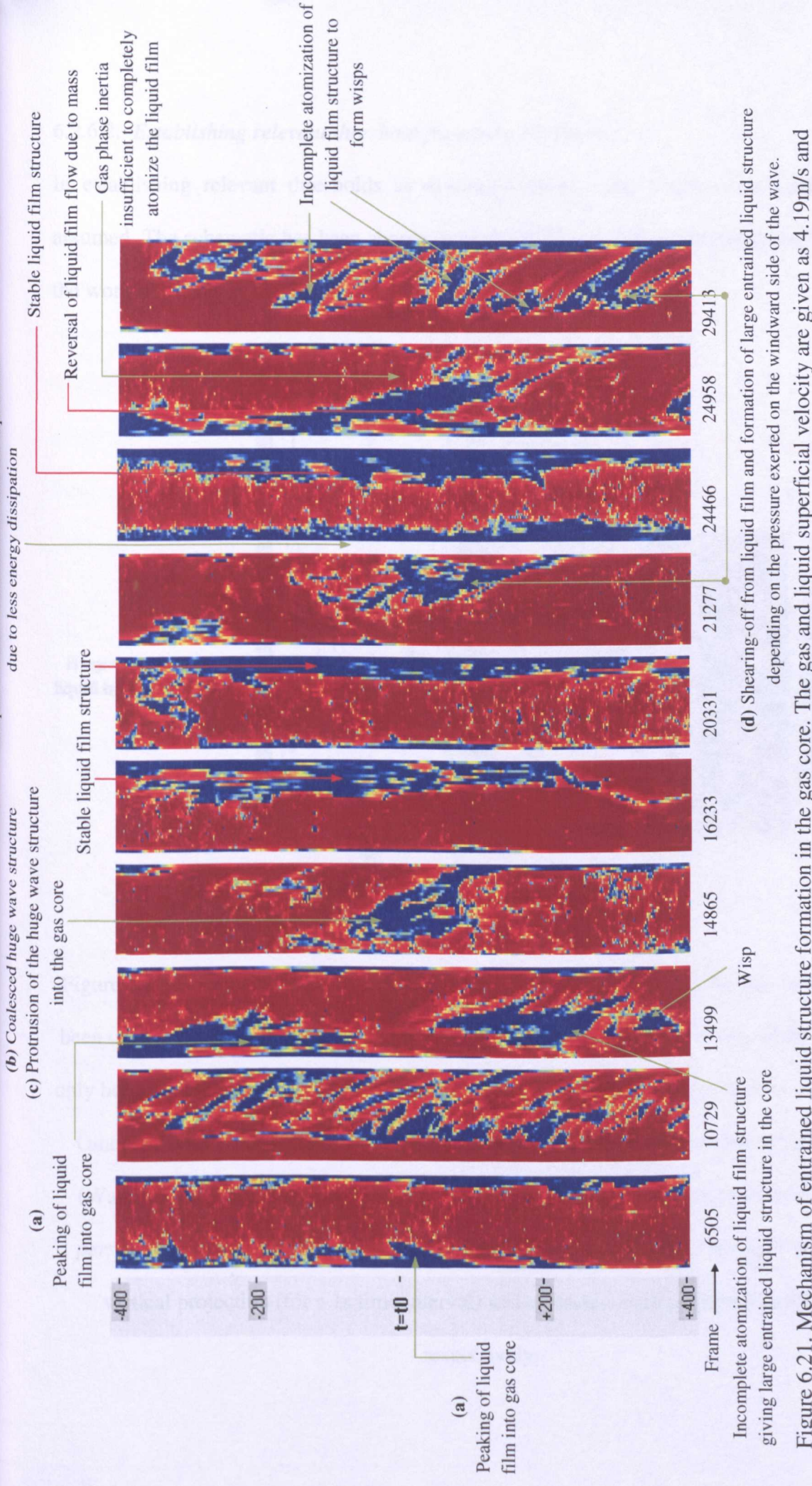


Figure 6.21. Mechanism of entrained liquid structure formation in the gas core. The gas and liquid superficial velocity are given as 4.19m/s and 0.27m/s respectively for the 12.2cP glycerol/water data.

6.2.6.2. Establishing relevant threshold from time series data

In establishing relevant thresholds as discussed above, quasi-steady state conditions are assumed. The schematic has been shown in Figure 6.22 and further reference can be made to the work of (Wang *et al.*, 2012).

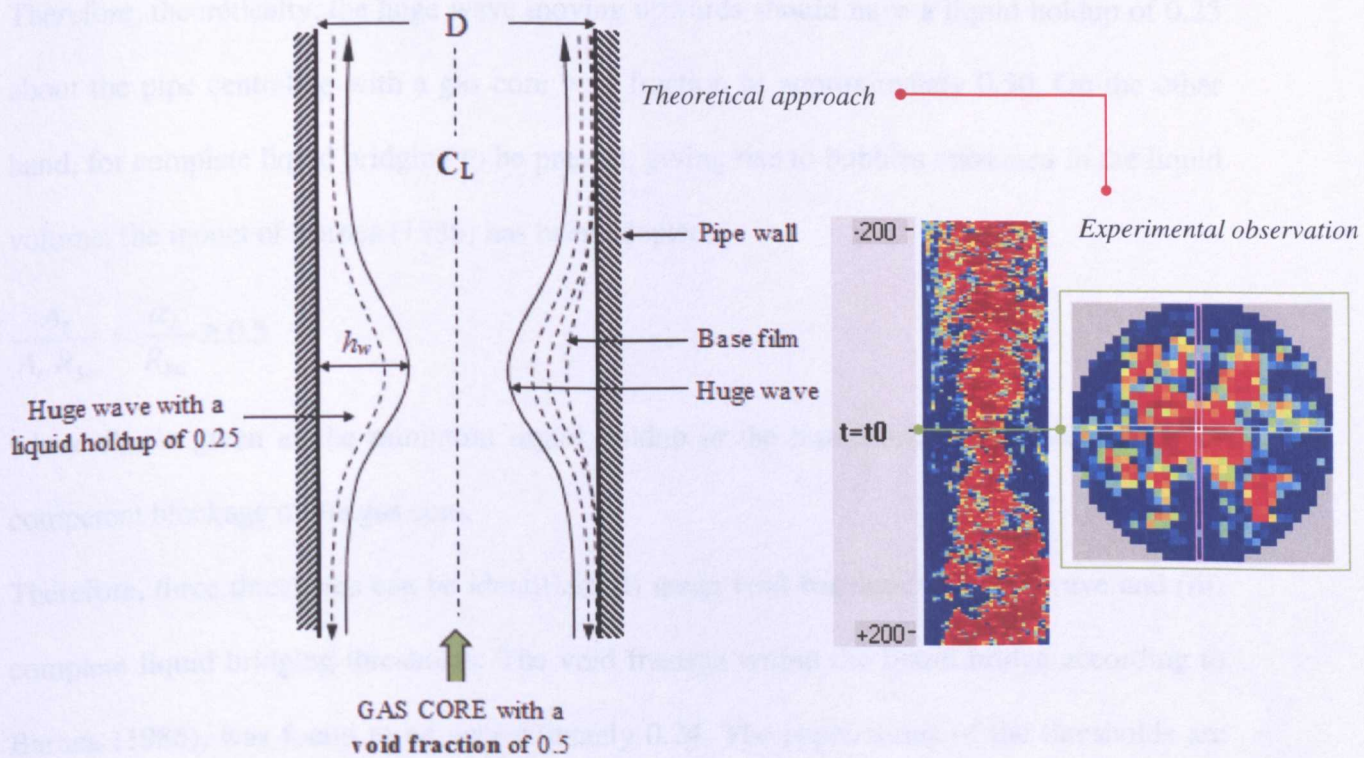


Figure 6.22. Schematic of the quasi-steady condition of churn flow on the left hand side has been used to obtain relevant churn flow thresholds based on *theoretical approach*. This may only hold for when the flow can be considered to be developed at $L/D = 65.5$ as suggested by Omebere-Iyari (2006) and as in the present work. Reference can be made to the work of (Wang *et al.*, 2012). Meanwhile, the gas-liquid phase distribution from the *experimental perspective* is shown on the right hand side depicting the occurrence of huge waves. The vertical projection (for a 1s time interval) and cross-sectional projection are shown respectively.

For huge waves to be present, the following equation has to be satisfied, that is, in consideration of both air-water experiments and the present work.

$$\frac{A_L}{A_C} \geq 0.5 \quad (6.2)$$

where A_L, A_C , are the areas occupied by the liquid and overall pipe cross-sectional area.

Therefore, theoretically, the huge wave moving upwards should have a liquid holdup of 0.25 about the pipe centreline with a gas core void fraction of approximately 0.50. On the other hand, for complete liquid bridging to be present, giving rise to bubbles entrained in the liquid volume, the model of Barnea (1986) has been adopted.

$$\frac{A_L}{A_C R_{sm}} = \frac{\alpha_L}{R_{sm}} \geq 0.5 \quad (6.3)$$

where R_{sm} is given as the minimum liquid holdup in the liquid bridge that will allow for competent blockage of the gas core.

Therefore, three thresholds can be identified: (i) mean void fraction, (ii) huge wave and (iii) complete liquid bridging thresholds. The void fraction within the liquid bridge according to Barnea (1986), was found to be approximately 0.24. The applications of the thresholds are shown in Figures 6.23 and 6.24.

The horizontal, vertical and cross sectional projections are matched to the time series data using the relevant thresholds. The vertical projections are shown for a 1s interval. When liquid structures/wisps are present, the void fraction does not change considerably. This is because the liquid structures are entrained in the gas core. However, this depends on the size of the structures.

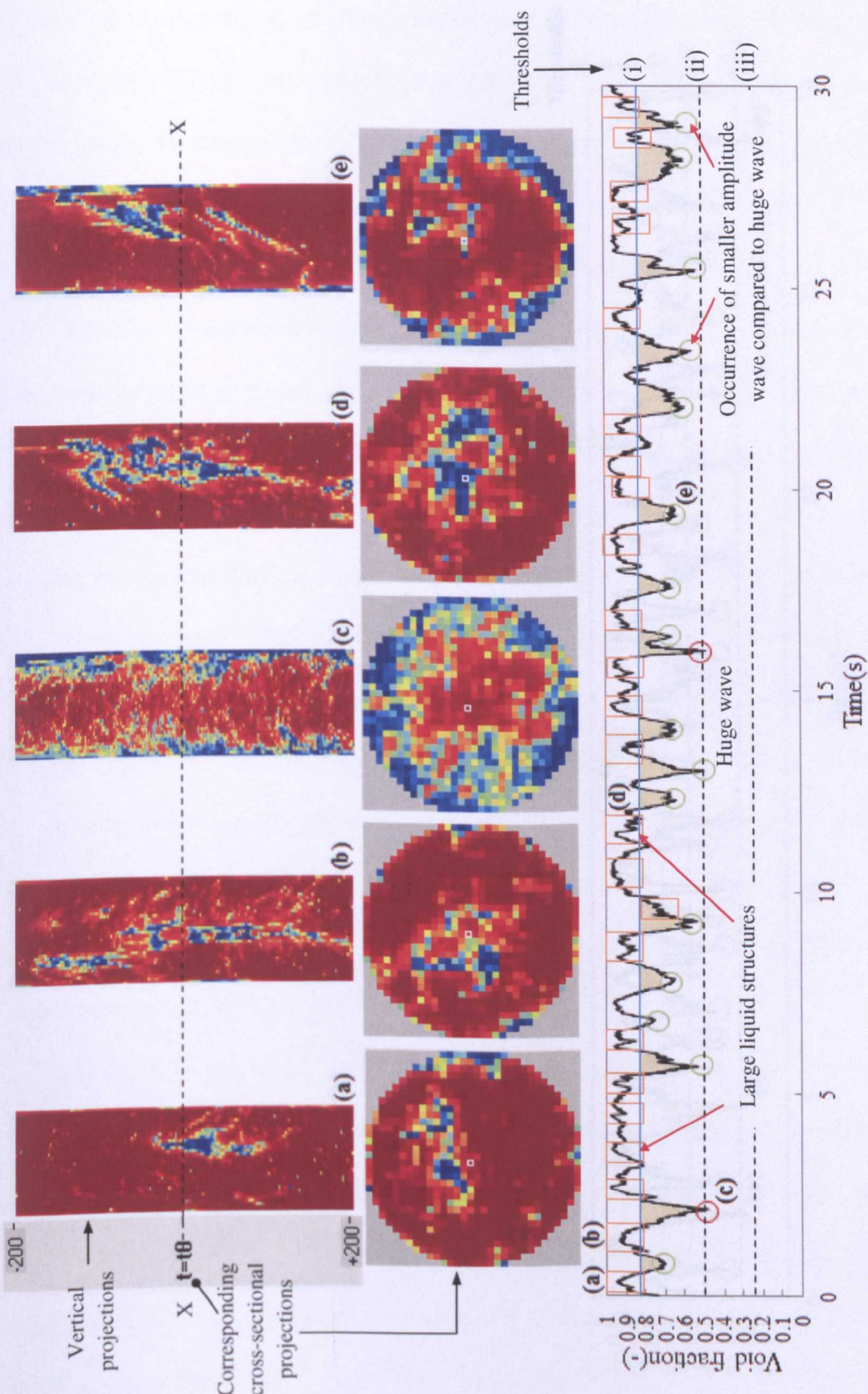


Figure 6.23. Applying thresholds to time series data based on figure 7.38 and tallying it to the occurrence of interfacial structures. Orange boxes represent where wisps were observed, red circles are for huge waves and green circles are probably smaller amplitude waves compared to huge wave for 12.2cP glycerol solution and gas and liquid superficial velocities of 4.85m/s and 0.11m/s.

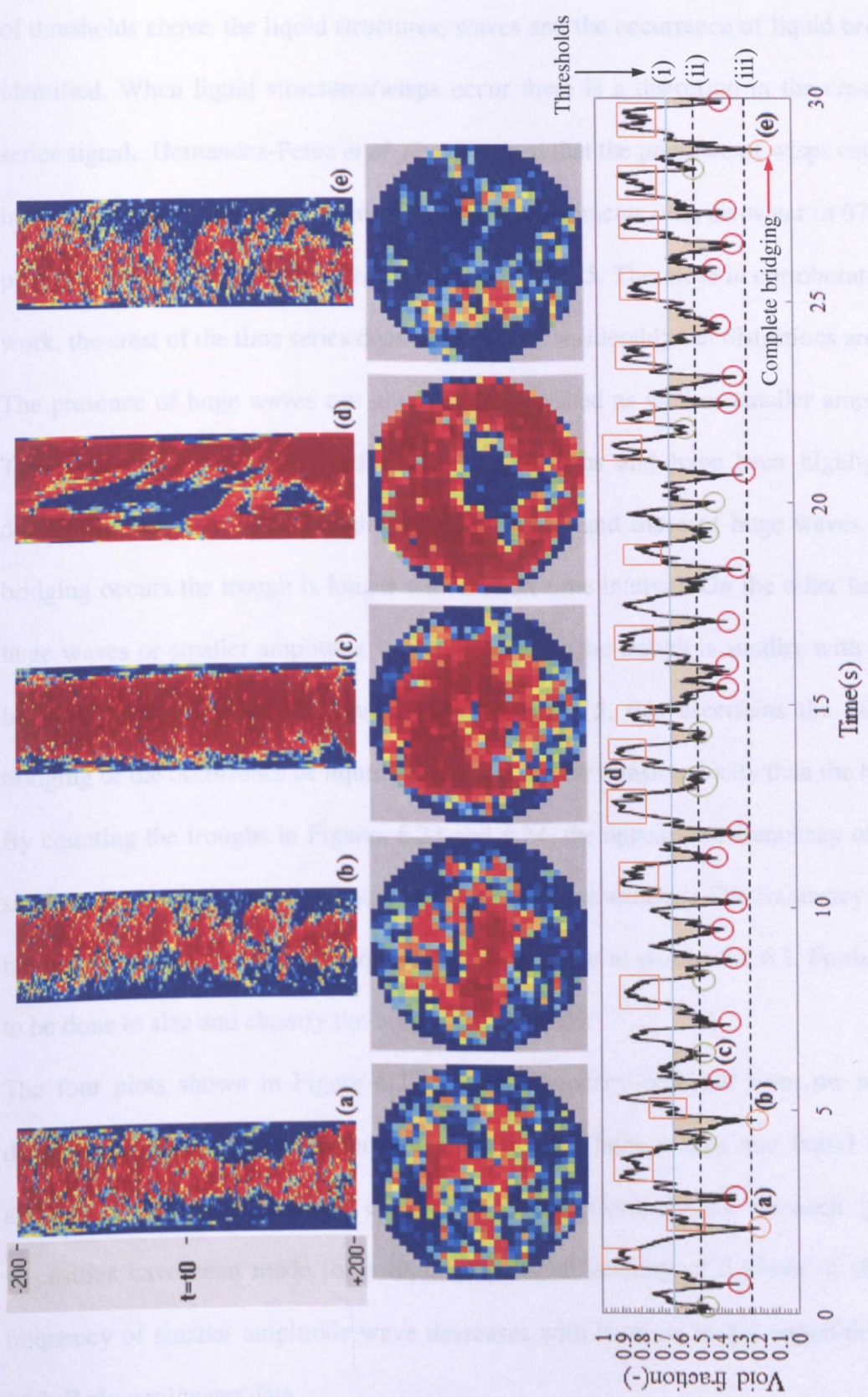


Figure 6.24. Similar identification as in figure 6.23 where the gas and liquid superficial velocities are given as 4.19 m/s and 0.27 m/s and pipe

With further increase in liquid superficial velocity to 0.27m/s in Figure 6.24 and application of thresholds above, the liquid structures, waves and the occurrence of liquid bridging can be identified. When liquid structures/wisps occur there is a distortion in the crest of the time series signal. Hernandez-Perez *et al.* (2010) stated that the presence of wisps can be observed in the time series of the void fraction. For their experiments with air-water in 67mm diameter pipe, this would lower the void fraction by only 0.0225. Therefore in corroboration with their work, the crest of the time series does not change considerably but distortions are present.

The presence of huge waves can also be distinguished as well as smaller amplitude waves. The areas under the mean void fraction are troughs and have been highlighted to also distinguish between liquid bridging of the gas core and those of huge waves. When liquid bridging occurs the trough is longer with a short time interval. On the other hand, when the huge waves or smaller amplitude waves are present the trough is smaller with a longer time interval. With reference to Figure 5.12 in chapter 5, this ascertains the fact that liquid bridging or the occurrence of liquid slugs has a shorter transit velocity than the huge waves. By counting the troughs in Figures 6.23 and 6.24, the appearance frequency of huge waves, smaller amplitude waves and liquid bridging can be estimated. The frequency of wisps was not obtained based on the above qualitative assessment in section 6.2.6.1. Further work needs to be done to size and classify the wisps appropriately.

The four plots shown in Figure 6.25 are the frequency obtained from the power spectral density, the appearance frequency of small waves, huge waves and liquid bridging after application of thresholds by counting method. Comparisons between glycerol-water viscosities have been made for a liquid superficial velocity of 0.17m/s. It shows that, the frequency of smaller amplitude wave decreases with increase in gas superficial velocity for 16.2cP glycerol/water data.

Contrary to the trend for the 16.2cP data, the frequency of the smaller amplitude waves increases for 12.2cP data. The huge wave frequency decreases with increase in viscosity and also no liquid bridging of the gas core was observed for the experimental range for 16.2cP glycerol/water experiments.

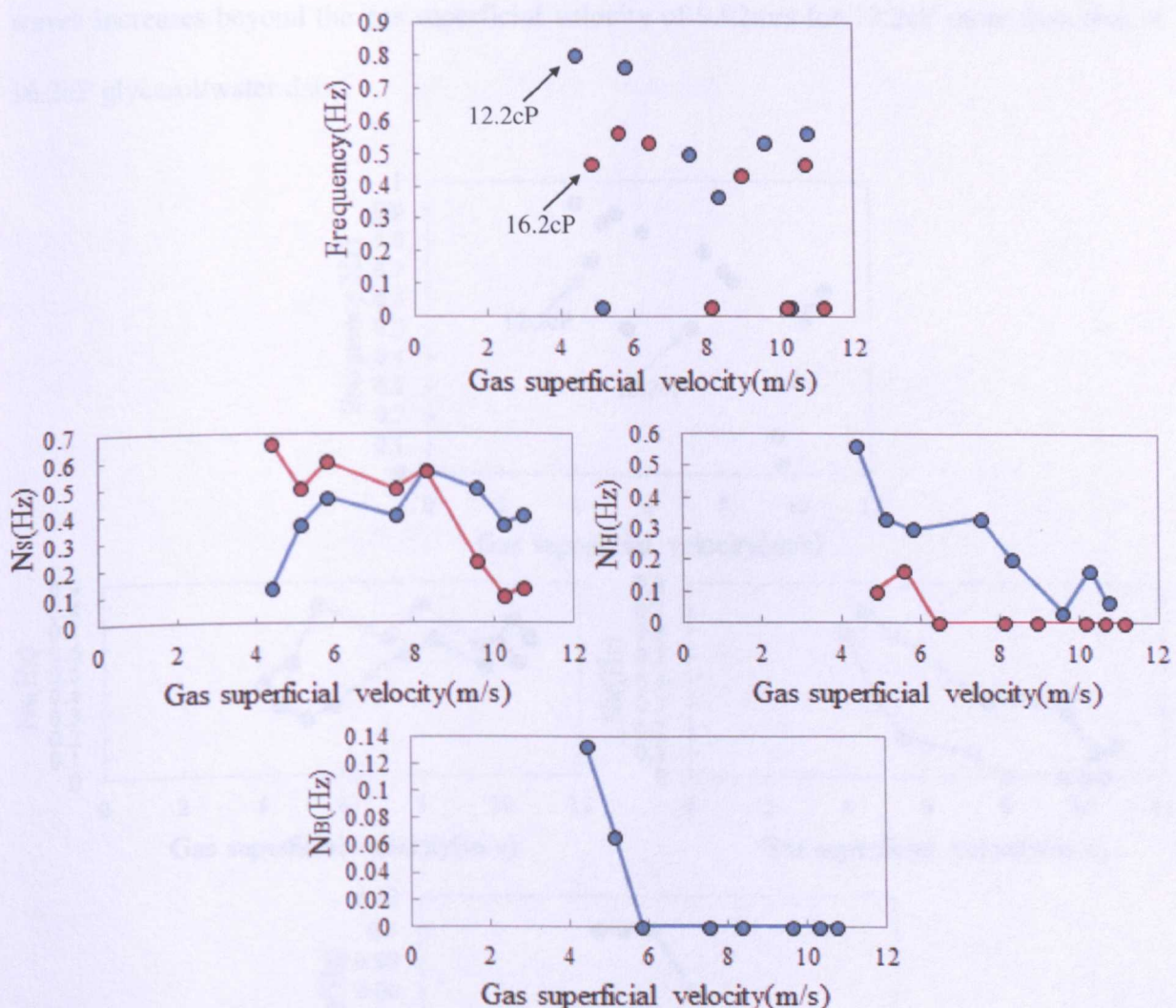


Figure 6.25. Dominant frequency variations with gas superficial velocity showing comparison of 12.2cP and 16.2cP data at an average constant liquid superficial velocity of 0.17m/s. Sub-frequency variations which can be regarded as appearance frequencies are also shown where N_s are small amplitude waves compared to huge waves N_h while N_b is the appearance frequency of liquid bridging of the gas core.

The effect of increase in liquid superficial velocity is shown in Figure 6.26 for an average constant liquid superficial velocity of 0.27m/s. The profile of the small amplitude waves for 16.2cP does not have the same decreasing trend. However, it remains higher than that of 12.2cP data until a gas superficial velocity of 9.92m/s. The frequency of the small amplitude waves increases beyond the gas superficial velocity of 9.92m/s for 12.2cP more than that of 16.2cP glycerol/water data.

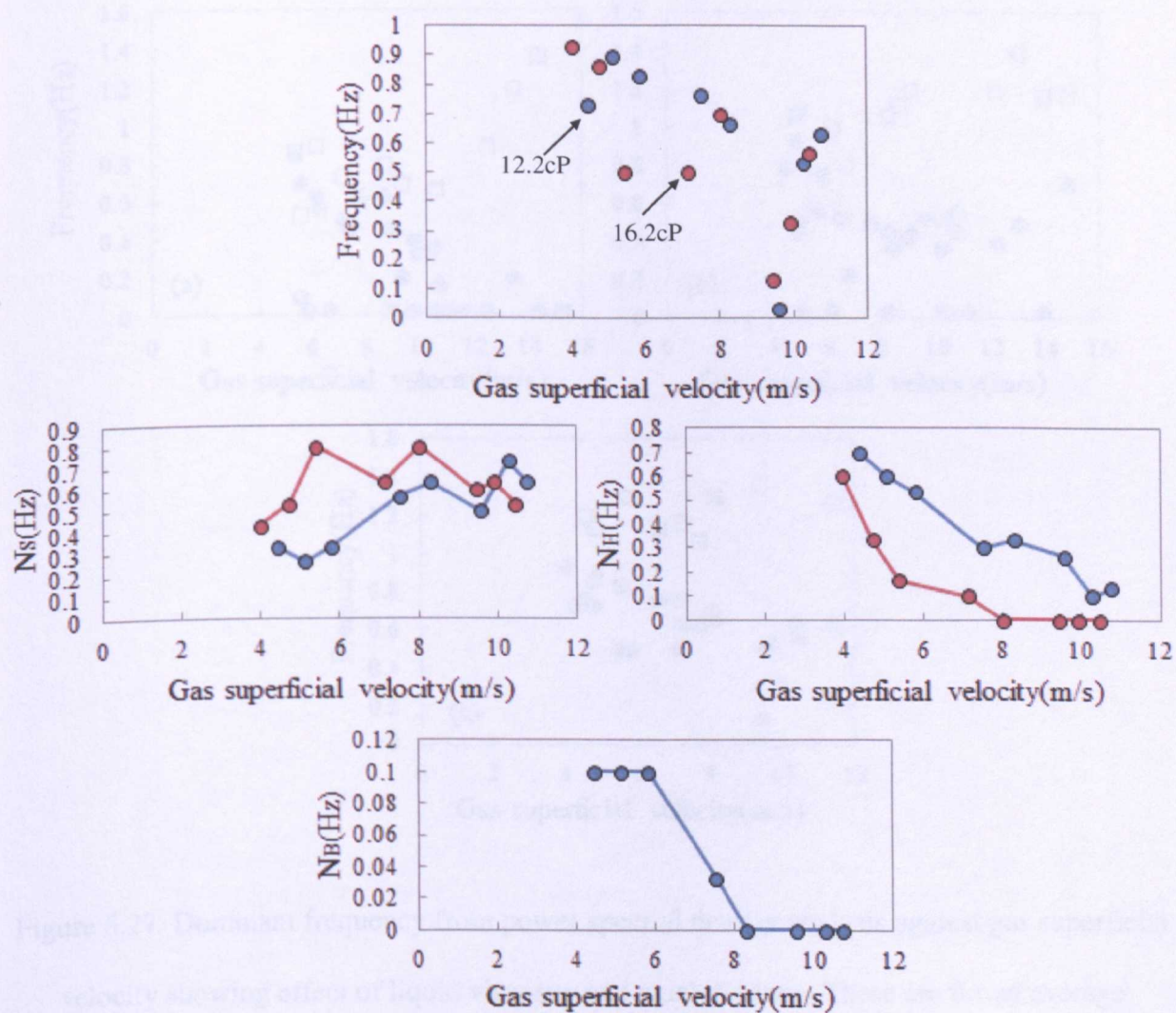


Figure 6.26. Dominant frequency variations with gas superficial velocity showing comparison of 12.2cP and 16.2cP data at an average constant liquid superficial velocity of 0.24m/s.

Furthermore, the dominant frequency values obtained from the power spectral density analysis, are compared to that of air-water at $L/D = 35.4$ and 82.7 in Figure 6.27. It shows that the frequency at $L/D = 35.4$ is higher than air-water data downstream at $L/D = 82.7$ and that of glycerol/water. The dominant frequencies have been found to be close to each other for air-water data at $L/D = 82.7$ compared to the glycerol/water data. This can be observed even at a high liquid superficial velocity of 0.27m/s in (c).

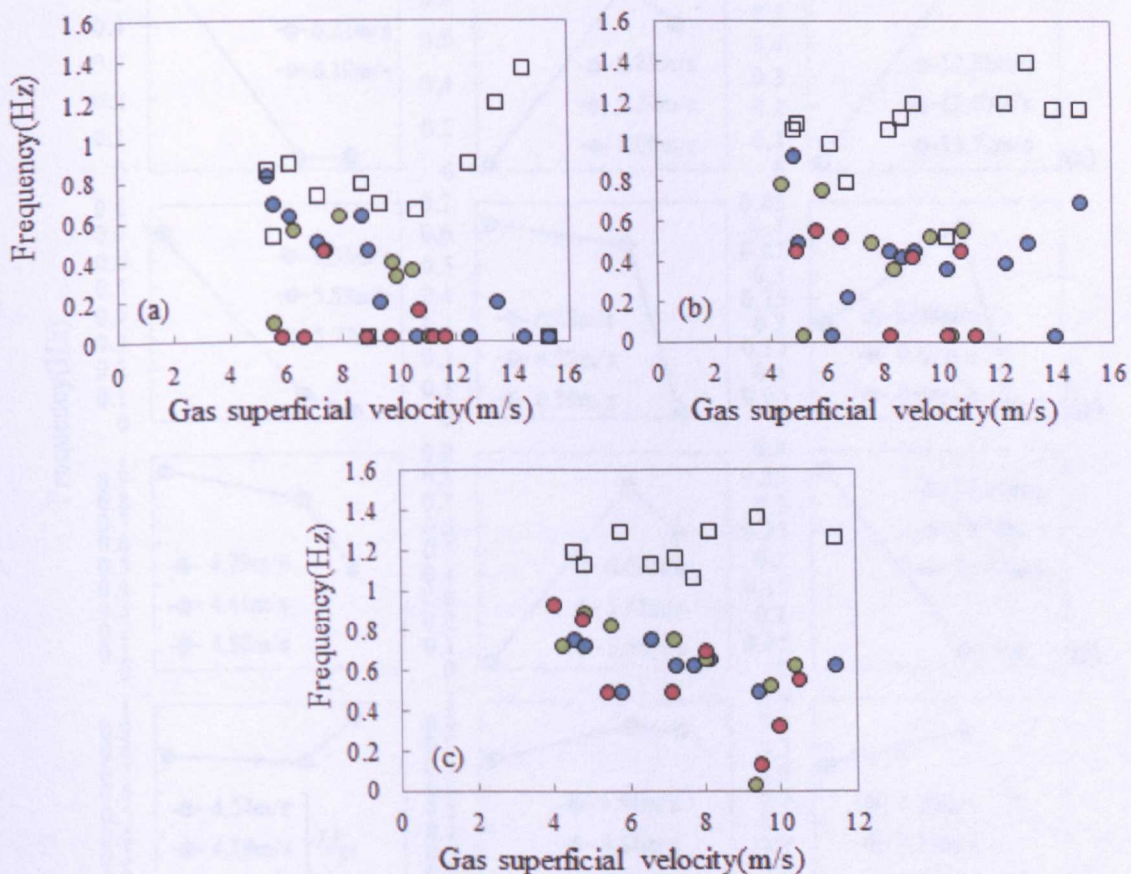


Figure 6.27. Dominant frequency from power spectral density analysis against gas superficial velocity showing effect of liquid viscosity and axial distance. These are for an average constant liquid superficial velocity in (a)-(c) of 0.11m/s , 0.17m/s and 0.26m/s respectively. Square indicates air-water data at $L/D = 35.4$. Blue, red and green circles represents 12.2cP , 16.2cP glycerol-water data and air-water data at $L/D = 82.7$.

Therefore, since there are more liquid structures entrained within the core for air-glycerol/water due to a higher viscosity, this is effectively compensated for by an increased frequency of huge waves with reference to the air-water at $L/D = 82.7$. Consequently, this makes the dominant frequency variations with gas superficial velocity close to each other as shown in Figure 6.27.

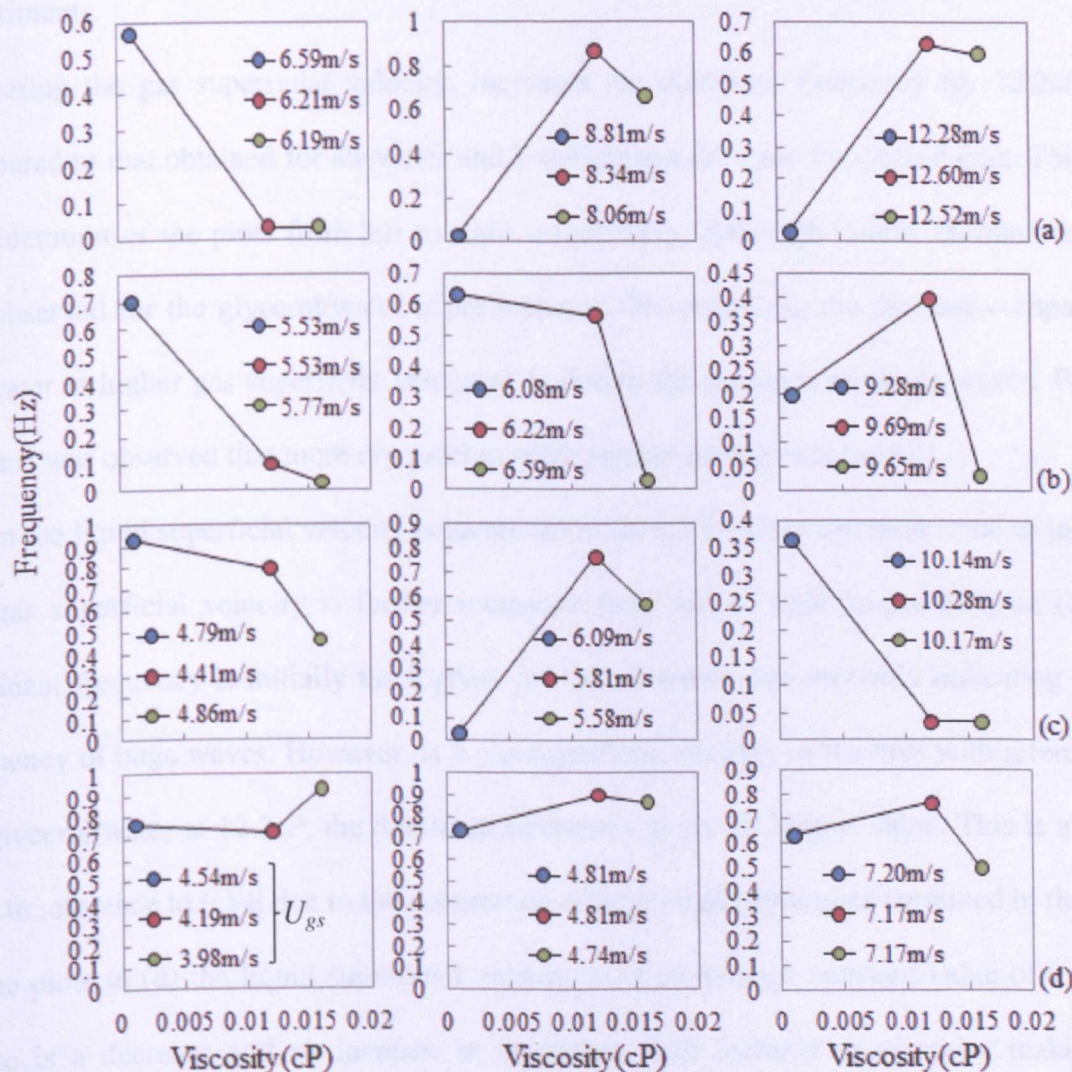


Figure 6.28. Dominant frequency variation with viscosity for an average constant liquid superficial velocity from (a) – (d) respectively of 0.03m/s , 0.11m/s , 0.17m/s and 0.27m/s for selected gas superficial velocities. Red, blue and green are air-water at $L/D = 82.7$ and air-glycerol/water at 12.2cP and 16.2cP respectively.

Nonetheless, the discrepancies in the magnitude of the dominant frequencies with respect to the operating fluids can be shown in Figure 6.28. The air-water data is for $L/D = 82.7$ since the cause of the high frequency at $L/D = 35.4$ has been attributed to liquid bridging. At low liquid superficial velocity in (a)-i, this gives a decrease in frequency for an increasing viscosity. This is with reference to the gas superficial velocity of 6.59m/s for the air-water experiments.

Increasing the gas superficial velocity, increases the dominant frequency for 12.2cP data compared to that obtained for air-water and a subsequent decrease for 16.2cP data. This is in consideration of the plots from left to right respectively. Although bubble entrainment was not observed for the glycerol/water experiments at this condition, the increase compared to air-water at higher gas superficial velocities is due to the presence of ripple waves. For air-water it was observed that more dry patches were present during experiments.

When the liquid superficial velocity is increased in (b)-i, this gives a similar trend to (a)-i. As the gas superficial velocity is further increased from left to right respectively in (b), the dominant frequency is initially the highest for the air-water data probably indicating a high frequency of huge waves. However, at a gas superficial velocity of 9.69m/s with reference to air-glycerol/water at 12.2cP, the dominant frequency gives the largest value. This is also the case in reference to (c)-ii due to the occurrence of large liquid structures entrained in the core. In the plots in (d) the liquid superficial velocity is at an average constant value of 0.27m/s. There is a decrease and an increase in frequency with increase in viscosity making the frequency value at 16.2cP the highest in (d)-i. This may be due to the fact that the smaller amplitude waves are more dominant. An increase in gas superficial velocity increases the frequency and size of liquid structures present in the case of 12.2cP glycerol-water data compared to 16.2cP and air-water. Comparing the dominant frequencies across the viscosity

scale reveals that the frequency of the huge waves, small waves and liquid structures may be dominant for a particular fluid pair but not for the other.

6.3. Further analysis of experimental data

From the analysis carried out above, due to an increase in viscosity the frequency and size of the large liquid structures increases. However, liquid bridging occurs more for air-water compared to air-glycerol/water. A schematic which represents the quasi-steady conditions for both air-water and air-glycerol/water has been used to identify relevant thresholds in figure 6.22. According to Barnea (1986), for a transition from annular flow to intermittent flow, that is, slug or churn flow, the minimum liquid holdup has been identified to be 0.24. On other hand, Govan *et al.* (1990) proposed that the critical void fraction for the transition from churn to annular is given as 0.75. This gives a liquid holdup value of 0.25, which is close to that proposed by (Barnea, 1986). Therefore, since the effect of increase in liquid viscosity makes the flow behaviour tend towards annular flow as identified earlier, the equation she proposed stated in chapter 5 is plotted in Figure 6.29.

Comparison are made for both liquid viscosities to that of air-water at $L/D = 35.4$ and 82.7 , for a liquid superficial velocity of 0.24m/s . Since the minimum liquid holdup that will cause bridging is 0.24, isoholdup lines are shown for both plots. Isoholdup lines are lines of constant liquid holdup. This has been shown for values ranging from that suggested by Barnea (1986) of liquid holdup of 0.24 to higher values of 0.40. Below the stability curve, she suggested annular flow conditions exist. To the right of the stability curve, is intermittent flow. Therefore, this means that the data at the lowest liquid superficial velocity of 0.039m/s and 0.036m/s is annular. For the 12.2cP data, most of the operating conditions are below the stability curve, even some of data point for high liquid superficial velocities. Although Barnea (1986) identified this to be annular, this is essentially not the case based on

experimental observations. The difference between the data at the low liquid superficial velocity of 0.039m/s and higher liquid superficial velocities within this region is that the former behaves more like annular while the latter like wispy-annular.

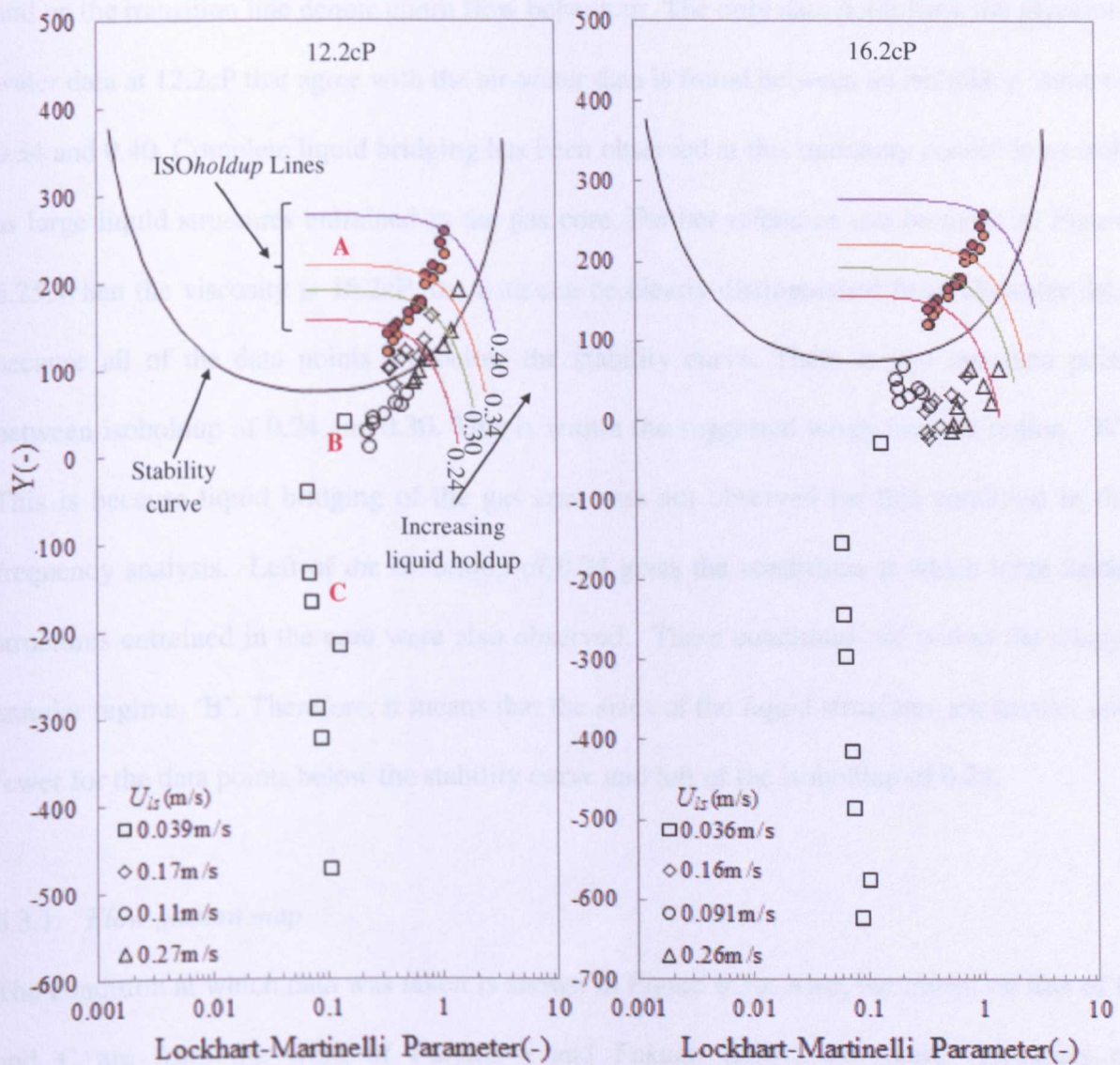


Figure 6.29. Variations of dimensionless parameter against Lockhart-Martinelli parameter according to Barnea (1986), Isoholdup lines have been indicated. Red and orange circles indicate air-water data at L/D = 35.4 and 82.7. ‘A’ is the typical churn flow behaviour region and ‘B’ wispy-annular flow region above x-axis. Below the x-axis is typical annular flow region, ‘C’.

Therefore, region 'C' may cater for the annular and region 'B' for wispy annular region, which was not previously identified by Barnea (1986) as she did not conduct experiments with higher viscosities than water. The data points lying within the stability curve, region 'A' and on the transition line denote churn flow behaviour. The only data point from the glycerol-water data at 12.2cP that agree with the air-water data is found between an isoholdup value of 0.34 and 0.40. Complete liquid bridging has been observed at this operating condition as well as large liquid structures entrained in the gas core. Further reference can be made to Figure 6.25. When the viscosity is 16.2cP, the data can be clearly distinguished from air-water data because all of the data points are below the stability curve. There is just one data point between isoholdup of 0.24 and 0.30. This is within the suggested wispy annular region, 'B'. This is because liquid bridging of the gas core was not observed for this condition in the frequency analysis. Left of the isoholdup of 0.24 gives the conditions at which large liquid structures entrained in the core were also observed. These conditions are within the wispy-annular regime, 'B'. Therefore, it means that the sizes of the liquid structures are smaller and fewer for the data points below the stability curve and left of the isoholdup of 0.24.

6.3.1. *Flow pattern map*

The condition at which data was taken is shown in Figure 6.30. Also, the transition line of **B** and **C** are from the work of Furukawa and Fukano (2001) for liquid viscosities of approximately 6cP and 17cP. A transition line has been plotted on the flow pattern map for the present work and is shown as **A**.

Beyond the line **A**, complete liquid bridging was not observed. In addition, Figure 6.30(b) shows the operating conditions where huge waves occur. The lines of Furukawa and Fukano (2001) occur at higher gas superficial velocities as this takes into consideration both the occurrence of liquid bridging and huge waves. There is no transition line for the 12.2cP and

16.2cP data because higher gas superficial velocities were not experimented. Figure 6.31 shows the flow pattern map at 16.2cP with the transition lines from Figure 6.30. Incomplete liquid bridging and huge waves both occur at one experimental condition.

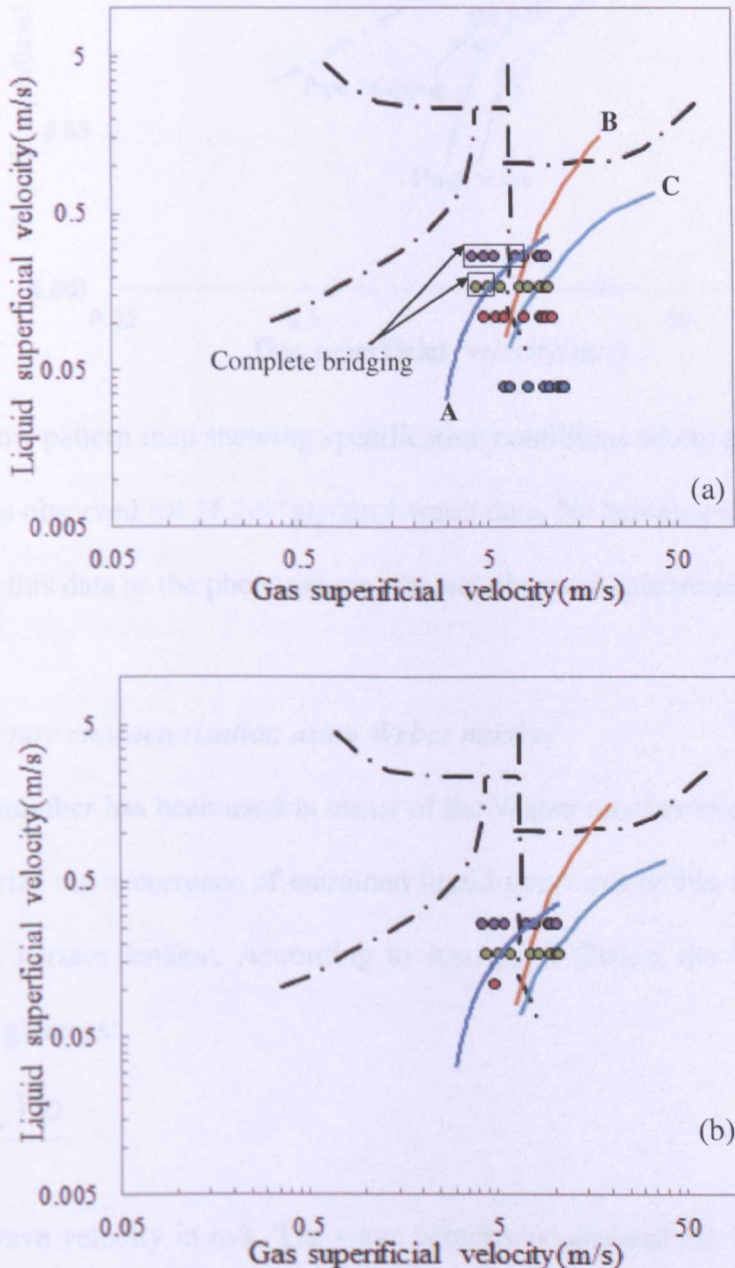


Figure 6.30. Flow pattern map (a) shows comparison of bridging transition lines of Furukawa and Fukano (2001), B and C to present data A for 12.2cP glycerol-water data. (b) Shows the conditions where huge waves are observed. Transition line to annular regime cannot be plotted as that data was not collected.

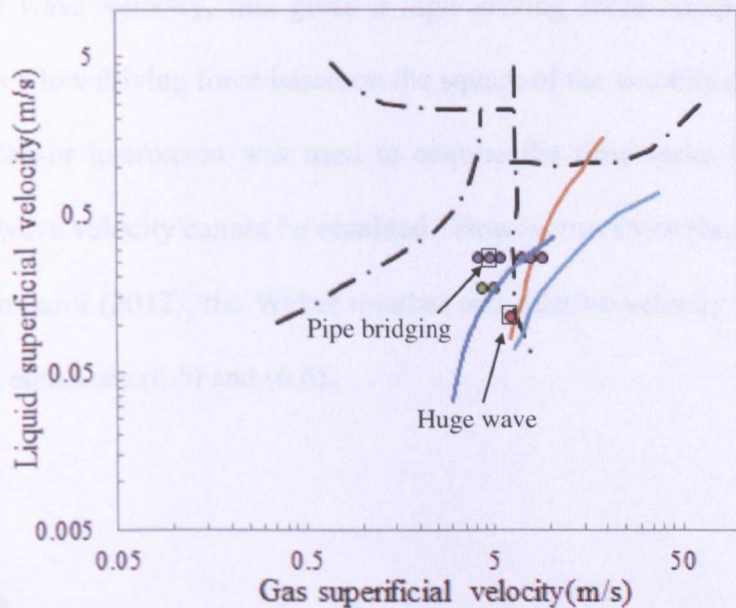


Figure 6.31. Flow pattern map showing specification conditions where pipe bridging and huge waves was observed for 16.2cP glycerol-water data. No bridging transition line has been obtained for this data as the phenomenon was not observed (please refer to Figure 6.25).

6.3.2. Flow structure characterisation using Weber number

A dimensionless number has been used in terms of the Weber number as discussed in section 6.2.4, to characterize the occurrence of entrained liquid structures within the core. This is the ratio of inertia to surface tension. According to Azzopardi (2012), the Weber number that should be used is given as:

$$We = \frac{\rho_g (U_{gs} - u_w)^2 D}{\sigma} \quad (6.4)$$

where u_w is the wave velocity in m/s. The wave velocity is obtained by cross-correlating the time series data acquired from two instruments simultaneously. Based on the suggestion of Azzopardi (2012), at higher Weber numbers, drops are formed and at lower Weber numbers liquid structures entrained in the gas core are formed due to incomplete atomisation. This is

because at a low wave velocity, this gives a high driving force compared to high wave velocity that gives a low driving force based on the square of the velocity difference.

One wire mesh sensor instrument was used to acquire the time series data in the present work, hence, the wave velocity cannot be obtained. However to show the above behaviour as suggested by Azzopardi (2012), the Weber number and relative velocity used in the present work are given in equations (6.5) and (6.6).

$$We = \frac{\rho_g U_{rs}^2 D}{\sigma} \quad (6.5)$$

$$u_{rel} = \frac{U_{rs}}{\alpha_g} - \frac{U_{ls}}{(1-\alpha_g)} \quad (6.6)$$

This also gives two distinct profiles for wisps structures and drops as shown in Figure 6.32. This is similar to the observations of Azzopardi (2012) when they used the wave velocity. This was further compared to the data of Azzopardi (2012) shown as green circles in Figure 6.33. It is important to note that he used the Weber number in equation (6.4) against the gas superficial velocity to show this effect. Interestingly, this seems to agree with the air-water data presented in chapter 5.

However, because there is tendency of the liquid film to behave more like annular flow as the liquid viscosity increases, a modified Weber number is used. This is given in equation (6.7).

$$We^* = \frac{\rho_g u_{rel}^2 h_w}{\sigma} \quad (6.7)$$

where h_w can be considered to be an estimated mean wave height shown in the schematic of Figure 6.22. The estimated mean wave height is obtained in equation (6.8) as:

$$h_w = \frac{D}{2} \left(1 - \sqrt{\alpha_g}\right) \quad (6.8)$$

In contrast to that suggested by Azzopardi (2012), based on the modified Weber number used, a low Weber number means that the relative velocity is high and the wave height is

small, therefore, this gives drops. At higher Weber number the relative velocity is low and the wave height is large. Consequently, this leads to the formation of entrained liquid structures in the gas core. This can be shown for both glycerol-water data in Figure 6.34.

Also, in comparison with the air-water experiments in Figure 6.35, this shows a decreased profile for glycerol-water data. However, this should give a higher profile revealing that more liquid structures are entrained in the gas core for the air-glycerol/water compared to air-water.

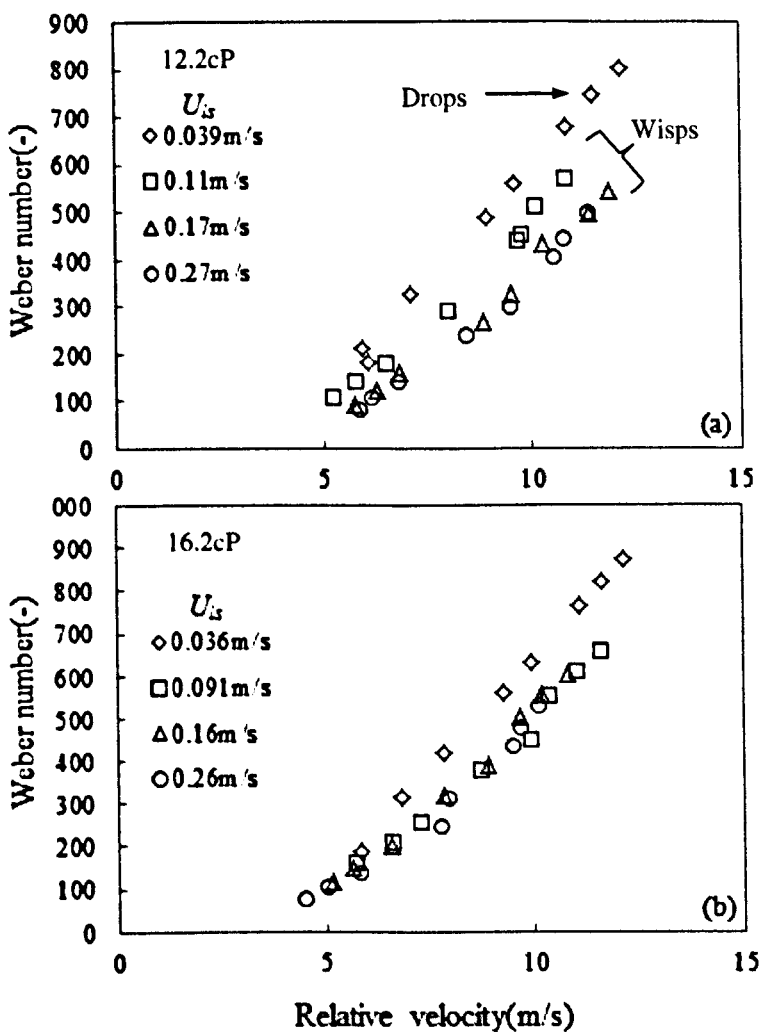


Figure 6.32. Variation of weber number against relative velocity for 12.2cP and 16.2cP glycerol-water data.

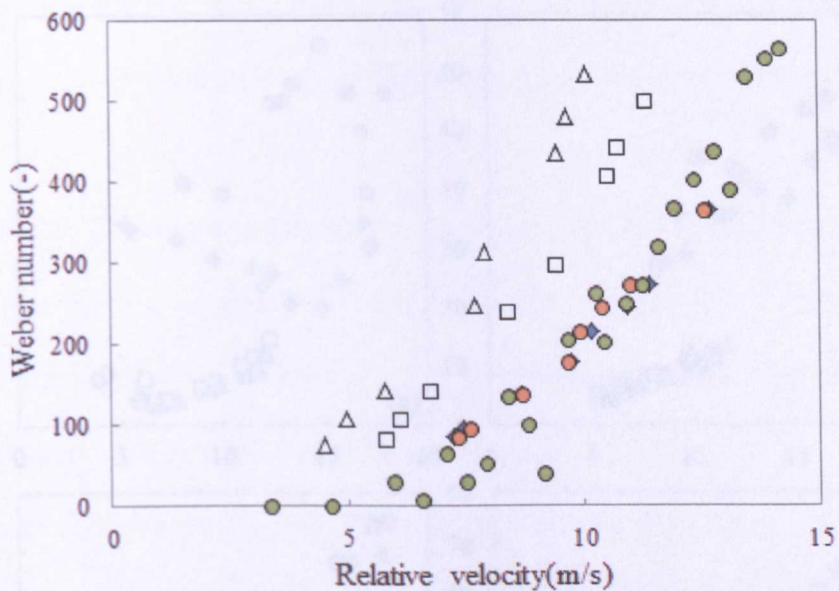


Figure 6.33. Variation of Weber number against Relative velocity. The 12.2cP and 16.2cP data are shown as square and triangle respectively. Air-water data at $L/D = 35.4$ and 82.7 are shown as orange circle and blue diamond while data of Azzopardi (2012) is shown as green circle.

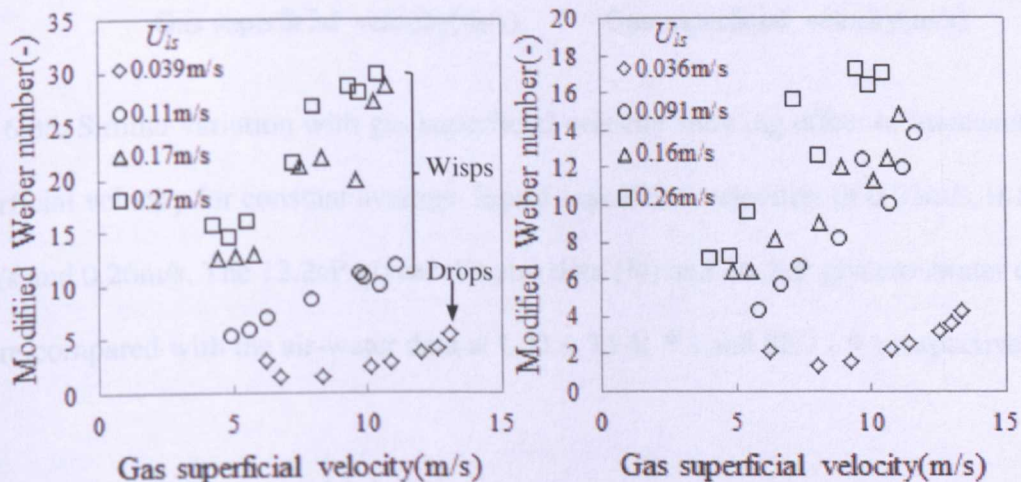


Figure 6.34. Proposed modification of Weber number and variation with gas superficial velocity for 12.2cP (left) and 16.2cP (right) glycerol-water data respectively.

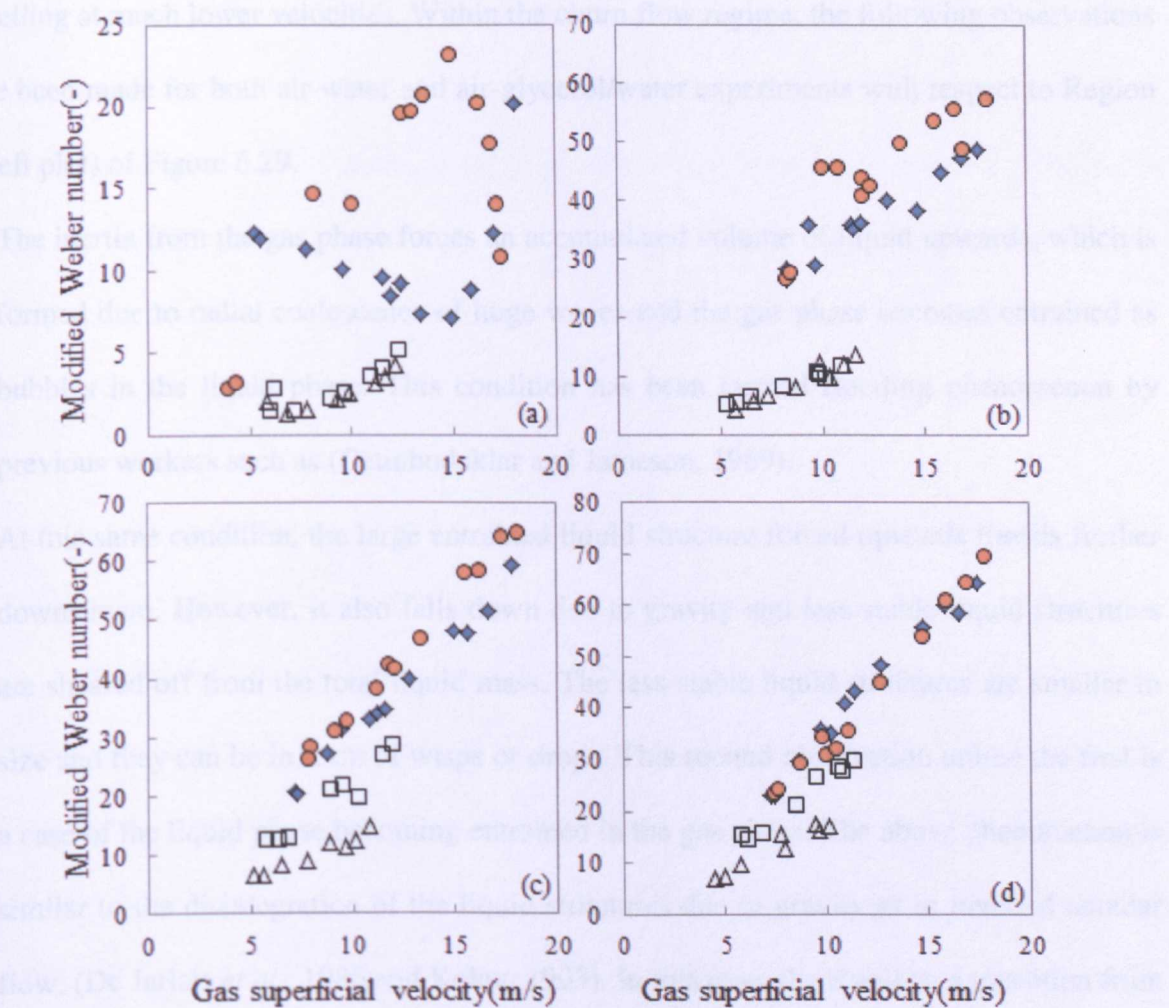


Figure 6.35. Similar variation with gas superficial velocity showing effect of increasing liquid superficial velocity for constant average liquid superficial velocities of 0.03m/s, 0.11m/s, 0.17m/s and 0.26m/s. The 12.2cP glycerol/water data (\square) and 16.2cP glycerol/water data (Δ) are compared with the air-water data at $L/D = 35.4$ (\blacklozenge) and 82.7 (\bullet) respectively.

6.4. Churn flow coalescer model development

The presence of large liquid structures entrained within the core and having a size that almost occupies the pipe cross section, act as ‘drop catchers’ that enable an increased degree of coalescence to occur. Due to the mass of the large liquid structures present, they reach their terminal velocity quicker in comparison to small liquid structures such as wisps or drops. These travel at high velocities, therefore, they impinge on the large liquid structures that are

travelling at much lower velocities. Within the churn flow regime, the following observations have been made for both air-water and air-glycerol/water experiments with respect to Region A (left plot) of Figure 6.29.

- (a) The inertia from the gas phase forces an accumulated volume of liquid upwards, which is formed due to radial coalescence of huge waves and the gas phase becomes entrained as bubbles in the liquid phase. This condition has been termed flooding phenomenon by previous workers such as (Cetinbudaklar and Jameson, 1969).
- (b) At this same condition, the large entrained liquid structure forced upwards travels further downstream. However, it also falls down due to gravity and less stable liquid structures are sheared off from the total liquid mass. The less stable liquid structures are smaller in size and they can be in form of wisps or drops. This second observation unlike the first is a case of the liquid phase becoming entrained in the gas phase. The above phenomenon is similar to the disintegration of the liquid structures due to gravity as in inverted annular flow, (De Jarlais *et al.*, 1986 and Kolev, 1993). In this case, there will be a transition from a continuous liquid jet into a flow with smaller entrained liquid structures.
- (c) The small liquid structures that fall due to gravity, breakup by bag-breakup mechanism, according to (Azzopardi, 1997). When they fall due to gravity, two processes may occur. It is either they coalesce with the large liquid entrained liquid structures that are flowing upwards from an upstream location or they breakup further.
- (d) The latter may occur when the large liquid structures do not occupy the entire cross section of the pipe. The gas travelling upwards finds its ways around the large liquid structures and causes the further breakup of the smaller liquid structures. On the other hand, this may carry the smaller liquid structures and cause them to impinge on the liquid film (supposing the gas phase momentum flux is sufficient enough). However, the latter

may occur at a reduced rate if the liquid structures are large enough to occupy the entire pipe cross section.

Based on the outlined observations in (a) – (d), the model initially predicts the critical gas superficial velocity for liquid bridging to occur. According to English *et al.* (1963), the critical gas superficial velocity that leads to liquid bridging or flooding is given as:

$$U_{gc} = 0.286 \left(\frac{D^{0.322} \rho_l^{0.419} \sigma^{0.097}}{\rho_l^{0.462} \eta_l^{0.15} U_k^{0.075}} \right) \quad (6.8)$$

where U_{lc} is the corresponding critical liquid superficial velocity. In this case, the critical liquid superficial velocity is the maximum liquid superficial velocity condition used for the present experiments. Therefore, when the properties of air-water and air-glycerol/water are substituted in equation (6.8), the plot in Figure 6.36 can be obtained. It is also important to note that at the proposed critical gas superficial velocity predicted by equation (6.8), liquid bridging has been observed to occur more frequently upstream ($L/D = 35.4$) than downstream ($L/D = 82.7$) for the air-water experiments. This behaviour may also be applicable to air-glycerol/water experiments. Further reference can be made to Figure 6.27, which shows the variation of the dominant frequency with gas superficial velocity.

The decrease in flooding velocity with increase in viscosity as in Figure 6.36 has also been observed by (Cetinbudaklar and Jameson, 1969). According to them, the reason for this is because a certain proportion of the viscous damping in the liquid is due to the dissipation near the wall, and as the liquid film becomes thicker, the effect of the wall will be reduced. Thus, with increasing viscosity, the wall damping decreases at a constant Reynolds number so that less energy is required to cause flooding, which will therefore take place at a lower gas superficial velocity.

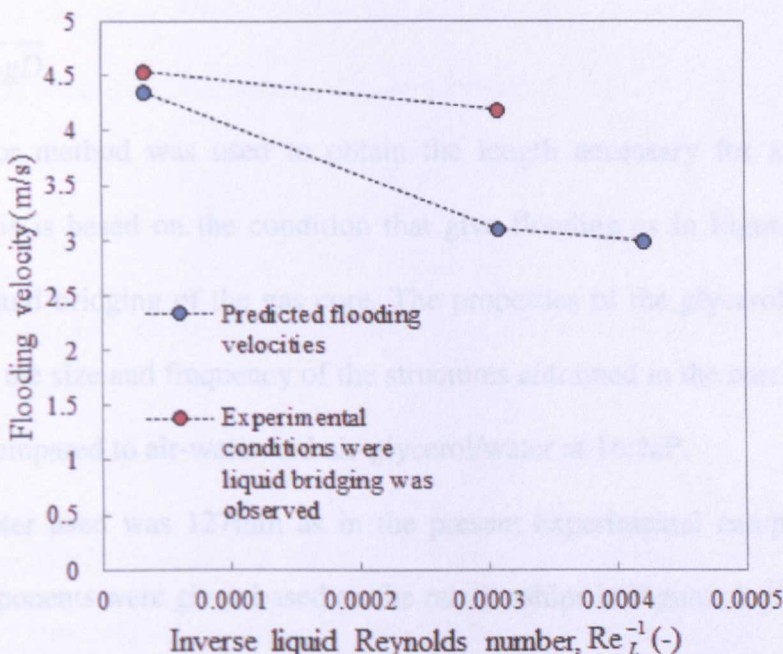


Figure 6.36. Flooding velocity against inverse liquid Reynolds number for air/water, air-glycerol/water (12.2cP) and air-glycerol/water (16.2cP) respectively. Predicted values of flooding are shown as blue filled circles while experimental conditions where liquid bridging was observed are shown as red filled circles.

In corroboration with Ousaka *et al.* (2006), the critical flooding gas superficial velocity is a function of the following:

$$Re_G = f\left(\frac{L}{D}, Re_L, Fr_L, We^*\right) \quad (6.9)$$

where L/D is the dimensionless axial distance, We^* is the modified Weber number given in equation (6.7). The gas Reynolds number, liquid Reynolds number and liquid densimetric Froude number are given below as:

$$Re_G = \frac{\rho_g U_{gc} D}{\mu_g} \quad (6.10)$$

$$Re_L = \frac{\rho_l U_{lc} D}{\mu_l} \quad (6.11)$$

$$Fr_L = \frac{\rho_l U_{lc}^2}{(\rho_l - \rho_g)gD} \quad (6.12)$$

A trial and error method was used to obtain the length necessary for a high degree of coalescence. This is based on the condition that give flooding as in Figure 6.36 or a high frequency of liquid bridging of the gas core. The properties of the glycerol/water at 12.2cP were used since the size and frequency of the structures entrained in the core was observed to be the highest compared to air-water and air-glycerol/water at 16.2cP.

The pipe diameter used was 127mm as in the present experimental campaign. The initial estimates for exponents were given based on the relationships in Figures 6.35 and 6.36 for the modified Weber number and inverse liquid Reynolds number respectively. In addition, the axial location of L/D = 35.4 was also implemented as an initial guess. This is because, the void fraction does not change considerably from this location to L/D = 82.7 as observed for the air-water experiments. Thus, the predicted flooding condition is given as:

$$Re_G = \left(\frac{L}{D} \right)^{1.342} (Re_L)^{-0.0226} (Fr_L)^{-1.879} (We^*)^{0.1342} \quad (6.13)$$

The predicted length from equation (6.13) is 6.45m. This means that the distance from L/D = 35.4 to this length is approximately 1.95m. It is important to note that the large liquid structures formed downstream that occupy the pipe cross-section, fall back upstream due to gravity. As a result, smaller liquid structures such as wisps are sheared off.

As suggested above, this is similar to the disintegration of a liquid jet in inverted annular flow. Therefore, the breakup length of the liquid structure as it falls due to gravity also needs to be accounted for, (De Jarlais *et al.*, 1986).

According to De Jarlais *et al.* 1986, the breakup length is given in equation (6.14). Therefore, the effective length of pipe can be obtained as in equation (6.15).

$$\lambda = 5.8D \quad (6.14)$$

$$E_L = L_p + \lambda \quad (6.15)$$

where L_p is the predicted length of 6.45m obtained in equation (6.13) and E_L is the effective length of 7.19m.

6.5. Summary

The present experiments investigated the effect of liquid viscosity in churn flow. To this end, the air-water data acquired and presented in chapter 5 was compared to the air-glycerol/water data in this chapter for viscosities of 12.2cP and 16.2cP. The time series of void fraction was extracted from the wire mesh sensor. Data was acquired at $L/D = 65.5$ from the injection point. From the time series data acquired, further analysis was carried out and the summary on this work is given below:

1. For churn flow conditions, the time average void fraction is higher for air-glycerol/water compared to air-water. The increase in void fraction is due to the fact that the surface tension decreases with increase in the glycerol/water viscosity.
2. The liquid structures entrained in the gas core are larger for the glycerol/water viscosity compared to air-water. In addition, the size and frequency of the liquid structures present is highest for glycerol/water viscosity of 12.2cP.
3. Comparisons made of void fraction obtained from the present experiment with predicted models show that correlation of Wallis (1962) and Hassan (1998) give reasonable predictions of the observed void fractions.
4. The Dominant frequencies obtained for air-glycerol/water from spectral analysis are similar to those for air-water. It is possible that a higher frequency of liquid structures

entrained in the gas core for air-glycerol/water is compensated for by a higher frequency of huge waves for the air-water.

5. The application of Barnea (1986) stability analysis to the experimental data has shown that at low liquid superficial velocities, the data for air-glycerol/water at 12.2cP and 16.2cP is within the annular flow regime. However, some of the data points exist within the stability curve at higher liquid superficial velocities for the 12.2cP glycerol/water data. Others fall just below the stability curve at higher liquid superficial velocities. Since liquid structures were present within the core for those conditions, the latter region can be regarded as the wispy-annular regime. The Barnea (1986) stability analysis at higher liquid superficial velocities for the 16.2cP glycerol/water has no data points within the stability curve but in the wispy-annular regime.
6. The churn flow model is proposed in equation (6.13) to predict the height that should induce a high degree of coalescence in the CFC. This is based on observation, in-depth analysis and comparison with air-water experimental data.

The bubble to churn flow experiments, churn flow experiments using air-water and air-glycerol/water as respective fluid phases have been conducted in this research work. Taking Figure 1.5 in chapter 1 into consideration, the conclusions and recommendation for future work are discussed in chapter 7.

CHAPTER 7

CONCLUSIONS

This chapter presents the conclusions of the research work performed per experimental chapter and recommendations for future work that may be considered in this area of research.

Reference can be made to Figure 1.5.

CHAPTER 4 Conclusions - Bubbly to Churn flow transition *air-water experiments*

The aim of these experiments was to delineate between the sub-regimes present for bubbly to churn flows in a large diameter pipe. Using a 32 x 32 capacitance wire mesh sensor, the spatio-temporal evolution in form of void fraction data was acquired. The void data is in form of a three-dimensional matrix. Although, this instrumentation is flow intrusive, this gives a high cross-sectional imaging resolution of the flow. The void data was acquired at 1000 cross sections per second for 30s. After subjecting the void data to in-depth analysis and from high speed camera and visual observations, the following conclusions can be drawn:

- (a) Slug flow was not observed in these experiments but a transition from bubbly to churning flows. The reason for this in agreement to previous workers can be attributed to Taylor instability. The upper surface of the large diameter bubble occupying the pipe cross-section become distorted and collapse thereby breaking up into daughter bubbles. The large diameter bubble occupies the cross-section of the pipe having a distorted frontal shape and a shorter axial length compared to Taylor bubbles.
- (b) Smaller diameter bubbles in the liquid, flowing behind the distorted large diameter bubble have the same nature as liquid slugs in slug flow. The unit, of a large diameter bubble and small diameter bubbles in liquid occur intermittently. This forms the spherical bubbly flow pattern. As regards the bubble size distribution this shows two distinctive peaks. The

areas below the peaks are large and small respectively indicative of the small diameter bubble distribution in the liquid and the large diameter bubble.

- (c) In transiting to the churn flow pattern, at higher gas flowrates, these large diameter bubbles are destroyed. This forms clusters of small diameter closely packed bubbles in the liquid having approximately the same bubble diameter, that is, when bubble size distribution analysis was performed. The latter is characterised as having a frothy nature. The distance between the bubbles is less than the bubble diameter itself. Therefore, this encourages coalescence of the bubbles within the frothy medium.
- (d) For the typical churn flow regime, liquid slugs having a frothy nature as described in (c), huge waves and liquid structures/wisps entrained in the gas core are the prevailing phenomena occurring. However, this can be classified into two major sub-regimes, liquid slugs and huge waves since the liquid structures are formed from radial coalescence of the crest of the huge waves. The huge waves have a sinusoidal shape and in most cases are axisymmetric.
- (e) Statistical methods such as standard deviation, skewness and probability density function of the time series data reveal the transition from bubbly to churn flow. The standard deviation increases to a maximum then decreases and eventually forms a plateau with increasing gas flowrate. The skewness demarcated between the wall and core peaking nature of the flow. The probability density function gives a shift in the distribution from left to right respectively of increasing void fraction.
- (f) Spectral methods applied to the time series data also reveal the transition from bubble to churn flows similar to the statistical analysis. Structure frequency at constant liquid flowrate increases with gas flowrate to a maximum, decreases and eventually forms a plateau when churn flow is the prevailing condition. This also shows that as the liquid flowrate increases the profile increases as it becomes more oscillatory.

In these experiments it was ascertained that the churn flow regime is made up of two sub-regimes, which are formation of liquid slugs and huge waves. However, the dominance of either of the phenomena upstream or downstream the vertical pipe was not ascertained. Therefore, this prompted further detailed experiments to be conducted in a longer length of pipe and within the churn flow regime.

CHAPTER 5 Conclusions - Further insights into Churn flow *air-water experiments*

The further detailed experiments were conducted within the churn flow regime at higher gas flowrates. Data was acquired at five axial distances from the injection using the same WMS instrumentation in the Chapter 4 experiments. The aim of the experiment was to identify where the liquid slugs and huge waves occur more frequently along the vertical pipe. From these experiments the following conclusions can be drawn:

- (a) At the inception of churn flow as identified from the previous experiments liquid bridging of the gas core takes place, which is essentially the formation of liquid slugs. This has the same frothy nature as previously observed and is characterised as small diameter bubbles entrained in the liquid phase. When this phenomenon occurs there is a momentary blockage of the pipe cross-section.
- (b) There is no shift in the bubble size distribution in churn flow as the gas flowrate increases. This has been shown in Figure D.1 in Appendix D for the range of conditions experimented. However, there is a decrease in size distribution. This is because the mechanism of bubble formation is by gas entrainment in the liquid.
- (c) When gas flows upwards it propagates the wave flowing on the inner walls of the pipe. The waves grow and the amplitude of the wave reaches a critical wave amplitude and liquid bridging of the gas core becomes the persisting condition upstream at the middle

section of the test section ($L/D = 35.4$) than further downstream due to the difference in hydrostatic pressure. In other words, liquid bridging decays downstream.

- (d) On the other hand, the well-defined sinusoidal shape of the huge wave observed in the experiments in chapter 4 is similarly more frequent downstream, that is, close to the outlet of the pipe at $L/D = 82.7$, due to axial coalescence of the huge waves. The transit velocities of the huge waves are longer in comparison to when liquid slugs are present. In other words, the time it takes before discontinuity of the gas core or radial coalescence of the huge waves is longer downstream than upstream. This also points to the fact that the huge waves are more stable/frequent downstream at $L/D = 82.7$ compared to upstream locations.
- (e) Apart from the liquid phase flowing as huge waves, they are entrained as large liquid structures occupying the pipe cross-section. Their sizes are larger and at higher frequencies downstream of the pipe at $L/D = 82.7$ than upstream. These liquid structures entrained in the gas core are initially formed upstream and they are propagated by the gas phase downstream.
- (f) The void fraction upstream of the vertical pipe at $L/D = 35.4$ and further downstream at $L/D = 82.7$ are more or less similar. Overall, this gives a logarithmic increase in void fraction with increase in axial distance from the injection. Since the magnitude of difference between the void fraction is not significant the flow can be considered developed based on the void fraction at $L/D = 82.7$.
- (g) The dominant frequency obtained from spectral analysis of the time series shows a general decrease in structure frequency with increase in axial distance from the injection. Comparison with the data of Omebere-Iyari (2006) who experimented at similar conditions in this facility shows a further decrease in the structure frequency at $L/D = 82.7$ from his point of data acquisition at $L/D = 65.5$ using conductance probes.

(h) Further Stability analysis according to Barnea proved useful in predicting the liquid bridging and huge wave dominant regimes based on the variation of her dimensionless parameter, Y , against the Lockhart-Martinelli parameter.

The experiments provided novel insight into the churn flow regime with increase in axial distance from the injection, which has not been previously investigated. This motivated further experiment to be carried out on the effect viscosity could have on the flow behaviour.

CHAPTER 6 Conclusions - Effect of liquid viscosity in Churn flow *air-glycerol/water experiments*

The viscosity of the continuous phase was changed to glycerol/water solutions of 12.2cP and 16.2cP respectively. The data was acquired at L/D = 65.5 based on the work previously done by (Omebere-Iyari, 2006). Comparative study was carried out with reference to air-water experiments previously performed in the same facility. The capacitance WMS used in previous experiments was used here for the same purpose. The aim of the experiments was to identify the effect of viscosity in churn flow. Therefore, from this work, the following conclusions can be drawn:

- (a) Increasing the viscosity in churn flow increases the void fraction. This is due to the decreasing surface tension as the viscosity of the continuous phase increases from air-water to air-glycerol/water. Also, the increase in viscosity leads to less dissipation of energy in the case of air-glycerol/water compared to air-water.
- (b) From statistical analysis of time series data set, the increase in viscosity is reflected as an increase in the mean void fraction and hence a shift in the probability distribution from air-water to air-glycerol/water. However, the shift in the PDF is characterised by the occurrence of two distinct peaks at high liquid flowrates for the glycerol/water experiments compared to the air-water. This is due to the fact that the liquid structures

observed for churn flow in the previous experiments are larger for air-glycerol/water compared to air-water.

- (c) A method for the formation of these large entrained liquid structures has been proposed taking the viscosity of the glycerol/water into consideration. These are (a) Peaking of the liquid film into the gas core (b) Coalescence of propagating huge waves from an upstream location to augment the amplitude of the wave within a reference control volume. (c) Protrusion of the augmented huge wave structure into the gas core after a critical wave amplitude/height has been attained and (d) Shearing-off of the huge wave structure from the liquid film and the formation of the entrained liquid structure.
- (d) A threshold method has been successfully applied to the time series data to reveal the occurrences that take place with respect to the operating conditions. The dominant frequency obtained from spectral analysis of the time series data gives similar frequency values for air-glycerol/water at $L/D = 65.5$ and air-water experiments at $L/D = 82.7$. The frequency across the viscosity scale increases in most cases to a maximum for the 12.2cP glycerol/water data.
- (e) The increased frequency of large liquid structures entrained in the gas core for the air-glycerol/water is compensated for, by an increased frequency of huge waves for air-water. Due to the abstraction of energy for the air-glycerol/water experiments the atomising force on the liquid film is much lower compared to air-water.
- (f) The presence of large liquid structures entrained in the gas core has similarities to the wispy-annular flow identified by (Bennet *et al.*, 1965). Thus, carrying out the stability analysis according to Barnea (1986) revealed that the region below the stability curve where Barnea observed typical annular flow, this has been proposed in this study to be the wispy-annular regime. That is, at high liquid flowrate, for $0 \leq Y \leq 100$. According to this analysis, three regions have been identified namely: A – Liquid bridging region (Large

liquid structures were observed), B – Wispy- annular flow region and C – Annular flow region.

(g) In the liquid bridging region – A, liquid bridging phenomenon has been observed for both air-glycerol/water and air-water. Based on this condition, the effective length of the CFC with respect to the comparative study performed and for this pipe diameter is 7.15m.

The provision of novel experimental data has been obtained for the glycerol/water experiments. The effective length of the CFC has been proposed based on the comparative study with the air-water experiments previously performed. The required conditions for the CFC are those that give a high frequency of liquid bridging hence high entrainment of large liquid structures in the gas core, which should effectively improve coalescence.

FUTURE WORK AND RECOMMENDATIONS

The following future work and recommendations are given below based on the observations and analysis of the data presented in this research work:

(a) The effect of fluid properties other than air-water and air-glycerol/water should also be investigated. Air-silicone oil experiments may be conducted to investigate the effect of surface tension. On other hand, sulphur hexafluoride-silicone or sulphur hexafluoride-water experiments may also be used to investigate the effect of gas phase density. This should be investigated as long as it is done safely.

(b) Two wire mesh sensors at a close distance should be used to acquire phase fraction data simultaneously at least three axial distances from the injection. This is to know the distance it takes for the huge wave to travel before liquid bridging takes place. Apart from monitoring the huge wave structure, the structure velocity can be obtained to find out what percentage of the gas superficial velocity it is. This percentage value may be compared to Barbosa *et al.* (2001a) that suggested that the wave velocity is 20% of the

gas superficial velocity. Using two wire mesh sensors may also help further size characterisation of the liquid structures that are entrained in the gas core.

- (c) From the further analysis of the wire mesh data from both sensors, the axial length of the liquid slug can be determined to obtain a plot of dimensionless axial length of liquid bridge against dimensionless axial distance. This is based on the recommendation that the two wire mesh sensors should be used at different axial distances.
- (d) Pressure drop experiments for the different fluid pairs should be carried out but this means conducting experiment from the bubbly flow condition. This is because the pressure drop will change significantly as the churn flow regime is entered. The region of concentration should be to know the pressure drop trace at the transition from spherical cap bubbly flow to liquid bridging conditions for large diameter pipes.
- (e) An instrument may be used simultaneously with the WMS that gives the structure frequency against time, that is, in comparison to the void fraction against time extracted from the WMS sensor data. The frequency-time analysis can be compared to frequency-time analysis obtained using Hilbert-Huang Transform (HHT). PDF of the experimental frequency, predicted frequency (HHT) and void fraction can be obtained to improve the understanding of churn flow.
- (f) Computational fluid dynamics simulation of churn flow may be conducted using the VOF method coupled with the Lagrangian model. This has been investigated and simulated but not presented in this work. Results may also be validated with experimental data, which will also help tune computational models.

REFERENCES

A

Abdulkadir, M., Zhao, D., Sharaf, S., Abdulkareem, L., Lowndes, I.S., Azzopardi, B.J., (2011). Interrogating and effect of 90° bends on air-silicone oil flows using advanced instrumentation, *Chemical Engineering Science*, Vol. 66, Issue 11, June 2011, pp 2453-2467.

Ahmad, M., Peng, D.J., Hale, C.P., Walker, S.P., Hewitt, G.F., (2010). Droplet Entrainment in Churn Flow, *7th Internal Conference on Multiphase Flow*, Tampa, Florida, U.S.A, May 30 – June 4.

Azzopardi, B. J., Taylor, S., and Gibbons, D.B., (1983). Annular two phase flow in large diameter pipes. *Proceedings of the International Conference on the Physical Modelling of Multiphase Flow*, Coventry, pp. 256-267.

Azzopardi, B.J., Zaidi, S.H., (2000). Determination of entrained fraction in vertical annular gas/liquid flow. *Journal of Fluid Engineering*, Vol 122, pp. 146–150.

Azzopardi, B. J., and Wren, E., (2004). What is entrainment in vertical two-phase churn flow? *International Journal of Multiphase Flow*, Vol. 30, pp. 89-103.

Azzopardi.B.J, (2005). Two-phase flow at T-junctions combining and dividing Gas/liquid and liquid/liquid. Presentation at Delft University.

Azzopardi, B. J., (2006). *Gas Liquid Flows*, Begell House Inc., New York.

Azzopardi, B.J., (2012). Churn flow investigated using electrical tomography (and other advanced instrumentation). *3rd Brazilian Conference on Boiling, Condensation and Multiphase flow*, Curitiba, May 7 – 9.

B

Baker, O., (1954). Simultaneous flow of oil and gas. *Oil and Gas Journal* 53, pp 185- 195

Bankoff, S.G., and Lee, S.C., (1986). A critical review of the flooding literature. *Multiphase Science and Technology*, Chapter 2, Hemisphere, New York.

- Barbosa, J., Richardson, S., Hewitt, G.F., (2001a). Churn flow: myth, magic and mystery. In: 39th European Two-Phase Flow Group Meeting, Aveiro, Portugal, June 18–20.
- Barbosa, J., Govan, A.H., Hewitt, G.F., (2001b). Visualisation and modelling studies of churn flow in a vertical pipe. International Journal of Multiphase Flow, Vol. 27, 2105–2127.
- Barbosa, J.R., Hewitt, G.F., König, G., Richardson, S.M., (2002). Liquid entrainment, droplet concentration and pressure gradient at the onset of annular flow in a vertical pipe. International Journal Multiphase Flow, Vol. 28, 943–961.
- Barnea, D., (1986). Transition from annular flow and from dispersed bubble flow-Unified models for the whole range of pipe inclinations. International Journal of Multiphase Flow, Vol. 12, Issue 5, pp. 733-744.
- Bennett, A.W., Hewitt, G. F., Kearsey, H. A., Keeys, R. K. F. and Lacey, P. M. C., (1965). Flow visualisation studies of boiling at high pressure, UKAEA Report AERE-R 4874.
- Bordel, S., Mato, R., Villaverde, S., (2006). Modelling of the evolution with length of bubble size distribution in bubble columns. Chemical Engineering Science, Vol. 61, 3663-3673.
- Brauner, N., and Barnea, D., (1986). Slug/churn transition in upward gas-liquid flow, Chemical Engineering Science, Vol. 41, No. 1, pp. 159-163.
- C**
- Cai, Y., Wambsganss W., Jendrzejczyk, J.A., (1995). A Chaotic System of Two-Phase Flow in a Small, Horizontal, Rectangular Channel. ASME/JSME Pressure Vessels and Piping Conference, Honolulu, Hawaii, July 23 – 27.
- Cetinbudaklar, A. G. and Jameson, A.G., (1969). The mechanism of flooding in vertical countercurrent two-phase flow. Chemical Engineering Science, Vol. 24, Issue 11, pp 1669 – 1680.
- Cha, J-E., Ahn Y-C., Kim M-H., (2002). Flow measurement with an electromagnetic flowmeter in two-phase bubbly and slug flow regimes, Vol. 12, pp 329 – 339.

Chen, X. T., and Brill, J.P., (1997). Slug to churn transition in upward vertical two-phase flow. *Chemical Engineering Science*, Vol. 52, Issue 23, pp 4269 – 4272.

Cheng, H., (1997). The bubble to slug flow pattern transition in vertical columns. PhD Thesis, University of Nottingham, UK.

Chen, R. C., Reese, J., and Fan, L.-S., (1994). Flow structure of a three-dimensional bubble column and three-phase fluidized bed. *A.I.C.H.E. J*, Vol. 40, 1093-1104.

Chirinos.W.A. (1998), Liquid Carry over in Gas-liquid cylindrical cyclone compact separators, MSc thesis, University of Tulsa, U.S.A.

Chisholm, D., (1972). An equation for velocity ratio in two-phase flow. N.E.L. Report No 535.

Cioncolini, A., Thome, J.R., (2012). Void fraction prediction in annular two-phase flow. *International Journal of Multiphase flow*, Vol. 43, pp 72-84.

Costigan, G., and Whalley, P. B., (1997). Slug flow regime identification from dynamic void fraction measurements in vertical air-water flows. *International Journal of Multiphase Flow*. Vol. 23, No.2, 263-282.

D

Da Silva M.J., Schleicher E., Hampel U., (2007). Capacitance Wire-Mesh Sensor for Fast Measurement of Phase Fraction Distributions. *Measurement Science and Technology*, Vol. 18, pp. 2245-2251.

De Jarlais, G., Ishii, M., and Linehan, J., (1986). Hydrodynamic Stability of Inverted Annular Flow in and adiabatic Simulation. *Transaction of American Society of Mechanical Engineers, Journal of Heat Transfer*, Vol. 108, pp 85 – 92.

Doubliez, L., (1991). The drainage and rupture of a non-foaming liquid film formed upon bubble impact with a free surface. *International Journal of Multiphase Flow*, Vol. 17, pp 783– 803.

Duinveld, P.C., (1994). Bouncing and coalescence of two bubbles in water. Ph.D. Dissertation, University of Twente, Netherlands.

Dukler, A.E., and Taitel, Y., (1986). Flow pattern transitions in gas-liquid systems: measurement and modelling. *Multiphase Science and Technology*, Vol. 2, pp 53-57.

E

English, K.G., Jones, W.T., Spillers, R.C., Orr, V., (1963). Flooding in a vertical updraft partial condenser. *Chemical Engineering Progress*. Vol. 59, Issue 7, pp 51–54.

F

Furukawa, T., Fukano T., (2001). Effect of liquid viscosity on flow patterns in vertical upward gas-liquid two phase flow. *International Journal of Multiphase flow*, Vol. 27, pp 1109 – 1126.

G

Govan, A.H., Hewitt, G.F., Richter, H.J., Scott, A., (1991). Flooding and Churn flow in Vertical pipes. *International Journal of Multiphase flow*, Vol. 17, Issue 1, pp 27 – 44.

H

Harmathy, T. Z., (1960), Velocity of large drops and bubbles in media of infinite or restricted extent, *AIChE Journal*, Vol. 6, No. 2, pp. 281-288.

Hasan, A.R., (1988). Void fraction in bubbly, slug and churn flow in vertical two-phase up-flow. *Chemical Engineering Communication*. Vol. 66, pp 101–111.

Hawkes, N.J., Lawrence, C.J., Hewitt, G.F., (2001). Prediction of transition from annular to wispy-annular flow using linear stability analysis of the gas-droplet core. *Chemical Engineering Science*, Vol. 56, Issue 5, pp 1925 – 1932.

Hernendez-Perez V., Azzopardi.B.J., Kaji R., Da Silva M.J., Beyer M., Hampel U., (2010). Wisplike structures in vertical gas-liquid pipe flow revealed by wire mesh sensor studies. *International Journal of Multiphase Flow*, Vol. 36 pp. 908–915

Hewitt, G. F., and Roberts, D. N., (1969). Studies of two-phase flow patterns by simultaneous x-rays and flash photography. Atomic Energy Research Establishment, Harwell, England, Report M-2159.

Hewitt, G.F., Hall-Taylor, N.S., (1970). Annular Gas–Liquid Flow. Pergamon Press, Oxford.

Hewitt, G.F., Martin, C.J., Wilkes, N.S., (1985). Experimental and modelling studies of annular flow in the region between flow reversal and pressure drop minimum. PCH Physicochemical and Hydrodynamics, Vol. 6, pp 69 – 86.

Howarth, W.J., (1964). Coalescence of drops in a turbulent flow field. Chemical Engineering Science, Vol.19, 33–38.

Hinze, J. O., (1955). Fundamentals of the hydrodynamic mechanism of splitting in dispersion processes. AIChE J., Vol. 1, pp. 289.

Hibiki, T., Ishii, M., (2003). Two-group interfacial area transport equations at bubble-slug flow transition. Nuclear Engineering and Design, Vol 202, Issue 1, pp 39 – 76.

Huang, Z., Wang, B., and Li, H., (2003). Application of electrical capacitance tomography to the void fraction measurement of two-phase flow. IEEE Transactions on Instrumentation and Measurement, Vol.52, 7-12.

J

Jayanti, S., and Hewitt, G. F., (1992). Prediction of the slug-to-churn flow transition in vertical two-phase flow. International Journal of Multiphase Flow, Vol. 18, Vol. 6, pp. 847-860.

Jayanti, S., Tokarz, A., and Hewitt, G. F., (1996). Theoretical investigation of the diameter effect on flooding in countercurrent flow. International Journal of Multiphase Flow, Vol. 22, No. 2, pp. 307-324.

Jeanmeure, L.F.C., Dyakowski, T., Zimmerman, W.B.J., (2002). Direct Flow-Pattern Identification using Electrical Capacitance Tomography. *Experimental Thermal and Fluid Science*, Vol. 26, Issue 6 – 7, pp. 763-773.

K

Kaji, R., (2008). Characteristics of Two-Phase Flow Structures and Transition in Vertical Upflow, PhD Thesis, University of Nottingham, U.K.

Kaji R., Azzopardi B.J., Lucas D., (2009). Investigation of flow development of co-current gas-liquid vertical slug flow. *International Journal of Multiphase flow*, Vol. 35, pp 335-348

Kaji, R., Azzopardi, B.J., (2010). The effect of pipe diameter on the structure of gas/flow in vertical pipe. *International Journal of Multiphase Flow*, Vol. 36, Issue 4, pp 303-313.

Kataoka, I., Ishii, M., (1987). Drift flux model for large diameter pipe and new correlation for pool void fraction. *International Journal of Heat and Mass Transfer*, Vol.30, Issue 9, pp 1927 – 1939.

Kolev,N.I.(1993). Fragmentation and coalescence dynamics in multiphase flows. *Experimental and coalescence dynamics in multiphase flows*. Vol. 6, Issue 3, pp 211 – 251.

Kouba, G.E., Shoham, O., (1995). A review of Gas-Liquid Cylindrical Cyclone (GLCC) technology. Internal Conference on Production Separation Systems Aberdeen, UK, April 23 – 24.

L

Legius, H. J. W. M., (1997). Propagation of pulsations and waves in two-phase pipe systems. PhD thesis, Delft University of Technology, Netherlands.

Lehr, F., Mewes, D., (1999). A transport equation for the interfacial area density applied to bubble columns, *Chemical Engineering Science*, Vol. 56, pp 1159 – 1166.

Lehr, F., Millies, M., Mewes, D., (2002). Bubble-size distributions and flow fields in bubble columns, *AIChE Journal*, Vol. 48, Issue 11, pp 2426 – 2443.

Liao, Y., and Lucas, D., (2010). A literature review on mechanisms and models for coalescence process of fluid particles. *Chemical Engineering Science*, Vol. 65, Issue 10, pp 2851 – 2864.

Lucas, D., Krepper, E. and Prasser, H.-M., (2005). Development of co-current air-water flow in a vertical pipe. *International Journal of Multiphase flow*, Vol. 31, pp 1304-1328.

Lucas, D., Krepper, E., Prasser, H.-M., (2007). Use of models for lift, wall and turbulent dispersion forces acting on bubbles for poly-disperse flows. *Chemical Engineering Science*, Vol. 62, Issue 15, pp 4146 – 4157.

Lucas, D., Beyer, M., Szalinski, L., Schutz, P., (2010). A new database on the evolution of air-water flows along a large vertical pipe. *International Journal of Thermal Sciences*, Vol. 49, Issue 4, pp 664 – 674.

Luo, H., and Svendsen, H. F. (1991). Turbulent circulation in bubble columns from eddy viscosity distributions of single-phase pipe flow. *Canadian Journal of Chemical Engineering*, 69, 1389-1394.

M

Marrucci.G., (1968). Theory of coalescence. *Chemical Engineering Science*, Vol.24, pp 975-985.

Mao, Z.-S., Dukler, A.E., 1989. An experimental study of gas–liquid slug flow. *Experimental Fluids*, Vol. 8, pp 169–182.

McKeen, T.R., Pugsley, T.S., (2002). The influence of permittivity models on phantom images obtained from electrical capacitance tomography. *Measurement Science and Technology*, Vol.13, pp 1822–1830.

McQuillan, K.W., and Whalley, P.B., (1985). Flow patterns in vertical two-phase flow. *International Journal of Multiphase Flow*, Vol. 11, pp 161-175.

Milles, M. and Mewes, D. (1999). Interfacial area density in bubbly flow. Chemical Engineering and Processing, Vol. 38, pp 307-319.

Mishima, K., and Ishii, M., (1984). Flow regime transition criteria for upward two-phase flow in vertical tubes. International Journal of Heat & Mass Transfer, Vol, 27, pp 723-737.

N

Nicklin, D. J., Wilkes, J. O., and Davidson, J. F., (1962). Two-phase flow in vertical tubes. Transaction of Institution of Chemical Engineers, Vol, 40, pp 61-68.

O

Ohnuki, A. and Akimoto, H., (2000). Experimental study on transition of flow pattern and phase distribution in upward air-water two-phase flow along a large vertical pipe. International Journal of Multiphase Flow, Vol. 26, pp 376–386.

Omebere-Iyari, N.K., (2006), “The effect of pipe diameter and pressure in vertical two-phase flow”, Ph.D. Thesis, The University of Nottingham, UK.

Omebere-Iyari, N.K., Azzopardi, B.J. and Lucas, D., (2008). The characteristics of gas/liquid flow in large risers at high pressures. International Journal of Multiphase flow, 34, 461-476.

Owen, D.G., (1986). An experimental and theoretical analysis of equilibrium annular flows. Ph.D. Thesis, University of Birmingham, U.K.

Ousaka, A., Deendarlianto, Kariyasaki, A., Fukano, T., (2006). Prediction of flooding gas velocity in gas-liquid counter-current two phase flow in inclined pipes. Nuclear Engineering and Design, Vol. 236, Issue 12, pp 1282 – 1292.

P

Prasser, H.-M., Böttger, A. and Zschau, J., (1998). A new electrode-mesh tomography for gas-liquid flows. Flow Measurement and Instrumentation, Vol 9, pp 111–119.

Prasser, H.-M., Scholz, D. and Zippe, C., (2001). Bubble size measurement using wire-mesh sensors. Flow Measurement and Instrumentation, Vol. 12, pp 299–312.

Prasser, H.-M., Beyer, M., Böttger, A., Carl, H., Lucas, D., Schaffrath, A., Schutz, P., Weiss, F.-P. and Zschau, J., (2005b). Influence of the pipe diameter on the structure of the gas–liquid interface in a vertical two-phase pipe flow. Nuclear Technology, Vol. 152, pp 3-22.

Premoli, A., Francesco, D., and Prina, A., (1970). An empirical correlation for evaluating two-phase mixture density under adiabatic conditions. European Two-Phase Flow Group Meeting, Milan, Italy.

Q

Qi, F.S., Yeoh, G.H., Cheung S.C.P., Tu, J.Y., Krepper, E., Lucas, D.,(2012). Classification of bubbles in vertical gas-liquid flow: Part 1 – Analysis of experimental data. International Journal of Multiphase Flow, Vol. 39, pp 121 – 134.

R

Radovcich, N. A., and Moissis, R., (1962). The transition from two phase bubble flow to slug flow”, Report of Massachusetts Institute of Technology, No. 7-7673-22, pp. 1-47.

S

Sawai, T., Kaji, M., Kasugai, T., Nakashima, H. and Mori, T., (2004). Gas-liquid interfacial structure and pressure drop characteristics of churn flow”, Experimental Thermal and Fluid Science, Vol. 28, pp. 597-606.

Schlegel, J.P., Sawant, P., Paranjape, S., Ozar, B., Hibiki, T., Ishii, M., (2009). Void fraction and flow regime in adiabatic upward two-phase flow in large diameter pipes. Nuclear Engineering and Design, Vol. 239, Vol. 12, pp 2864 – 2874.

Sekoguchi, K. and Mori, K., (1997). New development of experimental study on interfacial structure in gas-liquid two-phase flow. Experimental Heat Transfer, Fluid Mechanics and Thermodynamics (Ed. M.Giot, F.Mayinger and G.-P. Celata) Edizione ETS, Vol. 2, pp. 1177-1188.

- Sekoguchi, K., and Takeishi, M., (1989). Interfacial structure in upward Huge wave flow and Annular flow regimes. International Journal of Multiphase flow, Vol. 15, No.3, pp, 295-305.
- Serizawa, A. and Kataoka, I., (1988). Phase distribution in two-phase flow, in: N.H. Afgan (Ed.), Transient Phenomena in Multiphase Flow, Hemisphere, Washington, DC, pp 179–224.
- Shen, X., Mishima, K. and Nakamura, H. (2005). Two-phase distribution in vertical large diameter pipe. International Journal of Heat and Mass Transfer, 48, pp 211-225.
- Smith, T. R., Schlegel. J.P., Hibiki, T., Ishii, M., (2012). Mechanistic modelling of interfacial area transport in large diameter pipes. International Journal of Multiphase Flow, Vol. 47, pp 1 – 16.
- Spedding, P.L., Woods, G.S., Raghunathan, R.S. and Watterson, J.K., (1998). Vertical two-phase flow Part I: flow regimes, Transactions of the Institution of Chemical Engineers, Vol. 76 (A), pp. 612-619.
- Szalinski, L., Abdulkareem L.A, Da Silva, D.J., Thiele, S., Beyer, M., Lucas, D., Perez, H., Hampel, U. and Azzopardi, B.J. (2010). Comparative study of gas-oil and gas-water two phase flow in a vertical pipe. Chemical Engineering Science, Vol 65, pp 3836-3848.

T

Taitel, Y., Barnea, D. and Dukler, A.E., (1980), “Modelling flow pattern transitions for steady upward gas-liquid flow in vertical tubes”, AIChE Journal, Vol. 26, Issue 3, pp. 345-354.

Thiele S., Da Silva M., Hampel. U (2009) “Capacitance Planar Array Sensor for Fast Multiphase flow Imaging”. IEEE Sensors Journal, Vol. 9, Issue 5, pp 533 – 540.

V

Van Hout, R., Shemer, L., and Barnea, D., (1992). Spatial distribution of void fraction within a liquid slug and some other related slug parameters. International Journal of Multiphase flow Vol. 18, pp 831-845.

Vijayan, M., Jayanti, M., Balakrishnan, A.R., (2001). Effect of tube diameter on flooding. International Journal of Multiphase Flow, Vol. 27, Issue 5, pp 797 – 816.

W

Wang, K., Bai, B., Cui, J., Ma, W., (2012). A physical mode for huge wave movement in gas-liquid churn flow. Chemical Engineering Science, Vol. 79, pp 19 – 28.

Wallis, G. B., (1969). One dimensional two-phase flow. McGraw-Hill, London.

Weisman, J., Duncan. D., Gibson, J., Crawford, T., (1979). Effects of fluid properties and pipe diameter on two-phase flow patterns in horizontal lines. International Journal Multiphase Flow. Vol. 5, pp 437 – 462.

Wu, Y., (2001). Predictions of radical gas holdup profiles in bubble column reactors. Chemical Engineering Science, Vol. 56, pp 1207-1210.

Wolf, A., Jayanti, S., Hewitt, G.F., (1996). On the nature of ephemeral waves in vertical annular flow. International Journal Multiphase Flow, Vol. 22, Issue 2, pp 325 – 333.

Z

Zuber, N., Findlay, J.A., 1965. Average volumetric concentration in two phase flow systems. Trans. ASME: J. Heat Transfer 87, 453–468.

NOMENCLATURE

A	Constant in equation (5.8)	(-)
B	Constant in equation (5.8)	(-)
C	Constant in equation (5.9)	(-)
D	Constant in equation (5.9)	(-)
α_g	Void fraction	(-)
α_r	Radial void fraction	(-)
α_L	Liquid holdup	(-)
α_{gc}	Critical void fraction	(-)
α_{TB}	Void fraction in Taylor bubble	(-)
x_g	Gas quality	(-)
C_o	Distribution parameter	(-)
c	Gas holdup parameter	(-)
r/R	Dimensionless radial distance	(-)
n	Power law exponent	(-)
ϵ_r	Relative permittivity	(-)
A_g	Area occupied by gas	(m ²)
A_l	Area occupied by liquid	(m ²)
A_c	Cross sectional area	(m ²)
\dot{M}_g	Mass flowrate of gas	(kg/s)
\dot{M}_l	Mass flowrate of liquid	(kg/s)
\dot{M}_T	Total mass flowrate of phases	(kg/s)
U_{gs}	Gas superficial velocity	(m/s)
U_{ls}	Liquid superficial velocity	(m/s)
U_{gd}	Drift velocity	(m/s)
ρ_l	Density of liquid	(kg/m ³)
ρ_g	Density of gas	(kg/m ³)
\dot{m}_g	Gas mass flux	(kg/m ² s)
u_{rel}	Relative velocity	(m/s)
u_w	Wave velocity	(m/s)
\dot{m}_l	Liquid mass flux	(kg/m ² s)
f	Frequency of collisions	(s ⁻¹)
\bar{c}	Mean fluctuating velocity	(m/s)
D_b	Bubble diameter	(mm)
U_o	Rise velocity of bubbles	(m/s)
σ	Surface tension	(N/m)
g	Gravitational force	(m/s ²)
r_b	Bubble radius	(mm)

U_F	Liquid film velocity	(m/s)
U_{TB}	Velocity of Taylor bubble	(m/s)
L_S	Length of Liquid Slug	(mm)
L_{TB}	Length of Taylor bubble	(mm)
L_U	Total length of slug unit	(mm)
δ_F	Film thickness	(mm)
Q_v	Liquid flowrate through bubble generator	(m ³ /s)
D	Pipe diameter	(mm)
U_m	Liquid film velocity	(m/s)
$\Delta\rho$	Density difference	(kg/m ³)
μ_l	Liquid viscosity	(kg/ms)
ν_l	Kinematic viscosity	(m ² /s)
l_e	Entrance length	(m)
L	Pipe length	(m)
\dot{M}_{LE}	Mass flowrate of entrained droplet	(kg/s)
\dot{M}_l	Mass flowrate of liquid	(kg/s)
V_b	Volume of bubble	(mm ³)
h	Size distribution	(%/mm)
h_w	Wave height	(mm)
i	Vertical projection	(-)
j	Horizontal projection	(-)
k	Time sequence	(-)
τ	Delay time	(s)
R_{sm}	Minimum liquid holdup	(-)
X	Lockhart-Martinelli parameter	(-)
Y	Dimensionless parameter in equation (6.6)	(-)
V_o	Voltage	(volts)

Dimensionless Numbers

U_{ls}^*	Dimensionless gas velocity	(-)
U_{gs}^*	Dimensionless gas velocity	(-)
f_w	Friction factor	(-)
We	Weber number	(-)
Fr_L	Liquid based Froude number	(-)
Fr_G	Gas based Froude number	(-)
Str_G	Gas based Strouhal number	(-)
Str_m	Mixture based Strouhal number	(-)
Re_G	Gas based Reynolds number	(-)

APPENDIX A

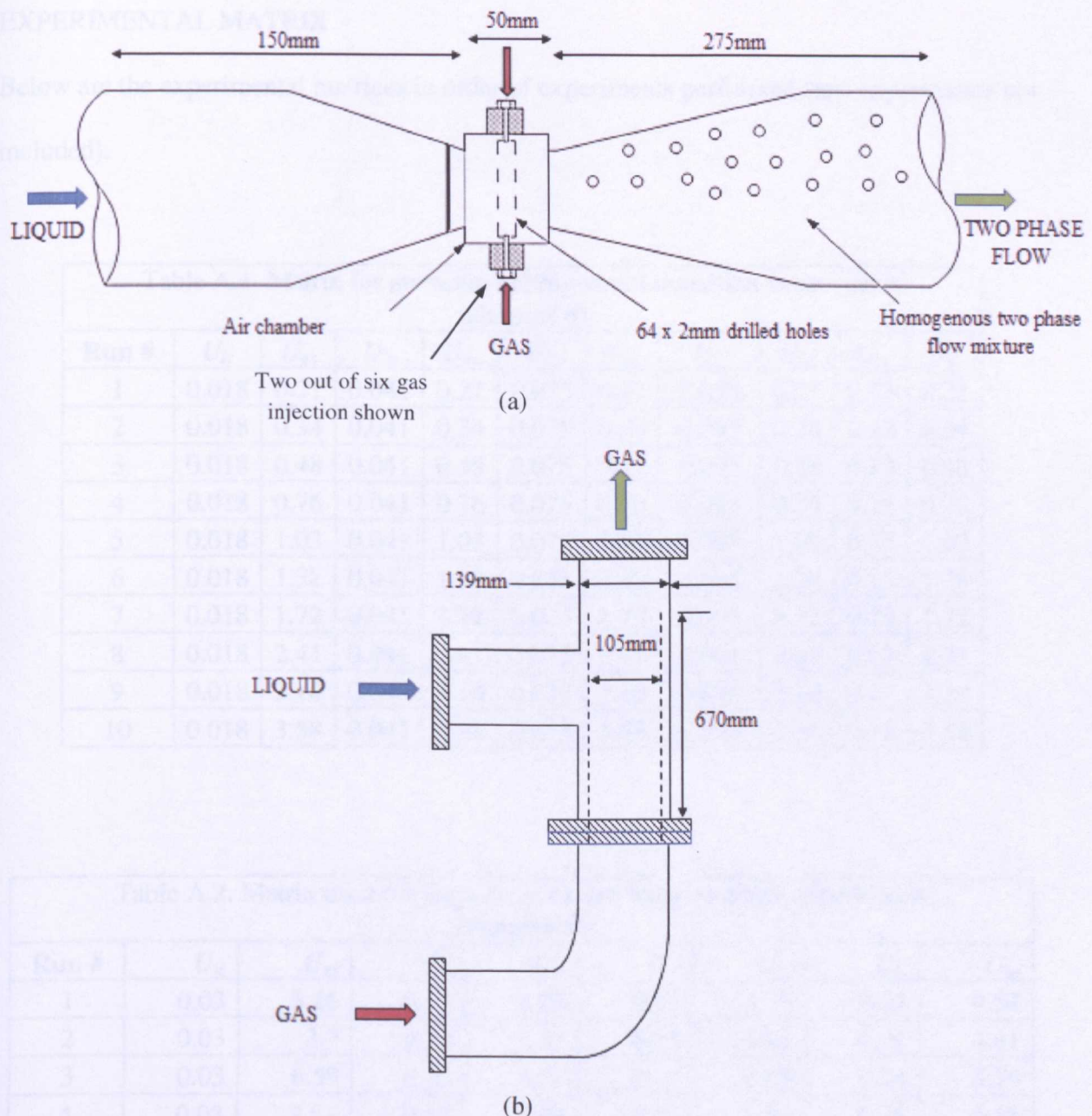


Figure A.1. Gas Liquid injection used in the 121mm internal diameter, 5.3m in length facility

and 127mm internal diameter, 11m in length facility in (a) and (b) respectively.

APPENDIX B

EXPERIMENTAL MATRIX

Below are the experimental matrices in order of experiments performed (test experiments not included).

**Table A.1. Matrix for air-water bubbly-churn transition experiments
(chapter 4)**

Run #	U_{ls}	U_{gs}								
1	0.018	0.21	0.041	0.21	0.075	0.21	0.095	0.21	0.13	0.21
2	0.018	0.34	0.041	0.34	0.075	0.34	0.095	0.34	0.13	0.34
3	0.018	0.48	0.041	0.48	0.075	0.48	0.095	0.48	0.13	0.48
4	0.018	0.76	0.041	0.76	0.075	0.76	0.095	0.76	0.13	0.76
5	0.018	1.03	0.041	1.03	0.075	1.03	0.095	1.03	0.13	1.03
6	0.018	1.38	0.041	1.38	0.075	1.38	0.095	1.38	0.13	1.38
7	0.018	1.72	0.041	1.72	0.075	1.72	0.095	1.72	0.13	1.72
8	0.018	2.41	0.041	2.41	0.075	2.41	0.095	2.41	0.13	2.41
9	0.018	3.10	0.041	3.10	0.075	3.10	0.095	3.10	0.13	3.10
10	0.018	3.58	0.041	3.58	0.075	3.58	0.095	3.58	0.13	3.58

**Table A.2. Matrix used for large-scale closed loop air-water experiments
(chapter 5)**

Run #	U_{ls}	U_{gs}	U_{ls}	U_{gs}	U_{ls}	U_{gs}	U_{ls}	U_{gs}
1	0.03	3.26	0.13	5.28	0.18	4.79	0.24	4.54
2	0.03	3.7	0.13	5.53	0.18	4.91	0.24	4.81
3	0.03	6.59	0.13	6.08	0.18	6.09	0.24	5.76
4	0.03	8.81	0.13	7.08	0.18	6.64	0.24	6.58
5	0.03	11.17	0.13	8.64	0.18	8.18	0.24	7.2
6	0.03	11.77	0.13	8.87	0.18	8.58	0.24	7.69
7	0.03	12.28	0.13	9.28	0.18	8.97	0.24	8.11
8	0.03	13.65	0.13	10.58	0.18	10.14	0.24	9.39
9	0.03	15.37	0.13	12.44	0.18	12.18	0.24	11.42
10	0.03	16.27	0.13	13.44	0.18	12.98	0.24	12.48
11	0.03	16.95	0.13	14.36	0.18	13.94	0.24	13.39
12	0.03	17.46	0.13	15.24	0.18	14.86	0.24	14.23

Table A.3. Matrix used for air-glycerol water experiments(chapter 6**)**

12.2cP Air-Glycerol/water experiments				
U_{ls} (m/s)	0.039	0.11	0.17	0.27
Run #	U_{gs} (m/s)			
1	6.21	4.85	4.41	4.19
2	6.72	5.53	5.12	4.81
3	8.34	6.22	5.81	5.51
4	10.17	7.86	7.52	7.17
5	10.9	9.69	8.31	7.98
6	12.04	9.84	9.58	9.31
7	12.6	10.46	10.28	9.72
8	13.06	11.04	10.74	10.33

16.2cP Air-Glycerol/water experiments				
U_{ls} (m/s)	0.036	0.091	0.16	0.26
Run #	U_{gs} (m/s)			
1	6.19	5.77	4.86	3.98
2	8.06	6.59	5.58	4.74
3	9.25	7.28	6.44	5.41
4	10.74	8.82	8.12	7.12
5	11.39	9.65	8.94	8.02
6	12.52	10.66	10.17	9.46
7	12.98	11.19	10.67	9.92
8	13.36	11.62	11.12	10.44

APPENDIX C

VOID FRACTION CORRELATIONS

Wallis (1969)

$$\frac{U_g^*}{(1 - 2.85(1 - \alpha_g))} + \frac{U_l^*}{2.85(1 - \alpha_g)} = 0.775 \quad (\text{C.1})$$

where

$$U_g^* = U_{gs} \left[\frac{\rho_g}{gD(\rho_l - \rho_g)} \right]^{0.5} \quad U_l^* = U_{ls} \left[\frac{\rho_l}{gD(\rho_l - \rho_g)} \right]^{0.5} \quad (\text{C.2})$$

Premoli *et al.* (1970)

$$U_R = 1 + E_1 \left(\frac{j}{1 + jE_2} - jE_2 \right)^{0.5} \quad \text{for } \frac{j}{1 + jE_2} > E_2 \quad (\text{C.3})$$

where

$$j = \frac{\alpha_{gH}}{1 - \alpha_{gH}}, \quad E_1 = 1.578 \text{Re}^{-0.19} \left(\frac{\rho_l}{\rho_g} \right)^{0.22}, \quad E_2 = 0.0273 \text{We} \text{Re}^{-0.51} \left(\frac{\rho_l}{\rho_g} \right)^{-0.08} \quad (\text{C.4})$$

$$\text{Re} = \frac{(M_l + M_g)D}{\eta_l}, \quad \text{We} = \frac{\rho_l(M_l + M_g)^2 D}{\sigma} \quad (\text{C.5})$$

Chisholm (1972)

$$\alpha_g = \frac{1}{1 + U_R \frac{1 - x_g}{x_g} \frac{\rho_g}{\rho_l}} \quad (\text{C.6})$$

where

$$U_R = \frac{U_g}{U_l} = \left[1 - x_g \left(1 - \frac{\rho_l}{\rho_g} \right) \right]^{\frac{1}{2}} \quad (\text{C.7})$$

Hassan (1988)

$$\alpha_g = \frac{U_{gs}}{1.15U_m + 0.345 \sqrt{\frac{gD}{\rho_l} (\rho_l - \rho_g)}} \quad (\text{C.8})$$

where $U_m = U_{gs} + U_{ls}$

Cioncolini and Thome (2012)

$$\alpha_g = \frac{hx^n}{1 + (h-1)x^n}; 0 < x < 1, \quad 10^{-3} < \frac{\rho_g}{\rho_l} < 1, \quad 0.7 < \alpha_g < 1 \quad (C.9)$$

$$h = -2.129 + 3.129 \left(\frac{\rho_g}{\rho_l} \right)^{-0.2186} \quad (C.10)$$

$$n = 0.3487 + 0.6513 \left(\frac{\rho_g}{\rho_l} \right)^{0.5150} \quad (C.11)$$

APPENDIX D

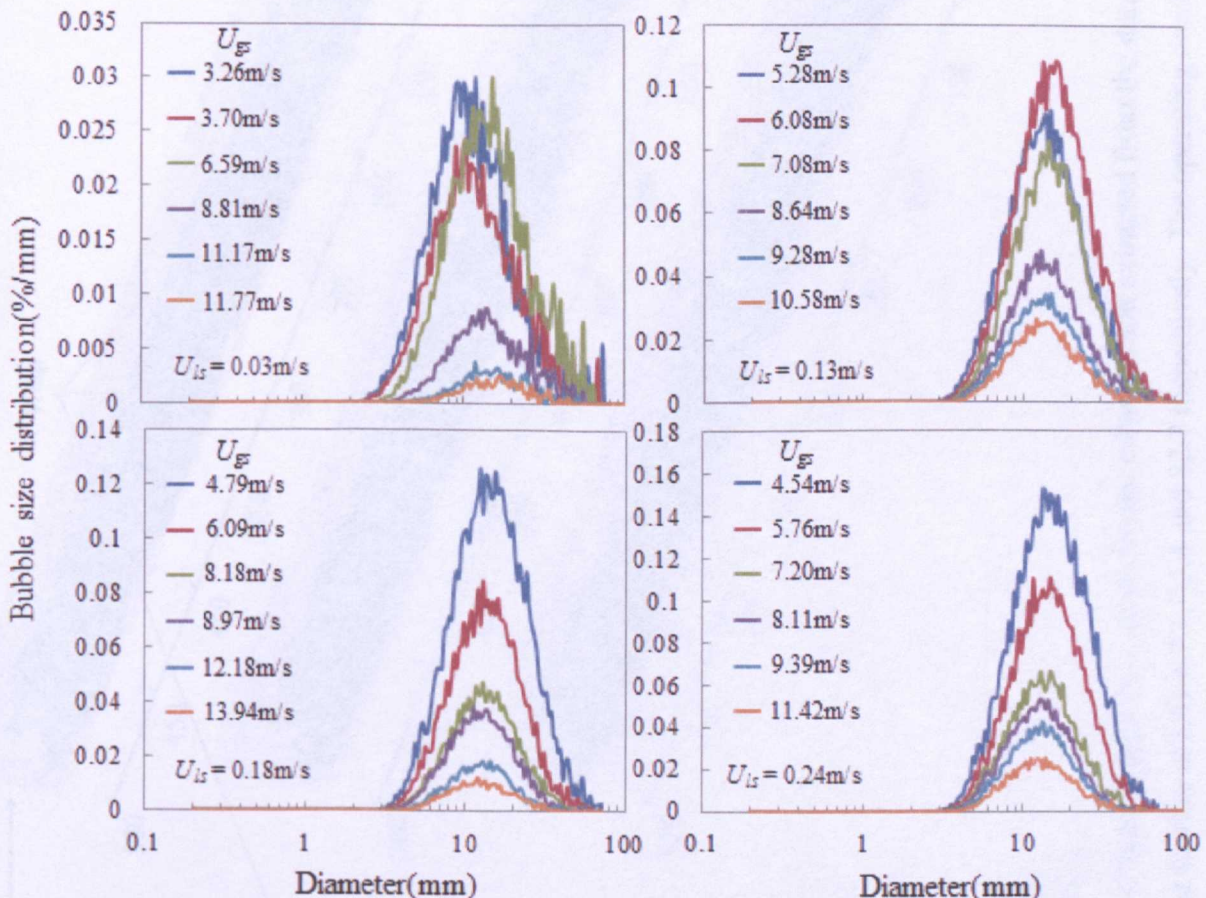


Figure D.1. Bubble size distribution from experiments performed on the large-scale closed loop facility. Air and water are the operating fluids for data at L/D = 35.4. An indication of the decrease in gas entrainment as gas superficial velocity increases.

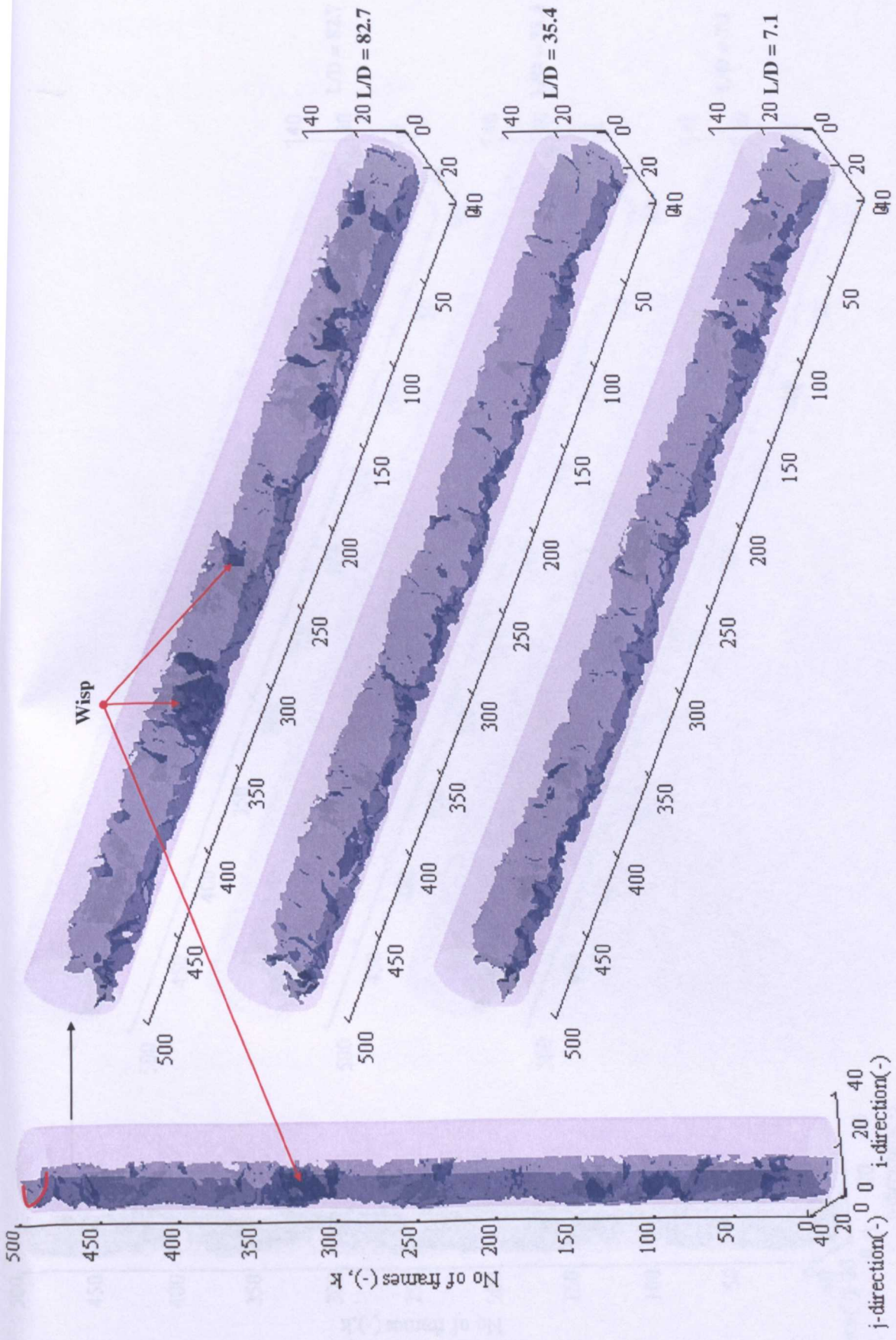


Figure D.2. Interfaces within the pipe on a semi-circular cross section extracted from the data acquired for air-water experiments on the 127mm internal diameter facility at $L/D = 7.1$, 35.4 and 82.7 respectively. The operating conditions are $U_{gs} = 7.08\text{m/s}$ and $U_s = 0.13\text{m/s}$. Comparisons can be made to the work of Sekoguchi and Takeishi (1989) in Figure 2.27.

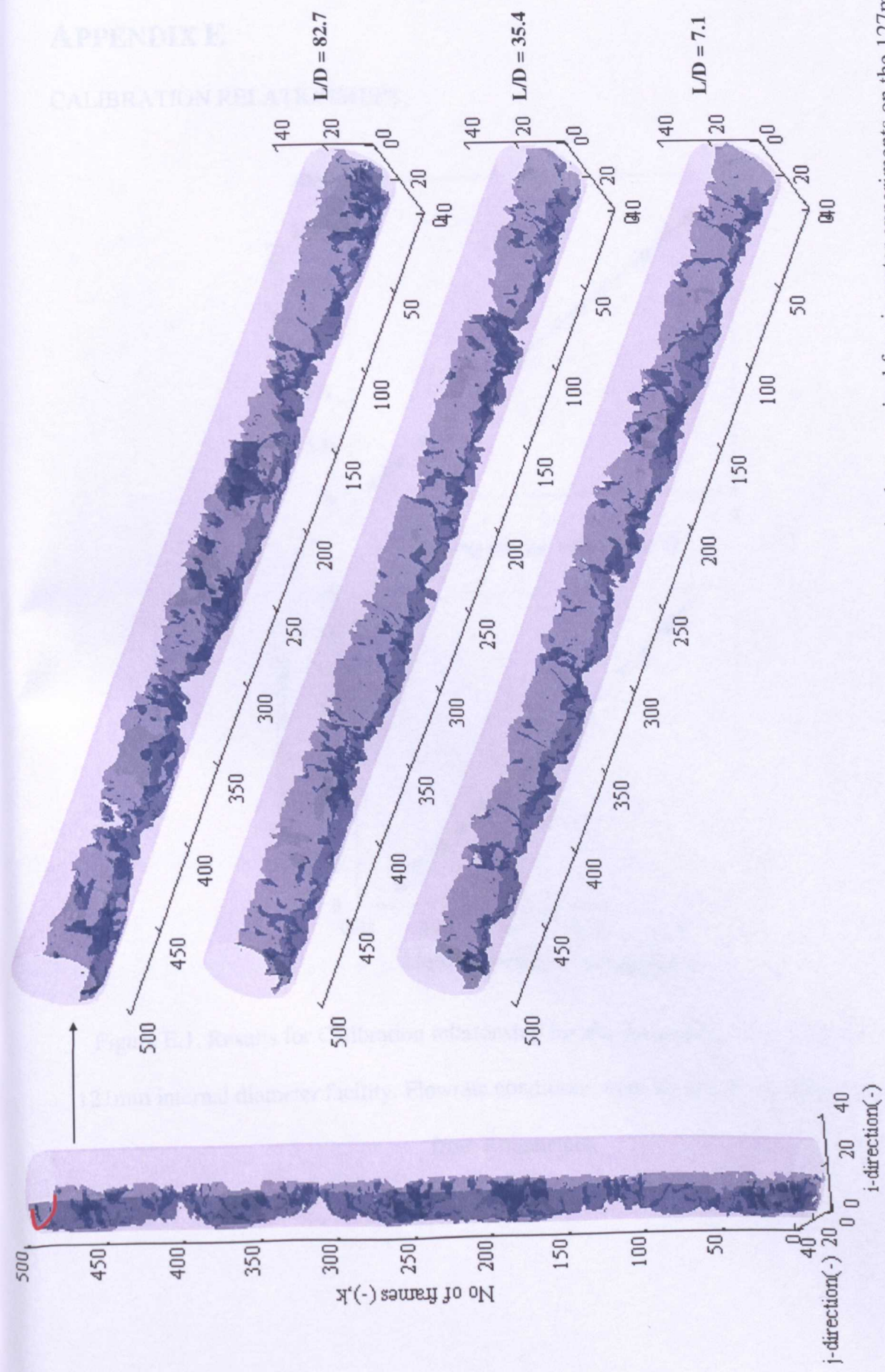


Figure D.3. Interfaces within the pipe on a semi-circular cross section extracted from the data acquired for air-water experiments on the 127mm internal diameter facility at $L/D = 7.1$, 35.4 and 82.7 respectively. The operating conditions are $U_{gs} = 7.08\text{m/s}$ and $U_{ls} = 0.24\text{m/s}$. Comparisons can be made to the work of Sekoguchi and Takeishi (1989) in Figure 2.27.

APPENDIX E

CALIBRATION RELATIONSHIPS

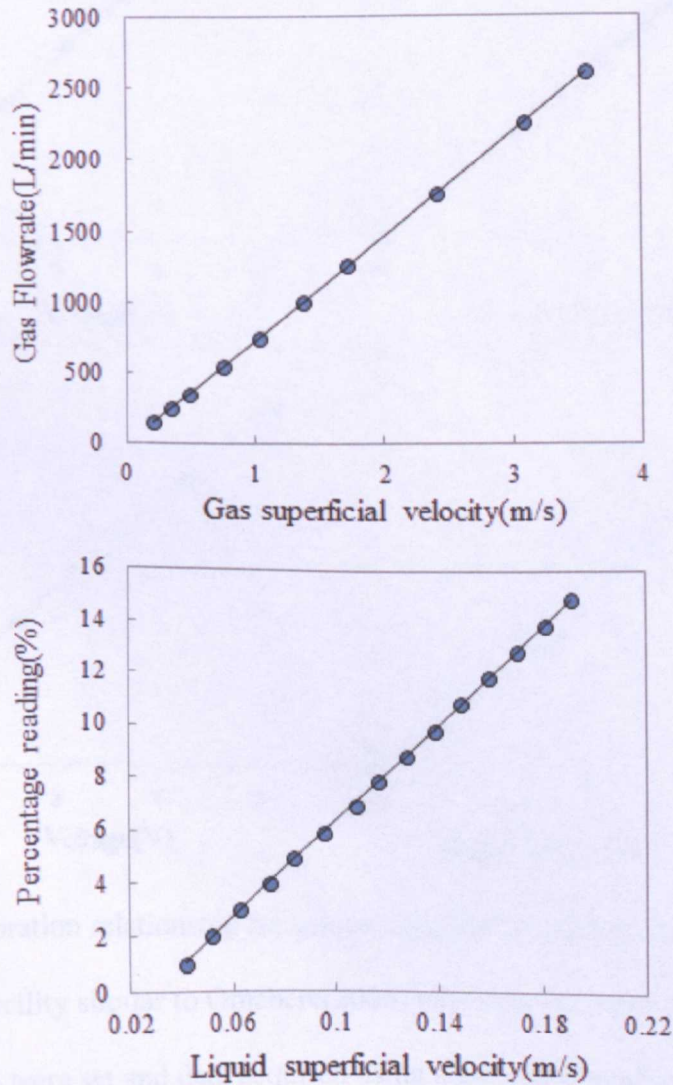


Figure E.2. Calibration

internal diameter facility

Flowrate conditions were set and

Figure E.1. Results for Calibration relationship for the gas and liquid flowmeters on the

121mm internal diameter facility. Flowrate conditions were set and data acquired manually

from Rotameters.

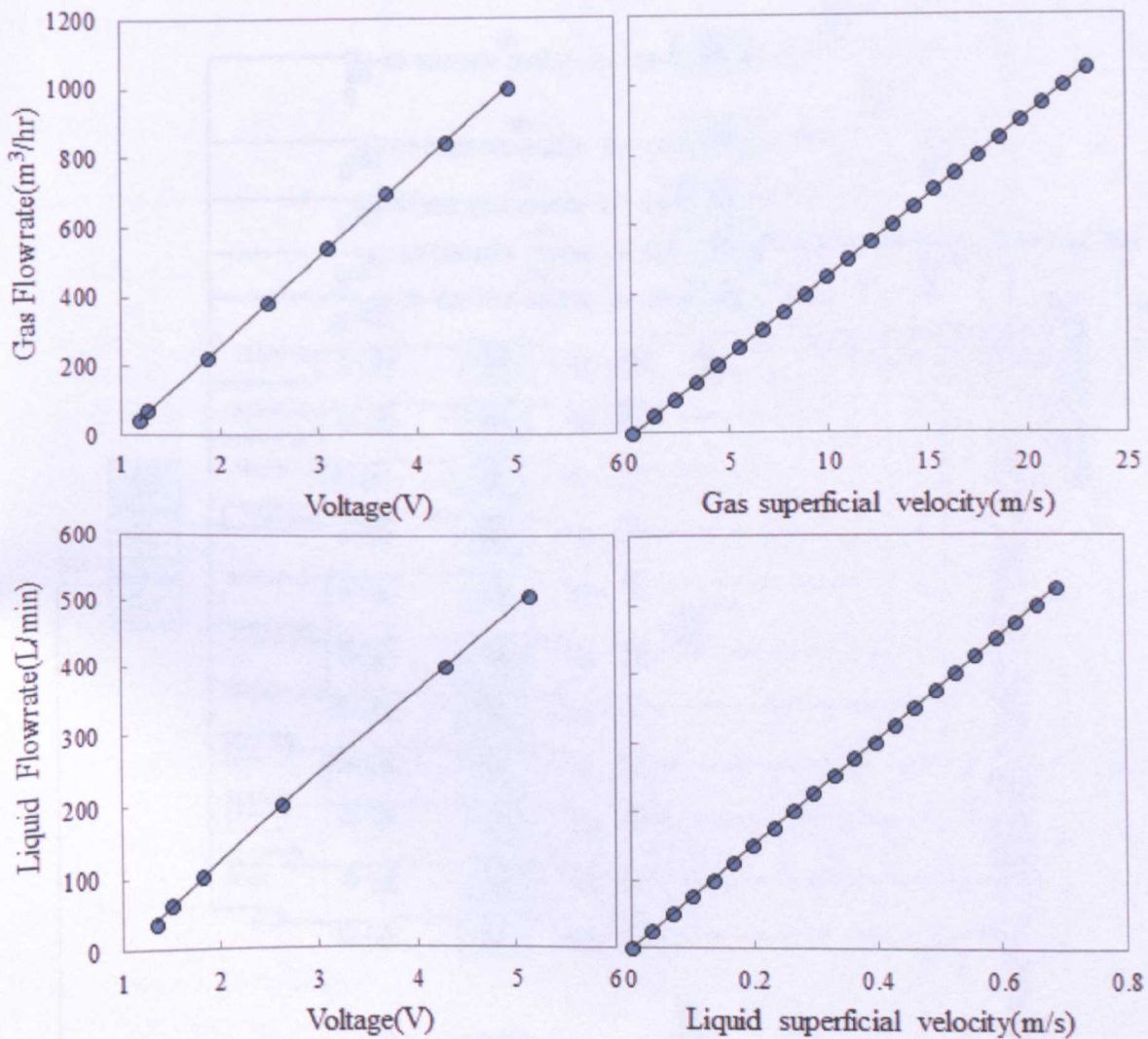


Figure E.2. Calibration relationship for gas and liquid flowmeters used on the 127mm internal diameter facility similar to Omebere(2006) who experimented on the same facility. Flowrate conditions were set and data acquired using a Labview program as shown in figure D.3.

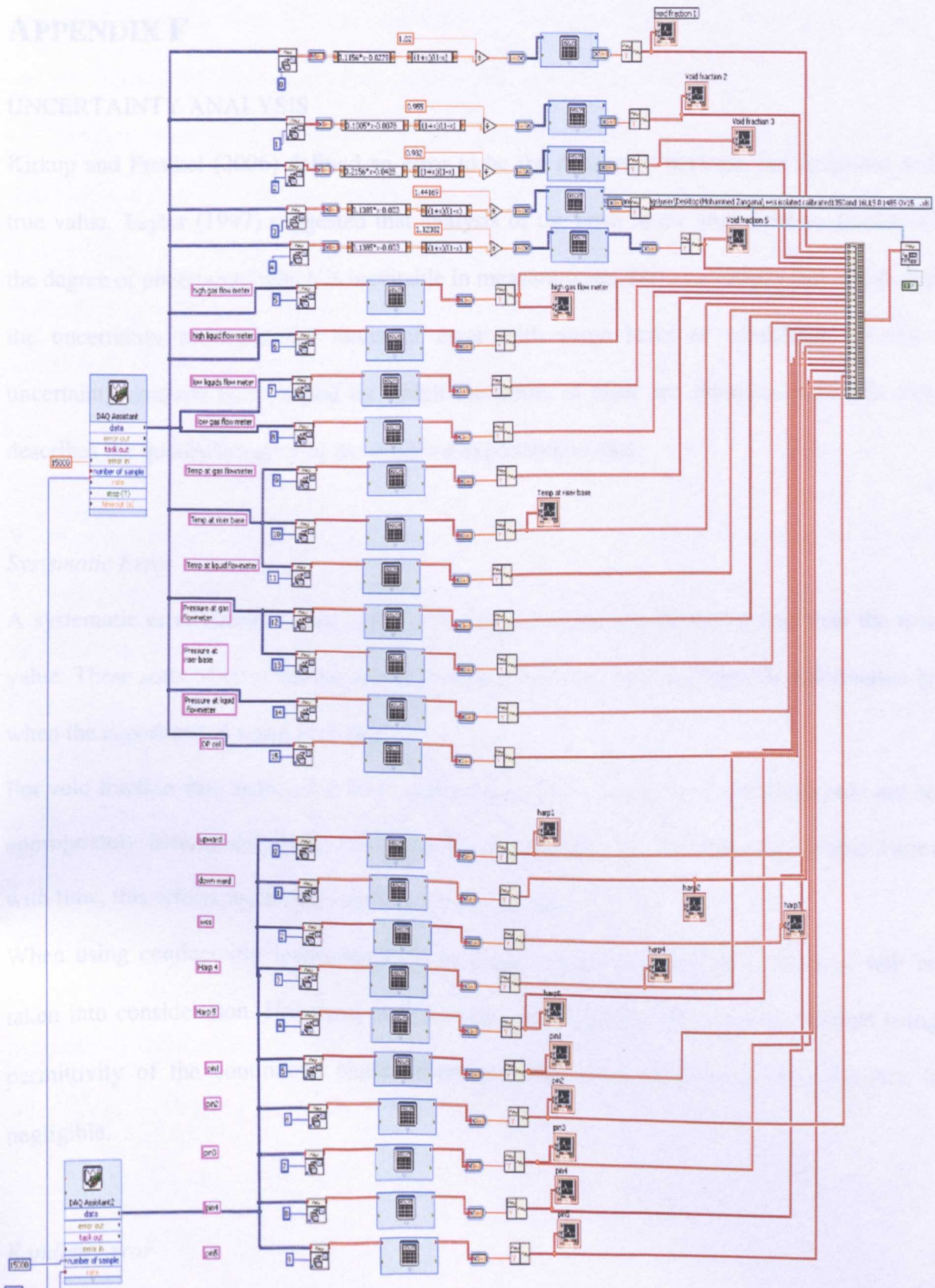


Figure E.3. Labview Data acquisition program used in flowrate acquisition for experiments

on the 127mm internal diameter facility.

APPENDIX F

UNCERTAINTY ANALYSIS

Kirkup and Frenkel (2006) defined an error to be the difference between the measured and true value. Taylor (1997) suggested that analysis of the error is the study and evaluation of the degree of uncertainty which is inevitable in measurements. Holman (2002) also stated that the uncertainty estimates the limits of error with some level of confidence. Overall, uncertainty analysis is a method by which the limits of error are estimated which in turn describes the quality/integrity of the acquired experimental data.

Systematic Error

A systematic error causes a measured value to be consistently greater or less than the true value. These sorts of error can be revealed in two ways: by means of specific information or when the experimental setup is changed.

For void fraction data acquired in this research work, the systematic uncertainty could not be appropriately determined. However, since the temperature of the continuous phase varies with time, this affects the surface tension, hence the void fraction.

When using conductivity instrumentation to acquire void fraction data, the above will be taken into consideration. However, in this study, void fraction data has been derived using permittivity of the continuous phase. Therefore, the effect of temperature difference is negligible.

Random Error

The difference between random errors and systematic error is best observed when the experiments are repeated using the same flow parameters. The aim of repeating the experiments or carrying out test experiments is to check the error while obtaining

reproducible results. However, since the WMS instrument will be affected by uncontrollable and small changes in the environment, exact results may not be obtained.

For instance, when using the WMS to acquire data under Churn flow conditions, the chaotic nature of the flow (during liquid bridging of the gas core) vibrated the test section. This in turn vibrates the WMS transmitter and receiver wires respectively, thus, generating instrumental noise that will affect the void fraction. However, as discussed in chapter 3, Thiele *et al.* (2009), suggested that this has a negligible effect on the void fraction itself.

Uncertainty propagation

When a parameter is not directly measured, but calculated from two or more directly measured parameters, the uncertainty in the derived parameter must be determined from the uncertainties in the measured parameters. This is the concept of propagation of uncertainty. Uncertainty propagation analysis was carried out for both gas and liquid superficial velocities.

If y is a given function of the independent variables x_1, x_2, \dots, x_n . The relationship can then be given as:

$$y = f(x_1, x_2, \dots, x_n) \quad (\text{E.1})$$

If δy is the uncertainty in the result and $\delta x_1, \delta x_2, \dots, \delta x_n$ are the uncertainties in the independent variables then δy can be given as:

$$\delta y = \frac{\partial y}{\partial x_1} \delta x_1 + \frac{\partial y}{\partial x_2} \delta x_2 + \dots + \frac{\partial y}{\partial x_n} \delta x_n \quad (\text{E.2})$$

where $\partial y / \partial x_1, \partial y / \partial x_2, \dots, \partial y / \partial x_n$ are the first-order partial derivatives of y with respect to x_1, x_2, \dots, x_n respectively.

(a) *Uncertainty in gas superficial velocity*

The gas superficial velocity U_{gs} is calculated from the measured mass flowrate of air M_g and the density of air, ρ_g .

$$U_{gs} = \frac{M_g}{\rho_g} \quad (E.3)$$

Also,

$$PV = nRT \quad (E.4)$$

where P, V, n, R and T are the pressure, volume, number of moles, Molar gas constant and temperature of the gas phase respectively. The number of moles can be calculated as follows:

$$n = \frac{m}{M} \quad (E.5)$$

where m and M are the mass and molar mass respectively of the gas phase.

When equation (E.5) is substituted in equation(E.4), taking equation(E.3) into consideration, the density of the gas phase and gas superficial velocity can also be calculated as:

$$\rho_g = \frac{PM}{RT} = \frac{P}{RT} \quad (E.6)$$

$$U_{gs} = \frac{M_g RT}{P} \quad (E.7)$$

The partial derivatives of U_{gs} with respect to T , M_g and P are:

$$\frac{\partial U_{gs}}{\partial T} = \frac{\partial}{\partial T} \left(\frac{M_g RT}{P} \right) = \frac{M_g R}{P} \quad (E.8)$$

$$\frac{\partial U_{gs}}{\partial M_g} = \frac{\partial}{\partial M_g} \left(\frac{M_g RT}{P} \right) = \frac{RT}{P} \quad (E.9)$$

$$\frac{\partial U_{gs}}{\partial P} = \frac{\partial}{\partial P} \left(\frac{M_g RT}{P} \right) = -\frac{M_g RT}{P^2} \quad (E.10)$$

The uncertainties in the calculated values of U_{gs} are then calculated as

$$\delta U_{gs} = \pm \sqrt{\left(\partial T \frac{M_g R}{P} \right)^2 + \left(\partial P \frac{-M_g RT}{P^2} \right)^2 + \left(\partial M_g \frac{RT}{P} \right)^2} \quad (E.11)$$

where $\partial P, \partial M_g, \partial T$ are the uncertainties in the pressure, mass flux and temperature within the test section respectively.

(b) *Uncertainty in liquid superficial velocity*

The liquid superficial velocity, U_{ls} , is calculated from the measured flow rate of the liquid and the cross-sectional area of the test section A_c .

$$U_{ls} = \frac{M_l}{A_c} \quad (\text{E.12})$$

This can also be expressed as a function of M_l and D as follows:

$$U_{ls} = \frac{4M_l}{\pi D^2} \quad (\text{E.13})$$

The partial derivatives of U_{ls} with respect to M_l and D are

$$\frac{\partial U_{ls}}{\partial M_l} = \frac{4}{\pi D^2} \frac{\partial}{\partial M_l} (M_l) = \frac{4}{\pi D^2} \quad (\text{E.14})$$

$$\frac{\partial U_{ls}}{\partial D} = \frac{4M_l}{\pi} \frac{\partial}{\partial D} \left(\frac{1}{D^2} \right) = -\frac{8M_l}{\pi D^3} \quad (\text{E.15})$$

The uncertainties in U_{ls} are then calculated as following:

$$\partial U_{ls} = \pm \sqrt{\left(\partial M_l \frac{4}{\pi D^2} \right)^2 + \left(\partial D \frac{-8M_l}{\pi D^3} \right)^2} \quad (\text{E.16})$$

where ∂D the uncertainty in the diameter and ∂M_l is the uncertainty in the measured liquid flow rate.

(c) *Uncertainty in mixture velocity*

The mixture velocity is obtained from both gas and liquid superficial velocities.

$$U_m = U_{ls} + U_{gs} \quad (\text{E.17})$$

The uncertainties in both phase velocities are:

$$\partial U_m = \partial U_{ls} + \partial U_{gs} \quad (\text{E.18})$$

$$\partial U_m = \pm \sqrt{(\partial U_{ls})^2 + (\partial U_{gs})^2} \quad (E.19)$$

The values of ∂U_{ls} and ∂U_{gs} in equations (E.11) and (E.16) are then substituted in the above equation (E.19) to obtain ∂U_m .